PACIFIC EARTHQUAKE ENGINEERING RESEARCH CENTER

Earthquake Simulator Tests on Reducing Residual Displacements of Reinforced Concrete Bridge Columns

Junichi Sakai

Stephen A. Mahin

Andres Espinoza

Pacific Earthquake Engineering Research Center
University of California, Berkeley

PEER Report No. 2005/17
Pacific Earthquake Engineering Research Center
Headquarters at the University of California, Berkeley

December 2005

PEER 2005/17
December 2005

Earthquake Simulation Tests on Reducing Residual Displacements of Reinforced Concrete Bridge Columns

Junichi Sakai

Stephen A. Mahin

Andres Espinoza

Pacific Earthquake Engineering Research Center
University of California, Berkeley

PEER Report 2005/17
Pacific Earthquake Engineering Research Center
College of Engineering
University of California, Berkeley

December 2005

ABSTRACT

Bridge columns located in regions of high seismicity are generally designed with a large ductility capacity. Although this design strategy is both economical and prevents collapse, such columns develop high ductility demands when subjected to strong-ground motion, resulting in large permanent displacements. To minimize such residual displacements in reinforced concrete (RC) columns, a design is proposed whereby longitudinal post-tensioning strands replace some of usual longitudinal mild reinforcing bars. The seismic performance of such partially prestressed RC columns under near-field strong ground excitation is investigated through a series of earthquake simulation tests.

Based on the results from a series of quasi-static and dynamic analyses conducted prior to the tests, a partially prestressed RC column model was designed that varied the configuration of the tendon, the number of the tendons and longitudinal mild reinforcement, and the prestressing force.

The earthquake simulation tests demonstrated that (1) the proposed design reduced residual displacement significantly; (2) the proposed design did not result in an increase in the maximum response displacement, despite reduced energy dissipation; and (3) the proposed design did not affect the failure mode. To offset the advantage gained by replacing mild reinforcing bars with unbonded tendons to mitigate residual displacements post-event, the tests also revealed the vulnerability of the proposed design to aftershocks.

ACKNOWLEDGMENTS

This work was supported in part by the Earthquake Engineering Research Centers Program of the U.S. National Science Foundation (NSF) under Award Number EEC-9701568 through the Pacific Earthquake Engineering Research Center (PEER). Any opinions, findings, and conclusions or recommendations expressed in this material are those of the author(s) and do not necessarily reflect those of NSF, PEER, or the University of California.

The thoughtful help and advice provided by the PEER staff, where most of this work was conducted, are gratefully appreciated. In particular, the authors extend their appreciation to Don Clyde, Wesley Neighbour, and David MacLam for their assistance in conducting the earthquake simulation tests.

CONTENTS

LIST OF TABLES

LIST OF FIGURES

1 Introduction

1.1 RESEARCH BACKGROUND

The poor performance of reinforced concrete (RC) bridge columns during the 1971 San Fernando, California, earthquake prompted a significant amount of research on the ductility capacities of RC bridge columns. As a result of this research, the ductility capacities of columns have been improved, and total collapse of bridges, as seen in the 1971 earthquake, is now preventable with current seismic engineering technology. Unfortunately, bridge columns designed to produce high ductility demands are likely to retain large permanent deformations following extreme ground shaking, resulting in the long-term closure of highways and significant repair costs. Thus, mitigation of such permanent deformations of bridge columns following seismic events has resulted in a major research effort.

A recent analytical study conducted by the authors [Sakai and Mahin 2004] proposed a new method to reduce such residual displacements by incorporating an unbonded prestressing strand at the center of a lightly reinforced cross section of a column. The study demonstrated the following: (1) incorporating an unbonded prestressing strand at the center of a lightly reinforced concrete cross section can achieve restoring force characteristics similar to a conventional RC column on loading but with substantially less residual displacement upon unloading; and (2) columns with unbonded center strands perform very well under uni-directional dynamic excitation with a relatively larger post-yield stiffness; the response displacements are only 10% larger than those of conventionally designed columns, while the residual displacements can be reduced by about 50%.

Although the analytical results show the effectiveness of the newly proposed design on reducing residual displacements, some uncertainties remain concerning the seismic performance of the proposed bridge columns, such as the behavior under bi-directional loading condition, the P-delta effects, etc.. To validate the effectiveness of this approach in improving seismic performance and study the dynamic behavior of the columns, earthquake simulation tests were conducted.

1.2 PREVIOUS RESEARCH

1.2.1 Studies on the Performance of Partially Prestressed Reinforced Concrete Columns

In the last decade, analytical and experimental research has been conducted to developed design strategies to reduce the residual displacements of RC bridge columns subjected to strong ground shaking and improve the seismic performance of partially prestressed RC columns. One such study can be found in a report by Sakai and Mahin [2004].

Several experimental studies on partially prestressed columns or columns with unbonded high-strength steel bars have been conducted under uni-directional quasi-static or pseudo-dynamic loading conditions. Ikeda [1998] and Zatar and Mutsuyoshi [2000], respectively, conducted a series of static and pseudo-dynamic tests for partially prestressed concrete bridge columns. Iemura et al. [2002] proposed using unbonded high-strength bars in RC bridge columns and investigated the effectiveness of the proposed design through quasi-static loading tests. Hewes and Priestley [2001] investigated the seismic performance of an unbonded post-tensioned precast concrete segmental bridge column through quasi-static loading tests.

These studies validated the seismic performance of partially prestressed concrete columns or similar columns under quasi-static uni-directional loading. To date, however, no earthquake simulation tests or tests under bi-directional conditions have been performed.

1.2.2 Earthquake Simulation Tests for Circular Reinforced Concrete Columns

A number of earthquake simulation tests have been performed on circular spirally RC columns. Most of these tests were tested under uni-directional loading conditions but with relatively small sections [i.e., 200 mm (7.9 in.) in diameter] because of the limited capacity of test facilities. Few studies on the dynamic behavior of columns under bi-directional loading are available. More detailed information of previous research on earthquake simulation tests can be found in Hachem et al. [2003].

Dodd and Cook [1992] and Kowalsky et al. [1997] tested 200-mm circular columns under uni-directional loading, respectively. Laplace et al. [2001], Yen et al. [2003], and Park et al. [2003] conducted shaking table tests on relatively larger specimens, but they were loaded uni-directionally. Hachem et al. [2003] conducted a series of earthquake simulation tests for circular RC columns designed according to a relatively new design code. The effects of multi-directional loading were investigated for a 406-mm- (16 in.-) diameter column, demonstrating that the bi-directionally loaded columns behaved similarly to the uni-directionally loaded columns under a design-level earthquake excitation.

1.3 RESEARCH SCOPE AND ORGANIZATION

The research presented herein describes earthquake simulation tests to determine the seismic performance of partially prestressed RC bridge columns under near-field strong-ground excitation. Chapter 2 details the design of RC bridge column models tested, construction of the models, material properties, and ground motions selected. Test set-up, instrumentation, and data acquisition are described in Chapter 3. Chapter 4 summarizes the dynamic behavior of a conventional RC column and a partially prestressed RC column under earthquake excitation. An analytical simulation of the dynamic behavior of the columns is presented in Chapter 5. Conclusions and recommendations are presented in Chapter 6.

2 Design and Construction of Bridge Column Specimens

A simple RC bridge column commonly used in bridge design in California was selected as a prototype column [Sakai and Mahin 2004]. The column was designed in accordance with the California Department of Transportation's *Seismic Design Criteria* (SDC) [Caltrans 2001]. Figure 2.1 shows the cross section, dimensions, and reinforcement of the prototype column. The column is 1.83 m (6 ft) in diameter, and the height from the bottom of the column to the center-of-gravity of the superstructure is 10.97 m (36 ft), for an aspect ratio of 6. The dead load, *P*, is assumed to be 4.5 MN. For the 34.5 MPa (5 ksi) unconfined concrete strength f'_{co} assumed, the ratio of axial force to nominal axial force capacity, $P/f'_{co}A_g$, is 5%. The inertial mass and the rotational moment of inertia of the superstructure are assumed to be 4.62×10^5 kg and 3.2×10^6 kg m^2, respectively.

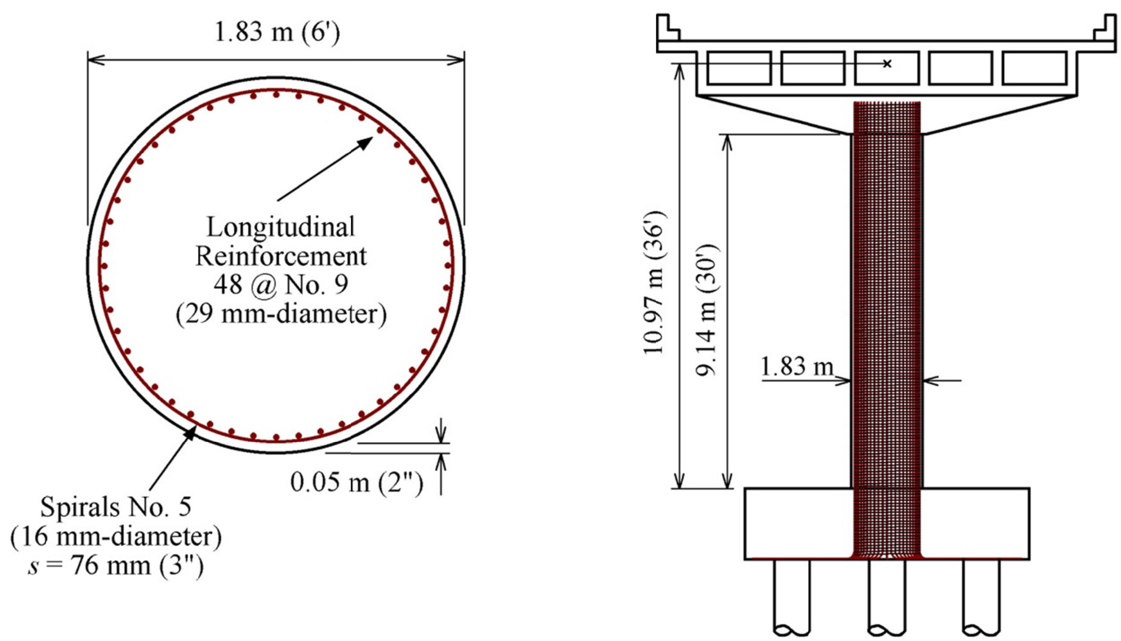

(a) (b)

Figure 2.1 Prototype column: (a) cross section and (b) bridge column.

The prototype column was reinforced longitudinally with 48 No. 9 [29-mm- (1.1-in.-) diameter] deformed bars, providing a longitudinal reinforcement ratio, ρ_l, of 1.18%. No. 5 [16-mm- (0.6-in.-) diameter) spirals were used to confine the concrete core; these were spaced at 76-mm (3-in.) pitch, resulting in a volumetric ratio ρ_s, of 0.61%. Reinforcing bars with a nominal yield strength of 420 MPa (Grade 60) were used for both the longitudinal and spiral reinforcement.

For a lateral load applied at the center-of-gravity of the superstructure, the static pushover analysis procedures recommended by the SDC resulted in an ultimate lateral load capacity of 1.29 MN, and a yield and ultimate displacement of 0.11 m (4.33 in.) and 0.58 m (22.83 in.), respectively, as shown in Figure 2.2. Thus, the column has a displacement ductility capacity of 5.2. The effective natural period of column was determined to be 1.26 sec.

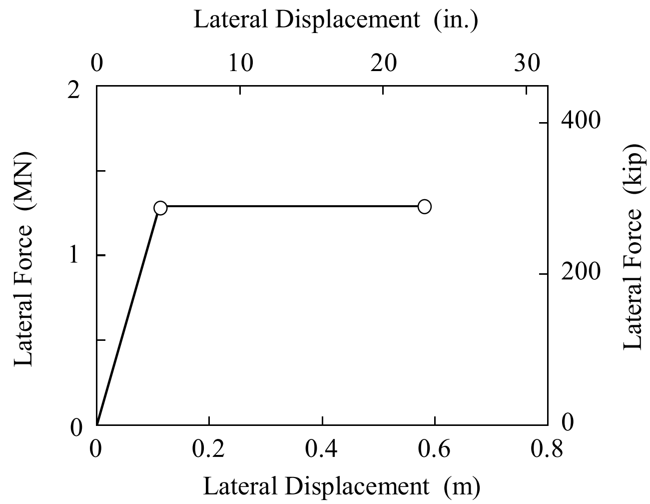

Figure 2.3 Ductility and flexural capacity of prototype column.

2.2 DESIGN OF SPECIMENS

2.2.1 Dimensional Analysis

Based on the capacity of the earthquake simulator at the University of California, Berkeley, and the configurations of specimens previously tested on the simulator, the diameter of the specimens was set at 406 mm (16 in.), resulting in a scale factor in length to the prototype column of 4.5.

Dimensional analyses [Krawinkler and Moncarz 1982] were conducted to determine appropriate scaling factors of other physical quantities and dimensions of the specimens. Dimensional similitude requirements for dynamic tests were determined with the following conditions: (1) the above scale factor in length was used; (2) the acceleration of gravity was maintained; and (3) modulus of elasticity of materials was identical. These conditions are expressed as follows:

$$L = 4.5 \tag{2.1}$$

$$LT^{-2} = 1 \tag{2.2}$$

$$ML^{-1}T^{-2} = 1 \tag{2.3}$$

According to the analyses, the three basic dimensions, mass, *M*, length, *L*, and time, *T*, were determined to be 20.25, 4.5, and 2.12, respectively. Table 2.1 summarizes the dimensions of physical quantities and target scaling factors. Weight density of concrete, inertia mass, and rotational moment of inertia was scaled by a factor of 0.22, 20.25, and 410.1, respectively. Strain and stress were identical as the same materials were used for both the prototype column and the specimen.

Table 2.1 Dimension of physical quantities and target scaling factors.

Physical quantity	Dimension		Target scale factor
Length	L	S	4.5
Acceleration	LT^{-2}	1	1
Modulus of elasticity	$ML^{-1}T^{-2}$	1	1
Time	T	$\sqrt{S}$	2.12
Frequency	T^{-1}	$1/\sqrt{S}$	0.471
Velocity	LT^{-1}	$\sqrt{S}$	2.12
Displacement	L	S	4.5
Area	L^2	S^2	20.25
Mass	M	S^2	20.25
Rotational mass	ML^2	S^4	410.06
Force	MLT^{-2}	S^2	20.25
Stiffness	MT^{-2}	S	4.5
Moment	ML^2T^{-2}	S^{-3}	91.13
Energy	ML^2T^{-2}	S^{-3}	91.13
Weight density	$ML^{-2}T^{-2}$	$1/S$	0.222
Strain	1	1	1
Stress	$ML^{-1}T^{-2}$	1	1

2.2.2 Conventionally Reinforced Concrete Column Specimen

The conventional specimen was designed following the target scale factors listed in Table 2.1 and will subsequently be referred to as the RC specimen. Figure 2.3 shows the effective height of the specimen with weighted blocks, which represent superstructure of the prototype bridge; Figure 2.4 shows the cross section and reinforcement details of the specimen. Figure 2.5 shows the assembled reinforcement of the column before the concrete was cast.

As mentioned above, the column was 0.41 m (16 in.) in diameter, and the height from the bottom of the column to the center-of-gravity of the assembly of the top slab and weighted blocks was 2.44 m (8 ft). The column was reinforced with 12 No. 4 [13-mm- (0.51-in.-) diameter] deformed bars longitudinally, and with W3.5 5.4-mm- (0.21in.-) diameter round wire at 32 mm (1.25 in.)-pitch as spiral reinforcement. The longitudinal reinforcement ratio, ρ_l, and the volumetric ratio of spiral reinforcement, ρ_s, are 1.19% and 0.76%, respectively. Normal density of concrete was used, and the design strength of concrete, f'_{co}, was specified to be 34.5 MPa (5 ksi). Grade 60 reinforcing bars were used for the longitudinal reinforcement, and Grade 80 wires were used for the spirals. The nominal yield strengths of the steels were 420 MPa and 550 MPa, respectively.

The dead load due to the top slab and the three weighted blocks was 290 kN (88 kip), resulting in an axial force ratio of 6.5%. The inertial mass and the rotational moment of inertia of the assembly of the top slab and weighted blocks were 2.9×10^4 kg and 2.6×10^4 kg m^2, respectively.

According to the static pushover analysis procedures recommended by the SDC, the yield and ultimate displacements, and lateral strength were determined to be 0.026 m (10.24 in.), 0.21 m (8.3 in.), and 67.6 kN (15 kip), respectively, as shown in Figure 2.6. Based on an equation proposed by Priestley et al. (1996), a plastic hinge length of 0.328 m (12.91 in.) was assumed. The ductility capacity of the column was 8, and the effective natural period of specimen was 0.67 sec.

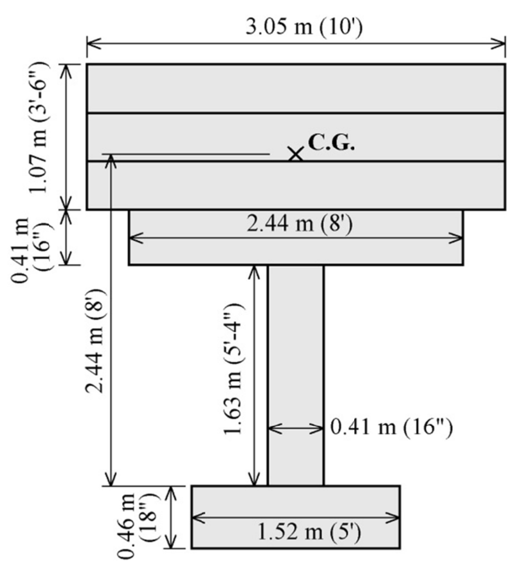

Figure 2.3 Specimen with weighted blocks.

.

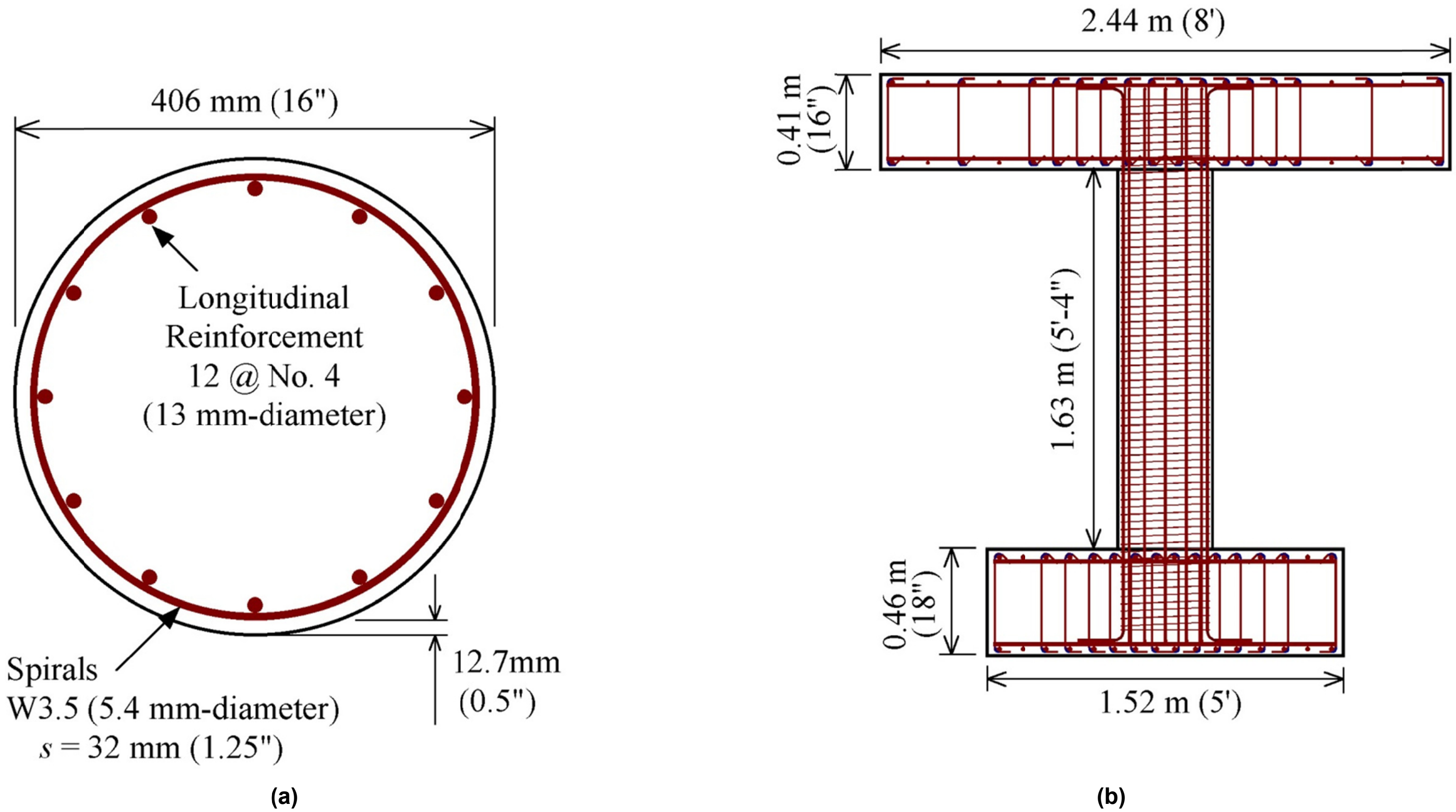

Figure 2.4 **Reinforcement details of conventional reinforced concrete column specimen: (a) cross section and (b) specimen.**

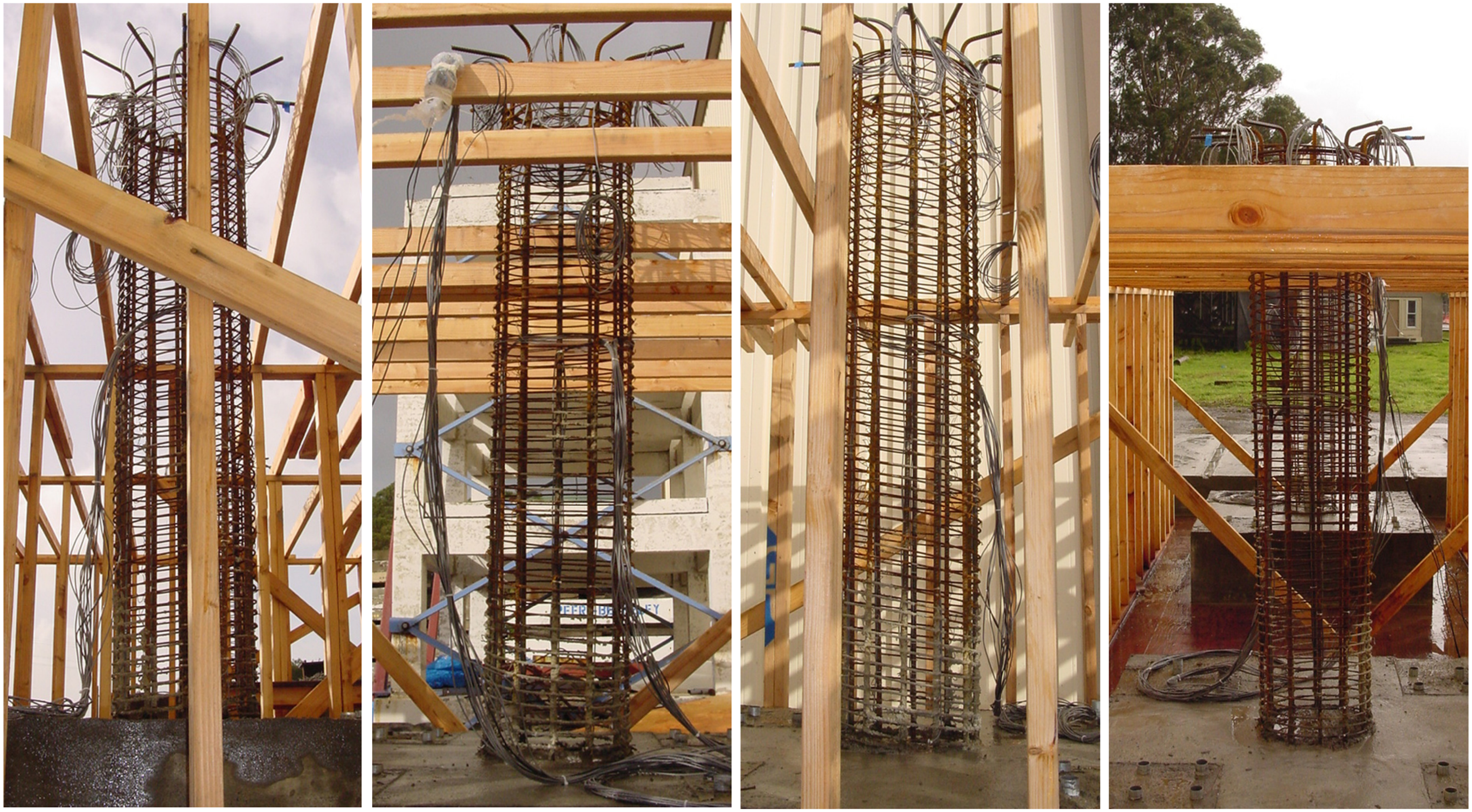

(a) (b) (c) (d)

Figure 2.5 Reinforcement of RC specimen: (a) north face; (b) east face; (c) south face; and (d) west face.

Table 2.2 compares the scale factors used in design of the specimen with the target scale factors. The RC specimen was designed based on the results from the dimensional analyses with the following exceptions: the specimen had a relatively large volumetric ratio of spiral reinforcement to avoid undesirable shear failure; this resulted in 50%-larger ductility capacity than the prototype column. The weight density was much smaller because normal density concrete was used instead of high-density concrete (which is not commonly used in bridge construction). In addition, the rotational mass of the test specimen was more than three times larger because of the large concrete blocks on the top of the specimen.

Table 2.2 Target scale factors and scale factors used.

Physical quantities	Target	Prototype	Specimen	S.F. used
Diameter (m)	4.5	1.83	0.406	4.5
Effective height (m)	4.5	10.97	2.438	4.5
Aspect ratio	1	6	6	1
Thickness of cover concrete (mm)	4.5	50.8	12.7	4
Diameter of longitudinal bar (mm)	4.5	28.7 (No. 9)	12.7 (No. 4)	2.26
No. of bars	1	48	12	4
Total area of longitudinal bar (mm^2)	20.25	0.03096	0.00155	20
Longitudinal rebar ratio (%)	1	1.18%	1.19%	0.99
Diameter of spiral (mm)	4.5	15.9 (No. 6)	5.4 (W3.5)	2.94
Spacing (mm)	4.5	76.2	31.75	2.4
Spiral ratio (%)	1	0.61%	0.76%	0.81
Design strength of concrete (MPa)	1	34.5	34.5	1
Yield strength of longitudinal bar (MPa)	1	475	475	1
Top mass (kg)	20.25	4.62×10^5	2.9×10^4	15.85
Rotational mass (kg m^2)	410	3.2×10^6	2.6×10^4	124
Axial force at bottom of column (kN)	20.25	4500	290	15.52
Axial force ratio (%)	1	5%	6.5%	0.77
Weight density of concrete (kN/m^3)	0.22	24	24	1
Effective natural period (sec)	2.12	1.26	0.72	1.74
Yield displacement (m)	4.5	0.112	0.0263	4.25
Ultimate displacement (m)	4.5	0.58	0.21	2.76
Ductility	1	5.18	7.97	0.65
Flexural strength (kN)	20.25	1290	67.6	19.07

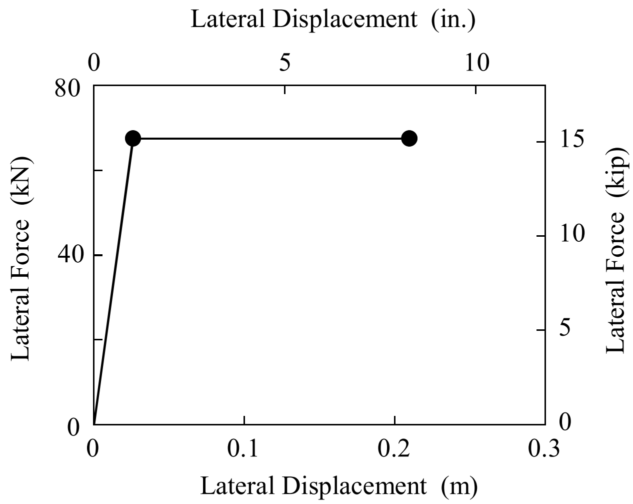

Figure 2.6 Ductility and flexural capacity of RC specimen.

2.2.3 Partially Prestressed Reinforced Concrete Column Specimen

Based on the findings from the analytical study by Sakai and Mahin [2004], a partially prestressed RC column was designed as a lightly-reinforced concrete column with a prestressing tendon arranged at the center of cross section that was debonded from concrete. This specimen will now be referred to as the PRC specimen. The longitudinal reinforcement ratio was fixed at about 0.6%, which is half of that of the RC specimen, and the prestressing tendon was unbonded from the bottom of the footing to the top of the top slab. Sakai and Mahin [2004] demonstrated that partially prestressed columns require additional confinement of concrete to prevent premature crushing of the core concrete. In this case, however, the same spiral arrangement as that used in the RC specimen was incorporated because the RC specimen already had higher confinement than standard and additional confinement would not be realistic. To select other design variables, such as size of tendon and magnitude of prestressing force, a series of quasi-static analyses was conducted.

Figure 2.7 shows the dimensions, cross section, and analytical model of the PRC specimen, and Figure 2.8 shows the assembled reinforcement of the specimen before the casting of the concrete. Twelve No. 3 [10-mm- (0.39-in.-) diameter] deformed bars were used as longitudinal reinforcement, resulting in a longitudinal reinforcement ratio of 0.66%. W3.5 round wire [5.4-mm- (0.21 in.-) diameter] at 32-mm (1.25-in.) pitch is used as spiral reinforcement. An aluminum duct, 76 mm (3 in.) in diameter, was incorporated at the center of the cross section from the bottom of the footing to the top slab to install the post-tensioning tendon.

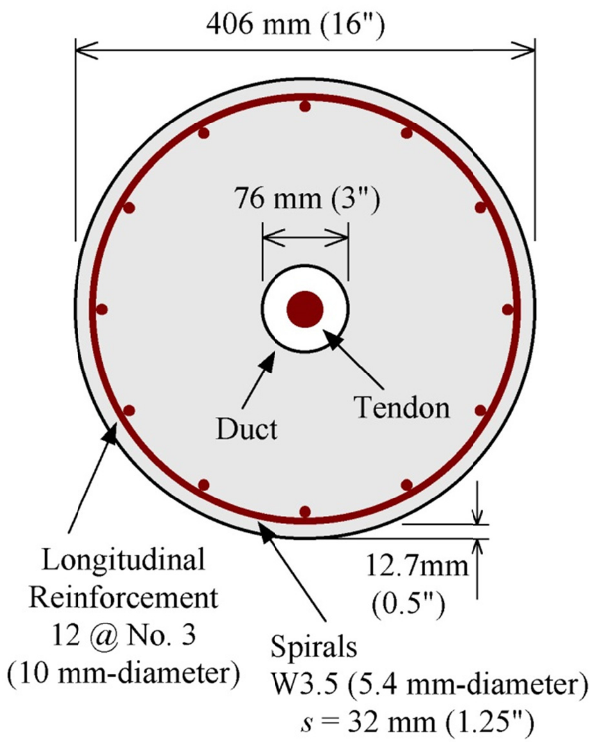

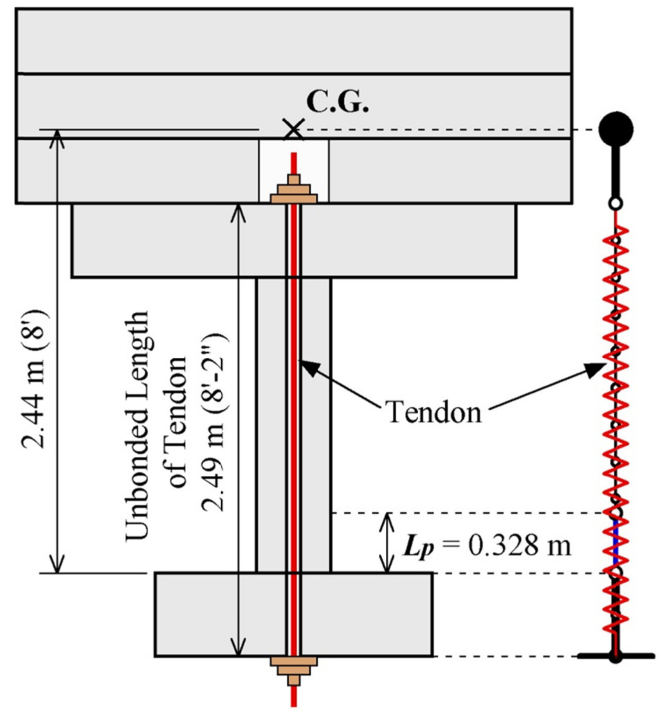

Figure 2.7 **Partially prestressed RC specimen (PRC specimen) and its analytical model: (a) cross section and (b) specimen and analytical model.**

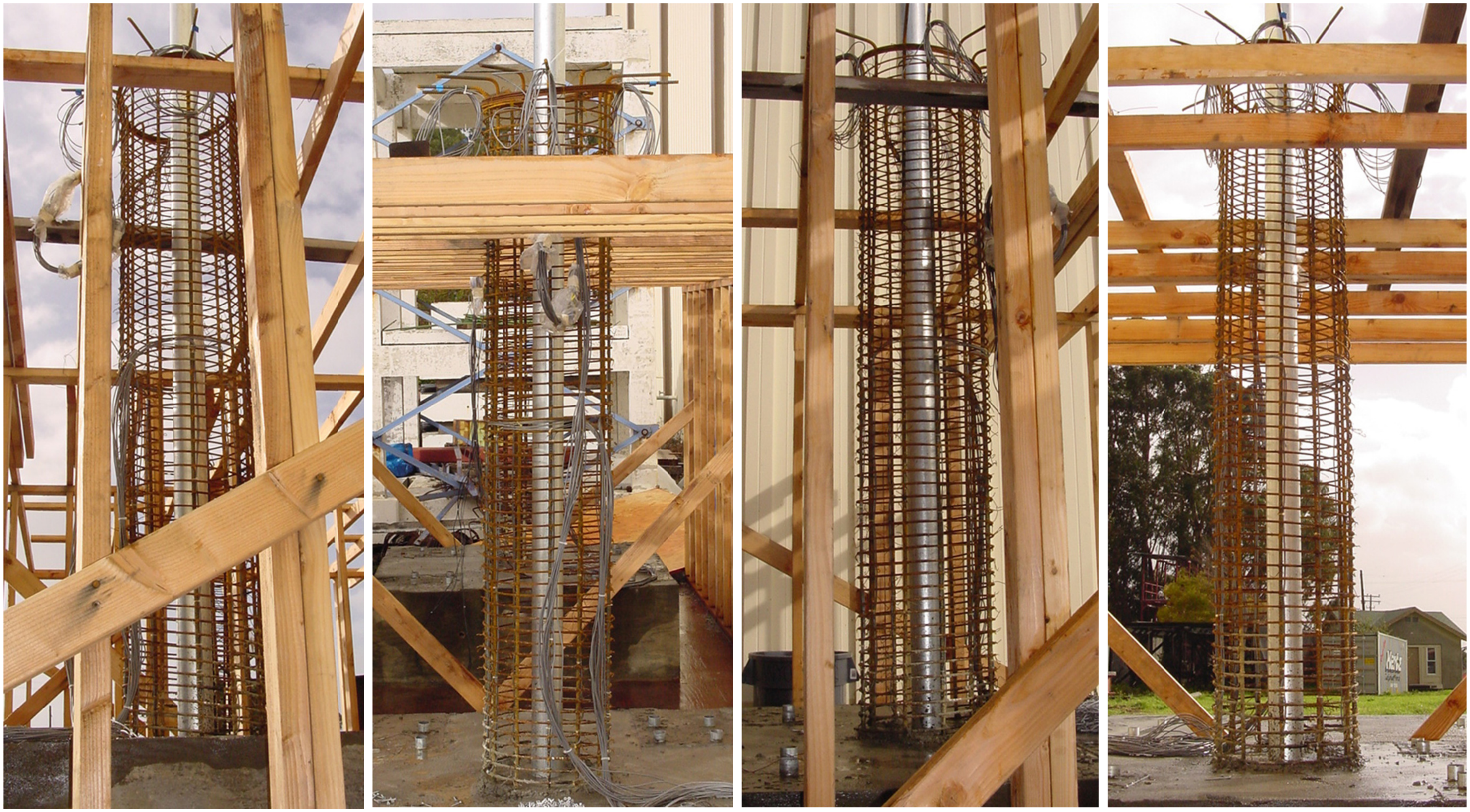

(a) (b) (c) (d)

Figure 2.8 Reinforcement of PRC specimen: (a) north face; (b) east face; (c) south face; and (d) west face.

The plastic hinge length was assumed to be 0.328 m (12.92 in.), and a three-dimensional fiber element was employed to represent flexural hysteretic behavior. Rigid bars were used to idealize the footing and the region from the top of the column to the center-of-gravity of the superstructure. Linear beam elements with cracked stiffness properties were used for the remainder of the column. An unbonded prestressing tendon was represented by a spring element spanning between assumed anchorage points.

The confinement effect of concrete was evaluated based on the model developed by Mander et al. [1988]. Unloading and reloading paths were represented by a model proposed by Sakai and Kawashima [2000 and 2006]. The envelope curves of longitudinal reinforcing bars and tendons were idealized as a bilinear model, with a strain-hardening ratio equal to 2%. A modified Menegotto–Pinto model proposed by Sakai and Kawashima [2003] was used to represent the hysteretic behavior of rebar and tendons taking into account the Bauschinger effect. More detailed information on the analytical model, including the material models, can be found in the report by Sakai and Mahin [2004]. P-Δ effects due to the dead load of the top slab and weighted blocks were included in the analyses; those due to the prestressing force of the tendon were disregarded.

Table 2.3 summarizes design variables considered. The diameter of the tendons varied from 26 mm (1 in.) to 45 mm (1.77 in.), and the prestressing force increased from 157 kN to 604 kN (35 to 136 kip), resulting in total axial force ratio between 10% to 20%, which is defined below as

$$\alpha_{\text{total}} = \frac{P + P_{ps}}{f'_{co} A_g} \tag{2.4}$$

where P_{ps} is the prestressing force. To determine the design variables, three required performance criteria were used based on the findings by Sakai and Mahin [2004].

1. The flexural strength of the PRC specimen should be similar to that of the RC specimen (a margin of error of 5% is allowed for the maximum forces);
2. The post-yield stiffness should be similar to the RC specimen; and
3. The quasi-static residual displacement should be smaller than 20% of that of the RC specimen.

Table 2.4 summarizes the quasi-static performance of partially prestressed concrete column specimens. Hysteresis of all the columns considered in this study can be found in Appendix A. Each column is identified by two design parameters: the first portion denotes the size of the tendon, and the second portion denotes the total axial force ratio. For instance: ϕ32-15% represents the column with a 32-mm (1.26 in.) diameter tendon, and its total axial force ratio is 15%.

Table 2.3 Variables considered.

Variables	Values
Diameter of tendon (mm) (Prestressing steel ratio ρ_{ps})	26 (1 in.), 32 (1-1/4 in.), 36 (1-3/8 in.), and 45 (1-3/4 in.) (0.42%, 0.62%, 0.79%, and 1.29%)
Total axial force ratio α_{total} (Prestressing force)	10%, 12.5%, 15%, 17.5%, and 20% (157 kN, 268 kN, 380 kN, 492 kN, and 604 kN) (35, 60, 85, 110, and 136 kip)

Table 2.4 Quasi-static performance of partially prestressed columns.

ID No.	Tendon size	α_{total}	μ	$d_{r\cdot sta}$ (mm)	$F_{\max}$ (kN)	F_u (kN)	K_1 (kN/m)	κ_{py} (%)	E_D (kNm)
RC	-----	6.5%	8.9	0.120	59.1	51.0	2460	-1.8	29.5
ϕ26-10%	26 mm	10%	7.7	0.068	51.3	45.9	2218	-1.6	18.6
ϕ26-12.5%		12.5%	7.2	0.034	56.4	49.1	2377	-2.0	18.7
ϕ26-15%		15%	6.5	0.023	60.9	51.4	2390	-2.7	18.9
ϕ26-17.5%		17.5%	6.0	0.021	64.9	52.2	2385	-3.8	19.2
ϕ26-20%		20%	5.8	0.018	68.5	54.3	2495	-4.2	19.3
ϕ32-10%	32 mm	10%	7.4	0.058	52.1	49.3	2222	-0.8	18.6
ϕ32-12.5%		12.5%	7.0	0.034	56.9	52.5	2379	-1.1	18.7
ϕ32-15%		15%	6.3	0.022	61.4	55.6	2392	-1.5	18.9
ϕ32-17.5%		17.5%	5.6	0.020	65.5	58.2	2389	-2.3	19.2
ϕ32-20%		20%	5.4	0.031	69.3	60.6	2497	-2.8	20.5
ϕ36-10%	36 mm	10%	7.2	0.054	53.3	51.7	2226	-0.2	18.6
ϕ36-12.5%		12.5%	6.8	0.034	57.4	54.8	2381	-0.5	18.8
ϕ36-15%		15%	6.2	0.025	61.8	57.6	2394	-1.0	19.0
ϕ36-17.5%		17.5%	5.5	0.032	65.9	60.3	2390	-1.7	20.4
ϕ36-20%		20%	5.3	0.033	69.6	62.7	2498	-2.2	20.7
ϕ45-10%	45 mm	10%	6.7	0.057	59.2	57.4	2235	1.3	18.9
ϕ45-12.5%		12.5%	6.3	0.048	61.7	58.6	2385	0.2	19.6
ϕ45-15%		15%	5.8	0.049	64.5	61.5	2398	-0.2	20.4
ϕ45-17.5%		17.5%	5.3	0.040	67.2	63.8	2395	-0.8	20.7
ϕ45-20%		20%	5.1	0.041	70.2	66.1	2500	-1.3	21.1

The quasi-static residual displacement, $d_{r\cdot sta}$, was determined as the residual displacement on the loading path from the peak displacement in the third cycle where most of the partially prestressed columns reached the ultimate state. The initial stiffness, K_1, the post-yield tangential stiffness, K_2, and the post-yield stiffness ratio, κ_{py}, are defined here as:

$$K_1 = \frac{F_{y0}}{d_{y0}} \tag{2.5}$$

$$K_2 = \frac{F_u - F_1}{d_u - d_1} \tag{2.6}$$

$$\kappa_{py} = \frac{K_2}{K_1} \tag{2.7}$$

where F_{y0} and d_{y0} are the force and displacement when the longitudinal bar at the tensile edge yields, F_1 and d_1 are the force and displacement at the maximum displacement in the first cycle, and F_u and d_u are the force and displacement when the core concrete at the compressive edge reaches the ultimate strain. The capacity of energy dissipation, E_D, is evaluated based on energy dissipated up to the third cycle. The column ductility, μ, is defined as the ratio of the ultimate displacement to the yield displacement of each column.

$$\mu = \frac{d_u}{d_y} \tag{2.8}$$

Table 2.4 suggests that only five of twenty columns, (ϕ26-15%, ϕ32-15%, ϕ36-15%, ϕ45-10%, and ϕ45-12.5%) satisfied criteria No. 1. Figure 2.9 compares quasi-static hysteresis of the first three columns with that of the RC specimen; ϕ45-10%, and ϕ45-12.5% columns were not included in this comparison because they obviously had skeleton curves different from that of the RC specimen as they had positive post-yield tangential stiffness.

The conventional specimen reached the ultimate state, where core concrete strain exceeded the ultimate strain, in the fifth cycle while the PRC specimens reached the ultimate state in the third or fourth cycle. The hysteresis after columns reached the ultimate state are shown in the dotted line in Figure 2.9 and Appendix A. Figure 2.9 suggests that ϕ26-15% and ϕ32-15% columns had similar skeleton curves to that of the RC specimen; however, ϕ26-15% column had a larger negative post-yield stiffness than the RC specimen, while ϕ32-15% column had a smaller post-yield stiffness. Because a column with a smaller negative post-yield stiffness performs better under dynamic excitation, the column with the 32-mm (1.26-in.) tendon and a total axial force ratio of 15% was selected. The prestressing force necessary to achieve 15% total axial force ratio was 380 kN (85 kip). The column also satisfies the third criteria, wherein the quasi-static residual displacement of the column in the third cycle was 0.022 m (0.87 in.), which is 18% of that of the RC specimen.

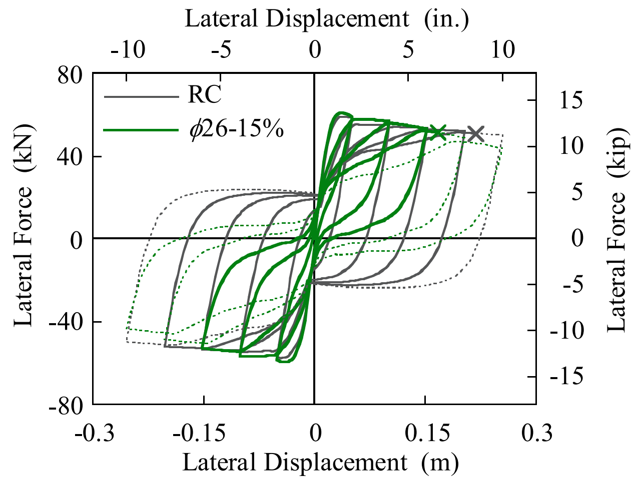

(a)

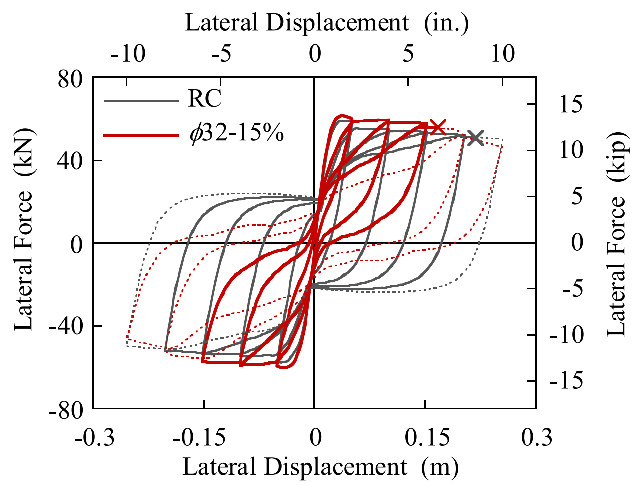

(b)

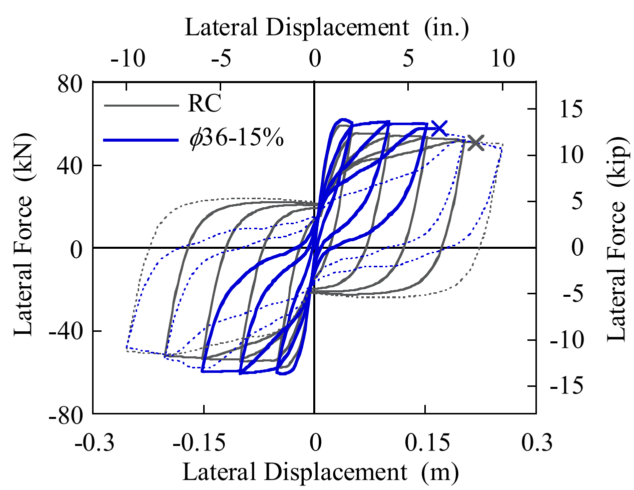

(c)

Figure 2.9 **Quasi-static behaviors of specimens with unbonded post-tensioning tendons: (a) ϕ26-15% specimen; (b) ϕ32-15% specimen; and (c) ϕ36-15% specimen.**

The tendon was 3.05 m (10 ft) long and 32 mm (1.25 in.) in diameter. Grade 150 KSI (1035 MPa) bar from Williams Form Engineering Corp. was used as a post-tensioning tendon. The ultimate strength of the tendon was 834 kN (188 kip).

2.2.4 Footing and Top Slab

A footing and a top slab were designed to fix the column to the earthquake simulator platform and to support the weighted blocks. Designed to remain elastic during the test, design forces to the footing were evaluated for the plastic moment capacity of the column when the plastic hinge was fully developed, while the top slab was checked for bending and shear due to the supported load of the weighted blocks.

The footing was 1.52-m (5-ft) square and 0.46-m (18-in) thick. Shown in Figure 2.10, it was reinforced longitudinally with No. 6 [19-mm- (0.75-in.) diameter] deformed bars and transversally with No. 3 [10-mm- (0.4-in.) diameter] stirrup ties. Figure 2.11 shows the top slab that is 2.44-m (8-ft) square and 0.41-m (16-in.) thick. No. 5 [16-mm- (0.24-in.-) diameter] reinforcing bars and No. 3 [10-mm- (0.4-in.-) diameter] stirrups were provided. The stirrup ties for both the footing and top slab had a 90° hook at one end and a 135° hook at the other end. The longitudinal reinforcing bars of the column were extended into the footing and the top slab, and fixed to the bottom longitudinal reinforcement of the footing and the upper longitudinal reinforcement of the top slab with a 90° hook, so that the anchorage length requirement by the SDC [Caltrans 2001] was satisfied. The weight of the footing and the top slab were 24.5 kN and 55.7 kN (6 and 13 kip), respectively. The total weight of one specimen was approximately 85 kN (19.11 kip), including the weight of the column.

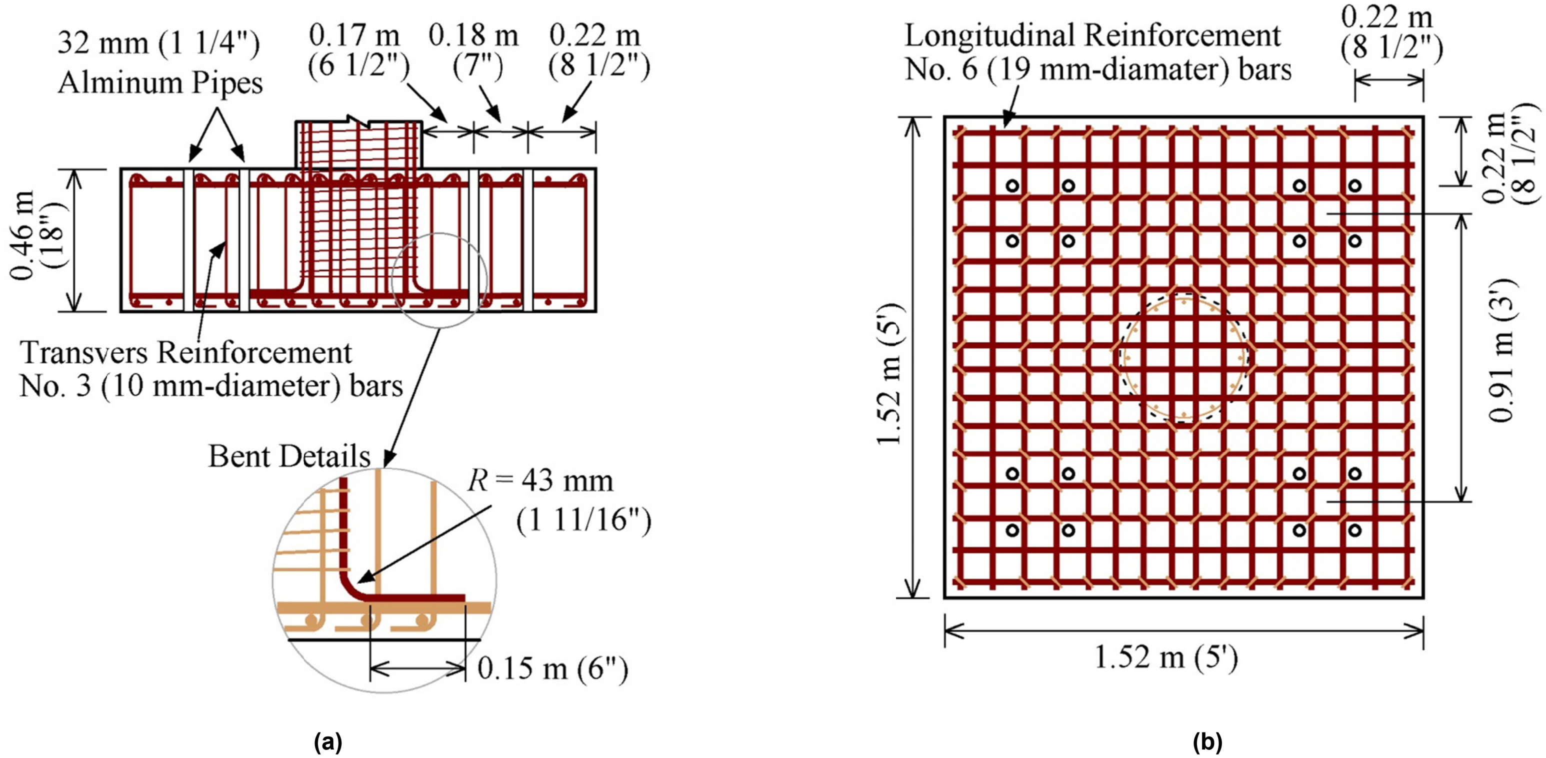

Figure 2.10 Reinforcement details of footing: (a) elevation and reinforcement details; and (b) plan view.

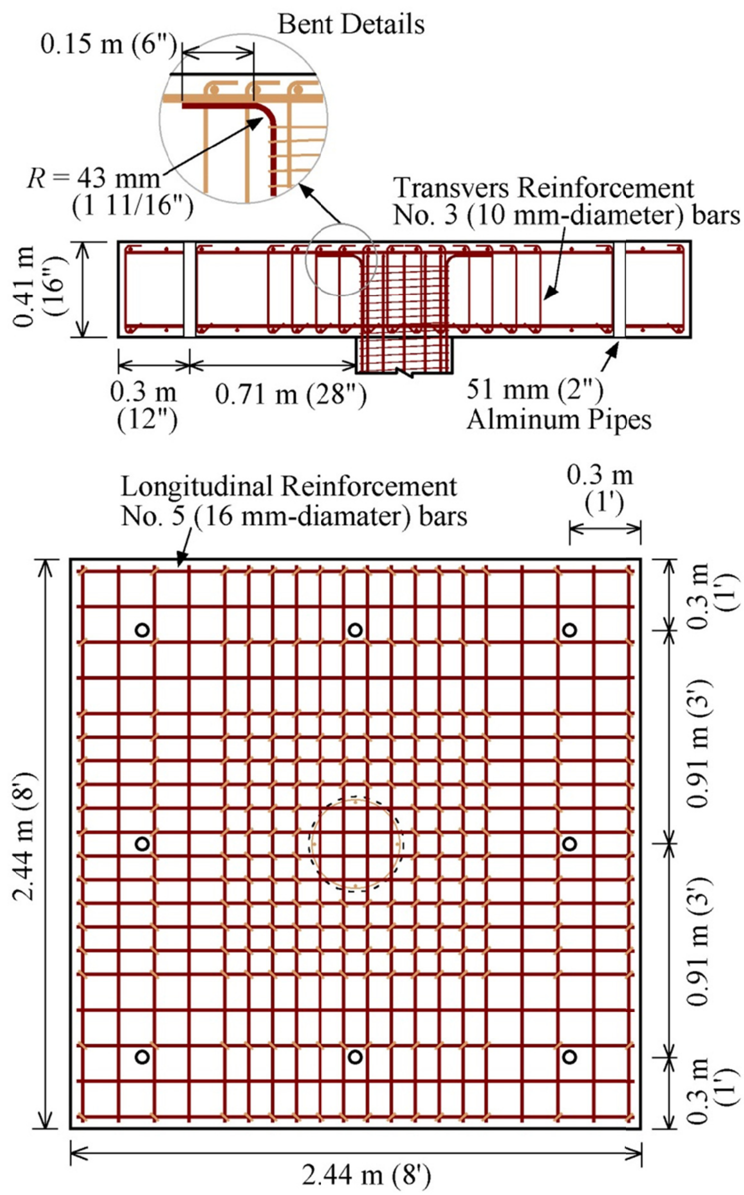

Figure 2.11 Reinforcement details of top slab.

2.2.5 Weighted Block

Three concrete blocks, designed as weighted blocks, represented the superstructure of a bridge. Figure 2.12 shows the weighted blocks. They were 3.05-m (10-ft) square in plane and 0.66-m (14-in.) thick. No. 4 [13-mm- (0.5-in.-) diameter] bars were arranged with 0.15-m (6-in.) pitch for longitudinal reinforcement; no transverse reinforcement was provided. The weight of each block was 76.2 kN (17.13 kip) for a total weight of 283 kN (64 kip) for the top block (which includes the weight of top slab). One block, which was placed directly on the top of the specimen, had a 0.38-m (15-in.) square hole to anchor the post-tensioning tendon; its weight was 1.5% smaller than the other blocks.

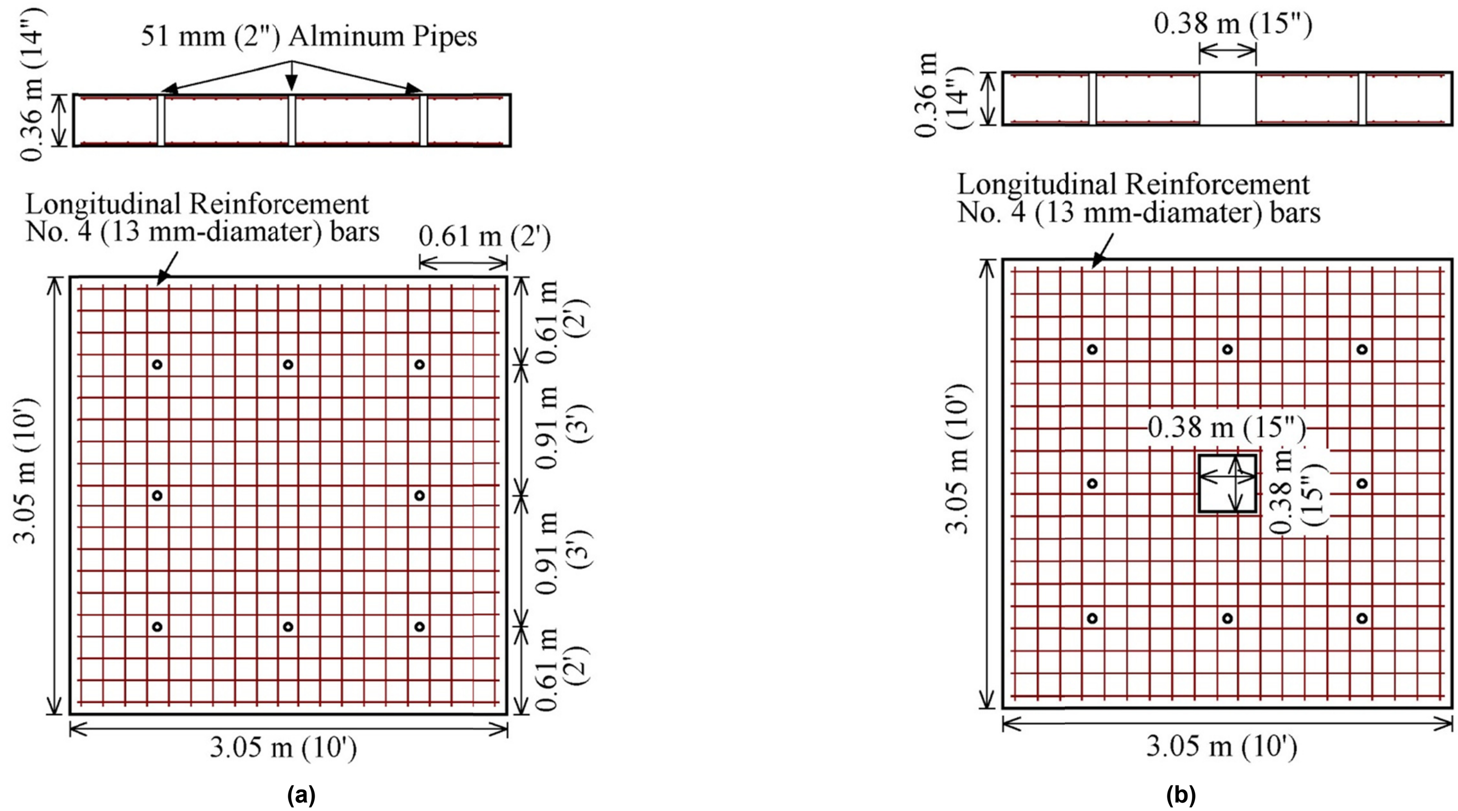

Figure 2.12 Reinforcement details of weighted blocks: (a) block without hole and (b) block with center hole.

2.3 CONSTRUCTION OF THE SPECIMENS

The construction of the specimens had eleven phases:

- Construction of the platform began in early October, 2002; see Figure 2.13
- Construction of forms for the footings; see Figure 2.14
- Gauging on longitudinal reinforcing bars; see Figure 2.15
- Assembly of steel cages; see Figure 2.16
- Casting footing concrete took place on November 27th, 2002 ; see Figure 2.17
- Gauging on spirals; see Figure 2.18
- Removal of the forms of footing
- Construction of forms for the columns and top slabs; see Figures 2.19 and 2.20
- Casting column and top slab concrete took place on January 31, 2003; see Figure 2.21)
- Removal of the forms was completed in finished in mid-February, 2003; see Figure 2.22
- Specimens were moved into the earthquake simulation laboratory on June 2, 2003; see Figure 2.23

Fifteen concrete cylinders, 305-mm (12-in.) long and 152 mm (6 in.) in diameter, were constructed for the material tests at the time the concrete was cast. Before casting of the column concrete, 13-mm (0.5 in.) threaded rods were inserted transversely through the column forms to provide a means for measuring the curvature distribution along the height of the columns. Slump of concrete [specified to be 127 mm (5 in.)] was 89 mm (3.5 in.) and 127 mm (5 in.) for the footing concrete and concrete for the columns and top slabs. The concrete was cured for about ten days before the forms were removed.

Figure 2.13 Construction of platform.

Figure 2.14 Construction of forms.

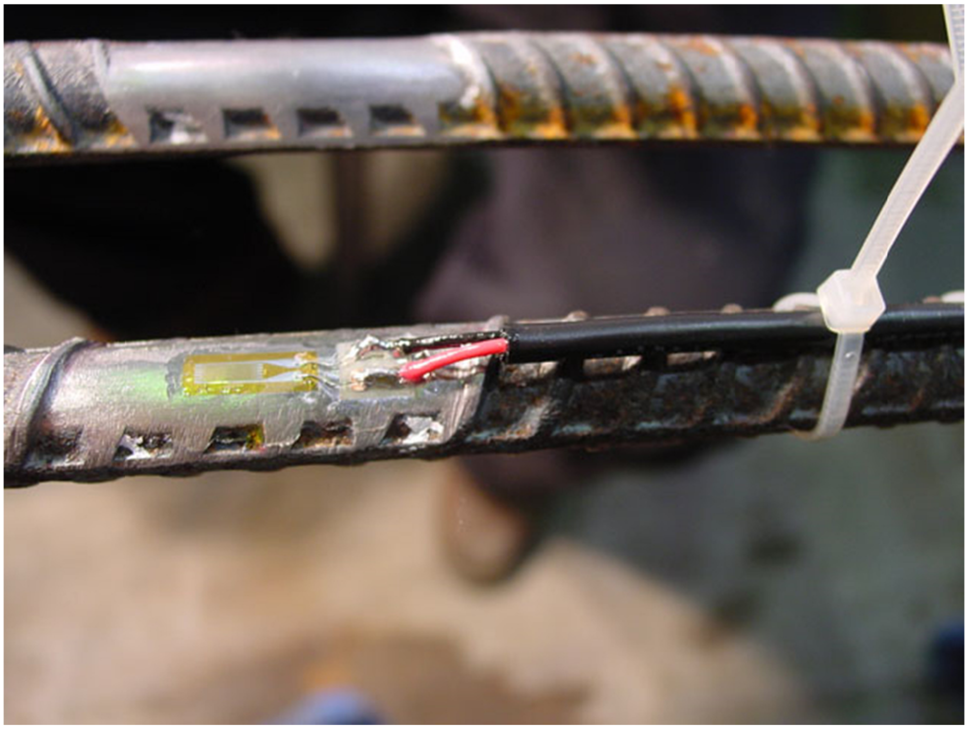

(a)

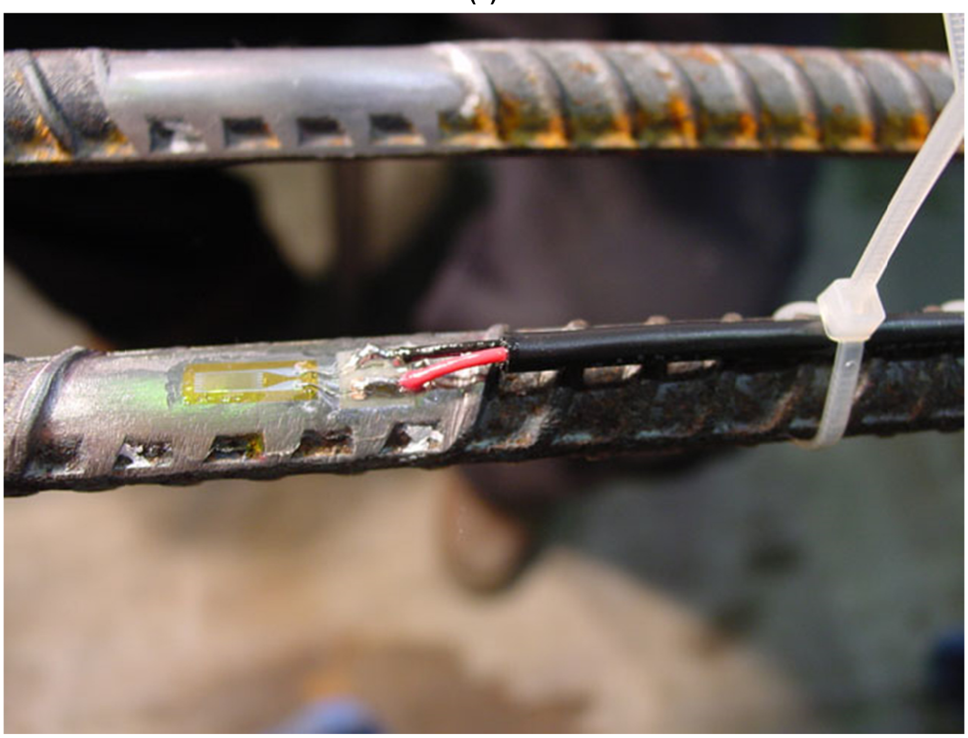

(b)

Figure 2.15 Gauging on longitudinal reinforcing bars: (a) strain gauge on steel and (b) coated gauge.

(a)

(b)

Figure 2.16 Assembly of steel cages: (a) assembly of spirals and (b) assembly of footing reinforcement.

(a)

(b)

Figure 2.17 Casting footing concrete: (a) specimens and concrete mixer truck; and (b) pouring concrete into forms.

(a)

(b)

Figure 2.18 Gauging on spirals: (a) strain gauge on spiral and (b) curing coating materials for two hours at 130° F (about 55° C).

(a)

(b)

Figure 2.19 Construction of top slabs: (a) forming work for top slabs and (b) top slab reinforcement.

Figure 2.20 Forms for columns.

(a)

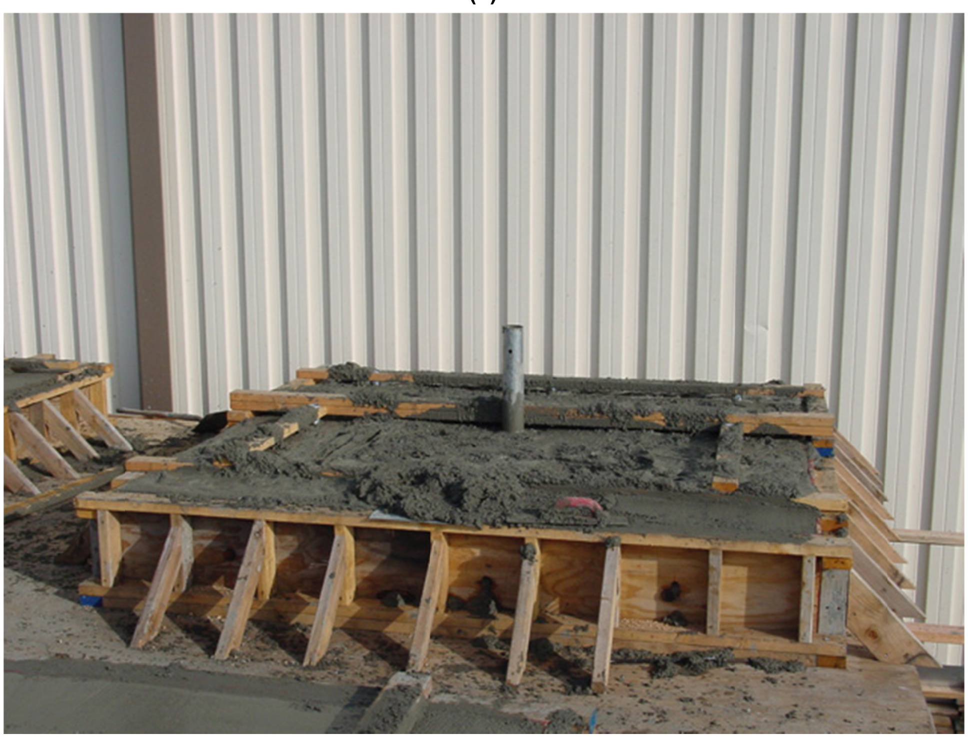

(b)

Figure 2.21 Casting of concrete for columns and top slabs: (a) pouring concrete into column from top slab; and (b) top slab of partially prestressed concrete specimen after cast concrete.

(a)

(b)

Figure 2.22 Completion of construction of specimens: (a) conventionally designed column specimen; and (b) partially prestressed column specimen.

(a)

(b)

Figure 2.23 Moving specimens into earthquake simulation laboratory: (a) moving weighted blocks into laboratory; and (b) moving specimens into laboratory.

2.4 MEASURED MATERIAL PROPERTIES

2.4.1 Mechanical Properties of Concrete

To represent the actual properties of concrete used in RC bridges, the concrete of the columns was specified as normal weight, with a 28-day design strength of no less than 27.6 MPa (4 ksi) and no more than 38 MPa (5.5 ksi). Details of the concrete mix design are shown in Table 2.5.

Table 2.5 Concrete mix design.

Mix specifications	
Portland cement	ASTM C-150 TYPE II
Fly ash	ASTM C-618 CLASS F, 15%
Admixture (water reducer)	ASTM C-494 TYPE A
Minimum 28-day strength	3850 psi (26.6 MPa)
Maximum 28-day strength	4350 psi (30.0 MPa)
Cementitious sacks	5.60
Maximum size aggregate	9.5 mm (0.37in.)
Slump	127 mm (5 in.)
Water/cement ratio	0.603

Mix design and quantities

Material	Specific gravity	Absolute volume	SSD weight
3/8”×#8 gravel	2.68	5.98 ft^3 (0.167 m^3)	1000 lbs (453 kg)
Regular top sand	2.67	9.02 ft^3 (0.253 m^3)	1503 lbs (681 kg)
SR blend sand	2.60	3.69 ft^3 (0.103 m^3)	599 lbs (271 kg)
Cement Type II	(3.15)	2.27 ft^3 (0.064 m^3)	447 lbs (202 kg)
Fly ash	(2~2.4)	0.55 ft^3 (0.015 m^3)	79 lbs (36 kg)
Water	1.00	5.08 ft^3 (0.142 m^3)	317 lbs (144 kg)
Water reducer	-----	0.41 ft^3 (0.011 m^3)	26.3 fl. oz. (778 ml)
Total	-----	27 ft^3 (0.756 m^3)	3945 lbs (1787 kg)

As shown in Figure 2.24, compressive strength tests were performed at 8 and 29 days after the casting of the footing concrete, and at 7, 14, 21, and 28 days after the casting the columns and top slab concrete. Additional cylinders were tested about 100 days after completing the earthquake simulation tests. Ideally, cylinder tests should have been conducted concurrently with the earthquake simulation tests; however, cylinder tests were not conducted because the compressive testing equipment was not available. Because the concrete was old enough to keep its strength constant, the concrete strength on the test day is adequately represented by that obtained 100 days later. Figure 2.25 shows concrete strength development with time for moist-cured concrete introduced by the ACI Committee 209 and the CEB-FIP Model Code [Mehta and

Monteiro 1993]. The cylinder test results described later are also shown in the figures for reference. These relations are given as follows:

$$f_{cm} = f_{c28}\left(\frac{t}{4+0.85t}\right)(\text{ACI}) \tag{2.9}$$

$$f_{cm} = f_{c28}\bullet\exp\left\{0.25\left[1-\left(\frac{28}{t}\right)^{0.5}\right]\right\}(\text{CEB-FIP}) \tag{2.10}$$

where f_{cm} is the mean compressive strength at age t days, and f_{c28} is the mean 28-day compressive strength. Moist-cured concrete increases its strength by 1% or less between ages of 500 and 600 days; therefore, the concrete strength of the specimens, which were in air 10 days after being cast, had almost the same strength as they would have had had they been tested at the same time as the earthquake simulation tests.

For each test, three cylinders were tested. Tables 2.6 and 2.7 summarize the test results, and Figure 2.26 shows stress–strain curves of the column concrete at 595 days. The column concrete had a 28-day strength of 31.4 MPa (4.56 ksi), while the footing concrete had 43.2 MPa (6.27 ksi). The strength of column concrete when the earthquake simulation tests were performed was about 42 MPa (6 ksi). The tangential and secant modulus of elasticity of concrete, which are defined below [McCormac 1986], were evaluated to be 22 GPa and 20 GPa, respectively.

$$E_{c\cdot tan} = \frac{f_{c\cdot 50}}{\varepsilon_{c\cdot 50}} \tag{2.11}$$

$$E_{c\cdot sec} = \frac{f_{c\cdot 50} - f_{c\cdot 25}}{\varepsilon_{c\cdot 50} - \varepsilon_{c\cdot 25}} \tag{2.12}$$

(a) (b)

Figure 2.24 Concrete cylinder tests: (a) test set-up and (b) gauge length.

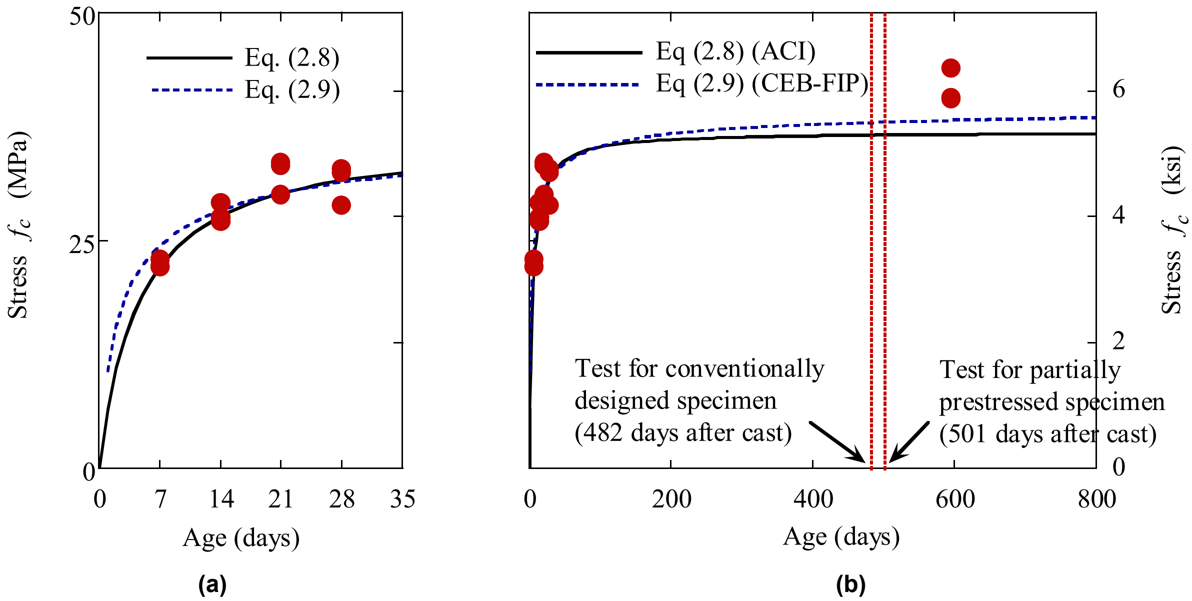

Figure 2.25 **Compressive strength development of concrete: (a) early age and (b) around test day.**

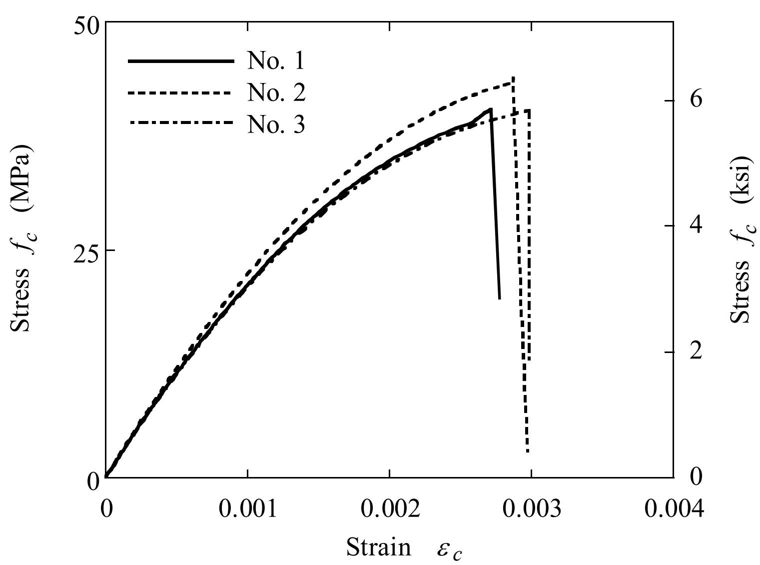

Figure 2.26 **Stress–strain curves of concrete cylinders.**

Table 2.6 Compressive strength of concrete.

Concrete for footings				
Day	**No. 1 (MPa)**	**No. 2 (MPa)**	**No. 3 (MPa)**	**Average (MPa)**
8	29.1	28.9	28.8	28.9
29	45.1	43.5	41.0	43.2
Concrete for columns and top slabs				
Day	**No. 1 (MPa)**	**No. 2 (MPa)**	**No. 3 (MPa)**	**Average (MPa)**
7	22.2	22.9	22.2	22.5
14	29.2	27.6	27.1	28.0
21	33.7	30.1	33.3	32.3
28	32.5	28.9	32.9	31.4
595	40.6	43.9	40.7	41.7

Table 2.7 Mechanical properties of concrete from cylinder tests.

	Strength (MPa)	Modulus of elasticity (GPa)	
		Tangent modulus $E_{c\cdot tan}$	Secant modulus $E_{c\cdot sec}$
No. 1	40.6	21.4	19.7
No. 2	43.9	22.5	20.8
No. 3	40.7	21.2	19.5
Average	41.7 (6.0 ksi)	21.7 (3145 ksi)	20.0 (2899 ksi)

2.4.2 Mechanical Properties of Steel Reinforcement

The column longitudinal steel was specified as ASTM A706 Grade 60 steel. Table 2.8 shows mechanical properties described on a certified mill test report. To obtain the mechanical properties of the reinforcing bars, tensile tests for steel coupons were conducted; see Figure 2.27. Three tensile tests were performed on the No. 4 reinforcing bars, which were used for the RC specimen, while two coupons were tested for the No. 3 bars used for the PRC specimen. Test results are summarized in Table 2.9 and Figure 2.28. The modulus of elasticity, yield strength, and ultimate strength of the No. 4 bars were 216 GPa, 490 MPa, and 728 MPa, respectively. The No. 3 bar had a similar yield strength to the No. 4 bars, although the ultimate strength was 9% greater and the modulus of elasticity was 9% smaller than the No. 4 bars.

The spiral reinforcement was specified as ASTM A82 Grade 80. No tensile tests were performed due to absence of coupons for the spirals, and a certified mill test report was available. The modulus of elasticity and yield strength was estimated to be 200 GPa and 607 MPa, respectively.

Table 2.8 Mechanical properties of steel from certified mill test report.

No. 4 (13 mm-diameter) reinforcing bar (ASTM A706)			
	Yield strength	**Tensile strength**	**Elongation in 203 mm (8 in.)**
No.1	517 MPa (75.0 ksi)	658 MPa (95.5 ksi)	14.1%
No.2	455 MPa (66.0 ksi)	662 MPa (96.0 ksi)	15.6%
No.3	465 MPa (67.5 ksi)	662 MPa (96.0 ksi)	14.1%
Average	479 MPa (69.4 ksi)	661 MPa (95.7 ksi)	14.6%
No. 3 (10 mm-diameter) reinforcing bar (ASTM A706)			
	Yield strength	**Tensile strength**	**Elongation in 200 mm (7.9 in.)**
No.1	424 MPa (61.5 ksi)	585 MPa (84.5 ksi)	20%
W3.5 wire for spiral (ASTM 82)			
	Yield strength	**Tensile strength**	**Elongation in 200 mm (7.9 in.)**
No.1	-----	-----	-----
32 mm-diameter tendon (ASTM A722)			
	Yield strength	**Tensile strength**	**Elongation in 668 mm (26.3 in.)**
No.1	974.3 MPa (141.2 ksi)	1145 MPa (166 ksi)	8.8%
No.2	1026.0 MPa (148.7 ksi)	1083 MPa (157 ksi)	6.5%
Average	1000.2 MPa (145.0 ksi)	1114 MPa (162 ksi)	7.7%

Table 2.9 Mechanical properties of steel from tensile tests.

No. 4 (13 mm-diameter) reinforcing			
	Yield strength (MPa)	**Ultimate strength (MPa)**	**Modulus of elasticity (GPa)**
No. 1	488.0	730.0	202
No. 2	496.7	727.2	192
No. 3	487.2	725.8	255
Average	490.6 (71.1 ksi)	727.7 (105.5 ksi)	216 (31300 ksi)
No. 3 (10 mm-diameter) reinforcing bar			
	Yield strength (MPa)	**Ultimate strength (MPa)**	**Modulus of elasticity (GPa)**
No. 1	485.9	795.5	203
No. 2	490.1	788.6	198
Average	488.0 (70.7 ksi)	792.1 (114.8 ksi)	200 (29000 ksi)
32 mm-diameter tendon			
	Yield strength (MPa)	**Ultimate strength (MPa)**	**Modulus of elasticity (GPa)**
No. 1	1024 (148 ksi)	1169 (169 ksi)	202 (29300 ksi)

(a) (b)

Figure 2.27 Tensile tests for reinforcing bars: (a) test set-up and (b) gauge length.

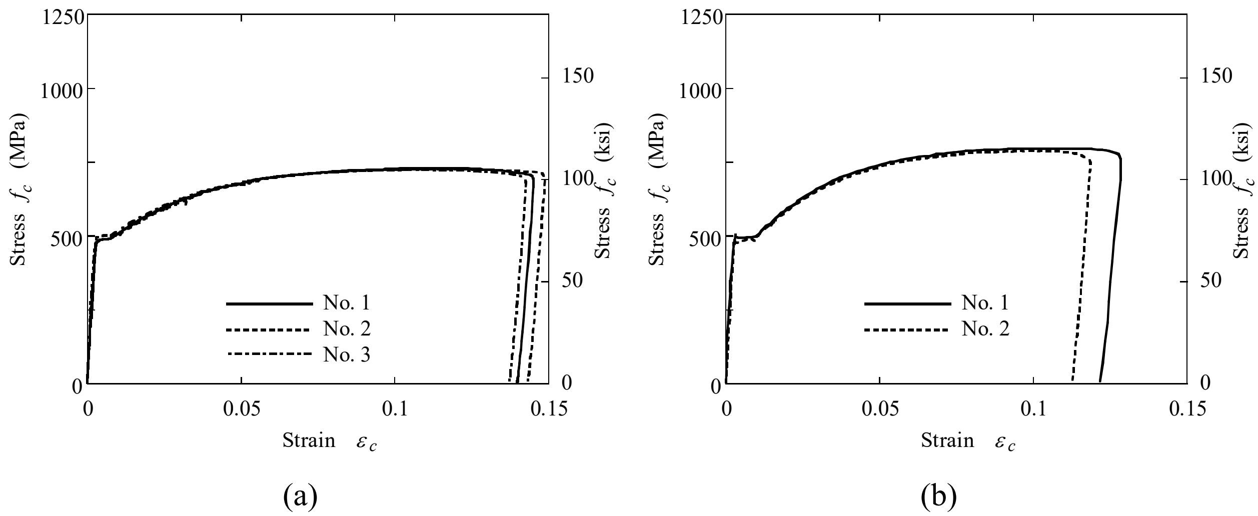

Figure 2.28 Stress–strain curves of reinforcing bars: (a) No. 4 bars and (b) No. 3 bars.

2.4.3 Mechanical Properties of Tendon

For the post-tensioning tendon, an ASTM A722 Grade 150 KSI (1035 MPa) bar from Williams Form Engineering Corp. was used. The size of tendon was determined to be 32-mm (1.26 in.) diameter, according to the analytical results described in Section 2.2.3. Table 2.8(d) shows mechanical properties described on a certified mill test report.

After the sequence of earthquake simulation tests, a 0.61 mm (24 in.) coupon was cut out of the 3.05 m (10 ft) tendon installed in the PRC specimen; see Figure 2.29. Thus, the coupon might have endured plastic deformation during the tests, although it came from the top portion where no plastic deformation was observed. The middle portion of the coupon was machined down to 19 mm (0.75 in.) in diameter to ensure that the ultimate strength did not exceed the capacity of a testing equipment used; a tensile test was then conducted.

Figure 2.30 shows the stress–strain curve obtained from the test. The modulus of elasticity, yield strength, and ultimate strength of the tendon were 203 GPa, 1024 MPa, and 1169 MPa, respectively. Thus, the yield and ultimate strengths in force were estimated to be 826 kN (186 kip), and 943 kN (212 kip), respectively.

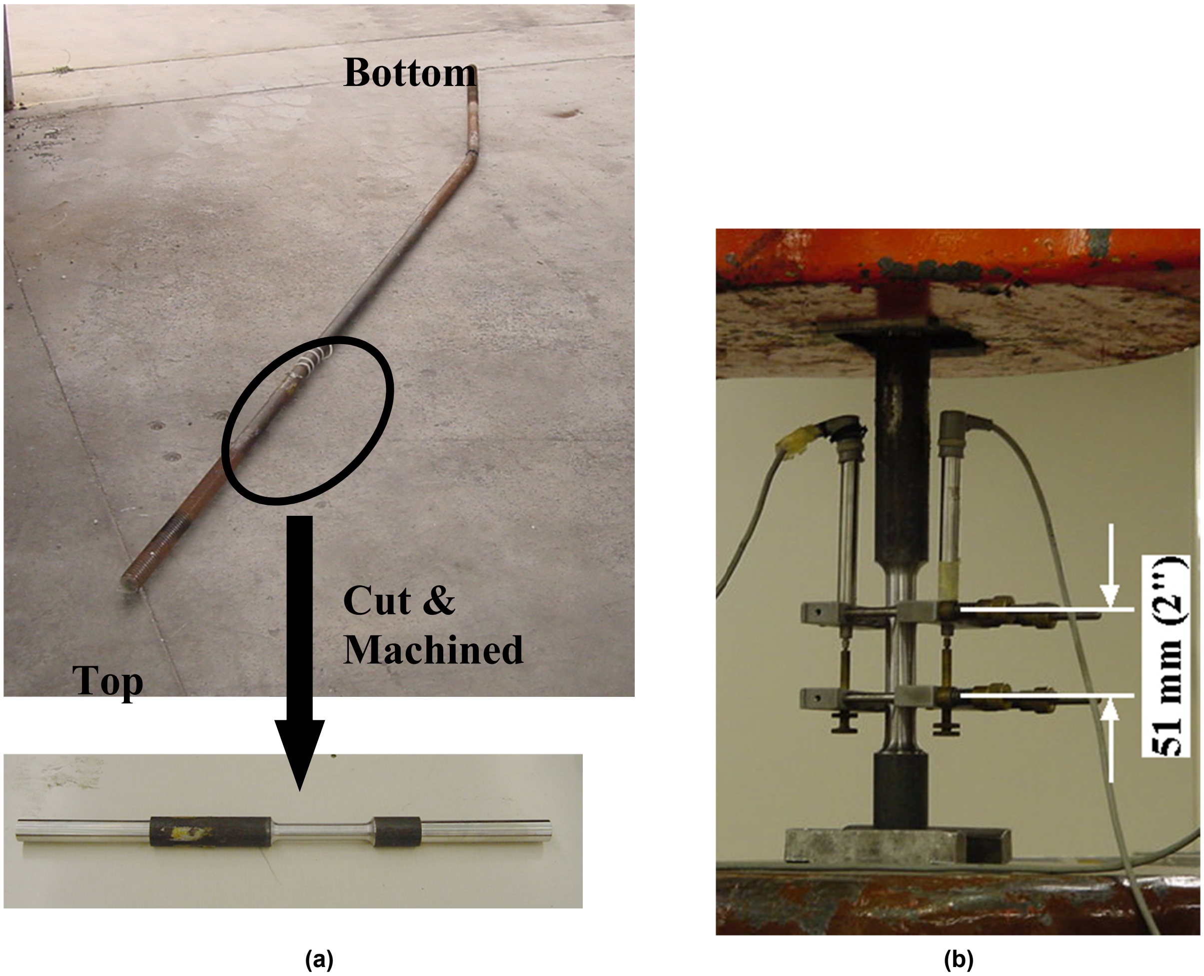

Figure 2.29 Tensile test for tendon: (a) test coupon; and (b) test set-up and gauge length.

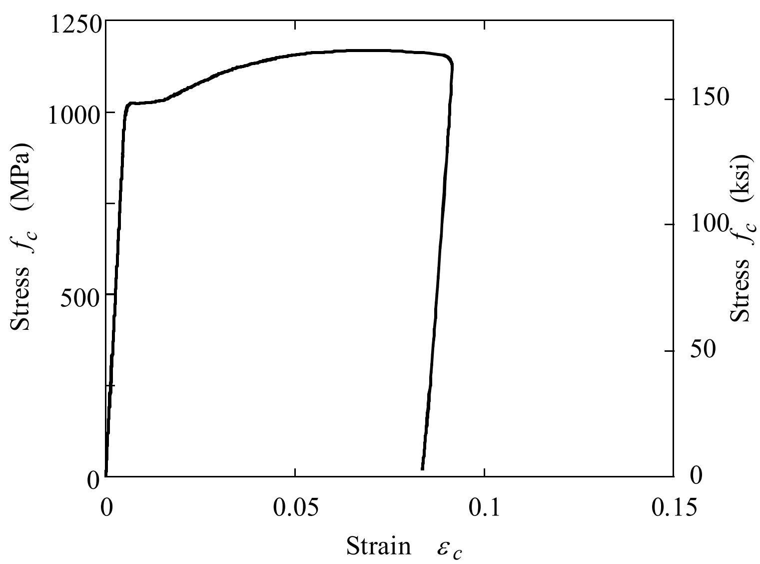

Figure 2.30 Stress–strain curves of the tendon.

2.5 SELECTION OF GROUND MOTIONS

Input ground motions used in the earthquake simulation tests were selected based on dynamic analyses for the conventionally designed RC specimen. A ground motion that produces large maximum and residual displacements was deemed appropriate because the test was aimed at investigating: (1) the mechanism behind how a conventionally designed column produces large residual displacement; (2) how the proposed design mitigates such a large residual displacement; and (3) how both the conventionally designed and proposed specimens behave when they experience a very large nonlinear response.

Table 2.10 shows ground motions used for the dynamic analyses. Ten pairs of near-field strong-ground motions from the SAC Steel Project [Somerville et al. 1997] were considered. Used in previous investigations by the Sakai and Mahin [2004], these ground motions were modified from the originally recorded ground acceleration to represent ground motions in the fault-normal and fault-parallel directions. Additionally, four pairs of original records from the 1989 Loma Prieta, California, earthquake, 1994 Northridge, California, earthquake, and 1995 Hyogo-Ken Nanbu, Japan, earthquake [PEER 2000] were considered. Response spectra of the ground motions that took into account the scaling factors can be found in Appendix B. The fault-normal and fault-parallel components were used for *X*- and *Y*-directions, respectively, for the SAC ground motions, while 000 or 360 and 090 components were used for *X*- and *Y*-directions for the original records.

The same analytical model as that used for the quasi-static analyses was implemented with an exception: a 28 day-concrete strength (f'_{co} = 32 MPa) and yield strength of steel from the mill certified report (f_{sy} = 455 MPa) were used.

Based on an eigenvalue analysis of a two-dimensional model assuming cracked stiffness properties for the model, the specimen had natural periods of 0.77, 0.09, and 0.02 sec for first, second, and third modes. Rayleigh damping was used to represent viscous damping. Based on the findings by Hachem et al. [2003], a damping ratio of 5% of critical damping was assumed for the first and third modes.

Figure 2.31 shows the maximum and residual displacements of the RC specimen obtained from dynamic analyses. Response displacement time histories, orbits of response displacements, and lateral force versus lateral displacement hysteresis of the specimen can be found in Appendix C. When the column was subjected to the modified Los Gatos records, the maximum response and residual displacement both show the largest value, 0.19 m (7.5 in.) and 0.027 m (1.06 in.), respectively, and the modified Los Gatos records were selected as the input ground motion for the earthquake simulation tests.

Figure 2.32 compares the response of the RC specimen and the PRC specimen subjected to the modified Los Gatos records. The maximum response of the RC specimen in *X*- and *Y*-directions was 0.16 m (6.3 in.) and 0.1 m (3.9 in.), respectively; the maximum response of the PRC specimen was 0.17 m (6.7 in.) and 0.11 m (4.3 in.), respectively. The residual displacements were similar for both specimens. These results do not correspond to the quasi-static behavior, and the analytical models may have to be refined based on these results.

The response mainly occurred in 45° rotated axis, as shown in Figure 2.32(a); the response in *X*- and *Y*-directions have almost simultaneous peaks; see Figure 2.32(b). Thus, the displacement time histories and lateral force versus displacement hysteresis were computed for a 45° rotated coordinate system to determine how the specimens responded to a very large nonlinear response. Figure 2.33 suggests that both the specimens have similar peaks and similar residual displacements, while the hysteresis of the PRC specimen shows an origin-oriented hysteresis as expected.

Table 2.10 Near-field earthquake ground motion records.

Ground motions from the SAC steel project				
Record ID	**Record**	**Earthquake**	**PGA (m/sec^2)**	
			Normal	**Parallel**
NF01, 02	Tabas	Tabas, Iran, 1978	8.83	9.59
NF03, 04	Los Gatos	Loma Prieta, USA, 1989	7.04	4.49
NF05, 06	Lexington Dam	Loma Prieta, USA, 1989	6.73	3.63
NF07, 08	Petrolia	Cape Mendocino, USA, 1992	6.26	6.42
NF09, 10	Erzincan	Erzincan, Turkey, 1992	4.24	4.48
NF11, 12	Landers	Landers, USA, 1992	7.00	7.84
NF13, 14	Rinaldi	Northridge, USA, 1994	8.73	3.81
NF15, 16	Olive View	Northridge, USA, 1994	.18	5.84
NF17, 18	JMA Kobe	Hyogo-ken Nanbu, Japan, 1995	10.67	5.64
NF19, 20	Takatori	Hyogo-ken Nanbu, Japan, 1995	7.71	4.16
Ground motions from PEER database				
Record ID	**Station**	**Earthquake**	**PGA (m/sec^2)**	
			000 or 360	**090**
LGP000, 090	LGPC	Loma Prieta, USA, 1989	5.52	5.94
SYL360, 090	Olive View	Northridge, USA, 1994	8.27	5.93
KJM000, 090	JMA Kobe	Hyogo-ken Nanbu, Japan, 1995	8.05	5.88
TAK000, 090	Takatori	Hyogo-ken Nanbu, Japan, 1995	5.99	6.04

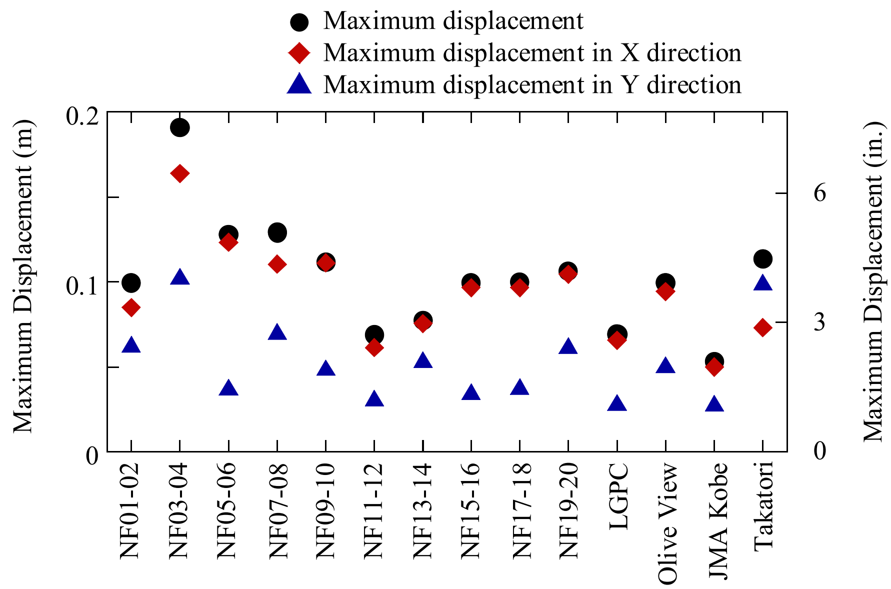

(a)

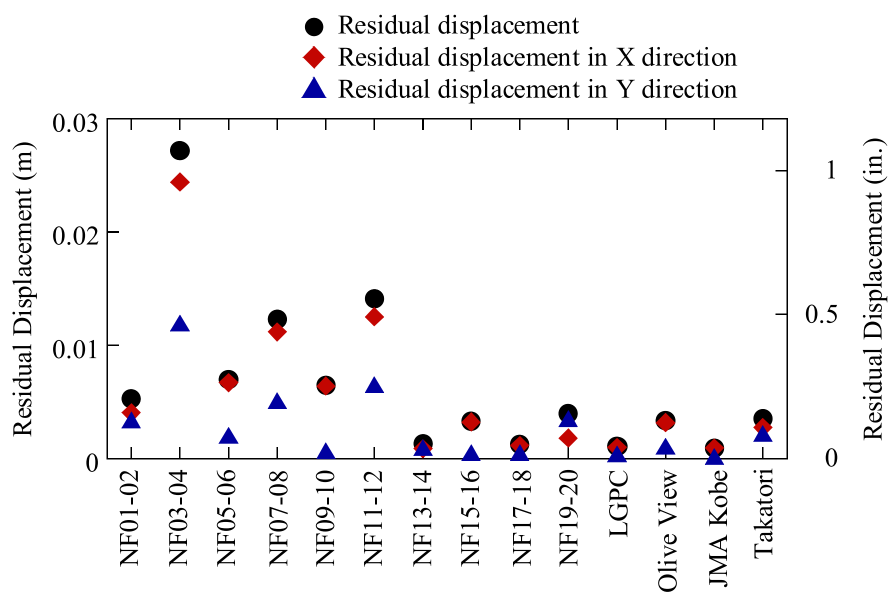

(b)

Figure 2.31 Response displacement of RC specimens: (a) maximum displacement and (b) residual displacement.

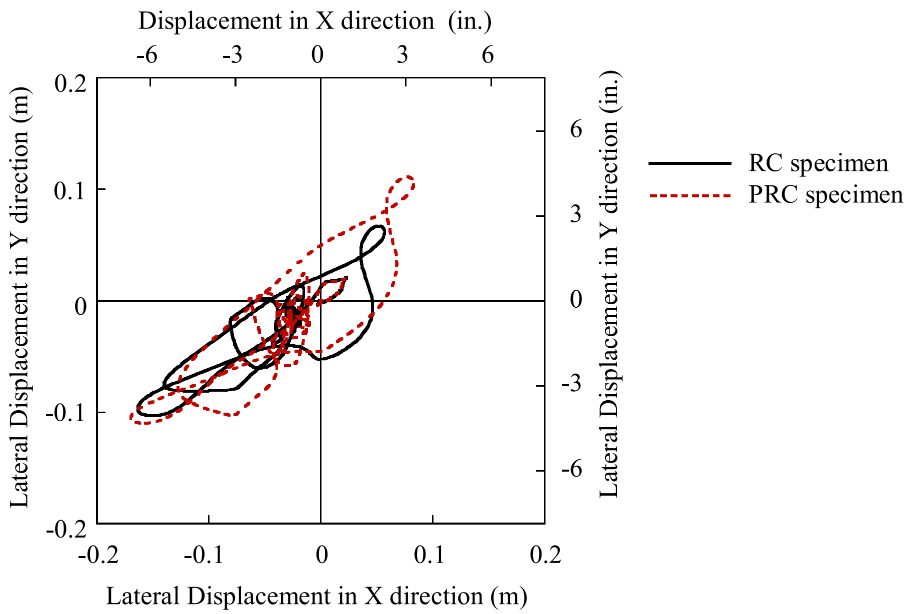

(a)

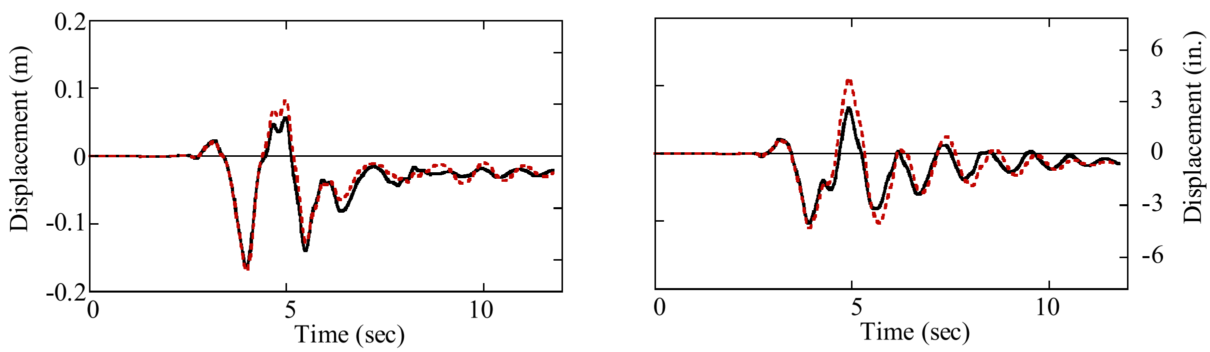

(b)

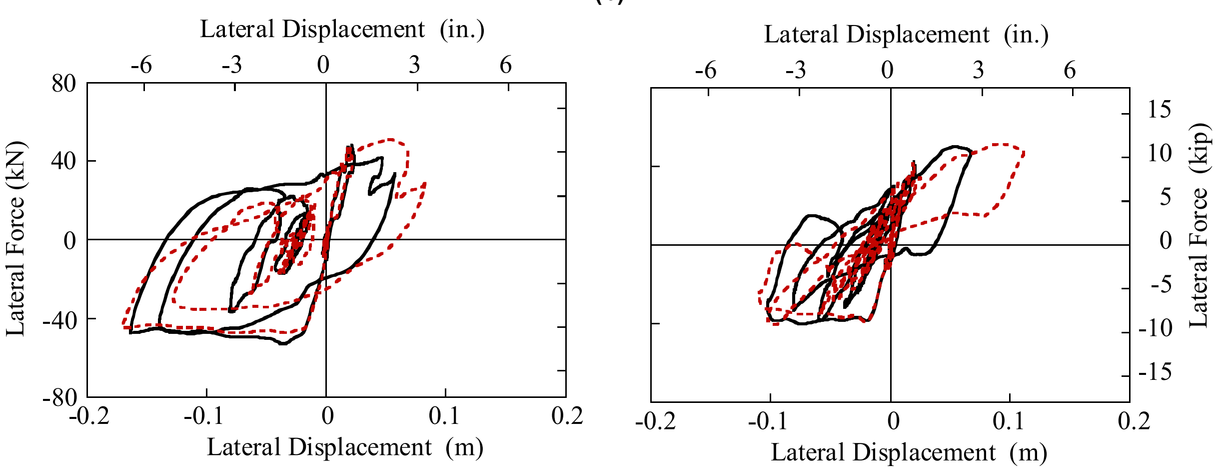

(c)

***X*-direction** **_Y_-direction**

Figure 2.32 Response of specimens subjected to modified Los Gatos record in the *X* and *Y*-directions: (a) orbit of lateral displacements; (b) response displacement at center-of-gravity of weighted blocks; and (c) lateral force–lateral displacement hysteresis.

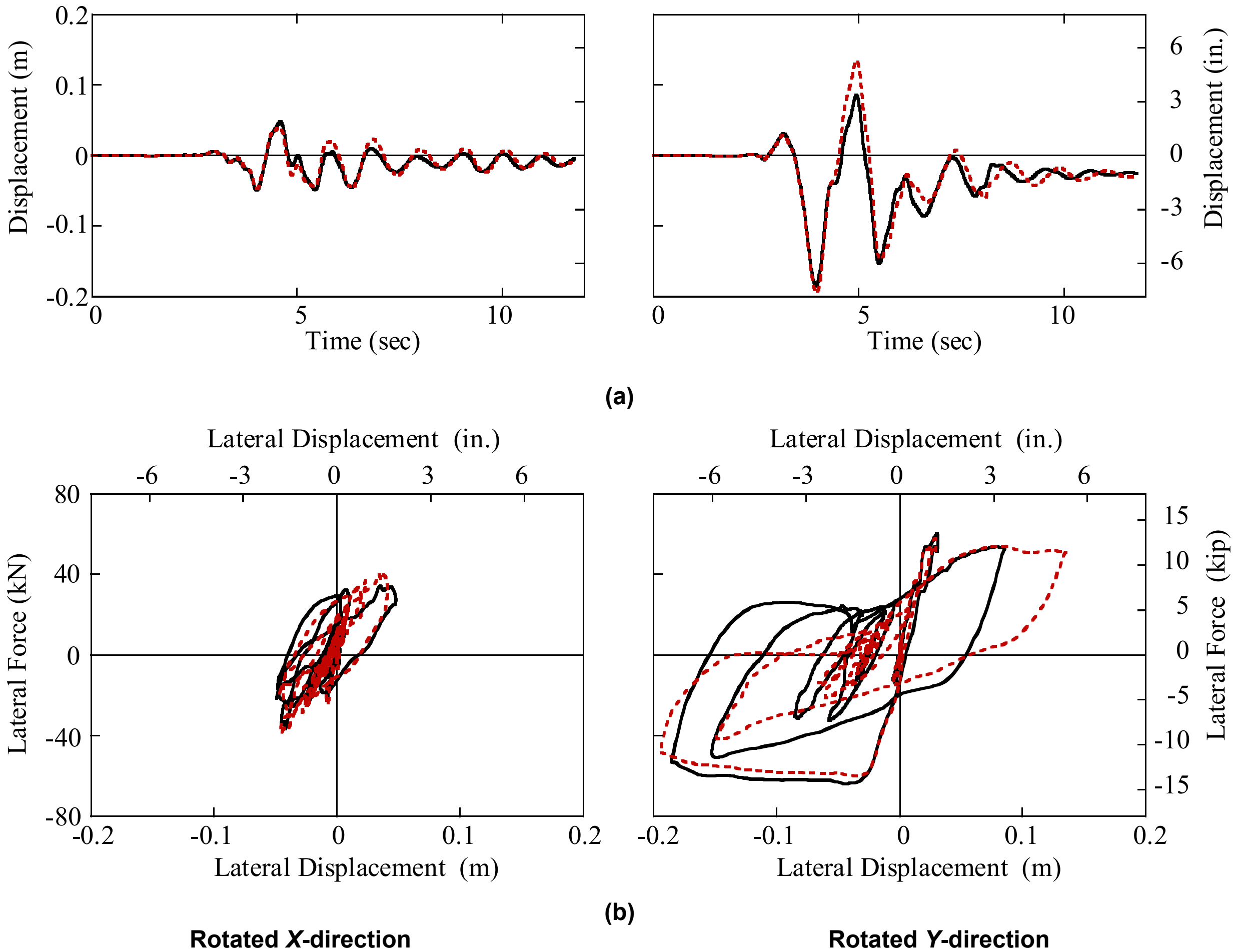

Figure 2.33 **Response in 45° rotated coordinate in the *X*- and *Y*-directions: (a) response displacement at weighted blocks; and (b) lateral force–lateral displacement hysteresis.**

3 Experimental Set-Up, Instrumentation, and Test Program

3.1 EARTHQUAKE SIMULATOR

A series of earthquake simulation tests were conducted with an earthquake simulator at the Richmond Field Station Earthquake Simulation Laboratory of the University of California, Berkeley; see Figure 3.1. The simulator was installed in the late 1960s as a two-dimensional (vertical and one horizontal) earthquake simulator, which was upgraded to a three-dimensional (vertical and two horizontal) simulator in 1994. The simulator has a 6.1-m (20-ft) square shaking table, which is heavily reinforced with both ordinary reinforcement and post-tensioning tendons so that it is stiff enough to have a natural frequency greater than 20 Hz; thus, it behaves essentially as a rigid body in the operating range of 0–10 Hz. The table itself weighs 445 kN (100,000 lbs). The table has prestressing holes that forms a 7×7 square grid, with spacings every 0.91 m (3 ft).

The shaking table is driven horizontally by eight 334-kN (75,000-lb) hydraulic actuators and vertically by four 334-kN (75,000-lb) actuators, which located in the pit; see Figures 3.2 and 3.3. An MTS model 469 controller controls the shaking table; see Figure 3.4. In operation, the air in the pit beneath the table is pressurized so that the total weight of the table and the structure being tested is balanced by the difference in air pressure in the pit and ambient air pressure. Table 3.1 summarizes the capacity of the earthquake simulator. Unloaded, the table can accelerate up to approximately 30 m/sec^2 (3g) and 0.76 m/sec (30 kips) in velocity. The table can subject structures weighing up to 445 kN (100,000 lbs) to horizontal accelerations of 14.8 m/sec^2 (1.5g). The data acquisition system has 192 channels.

Table 3.1 Earthquake simulator characteristics.

Table dimensions	6.1 m (20 ft)×6.1 m (20 ft), 445 kN (100 kips)
Maximum specimen height	12.2 m (40 ft) to ceiling, 9.75 m (32 ft) to crane hook
Component of motion	Six DOF, *X*, *Y*, and *Z* plus rotational components, pitch, roll and yaw.
Displacement limits	*X* and *Y* limits are ±127 mm (5 in.), Z limit is ±51 mm (2 in.)
Velocity limits	762 mm/sec (30 in./sec) in all axis with an unloaded table
Acceleration limits	Approximately 30 m/sec^2 (3g) in all axis with an unloaded table
Data acquisition system	192 channels at 200 Hz

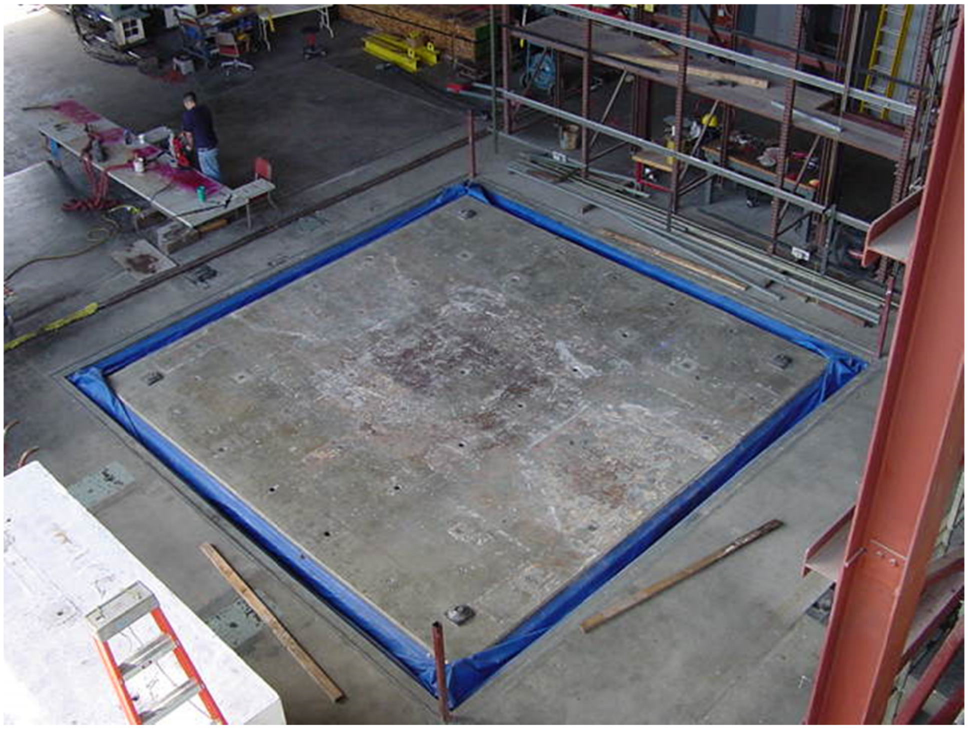

(a)

(b)

Figure 3.1 Earthquake simulator: (a) shaking table and (b) earthquake simulator laboratory.

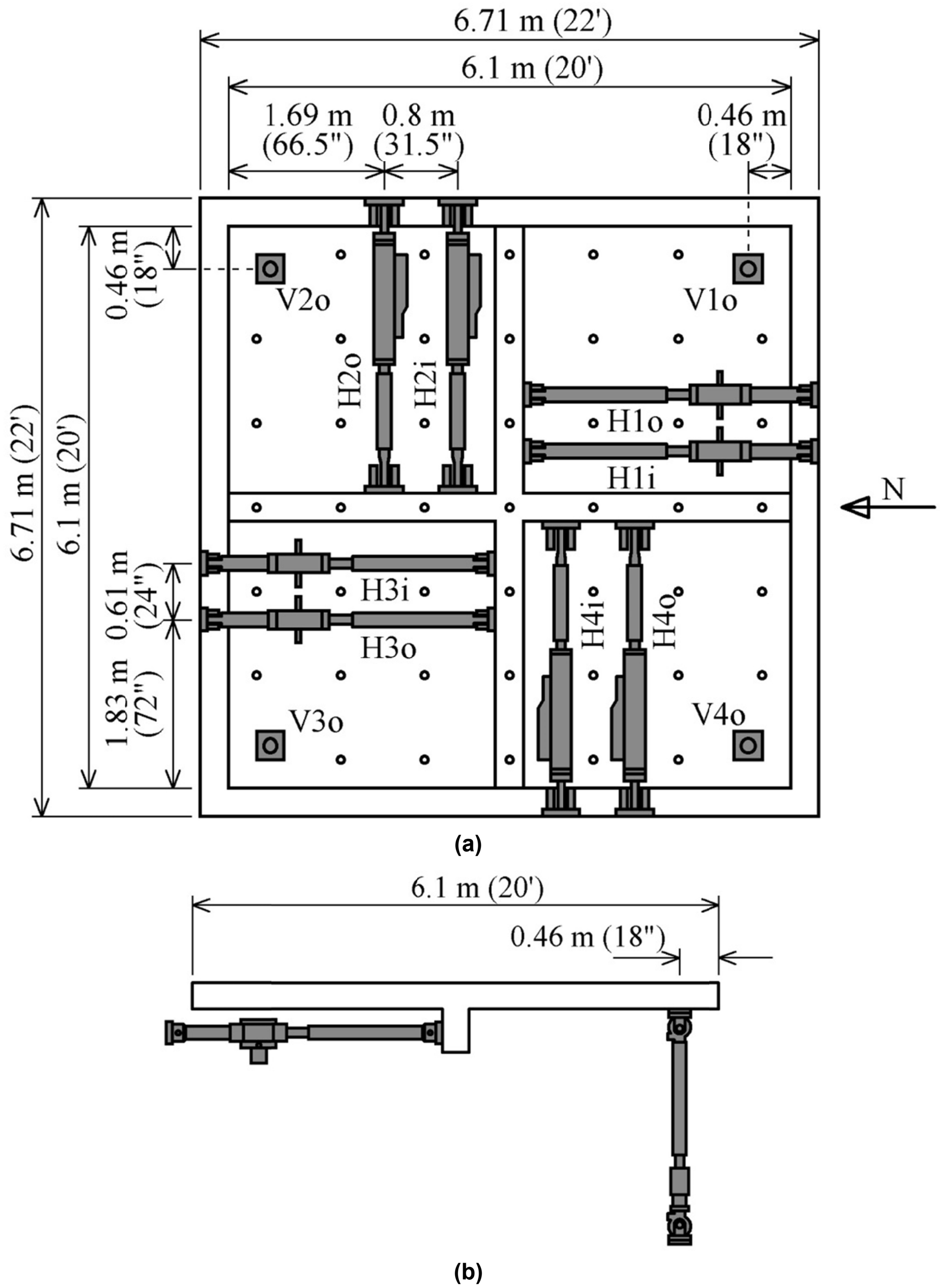

Figure 3.2 Arrangement of actuators: (a) plan and (b) elevation.

(a)

(b)

Figure 3.3 Actuators: (a) horizontal actuators and (b) vertical actuators.

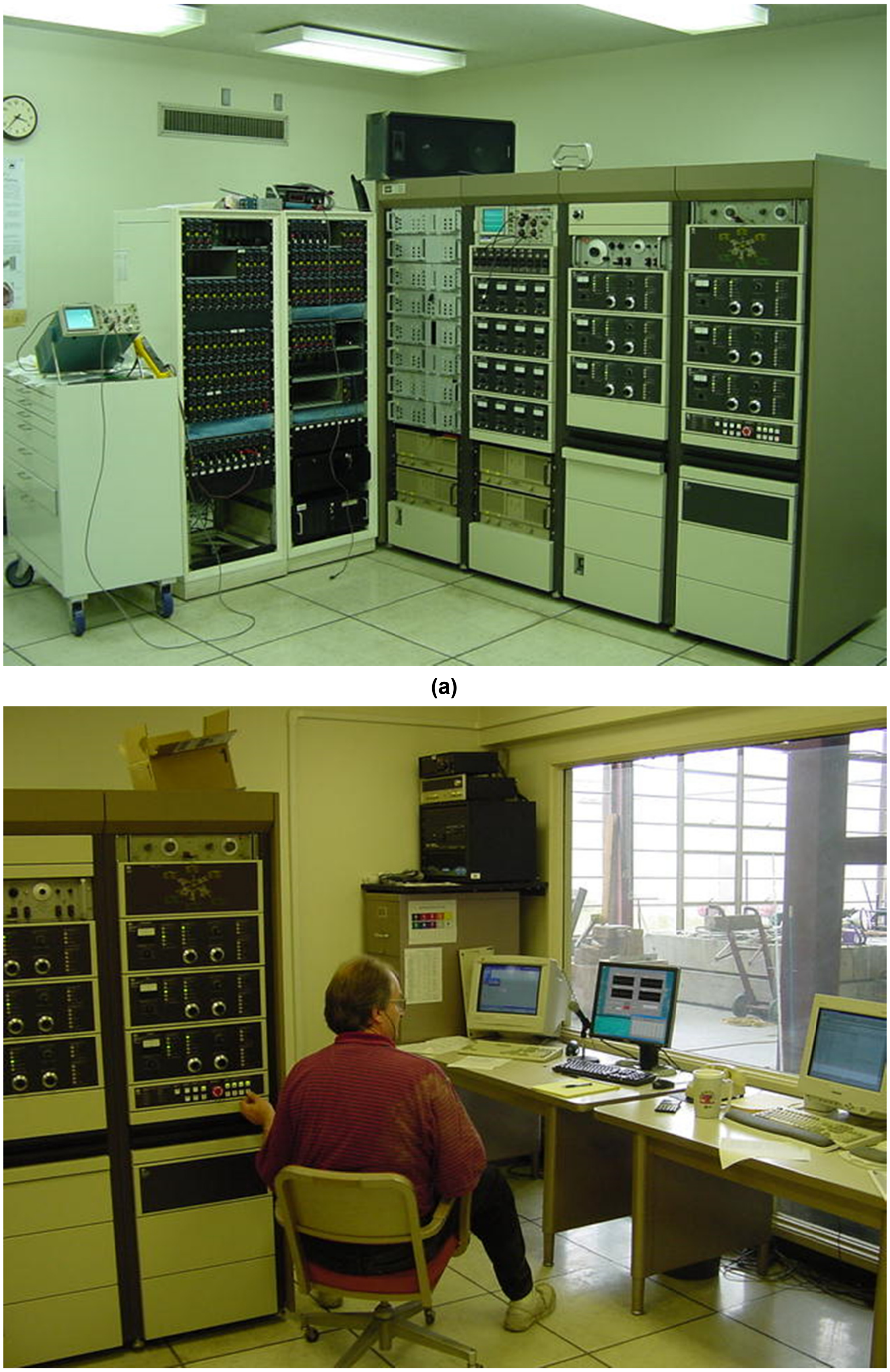

(a)

(b)

Figure 3.4 Control room: (a) controller and (b) data acquisition system.

3.2 TEST SET-UP

3.2.1 Conventional Reinforced Concrete Column Specimen

Figure 3.5 shows the specimen set-up. To arrange the specimen on the center of shaking table, steel plates with threaded holes for bolts to fix the tri-axial load cells were placed on the table. The plates were fixed to the shaking table with 19 prestressed tendons. The load cells (with four holes each to match the locations of holes for post-tensioning tendons of the specimen footing) were fixed to the steel plates with four 22-mm (7/8-in.) diameter high-strength bolts. Then, the RC specimen was carried by a 98 kN (22,000 lb) bridge crane and placed onto the load cells; see Figure 3.6. The specimen was fixed onto the load cells with a total of sixteen 22-mm (7/8-in.) diameter post-tensioning tendons. To provide a uniform contact surface, a layer of hydrostone was placed between the base steel plates and table, the plates and load cells, and the load cells and the bottom of the footing.

Weighted blocks were then placed on the top slab of the specimen; see Figure 3.7. The block with a center hole was placed directly onto the top slab of specimen to ensure the same dead load and inertia mass to that for the PRC specimen. Hydrostone was also used between the slab and the block, and between the blocks for the same reason described above. Eight 25-mm- (1-in.-) diameter post-tensioning tendons were used to tie the top slab and three weighed blocks together.

To prevent catastrophic collapse of the specimen during the tests, two 26-mm- (1-in.-) diameter steel cables were connected to each corner of the top slab; see Figure 3.8. Each of the cables had an allowable strength of 96 kN (21.6 kip). The breaking strength was estimated to be about 380 kN (86 kip) with a safety factor of 4, which was strong enough to catch the weight of top slab-weight blocks assembly by a single cable. The cables were designed to accommodate a displacement of at least 0.25 m (10 in.), which corresponded to a displacement ductility of about 10. The safety cables were designed to affect the damping properties of the specimen when the response was sufficiently large that the cables were pulled and vibrated.

The test set-up was completed in late July of 2003, but the earthquake simulation tests were conducted on May 27, 2004, because of problems with the hydraulic system and data acquisition system.

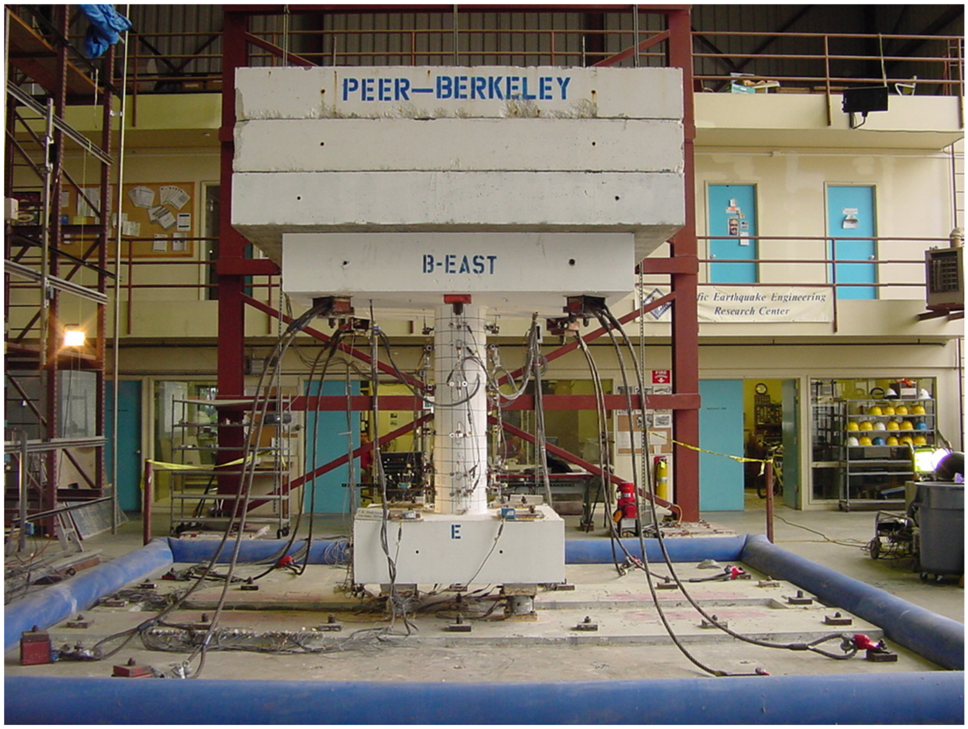

(a)

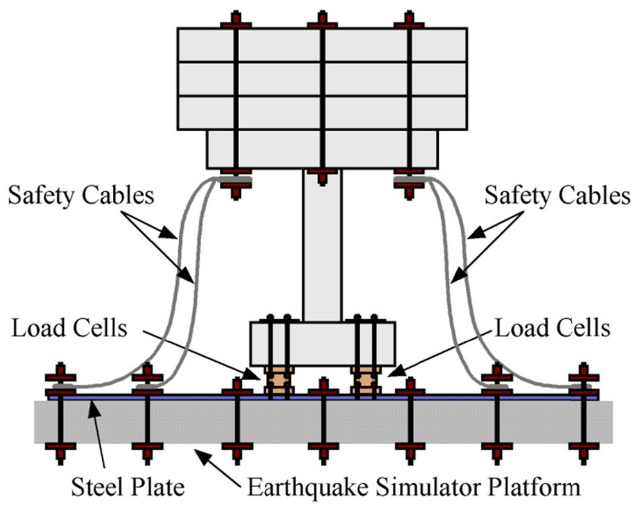

(b)

Figure 3.5 Set-up of RC specimen: (a) specimen on table and (b) test set-up.

Figure 3.6 Loading the specimen onto table.

Figure 3.7 Placing the weighted blocks on specimen.

(a)

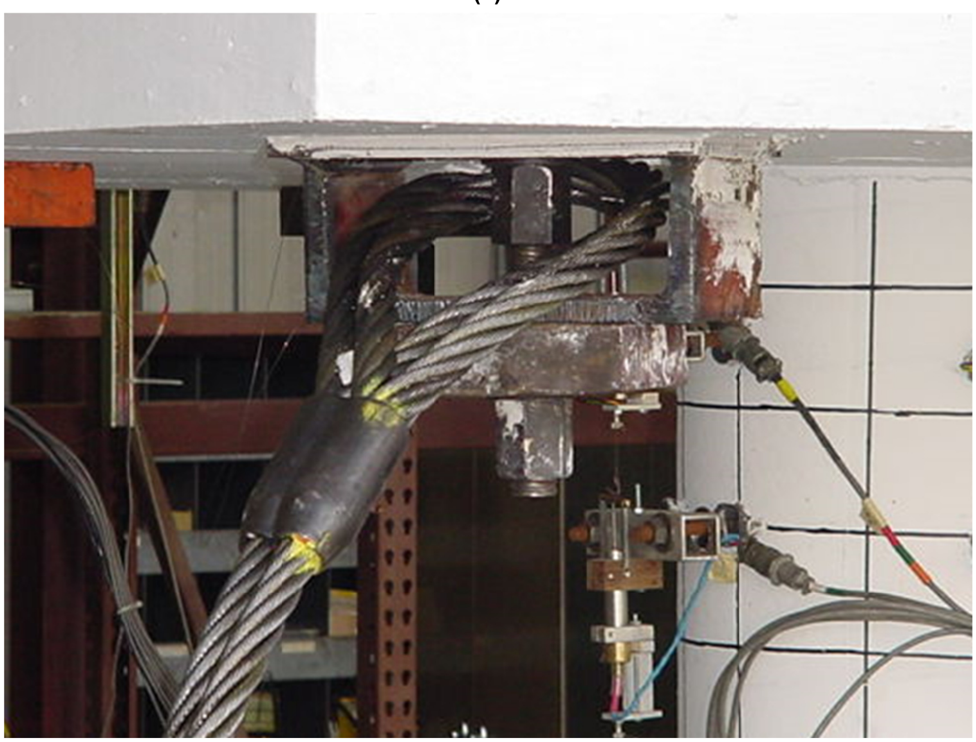

(b)

Figure 3.8 Safety system: (a) safety cables and (b) anchorage to top slab.

3.2.2 Partially Prestressed Reinforced Concrete Column Specimen

Figure 3.9 shows the specimen set-up on the shaking table. A 32-mm (1-1/4-in.) diameter post-tensioning tendon was installed into the PRC specimen prior to bringing the specimen onto the table. Steel plates [229-mm (9-in.) square and 41-mm (1-5/8-in.) thick] were used at the both ends of the tendon. The steel plate placed at the bottom end had a groove for threading instrumentation cables out from the center duct. A layer of hydrostone was placed between the plates and the specimen surface. A load cell with a center hole was placed underneath the specimen to monitor the prestressing force induced in the column.

The prestressing force was then applied to the tendon with a hydraulic jack; see Figure 3.10. Based on the analyses described in Section 2.2.3, a target prestressing force was determined to be 380 kN (85 kip), and the prestressing force applied was 394 kN (89 kip). After three days, the prestressing force in the specimen decreased down to 381 kN (86 kip) due to creep. Thus, the prestressing tendon was re-tied with a hydraulic jack before placement of the top blocks. The prestressing force was set at 399 kN (90 kip), taking into consideration the decrease due the weighted blocks and creep. As expected, the force decreased to 387 kN (87 kip) when the weight blocks were placed onto the specimen. Figure 3.11 shows the variation of the prestressing force with time. The force on the test day was 379 kN (85 kip), which was seven days after the blocks were placed. The total axial force ratio based on the design concrete strength (f'_{co} = 34.5 MPa) was 14.8%, and that for the concrete strength from cylinder tests (41.2 MPa) was 12.4%.

The specimen and weighted blocks were fixed in the same manner to the RC specimen. Safety cables were also provided, but the triggering displacement for the PRC specimen was set at 305 mm (12 in.).

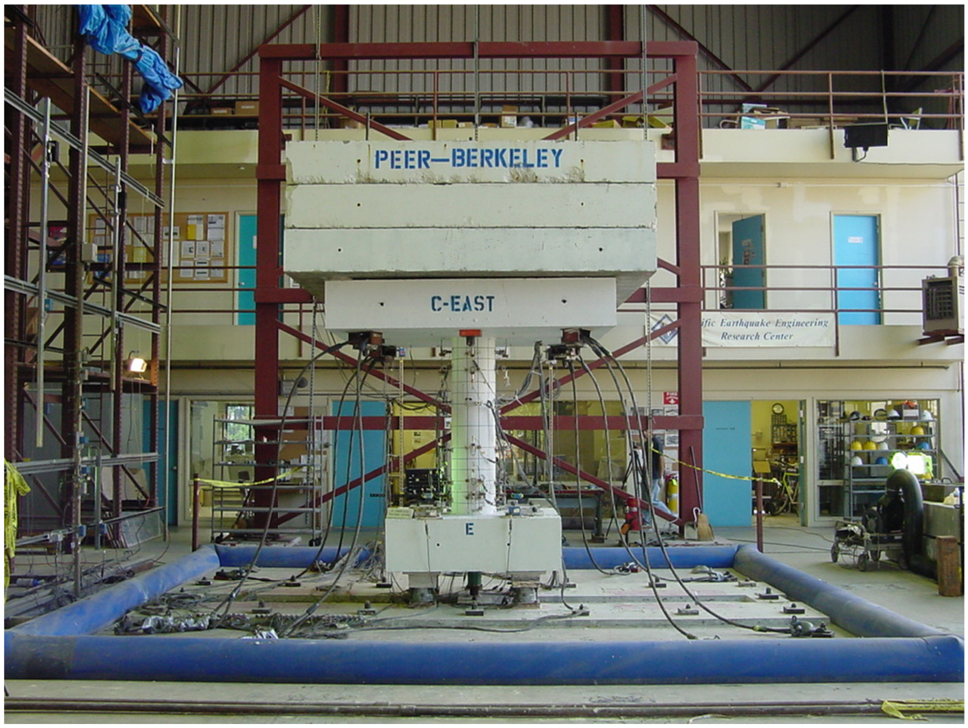

(a)

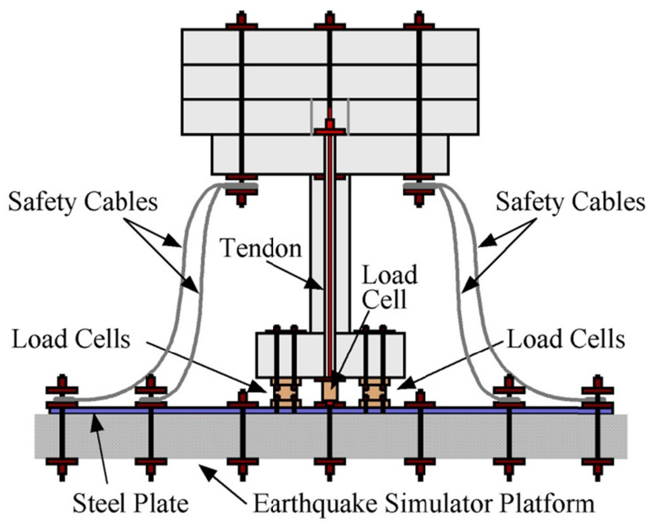

(b)

Figure 3.9 Set-up of PRC specimen: (a) specimen on table and (b) test set-up.

(a)

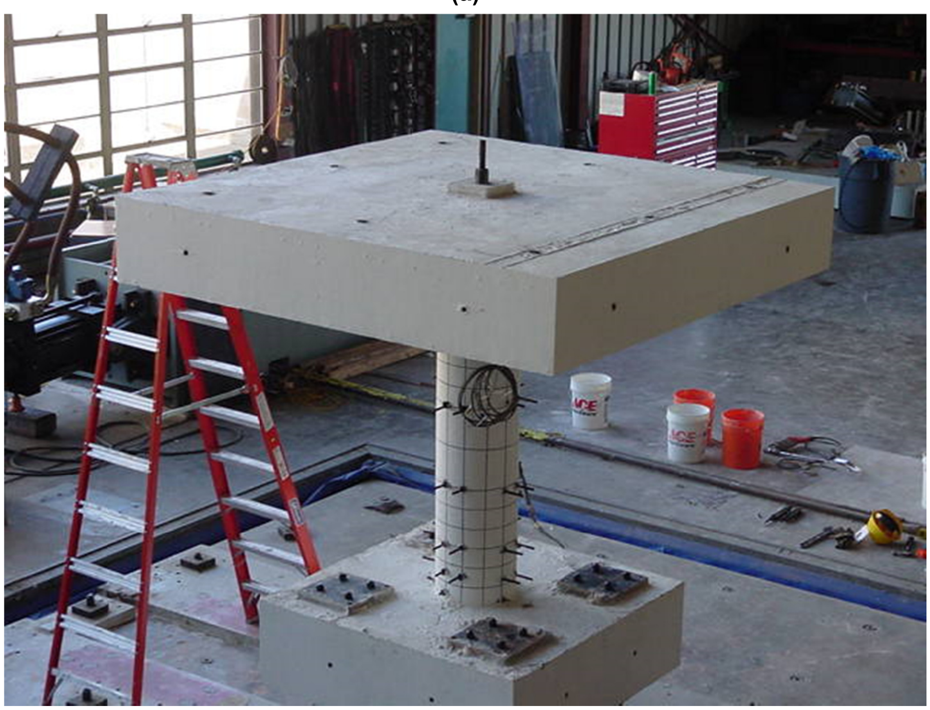

(b)

Figure 3.10 Installation of the prestressing force: (a) post-tensioning of specimen; and (b) anchorage of tendon at top.

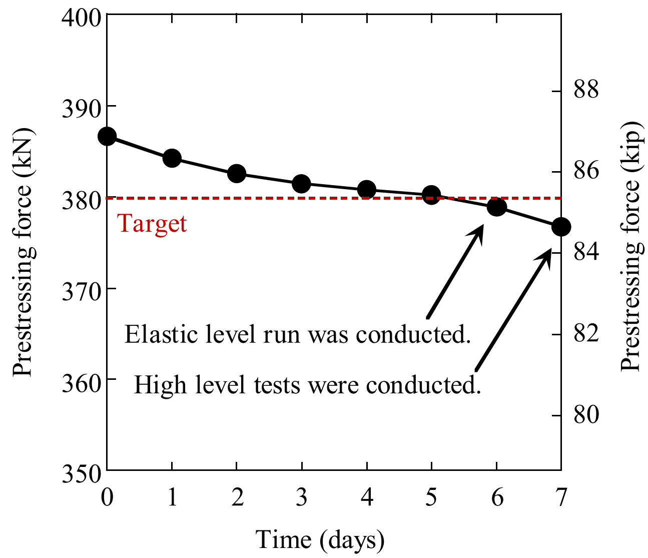

Figure 3.11 Variation of prestressing force due to creep.

3.3 COORDINATE SYSTEM

Figure 3.12 shows the global coordinate system of a specimen on the shaking table. In this study, the north–south direction was assigned to the *X*-direction, and the east–west direction was assigned to the *Y*-direction. The vertical direction is thus the *Z*-direction. The origin of the *XY*-plane of the coordinate system was taken at the center of the column. The origin of the *Z*-axis was assumed to be at the top of the footing of the specimen; see Figure 3.12(b).

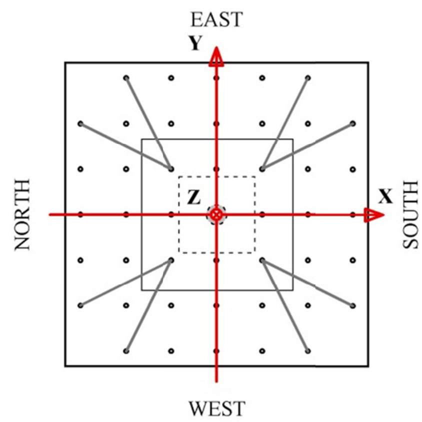

(a)

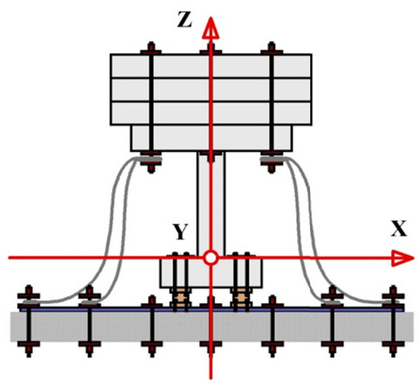

(b)

Figure 3.12 Coordinate system: (a) *XY* plane and (b) *XZ* plane.

3.4 INSTRUMENTATION OVERVIEW

3.4.1. RC Specimen

A total of 137 channels were used in the tests for the RC specimen. The channels were distributed as follows:

- 16 channels for monitoring accelerations and displacements of the shaking table
- 20 channels for tri-axial load cells monitoring restoring force of the specimen
- 17 channels for accelerometers
- 32 channels for linear potentiometers monitoring global displacement
- 28 channels for displacement transducers monitoring column local deformation
- 24 channels for strain gauges: 12 each for longitudinal reinforcing bars and spirals

3.4.2 PRC Specimen

A total of 138 channels were used in the tests for the PRC specimen. The channels were distributed as follows:

- 16 channels for monitoring accelerations and displacements of the shaking table
- 20 channels for tri-axial load cells monitoring restoring force of the specimen
- 17 channels for accelerometers
- 32 channels for linear potentiometers monitoring global displacement
- 24 channels for displacement transducers monitoring column local deformation
- 20 channels for strain gauges of reinforcement: 12 for longitudinal reinforcing bars, and 8 for spirals
- 1 channel for load cell and 8 channels for strain gauges monitoring tendon behavior

3.4.3 Shaking Table Instrumentation

Table 3.2 and Figure 3.13 show the channels and locations of the shaking table instrumentation, respectively. Horizontal accelerations and displacements were monitored through four accelerometers placed beams of the table and four displacement transducers acting along the outer horizontal actuators. Vertical accelerations and displacements were monitored through four accelerometers and four displacement transducers placed near the four corners of the table.

Table 3.2 Channels for shaking table instrumentation.

Channel ID	Transducer	Orientation	Coordinate (m)			Note
			X	*Y*	*Z*	
H1O	LVDT	N-S (X)	0	1.22	-----	SE Actuator
H2O	LVDT	E-W (Y)	-1.36	0	-----	NE Actuator
H3O	LVDT	N-S (X)	0	-1.22	-----	NW Actuator
H4O	LVDT	E-W (Y)	1.36	0	-----	SW Actuator
V1O	LVDT	Vertical (Z)	2.59	2.59	-----	SE Actuator
V2O	LVDT	Vertical (Z)	-2.59	2.59	-----	NE Actuator
V3O	LVDT	Vertical (Z)	-2.59	-2.59	-----	NW Actuator
V4O	LVDT	Vertical (Z)	2.59	-2.59	-----	SW Actuator
H1-2	Accelerometer	N-S (X)	-0.15	2.44	-----	East side
H3-4	Accelerometer	N-S (X)	-0.15	-2.44	-----	West side
H4-1	Accelerometer	E-W (Y)	2.44	-0.15	-----	South side
H2-3	Accelerometer	E-W (Y)	-2.44	-0.15	-----	North side
V1ACC	Accelerometer	Vertical (Z)	2.59	2.59	-----	SE Actuator
V2ACC	Accelerometer	Vertical (Z)	-2.59	2.59	-----	NE Actuator
V3ACC	Accelerometer	Vertical (Z)	-2.59	-2.59	-----	NW Actuator
V4ACC	Accelerometer	Vertical (Z)	2.59	-2.59	-----	SW Actuator

Note: Coordinates in *Z*-axis are not available.

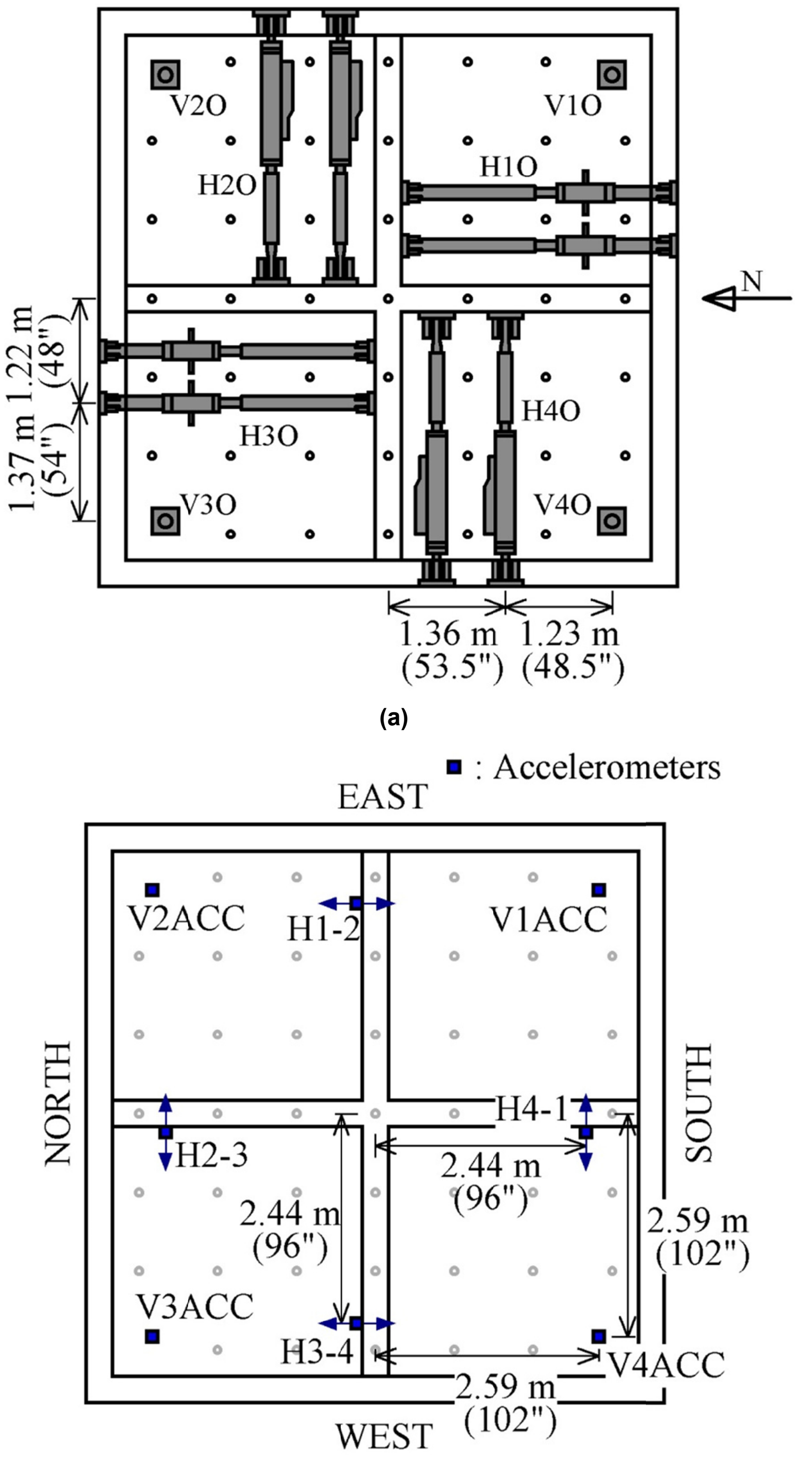

Figure 3.13 Shaking table instrumentation: (a) LVDTs and (b) accelerometers.

3.4.4 Tri-Axial Load Cells Monitoring Restoring Force of Columns

Table 3.3 summarizes the channels, and Figure 3.14 shows the set-up of four tri-axial load cells. Four load cells supported a specimen at four corners, and monitored the axial load, shear forces in the X- and Y-directions, and bending moments about X and Y axes. The recorded axial loads were used to compute bending moment capacity of the columns, and the shear forces were used to estimate shear force applied to the columns. Although bending moments monitored by the load cells do not produce any useful information, they were recorded during the tests.

Table 3.3 Channels for tri-axial load cells monitoring restoring force of columns.

Channel ID	Transducer	Orientation	Coordinate (m)			Note
			X	*Y*	*Z*	
lc1p	Load cell (Axial)	Vertical (Z)	-0.46	-0.46	-0.46	LC4, NW corner
lc1mx	Load cell (Moment)	About N-S (X)	-0.46	-0.46	-0.46	LC4, NW corner
lc1my	Load cell (Moment)	About E-W (Y)	-0.46	-0.46	-0.46	LC4, NW corner
lc1vx	Load cell (Shear)	N-S (X)	-0.46	-0.46	-0.46	LC4, NW corner
lc1vy	Load cell (Shear)	E-W (Y)	-0.46	-0.46	-0.46	LC4, NW corner
lc2p	Load cell (Axial)	Vertical (Z)	-0.46	0.46	-0.46	LC6, NE corner
lc2mx	Load cell (Moment)	About N-S (X)	-0.46	0.46	-0.46	LC6, NE corner
lc2my	Load cell (Moment)	About E-W (Y)	-0.46	0.46	-0.46	LC6, NE corner
lc2vx	Load cell (Shear)	N-S (X)	-0.46	0.46	-0.46	LC6, NE corner
lc2vy	Load cell (Shear)	E-W (Y)	-0.46	0.46	-0.46	LC6, NE corner
lc3p	Load cell (Axial)	Vertical (Z)	0.46	0.46	-0.46	LC5, SE corner
lc3mx	Load cell (Moment)	About N-S (X)	0.46	0.46	-0.46	LC5, SE corner
lc3my	Load cell (Moment)	About E-W (Y)	0.46	0.46	-0.46	LC5, SE corner
lc3vx	Load cell (Shear)	N-S (X)	0.46	0.46	-0.46	LC5, SE corner
lc3vy	Load cell (Shear)	E-W (Y)	0.46	0.46	-0.46	LC5, SE corner
lc4p	Load cell (Axial)	Vertical (Z)	0.46	-0.46	-0.46	LC2, SW corner
lc4mx	Load cell (Moment)	About N-S (X)	0.46	-0.46	-0.46	LC2, SW corner
lc4my	Load cell (Moment)	About E-W (Y)	0.46	-0.46	-0.46	LC2, SW corner
lc4vx	Load cell (Shear)	N-S (X)	0.46	-0.46	-0.46	LC2, SW corner
lc4vy	Load cell (Shear)	E-W (Y)	0.46	-0.46	-0.46	LC2, SW corner

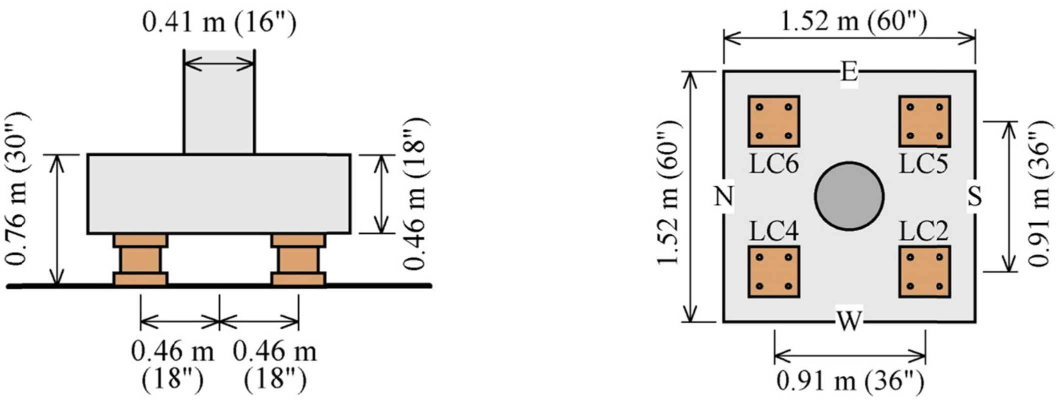

(a) side view **(b) top view**

(1)

(2)

Figure 3.14 Tri-axial load cells: (1) arrangement of load cells; and (2) load cells fixed on steel plates.

3.4.5 Accelerometers

Accelerations were measured by accelerometers mounted at seven locations on the specimens and the weighted blocks; see Figure 3.15. Table 3.4 summarizes the channels of the accelerometers. The same configuration was used for both the RC and PRC specimens. Groups of three accelerometers, which monitored accelerations in the two horizontal (X and Y) and vertical (Z) directions were placed on the west and south faces of the footing and the weighted blocks, and the top of the weighted blocks. Additional two accelerometers were placed on the middle of the columns to measure column accelerations in the X- and Y-directions.

Table 3.4 Channels for accelerometers.

Channel ID	Transducer	Orientation	Coordinate (m)			Note
			X	*Y*	*Z*	
accel1	Accelerometer	N-S (*X*)	0	-0.76	-0.23	Footing, west
accel2	Accelerometer	E-W (*Y*)	0	-0.76	-0.23	Footing, west
accel3	Accelerometer	Vertical (*Z*)	0	-0.76	-0.23	Footing, west
accel4	Accelerometer	N-S (*X*)	0.76	0	-0.23	Footing, south
accel5	Accelerometer	E-W (*Y*)	0.76	0	-0.23	Footing, south
accel6	Accelerometer	Vertical (*Z*)	0.76	0	-0.23	Footing, south
accel7	Accelerometer	N-S (*X*)	0	-1.52	2.44	C.G., west
accel8	Accelerometer	E-W (*Y*)	0	-1.52	2.44	C.G., west
accel9	Accelerometer	Vertical (*Z*)	0	-1.52	2.44	C.G., west
accel10	Accelerometer	N-S (*X*)	1.52	0	2.44	C.G., south
accel11	Accelerometer	E-W (*Y*)	1.52	0	2.44	C.G., south
accel12	Accelerometer	Vertical (*Z*)	1.52	0	2.44	C.G., south
accel13	Accelerometer	N-S (*X*)	0	0	3.10	Top
accel14	Accelerometer	E-W (*Y*)	0	0	3.10	Top
accel15	Accelerometer	Vertical (*Z*)	0	0	3.10	Top
accel16	Accelerometer	N-S (*X*)	0.20	0	0.81	Column, south
accel17	Accelerometer	E-W (*Y*)	0	-0.20	0.81	Column, west

Note: C.G.: Center-of-gravity of top slab-weighted blocks assembly; Top: top of weighted blocks; and Column: mid-height of column.

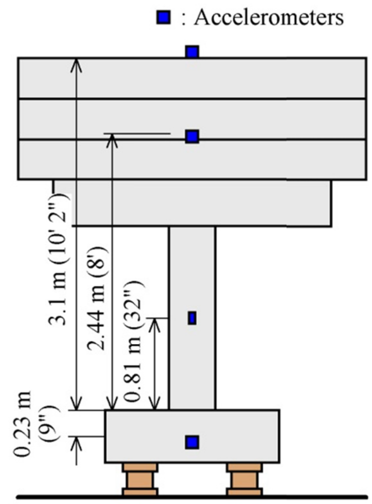

Figure 3.15 Locations of accelerometers.

3.4.6 Linear Potentiometers Monitoring Global Displacement

Specimen movements and deformations during the tests were captured by a total of 32 linear potentiometers (LPs); see Figure 3.16. Table 3.5 summarizes the channels of the LPs. The same configuration was used for both of the specimens. The displacement of the footing was measured by three LPs for each direction at the south and west faces. Because it is essential to capture the footing movement to obtain relative displacement of the weighted blocks to assess the response and local damage of the specimens during the tests, three LPs were used for each direction in the event of failure of an LP.

To capture the responses of the columns, five LPs for each direction were placed at the south and west faces of the top slab-weighted blocks assembly. One of them was placed at the center-of-gravity of the assembly, and two were placed near the top edge of the weighted blocks. The other two were placed at the middle height of the top slab; these pairs of the LPs were arranged to capture rotational movement of the specimen.

Twelve LPs were used to capture local deformations of the columns. Six LPs for each direction were placed at heights of 152 mm (6 in.), 305 mm (12 in.), 610 mm (24 in.), 1016 mm (40 in.), 1321 mm (52 in.) and 1473 mm (58 in.) from the bottom of the column. An additional 4 LPs were placed at the four corners of the footing to monitor vertical displacements between the footing and top slab.

As shown in Appendix D, measured lateral displacements did not exactly represent lateral movement of specimens under bi-directional loading conditions. Because the effects of bi-directional movement are minor, the measured values were used to investigate dynamic behavior of the specimens.

Table 3.5 Channels for linear potentiometers (wire pods).

Channel ID	Transducer	Orientation	Coordinate (m)			Note
			X	*Y*	*Z*	
WP1	Linear potentiometer	N-S (*X*)	0.76	-0.61	-0.23	Footing, south (W)
WP2	Linear potentiometer	N-S (*X*)	0.76	0	-0.23	Footing, south
WP3	Linear potentiometer	N-S (*X*)	0.76	0.61	-0.23	Footing, south (E)
WP4	Linear potentiometer	E-W (*Y*)	-0.61	-0.76	-0.23	Footing, west (N)
WP5	Linear potentiometer	E-W (*Y*)	0	-0.76	-0.23	Footing, West
WP6	Linear potentiometer	E-W (*Y*)	0.61	-0.76	-0.23	Footing, West (S)
WP7	Linear potentiometer	N-S (*X*)	1.22	-1.07	1.83	Top slab, South (W)
WP8	Linear potentiometer	N-S (*X*)	1.22	1.07	1.83	Top slab, South (E)
WP9	Linear potentiometer	E-W (*Y*)	-1.07	-1.22	1.83	Top slab, West (N)
WP10	Linear potentiometer	E-W (*Y*)	1.07	-1.22	1.83	Top slab, West (S)
WP13	Linear potentiometer	N-S (*X*)	1.52	0	2.44	C.G., South
WP12	Linear potentiometer	E-W (*Y*)	0	-1.52	2.44	C.G., West
WP11	Linear potentiometer	N-S (*X*)	1.52	-1.07	3.07	Top, South (W)
WP14	Linear potentiometer	N-S (*X*)	1.52	1.07	3.07	Top, South (E)
WP15	Linear potentiometer	E-W (*Y*)	-1.07	-1.52	3.07	Top, West (N)
WP16	Linear potentiometer	E-W (*Y*)	1.07	-1.52	3.07	Top, West (S)
WP17	Linear potentiometer	N-S (*X*)	0.20	0	0.15	Column 6 in., South
WP18	Linear potentiometer	N-S (*X*)	0.20	0	0.30	Column 12 in., South
WP19	Linear potentiometer	N-S (*X*)	0.20	0	0.61	Column 24 in., South
WP20	Linear potentiometer	N-S (*X*)	0.20	0	1.02	Column 40 in., South
WP21	Linear potentiometer	N-S (*X*)	0.20	0	1.32	Column 52 in., South
WP22	Linear potentiometer	N-S (*X*)	0.20	0	1.47	Column 58 in., South
WP23	Linear potentiometer	E-W (*Y*)	0	-0.20	0.15	Column 6 in., West
WP24	Linear potentiometer	E-W (*Y*)	0	-0.20	0.30	Column 12 in., West
WP25	Linear potentiometer	E-W (*Y*)	0	-0.20	0.61	Column 24 in., West
WP26	Linear potentiometer	E-W (*Y*)	0	-0.20	1.02	Column 40 in., West
WP27	Linear potentiometer	E-W (*Y*)	0	-0.20	1.32	Column 52 in., West
WP28	Linear potentiometer	E-W (*Y*)	0	-0.20	1.47	Column 58 in., West
WP29	Linear potentiometer	Vertical (*Z*)	0.61	-0.61	0	Top of footing, SW
WP30	Linear potentiometer	Vertical (*Z*)	0.61	0.61	0	Top of footing, SE
WP31	Linear potentiometer	Vertical (*Z*)	-0.61	-0.61	0	Top of footing, NW
WP32	Linear potentiometer	Vertical (*Z*)	-0.61	0.61	0	Top of footing, NE

Note: C.G.: Center-of-gravity of top slab-weight blocks assembly; and Top: Near top of weight blocks.

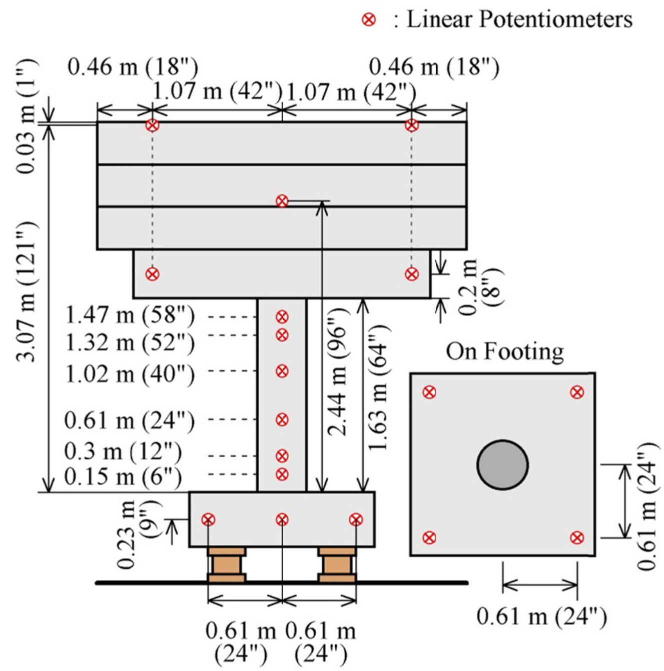

Figure 3.16 Locations of linear potentiometers (wire pods).

3.4.7 Displacement Transducers Monitoring Column Local Deformation

Twenty-eight direct current displacement transducers (DCDTs) and 24 DCDTs were used for the RC and PRC specimens, respectively, to monitor vertical deformation at the specimen surfaces in estimating the average curvatures of the columns. Table 3.6 and Figure 3.17 show the channels and locations of the DCDTs.

The DCDTs measured the vertical displacements between the 13-mm (1/2-in.) threaded rods crossing the section. The rods were placed at 51 mm (2 in.), 152 mm (6 in.), 305 mm (12 in.), 610 mm (24 in.), 1016 mm (40 in.), 1321 mm (52 in.) and 1473 mm (58 in.) during the construction. The DCDTs were placed at about 100 mm (4 in.) from the column surface. The actual horizontal distance between the DCDTs and the surface, and vertical distance between the rods or the rod and surface of footing or top slab were measured prior to the tests (see Table 3.6). The readings from pairs of DCDTs located at 152 mm (6 in.) were used to estimate the amount of rebar pullout from the footing. Vertical deformations between the rods at 1016 mm (40 in.) and 1321 mm (52 in.) were not measured due to limitation of channels of the data acquisition system. For the PRC specimen, vertical deformations between the rods 1321 mm (52 in.) and 1473 mm (58 in.) were not measured for the same reason. Figure 3.18 shows a set-up of the DCDTs. Targets of the DCDTs were placed at the top of equipment that fixed the DCDTs to the rods with bolts and nuts.

Table 3.6(a) Channels for direct current displacement transducer: RC specimen.

Channel ID	Transducer	Vertical distance	Horizontal distance from column surface	Note
dcdt1	DCDT	179 mm (7-1/16 in.)	101 mm (3-31/32)	Pullout, North
dcdt2	DCDT	146 mm (5-3/4 in.)	92 mm (3-5/8 in.)	Pullout, East
dcdt3	DCDT	152 mm (6 in.)	76 mm (3 in.)	Pullout, South
dcdt4	DCDT	143 mm (5-5/8 in.)	95 mm (3-3/4 in.)	Pullout, West
dcdt5	DCDT	148 mm (5-13/16 in.)	102 mm (4-1/32 in.)	Column 12, North
dcdt6	DCDT	152 mm (6 in.)	85 mm (3-11/32 in.)	Column 12, East
dcdt7	DCDT	166 mm (6-17/32 in.)	76 mm (3 in.)	Column 12, South
dcdt8	DCDT	159 mm (6-1/4 in.)	92 mm (3-5/8 in.)	Column 12, West
dcdt9	DCDT	314 mm (12-3/8 in.)	102 mm (4 in.)	Column 24, North
dcdt10	DCDT	310 mm (12-3/16 in.)	87 mm (3-7/16 in.)	Column 24, East
dcdt11	DCDT	264 mm (10-3/8 in.)	76 mm (3 in.)	Column 24, South
dcdt12	DCDT	308 mm (12-1/8 in.)	84 mm (3-5/16 in.)	Column 24, West
dcdt13	DCDT	321 mm (12-5/8 in.)	80 mm (3-5/32 in.)	Column 40, North
dcdt14	DCDT	305 mm (12 in.)	87 mm (3-7/16 in.)	Column 40, East
dcdt15	DCDT	268 mm (10-9/16 in.)	73 mm (2-7/8 in.)	Column 40, South
dcdt16	DCDT	313 mm (12-5/16 in.)	76 mm (3 in.)	Column 40, West
dcdt17	DCDT	152 mm (6 in.)	75 mm (2-31/32 in.)	Column 52, North
dcdt18	DCDT	162 mm (6-3/8 in.)	90 mm (3-9/16 in.)	Column 52, East
dcdt19	DCDT	151 mm (5-15/16 in.)	84 mm (3-5/16 in.)	Column 52, South
dcdt20	DCDT	144 mm (5-11/16 in.)	75 mm (2-31/32 in.)	Column 52, West
dcdt21	DCDT	164 mm (6-7/16 in.)	81 mm (3-3/16 in.)	Column 58, North
dcdt22	DCDT	156 mm (6-1/8 in.)	95 mm (3-3/4 in.)	Column 58, East
dcdt23	DCDT	175 mm (6-7/8 in.)	89 mm (3-1/2 in.)	Column 58, South
dcdt24	DCDT	156 mm (6-1/8 in.)	88 mm (3-15/32 in.)	Column 58, West
dcdt25	DCDT	135 mm (5-5/16 in.)	73 mm (2-7/8 in.)	Column 6, North
dcdt26	DCDT	124 mm (4-7/8 in.)	66 mm (2-19/32 in.)	Column 6, East
dcdt27	DCDT	124 mm (4-7/8 in.)	57 mm (2-1/4 in.)	Column 6, South
dcdt28	DCDT	114 mm (4-1/2 in.)	73 mm (2-7/8 in.)	Column 6, West

Table 3.6(b) Channels for direct current displacement transducer: PRC specimen.

Channel ID	Transducer	Vertical distance	Horizontal distance from column surface	Note
dcdt1	DCDT	124 mm (4-7/8 in.)	89 mm (3-1/2 in.)	Pullout, North
dcdt2	DCDT	159 mm (6-1/4 in.)	79 mm (3-1/8 in.)	Pullout, East
dcdt3	DCDT	124 mm (4-7/8 in.)	92 mm (3-5/8 in.)	Pullout, South
dcdt4	DCDT	159 mm (6-1/4 in.)	95 mm (3-3/4 in.)	Pullout, West
dcdt5	DCDT	146 mm (5-3/4 in.)	84 mm (3-5/16 in.)	Column 12, North
dcdt6	DCDT	159 mm (6-1/4 in.)	76 mm (3 in.)	Column 12, East
dcdt7	DCDT	165 mm (6-1/2 in.)	92 mm (3-5/8 in.)	Column 12, South
dcdt8	DCDT	146 mm (5-3/4 in.)	86 mm (3-3/8 in.)	Column 12, West
dcdt9	DCDT	318 mm (12-1/2 in.)	83 mm (3-1/4 in.)	Column 24, North
dcdt10	DCDT	302 mm (11-7/8 in.)	83 mm (3-1/4 in.)	Column 24, East
dcdt11	DCDT	305 mm (12 in.)	92 mm (3-5/8 in.)	Column 24, South
dcdt12	DCDT	302 mm (11-7/8 in.)	89 mm (3-1/2 in.)	Column 24, West
dcdt17	DCDT	157 mm (6-3/16 in.)	95 mm (3-3/4 in.)	Column 52, North
dcdt18	DCDT	149 mm (5-7/8 in.)	95 mm (3-3/4 in.)	Column 52, East
dcdt19	DCDT	159 mm (6-1/4 in.)	94 mm (3-11/16 in.)	Column 52, South
dcdt20	DCDT	146 mm (5-3/4 in.)	102 mm (4 in.)	Column 52, West
dcdt21	DCDT	130 mm (5-1/8 in.)	105 mm (4-1/8 in.)	Column 58, North
dcdt22	DCDT	159 mm (6-1/4 in.)	98 mm (3-7/8 in.)	Column 58, East
dcdt23	DCDT	121 mm (4-3/4 in.)	95 mm (3-3/4 in.)	Column 58, South
dcdt24	DCDT	159 mm (6 1/4 in.)	86 mm (3-3/8 in.)	Column 58, West
dcdt25	DCDT	105 mm (4 1/8 in.)	64 mm (2-1/2 in.)	Column 6, North
dcdt26	DCDT	108 mm (4 1/4 in.)	64 mm (2-1/2 in.)	Column 6, East
dcdt27	DCDT	111 mm (4 3/8 in.)	83 mm (3-1/4 in.)	Column 6, South
dcdt28	DCDT	108 mm (4 1/4 in.)	83 mm (3-1/4 in.)	Column 6, West

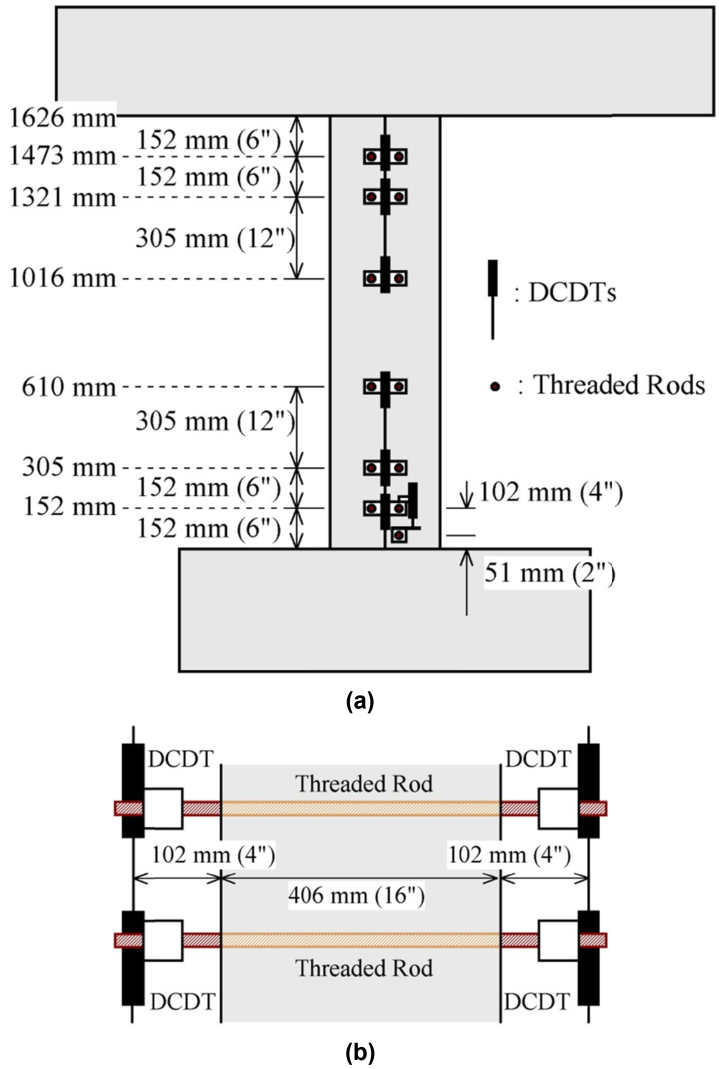

Figure 3.17 **DCDTs monitoring column vertical deformation: (a) locations of DCDTs and (b) side view.**

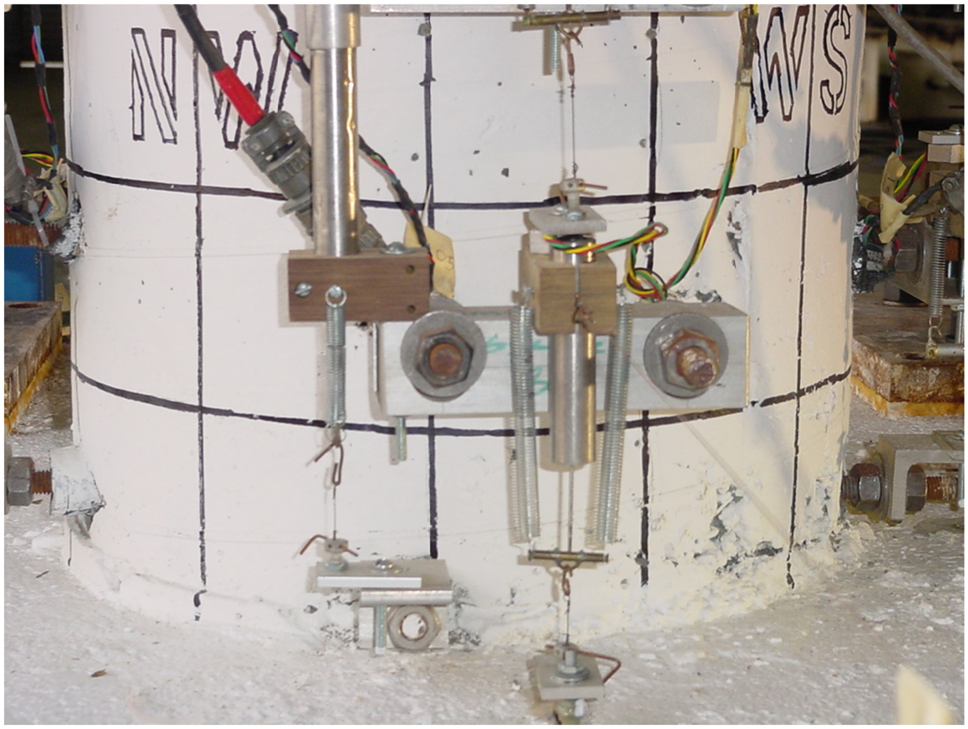

Figure 3.18 Set-up of DCDTs at bottom of column.

3.4.8 Strain Gauges

A total of 24 strain gauges were used in the RC specimen, and 20 gauges were used in the PRC specimen. Table 3.7 summarizes the channels for the gauges. Figure 3.19 shows the location of the strain gauges. For both specimens, 12 strain gauges monitored strain of the longitudinal reinforcement; the gauges (labeled as YFLA-5) were supplied by Tokyo Sokki Kenkyujo Co. Prior to construction, four reinforcing bars, which were at the north, east, south and west side, were gauged and protected with coating materials from Vishay Micro-Measurements. The gauges were placed at the rebar surface facing outside. The gauges were located at a height of 13 mm (1/2 in.) and 108 mm (4 1/4 in.) from the bottom of the column, and 13 mm (1/2 in.) from the top of the column.

The gauges labeled as YFLA-2 and supplied by the Tokyo Sokki Kenkyujo Co., Ltd. was used on the spirals. Three layers of spirals for the RC specimen and two layers for the PRC specimen were gauged. The gauge locations were same as those on longitudinal bars except for absence of spiral gauges for the top of PRC specimen. The gauges were attached at the upper side of spirals and properly protected after casting footing concrete but prior to the construction of column forms.

Although the gauges were carefully attached and properly protected, some of the gauges were not available at the tests, as shown in Table 3.7. Although some of the gauges were operational, their data was not used because they could not be identified due to absence of labels. All the spiral gauges of the PRC specimen were not identified because the labels were misplaced during construction.

Table 3.7(a) Channels for strain gauges: RC specimen.

(a) RC specimen						
Channel ID	**Transducer**	**Reinforcement**	**Coordinate (mm)**			**Note**
			X	***Y***	***Z***	
sg1	Strain gauge	Longitudinal	-184	0	13	Bottom 1, North
sg2	Strain gauge	Longitudinal	0	184	13	Bottom 1, East
sg3	Strain gauge	Longitudinal	184	0	13	Bottom 1, South
sg4	Strain gauge	Longitudinal	0	-184	13	Bottom 1, West
sg5	Strain gauge	Spiral	-188	0	13	Bottom 1, North
sg6	Strain gauge	Spiral	0	188	13	Bottom 1, East
sg7	Strain gauge	Spiral	188	0	13	Bottom 1, South
sg8	Strain gauge	Spiral	0	-188	13	Bottom 1, West
sg9	Strain gauge	Longitudinal	-184	0	108	Bottom 2, North
sg10	Strain gauge	Longitudinal	0	184	108	Bottom 2, East
sg11	Strain gauge	Longitudinal	184	0	108	Bottom 2, South
sg12	Strain gauge	Longitudinal	0	-184	108	Bottom 2, West
sg13	Strain gauge	Spiral	-188	0	108	Bottom 2, North
~~sg14~~	~~Strain gauge~~	~~Spiral~~	~~0~~	~~188~~	~~108~~	~~Bottom 2, East~~, **DEAD**
sg15	Strain gauge	Spiral	188	0	108	Bottom 2, South
sg16	Strain gauge	Spiral	0	-188	108	Bottom 2, West
sg17	Strain gauge	Longitudinal	-184	0	1613	Top, North
~~sg18~~	~~Strain gauge~~	~~Longitudinal~~	~~0~~	~~184~~	~~1613~~	~~Top, East~~, **DEAD**
sg19	Strain gauge	Longitudinal	184	0	1613	Top, South
sg20	Strain gauge	Longitudinal	0	-184	1613	Top, West
sg21	Strain gauge	Spiral	-188	0	1613	Top, North
sg22	Strain gauge	Spiral	0	188	1613	Top, East
sg23	Strain gauge	Spiral	188	0	1613	Top, South
sg24	Strain gauge	Spiral	0	-188	1613	Top, West

Table 3.7(b) Channels for strain gauges: PRC specimen.

(b) PRC specimen						
Channel ID	Transducer	Reinforcement	Coordinate (mm)			Note
			X	*Y*	*Z*	
sg1	Strain gauge	Longitudinal	-184	0	13	Bottom 1, North
sg2	Strain gauge	Longitudinal	0	184	13	Bottom 1, East
sg3	Strain gauge	Longitudinal	184	0	13	Bottom 1, South
sg4	Strain gauge	Longitudinal	0	-184	13	Bottom 1, West
sg5	Strain gauge	Longitudinal	-184	0	108	Bottom 2, North
sg6	Strain gauge	Longitudinal	0	184	108	Bottom 2, East
sg7	Strain gauge	Longitudinal	184	0	108	Bottom 2, South
sg8	Strain gauge	Longitudinal	0	-184	108	Bottom 2, West
sg9	Strain gauge	Longitudinal	-184	0	1613	Top, North
sg10	Strain gauge	Longitudinal	0	184	1613	Top, East
~~sg11~~	~~Strain gauge~~	~~Longitudinal~~	~~184~~	~~0~~	~~1613~~	~~Top, South~~, **DEAD**
~~sg12~~	~~Strain gauge~~	~~Longitudinal~~	~~0~~	~~-184~~	~~1613~~	~~Top, West~~, **DEAD**
sg13	Strain gauge	Spiral	-188	0	13	~~Bottom 1, North~~
sg14	Strain gauge	Spiral	0	188	13	~~Bottom 1, East~~
sg15	Strain gauge	Spiral	188	0	13	~~Bottom 1, South~~
sg16	Strain gauge	Spiral	0	-188	13	~~Bottom 1, West~~
sg17	Strain gauge	Spiral	-188	0	108	~~Bottom 2, North~~
sg18	Strain gauge	Spiral	0	188	108	~~Bottom 2, East~~
sg19	Strain gauge	Spiral	188	0	108	~~Bottom 2, South~~
sg20	Strain gauge	Spiral	0	-188	108	~~Bottom 2, West~~

Note: Spiral gauges could not be specified due to missing of labels.

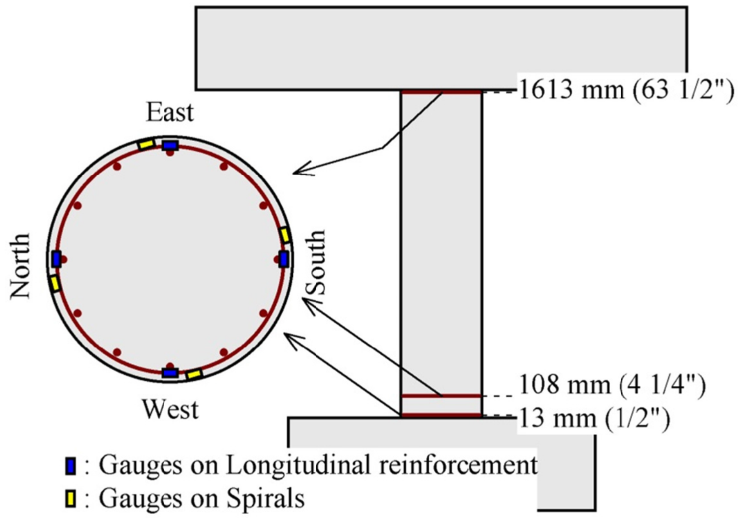

Figure 3.19 Locations of strain gauges.

3.4.9 Strain Gauges and Load Cell Monitoring Tendon Behavior

A total of 8 strain gauges were attached to the tendon of the PRC specimen, and a load cell with a center hole was placed underneath the specimen to monitor its behavior. Table 3.8 and Figure 3.20 show the channels and locations of the instruments for the tendon. Two groups of four gauges were attached at a height of 0.77 m (30-1/2 in.) from the bottom and at a height of 0.67 m (26-1/2 in.) from the top of the 3.05-m (10-ft) long tendon, i.e., located at a height of 13 mm (1/2 in.) from the bottom and top of the column. The gauges (designated as YFLA-5 and supplied by Tokyo Sokki Kenkyujo Co., Ltd.) were attached to the four sides to evaluate axial and flexural deformation of the tendon. A load cell with a center hole was placed underneath the specimen to monitor variation of prestressing force due to creep during the tests. The capacity of the load cell was 890 kN (200 kip).

Table 3.8 Channels for strain gauges and load-cell monitoring tendon behavior.

Channel ID	Transducer	Reinforcement	Coordinate (mm)			Note
			X	*Y*	*Z*	
sg21	Strain gauge	Vertical (Z)	-16	0	13	Bottom, North
sg22	Strain gauge	Vertical (Z)	0	16	13	Bottom, East
sg23	Strain gauge	Vertical (Z)	16	0	13	Bottom, South
sg24	Strain gauge	Vertical (Z)	0	-16	13	Bottom, West
sg25	Strain gauge	Vertical (Z)	-16	0	1613	Top, North
sg26	Strain gauge	Vertical (Z)	0	16	1613	Top, East
sg27	Strain gauge	Vertical (Z)	16	0	1613	Top, South
sg28	Strain gauge	Vertical (Z)	0	-16	1613	Top, West
TendonLC	Load cell	Vertical (Z)	0	0	-610	Tendon Load Cell

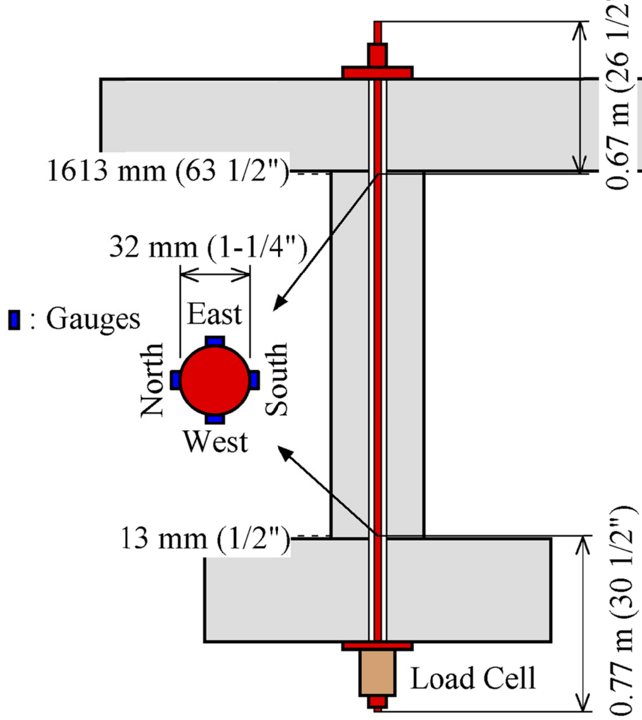

Figure 3.20 Locations of instrumentation monitoring tendon behavior.

3.5 DATA ACQUISITION AND DOCUMENTATION OF DAMAGE

Data was recorded during the tests by the earthquake simulator's data acquisition system. The system consists of 192 channels: the first 16 channels (Channel No. 1–16) are reserved for the shaking table instrumentation; 128 channels (Channel No. 17–144) are channels with gain; and 48 channels (Channel No. 145–192) are ones without gain. All the instruments of each specimen were calibrated with cables used prior to the tests. Data was read from the channels once every 0.005 sec (200 Hz) and saved in a text file.

Data recording was initiated a few seconds prior to the beginning of the earthquake signal. The lead time was eliminated in the data processing to allow comparison of the specimen behaviors between the RC specimen and the PRC specimen. Earthquake simulation tests were conducted in number of steps, as described in Section 3.7. Data was corrected if necessary to ensure continuity from the last data of the previous level test in order to follow residual deformation and strains.

In addition to the digital data recorded, digital videos were taken during the tests to document specimen behaviors and progress of local damage. Three video cameras were used simultaneously: two cameras were focused on the bottom portion of the column where the plastic hinge was expected to develop at the east–south and the north–west faces, while the third camera was used to capture a global response of the specimen from the east side.

Digital photographs were taken prior to the tests and after each test to document local damage of the columns. In the intervals between the tests, concrete cracks that occurred during the tests were traced by colored makers, and then photographs of these cracks were taken using digital cameras. Crack patterns were drawn according to the digital photographs after all the tests were finished. Crack pattern drawings, shown in Chapter 4, were drawn as a flattened surface; see Figure 3.21). The sides were marked as W, S, E and N from the left to right, standing for the west, south, east, and north faces, respectively.

To help identifying the location of local damage (such as concrete cracks, spalling of cover concrete, and buckling of longitudinal reinforcing bars), the specimens were painted in white, and a grid pattern was drawn with black markers on the specimen prior to testing. The grid lines were spaced at 102 mm (4 in.) vertically along the column and at 30° increments around the perimeter horizontally.

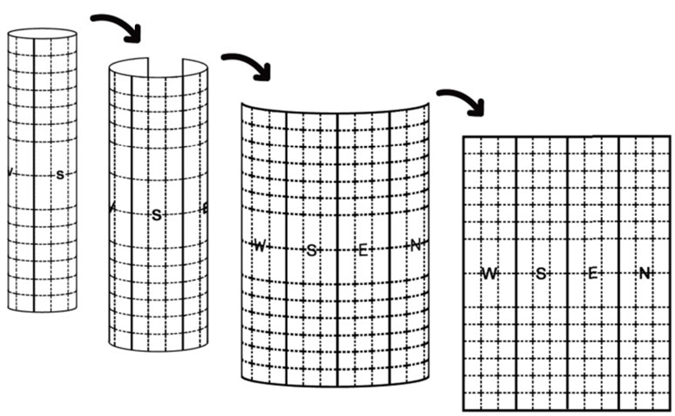

Figure 3.21 Crack pattern drawing.

3.6 GROUND MOTION

As described in Section 2.5, the modified Los Gatos records were selected as input signals used in the earthquake simulation tests based on the results from dynamic analyses. Figure 3.22 shows Fourier spectra and ground acceleration, velocity, and displacement time histories of the pre-processed records taking into account the scaling factor of the specimens. The processed records are also shown in the figure for comparison. Each record has 2500 data points, for a duration of 11.8 sec. The peak ground acceleration, velocity, and displacement of the stronger component were 7.1 m/sec^2 (0.72*g*), 0.82 m/sec (32.1 in./sec) and 0.14 m (5.5 in.), respectively. A shown in Table 3.1, the displacement capacity of the simulator is 0.13 m (5 in.); therefore, preprocessing was performed for the records.

The first step in processing of the data was to eliminate the first 150 data and last 100 data to reduce the data size obtained from the tests, thereby decreasing the number of data and duration of the records to 2250 and 10.6 sec, respectively. The records were then band-pass filtered to reduce the peak ground displacement. The filter was characterized using two cutoff frequencies and two corner frequencies. Using a trial-and-error procedure, they were determined as 0.4 and 0.5 Hz for the lower frequency and 12 and 15 Hz for the higher frequency.

As input signals for the earthquake simulator, the displacements at the beginning and the end are required to be zero. Thus, the filtered displacement time histories were then processed with a time window as follows:

$$d_{\text{input}}\left(t\right)=\begin{cases} d\left(t\right)\cdot\sin\left(0.5\pi\cdot t\right) & 0\le t<1 \\ d\left(t\right) & 1\le t\le dt\cdot N-1 \\ -d\left(t\right)\cdot\sin\left[0.5\pi\left(t-dt\cdot N\right)\right] & dt\cdot N-1<t\le dt\cdot N \end{cases} \tag{3.1}$$

where $d_{\text{input}}\left(t\right)$ is the input signal for the earthquake simulator, $d\left(t\right)$ is the filtered ground displacement, *dt* is the time increment of the data taking account of a scaling factor, and *N* is the number of data.

The peak ground acceleration increased by 3%, while the peak velocity and displacement decreased; see Figure 3.22. The response spectra is compared in Figure 3.23. The response of the structures that has a fundamental natural period of 0.67 sec is similar, even after the records were filtered.

The ground motion with the stronger intensity, which is the fault-normal component, was used for the *X*-direction (north–south); the motion with the weaker intensity (the fault-parallel component) was used for *Y*-direction (east–west).

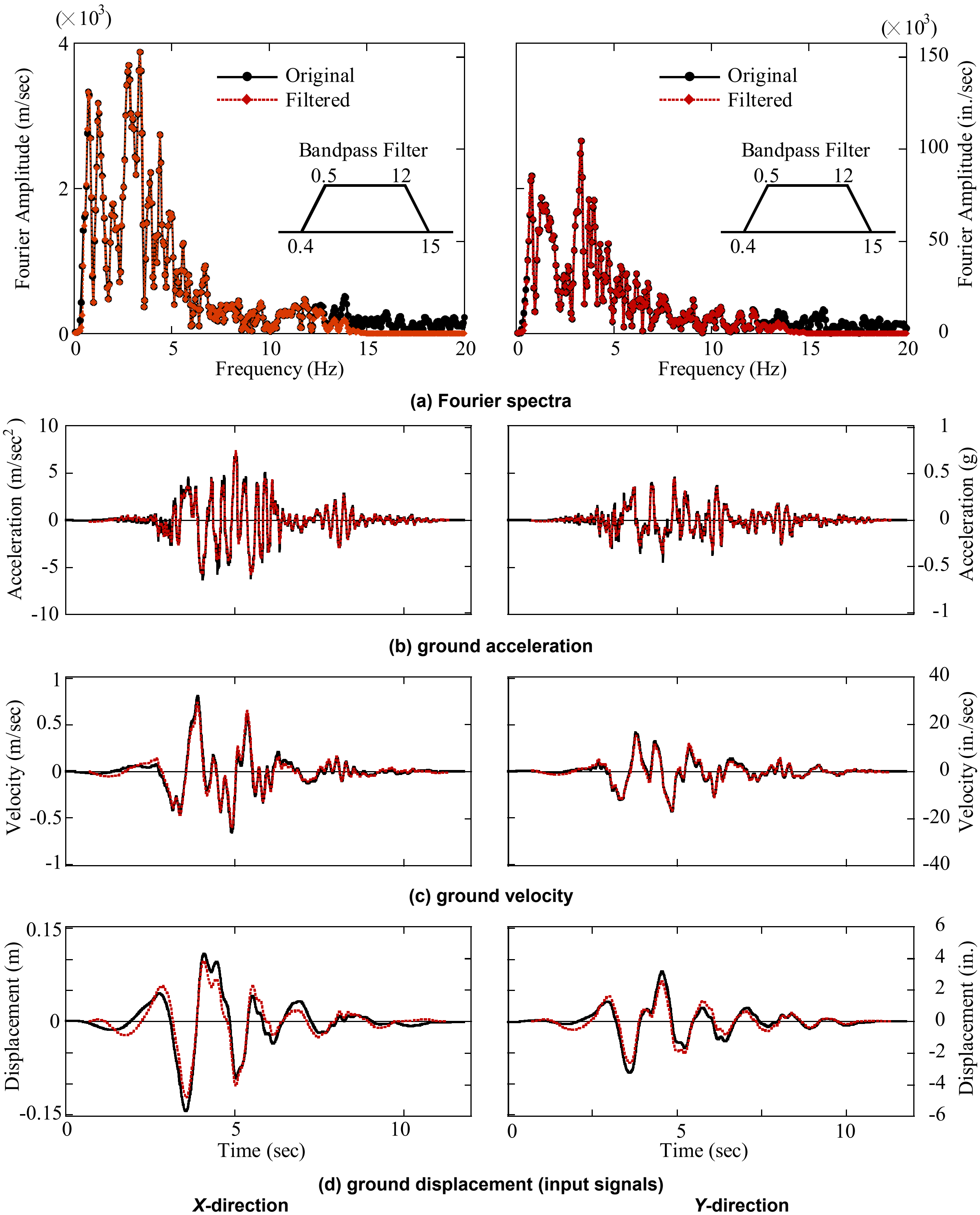

Figure 3.22 **Filtered ground motion in the fault-normal (*X*) and fault-parallel (*Y*) directions: (a) Fourier spectra; (b) ground acceleration; (c) ground velocity; and (d) ground displacement (input signals).**

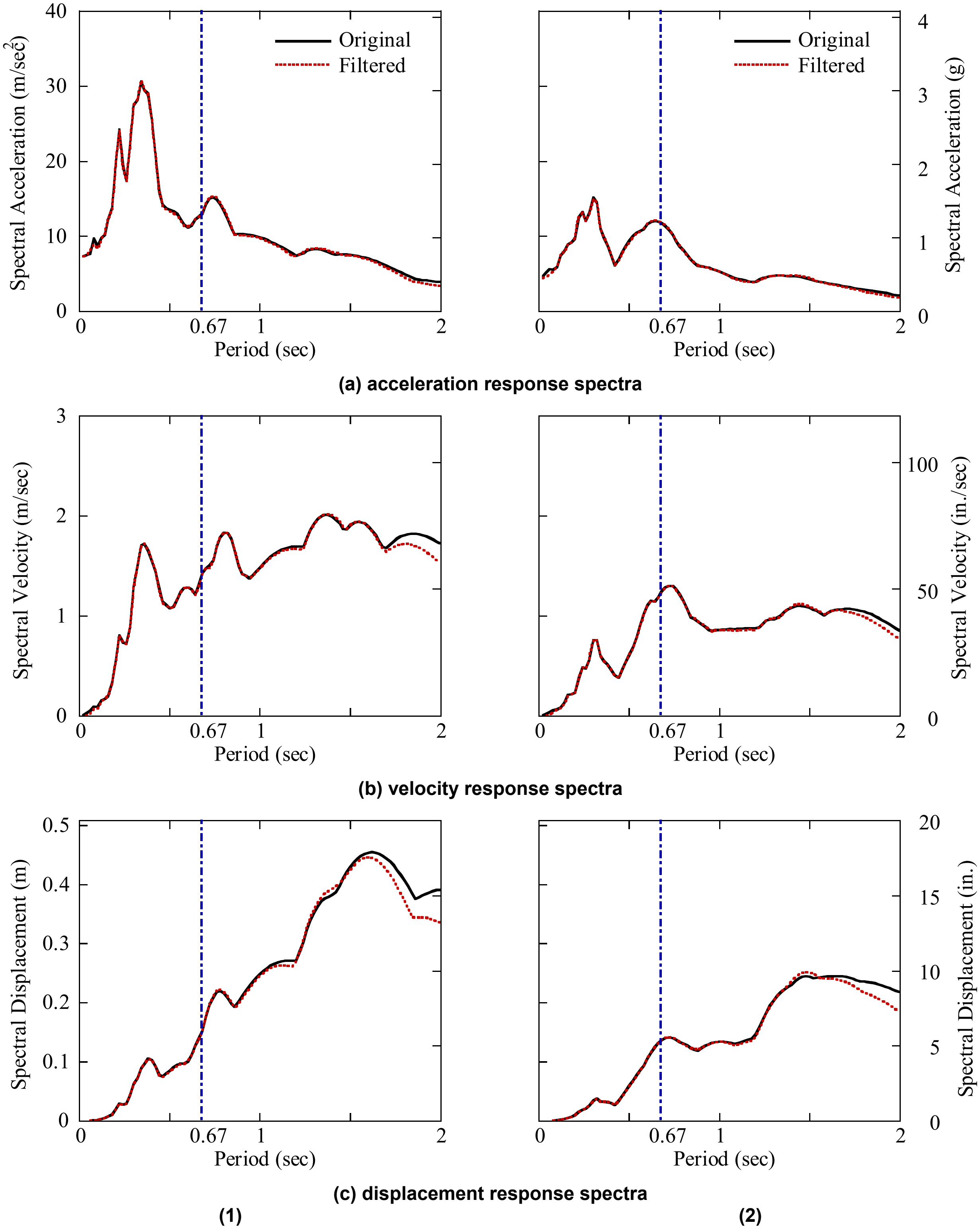

Figure 3.23 Response spectra (5% damping) in the fault-normal (*X*) and fault-parallel (*Y*) directions: (a) acceleration response spectra; (b) velocity response spectra; and (c) displacement response spectra.

3.7 TEST SEQUENCE

In the earthquake simulation test program, the ground-motion intensity was subjected to four levels of testing. The first test level will be referred to as the elastic-level test, which was intended to check the instrumentation and the data acquisition system, and the specimen was to remain elastic. The second test level will be referred to as the yield-level test, which was used to check the dynamic initial stiffness of the specimens; yielding of some of the longitudinal bars was expected. The third and fourth levels of the tests were the actual tests to investigate nonlinear dynamic response of the specimens. The third test level will be referred to as the design-level test where the specimens were expected to experience a response ductility of 4. The fourth and final test level will be referred to as final level was the maximum-level test where the specimens were expected to endure a response ductility of 8.

To determine the scaling factors of amplitude for each level of test, another series of nonlinear dynamic analyses was conducted for the RC specimen. The same model and conditions described in Section 2.5 were used for the analyses. Based on a trial-and-error procedure, the scaling factors were determined to be 7%, 10%, 70%, and 100% for the elastic-, yield-, design-, and maximum-level tests, respectively. Figure 3.24(a) and (b) shows input signals and predicted response of the specimen. For the analyses, signals for each run were combined together, and zeros for about 10 sec were added between the signals to allow response damping out after each run.

Table 3.9 shows test sequences. Several free-vibration tests were conducted to investigate dynamic properties of the specimen, such as natural period and damping properties prior to a series of earthquake simulation tests. White-noise tests were performed prior to each test to investigate variation in the dynamic properties of the columns due to accumulated damage.

Several free-vibration tests and white-noise tests were conducted in late July and early August of 2003; however, tests were terminated before earthquake simulation tests were performed because it was determined that the data acquisition system did not work properly during the white-noise test conducted on July 29th, 2003. Free-vibration tests were again performed in early August of 2003 to check the status of the data acquisition system.

Another series of free-vibration tests and white-noise tests were conducted in mid-November 2003. After it was confirmed that the data acquisition system was working properly, the earthquake simulation tests were conducted. Unfortunately, it was then discovered that the actuators in the *Y*-direction did not work properly as the response of the table was about half of the command. The tests were terminated to repair the hydraulic system of the simulator.

The tests for the RC specimen were conducted on May 27, 2004. After the free-vibration tests, white-noise tests and an elastic-level test, the bolts that tied the load cells to the base plates were found to be loose. The bolts were re-tied firmly and the actual tests were then conducted.

The tests for the RC specimen were terminated after the maximum-level test due to large residual displacement (see Chapter 4). Additional tests were conducted for the PRC specimen as this specimen did not exhibit a large residual displacement or any critical local damage after the maximum-level run. The PRC specimen totally collapsed during the second design-level test. Damage to the earthquake simulator was prevented as one of the safety cables caught the specimen.

Table 3.9 Input signals.

	Original	Filtered	Original	Filtered
	NF03 (Fault normal)	**Signal in *X* (N-S) component**	**NF04 (Fault parallel)**	**Signal in *Y* (E-W) component**
Acceleration	7.04 m/sec^2 (0.72*g*)	7.30 m/sec^2 (0.74*g*)	4.49 m/sec^2 (0.46*g*)	4.46 m/sec^2 (0.45*g*)
Velocity	0.815 m/sec (32.1 kips)	0.739 m/sec (29.1 kips)	0.429 m/sec (16.9 kips)	0.422 m/sec (16.6k kips)
Displacement	0.144 m (5.7 in.)	0.122 m (4.8 in.)	0.082 m (3.2 in.)	0.067 m (2.6 in.)

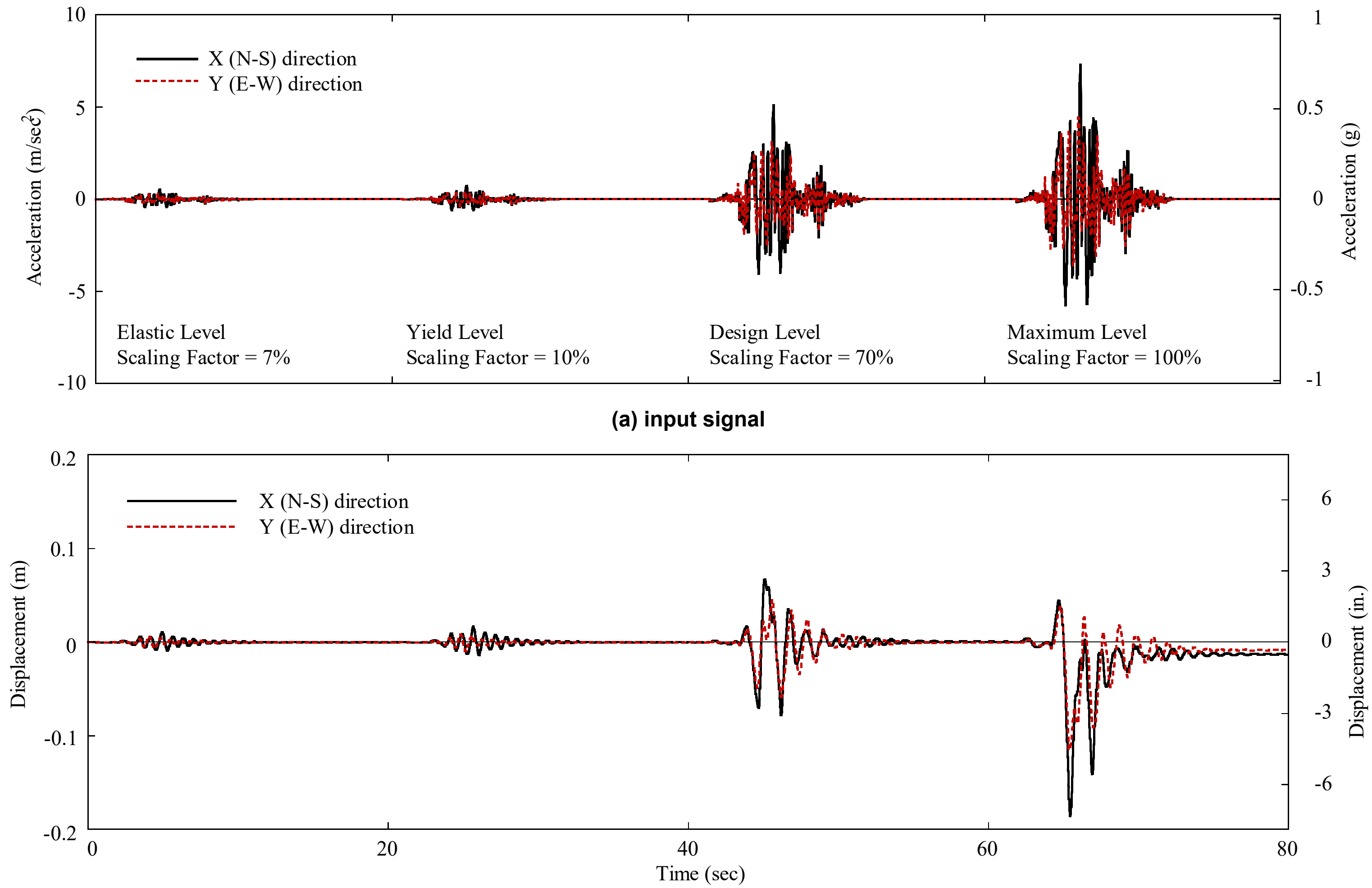

(a) input signal

(b) response displacement at center-of-gravity of top slab–weighted blocks assembly

Figure 3.24(a) Input signals and predicted response of RC specimens: (a) input signals and (b) response displacement at center-of-gravity of top slab–weighted blocks assembly.

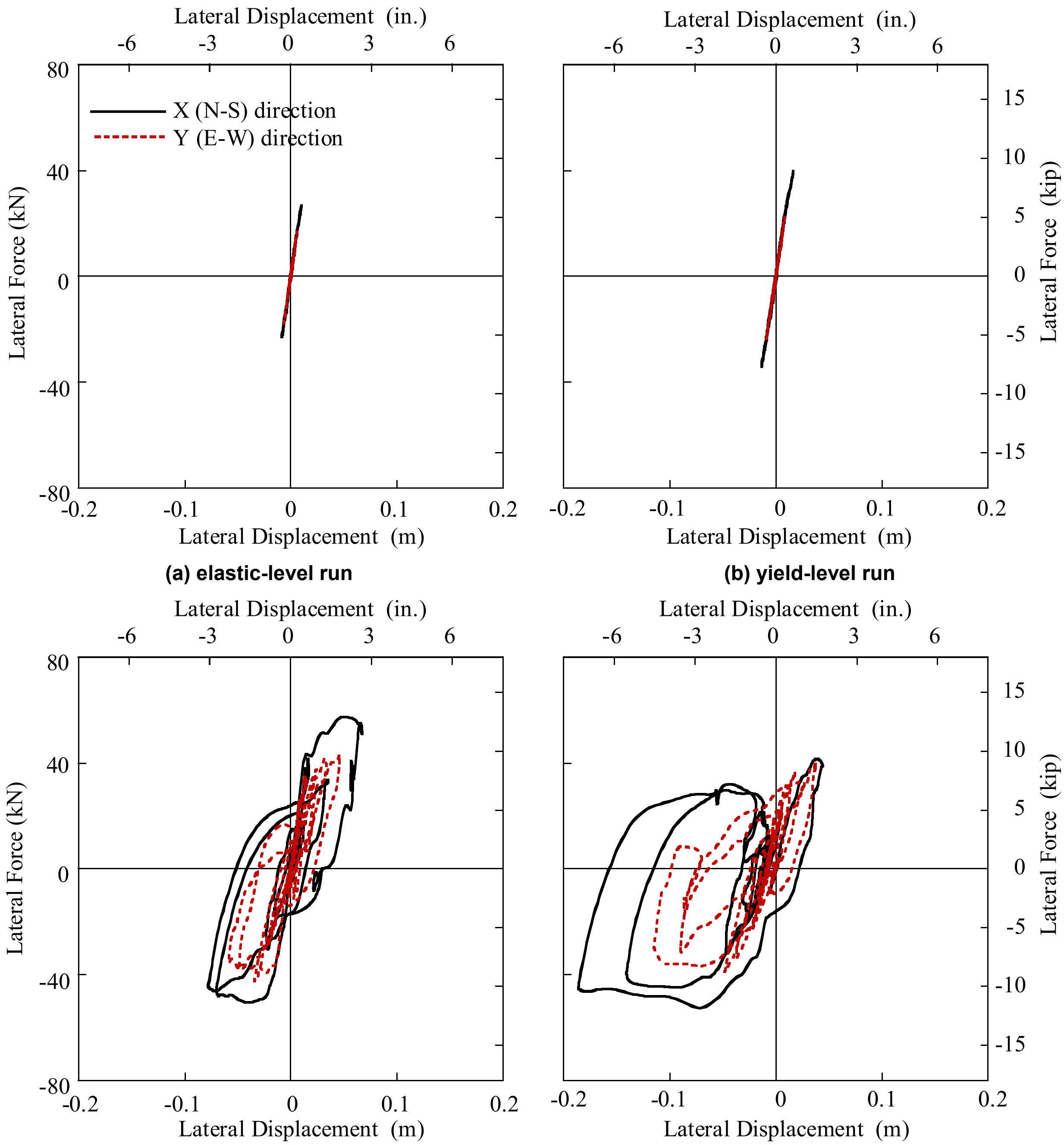

(a) elastic-level run

(b) yield-level run

(c) design-level run

(d) maximum-level run

(3) Lateral force–lateral displacement hysteresis

Figure 3.24(b) Lateral force–lateral displacement hysteresis; (a) elastic-level run; (b) yield-level run; (c) design-level run; and (d) maximum-level run.

4 Dynamic Behavior of Bridge Columns

4.1 DYNAMIC PROPERTIES OF SPECIMENS PRIOR TO TESTING

4.1.1 Natural Period

Prior to the earthquake simulation tests, free-vibration tests and white-noise tests were performed to investigate the dynamic properties of the specimens. Because of problems with the hydraulic and data acquisition systems, the conventional RC column specimen remained anchored on the table for ten months. Given that the specimen was subjected to a number of free-vibration tests, white-noise tests, and even a yield-level test prior to the actual tests conducted on May 27, 2004 (see Section 3.7), the specimen might have had different dynamic properties from those of the partially prestressed RC column specimen (PRC specimen). Thus, it was necessary to clarify the dynamic properties of the specimens prior to the testing sequence based on the results from the free-vibration tests and white-noise tests.

Figure 4.1 shows the set-up of the free-vibration test. A cable was connected from the anchor on the floor to the top slab of the specimen. The cable had a load cell and a come-along winch at the anchor end, and a machined bolt at the other end. A force of 5.3 kN (1.2 kips) was applied to the top slab with the come-along winch, and then the machined bolt was cut with a bolt cutter to initiate a free vibration. The shaking table was fixed with wood blocks to minimize the effects of table movements during vibration. Free-vibration tests were performed only in the *Y*-direction.

Figure 4.2 shows acceleration time histories of the RC specimen measured at the center-of-gravity of the top slab-weighted block assembly (the top blocks) during a free-vibration test and a white-noise test performed on the actual test day. Two accelerometers measured at the south face are shown; see "accel11" in Table 3.4. For the free-vibration tests, portions where acceleration amplitude was smaller than about 0.1 m/sec^2 (0.01g) were used to investigate dynamic properties of the specimen. Fourier spectra computed for the measured acceleration are also shown. To compare Fourier spectra between free-vibration tests and white-noise tests (which had different durations), the Fourier amplitude obtained from the free-vibration tests were amplified ten times. Based on the Fourier analyses, the RC specimen had a fundamental frequency of 1.56 Hz (a natural period of 0.64 sec) in the *Y*-direction at the beginning of the test series.

(a)

(b)

Figure 4.1 Free-vibration test: (a) set-up and (b) cutting machined bolt to initiate vibration.

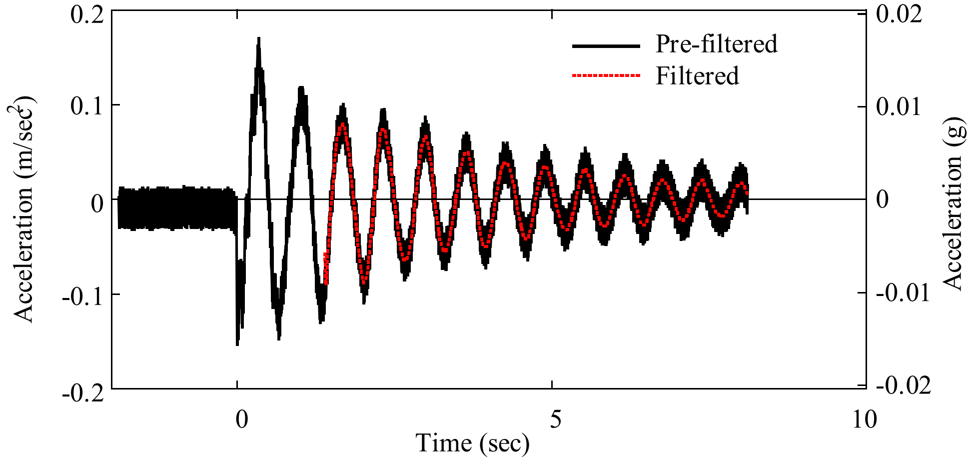

(a)

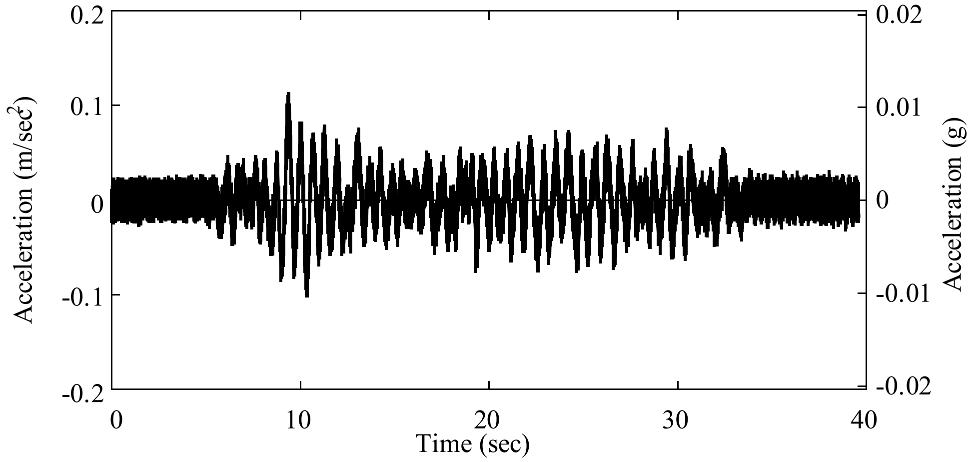

(b)

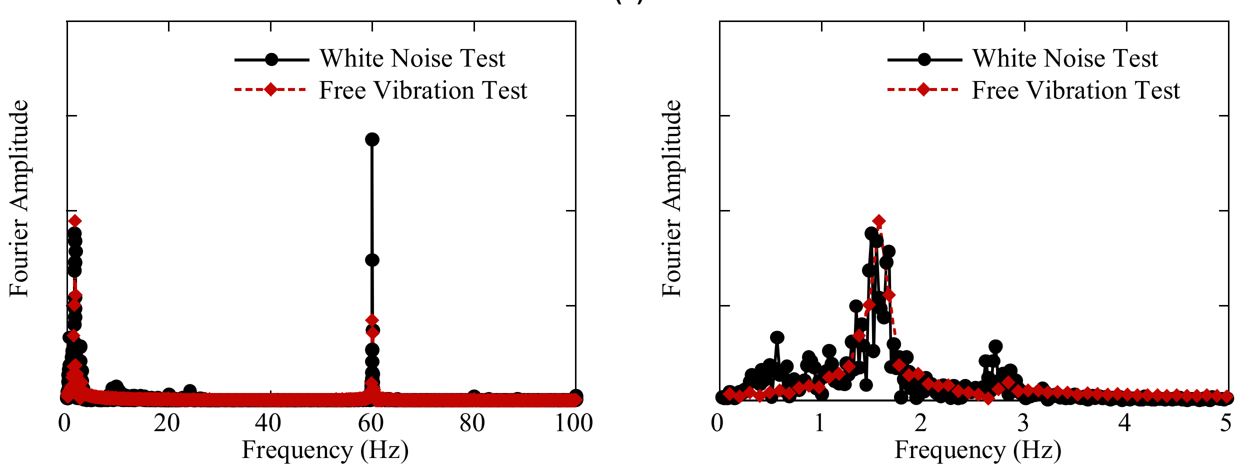

entire range **close up**

(c)

Figure 4.2 **Free vibration and white-noise tests: (a) free-vibration test; (b) white-noise test; and (c) Fourier spectra.**

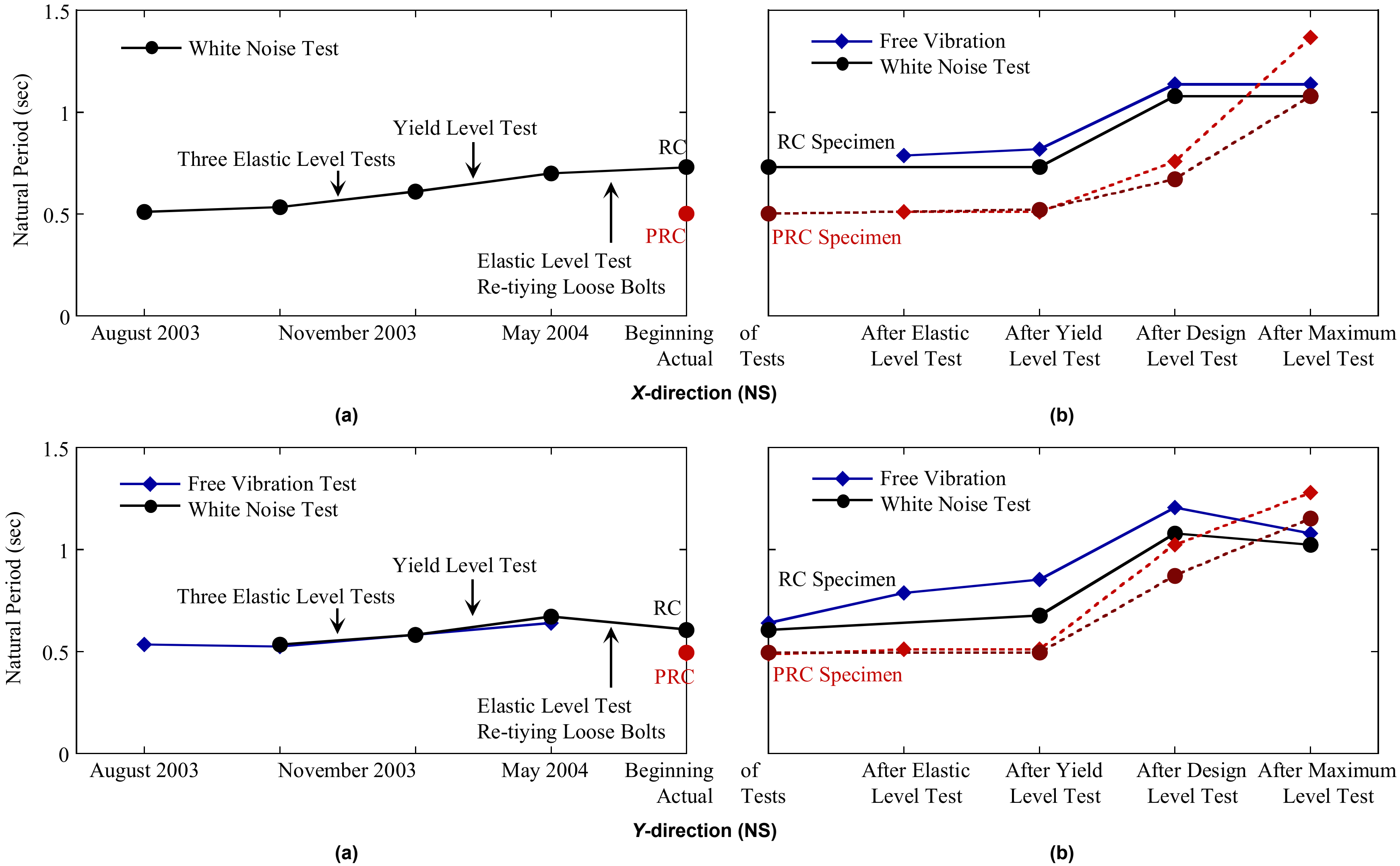

Figure 4.3 **Natural periods of specimens: (a) prior to earthquake simulation tests; and (b) during earthquake simulation tests.**

Similar analyses were conducted for measured acceleration from free-vibration tests and white-noise tests conducted in August and November of 2003; the variation in the natural period of the RC specimen was also investigated; see Figure 4.3. The natural period of the PRC specimen on the day of testing and variation in the natural periods during earthquake simulation tests are also shown Figure 4.3. In August 2003, the RC specimen had a natural period of 0.51 and 0.53 sec in the *X*- and *Y*-directions, respectively; however, the natural period increased up to about 0.7 sec in both directions after experiencing a number of free-vibration tests, white-noise tests, and a yield-level test. As described in Section 3.7, bolts tying load cells to the base plates were found loose after the free-vibration tests, white-noise tests, and an elastic-level test. After the bolts were re-tied, another series of white-noise tests were performed. Re-tightening of the bolts resulted in the natural period of the specimen decreasing in the *Y*-direction while elongating in the *X*-direction. The PRC specimen had a natural period of 0.5 sec in both directions, which is similar to the natural period found for the RC specimen in August 2003.

4.1.2 Damping Properties

Figure 4.4 compares the acceleration response during a free-vibration test between the RC and PRC specimens. To investigate damping properties, the accelerations were low-pass filtered with a cutoff frequency of 20 Hz. As described above, the RC specimen had a longer natural period and a larger damping as the acceleration decayed faster. Note that loose bolts might have affected the damping properties of the specimen.

To investigate damping properties, the damping ratio ξ was computed from the peak accelerations, as follows:

$$\xi = \frac{\xi_p + \xi_n}{2} \tag{4.1}$$

where

$$\xi_p = \frac{1}{2\pi} \cdot \frac{1}{n} \cdot \ln\left(\frac{a_{p\cdot 1}}{a_{p\cdot 1+n}}\right) \tag{4.2}$$

$$\xi_n = \frac{1}{2\pi} \cdot \frac{1}{n} \cdot \ln\left(\frac{a_{n\cdot 1}}{a_{n\cdot 1+n}}\right) \tag{4.3}$$

where $a_{p\cdot 1}$ and $a_{n\cdot 1}$ are the positive and negative peak accelerations in the first wave, and $a_{p\cdot 1+n}$ and $a_{n\cdot 1+n}$ are the positive and negative peak accelerations in the n + 1th wave. In this study, $a_{p\cdot 1}$ and $a_{n\cdot 1}$ are taken values near ± 0.1 m/sec^2 (0.01g), and n is assumed to be 5.

Table 4.1 summarizes the damping properties along with the natural periods obtained from the three free-vibration tests. The damping ratios of the RC and PRC specimens were estimated to be 2.84% and 0.84%, respectively, before the specimens were subjected to the earthquake simulation tests.

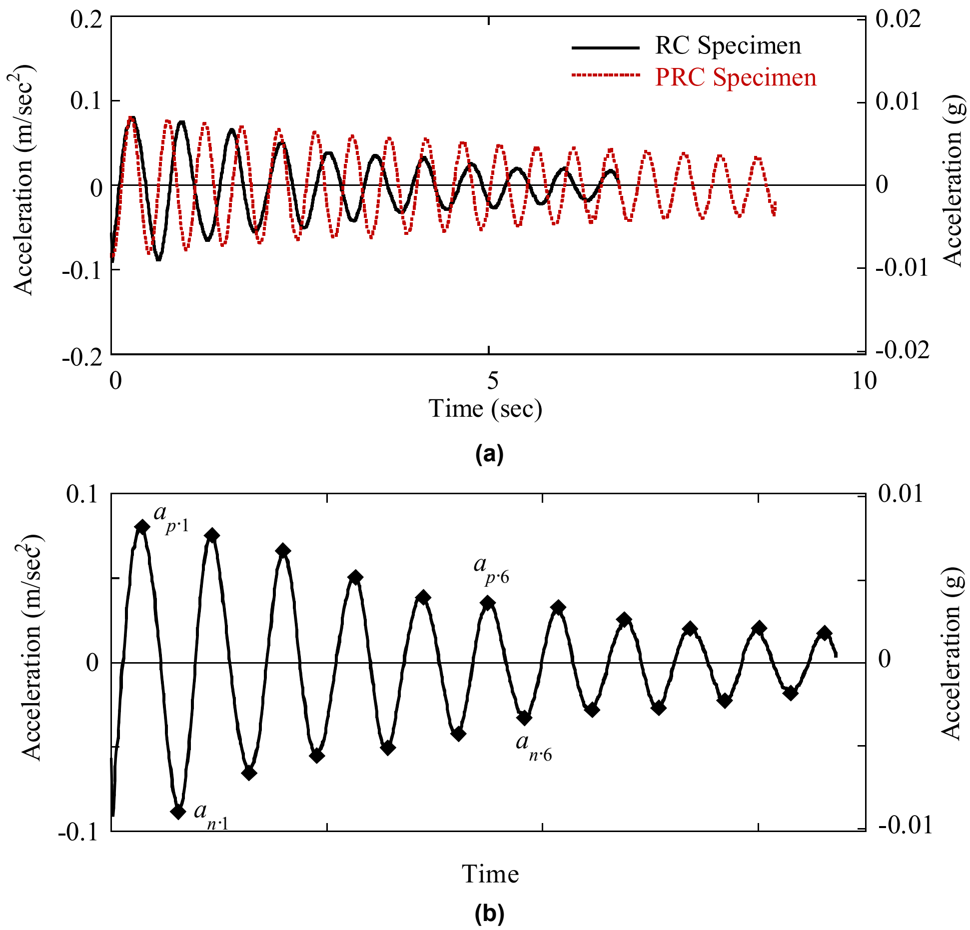

Figure 4.4 **Decay of acceleration response: (a) comparison between RC and PRC specimens; and (b) peaks used to compute damping properties.**

Table 4.1 Dynamic properties of specimens.

Beginning of tests (*Y*-direction)

	RC specimen		PRC specimen	
	Natural period	Damping ratio	Natural period	Damping ratio
Free-vibration test 1	0.64 sec	2.89%	0.49 sec	0.83%
Free-vibration test 2	0.64 sec	2.85%	0.49 sec	0.88%
Free-vibration test 3	0.64 sec	2.79%	0.49 sec	0.81%
Average	0.64 sec	2.84%	0.49 sec	0.84%

After earthquake simulation tests

		RC specimen		PRC specimen	
		Natural period	Damping ratio	Natural period	Damping ratio
RC specimen	Elastic-level test	0.79 sec	3.94%	0.79 sec	5.96%
	Yield-level test	0.82 sec	4.48%	0.85 sec	4.26%
	Design-level test	1.14 sec	4.21%	1.20 sec	3.59%
	Maximum-level test	1.14 sec	2.73%	1.08 sec	3.23%
		***X*-direction**		***Y*-direction**	
		Natural period	**Damping ratio**	**Natural period**	**Damping ratio**
PRC specimen	Elastic-level test	0.51 sec	2.56%	0.51 sec	2.03%
	Yield-level test	0.51 sec	1.61%	0.51 sec	1.46%
	Design-level test	0.76 sec	2.85%	1.02 sec	4.64%
	Maximum-level test	1.37 sec	4.24%	1.28 sec	4.35%

4.1.3 Initial Stiffness

During the tests, the specimens were pulled with the come-along winch for the free-vibration tests, and applied force and displacement at the center-of-gravity of the top blocks were measured to investigate initial stiffness of the specimens. A theoretical initial stiffness for an un-cracked section was estimated to be about 6 kN/mm (35 kips/in.). Assuming a single degree-of-freedom (DOF) system, the initial stiffness was estimated to be 2.8 kN/mm (16 kips/in.) and 4.5 kN/mm (26 kips/in.) for the RC and PRC specimens, respectively, by providing a top weight of 2.9×10^4 kg and the natural periods described above. Table 4.2 summarizes decay of stiffness of the specimens.

Figure 4.5 shows lateral force–lateral displacement hysteresis of the specimens obtained during pullback. The lateral force was obtained from summation of the shear force measured by four load cells. The applied force was 7% of the flexural strength of the specimens; the applied lateral displacement at the center-of-gravity of top blocks was 2 mm (0.08 in.) for the RC specimen and 0.2 mm (0.008 in.) for the PRC specimen. The estimated initial stiffness was 10 kN/mm (2.25 kips/in.) and 20 kN/mm (4.5 kips/in.) for the RC and PRC specimens, respectively, which is far greater than the estimated stiffness described above, and the estimated stiffness during the elastic- and yield-level tests shown in Table 4.2. Although the reasons behind these discrepancies are difficult to identify, it is assumed that the measured lateral displacement might be too small to be accurately captured by a linear potentiometer with a range of ±1.27 m (50 in.). In addition, some of the longitudinal bars might have already yielded, and concrete cracks having already had occurred in the RC specimen at the beginning of the earthquake tests, as the specimen showed decay of stiffness when the applied force exceeded around 2 kN (0.45 kips).

Table 4.2 Stiffness of specimens.

	RC specimen		PRC specimen	
	***X*-direction**	***Y*-direction**	***X*-direction**	***Y*-direction**
Prior to tests	-----	2.8 kN/mm (16 kip/in.)	-----	4.5 kN/mm (26 kip/in.)
After elastic-level test	2.1 kN/mm (12 kip/in.)	2.1 kN/mm (12 kip/in.)	5.0 kN/mm (28 kip/in.)	5.7 kN/mm (33 kip/in.)
After yield-level test	2.1 kN/mm (12 kip/in.)	2.2 kN/mm (13 kip/in.)	4.7 kN/mm (27 kip/in.)	5.5 kN/mm (32 kip/in.)
After design-level test	0.9 kN/mm (5 kip/in.)	1.1 kN/mm (6 kip/in.)	1.6 kN/mm (9 kip/in.)	1.4 kN/mm (8 kip/in.)
After maximum-level test	1.0 kN/mm (6 kip/in.)	1.3 kN/mm (7 kip/in.)	0.8 kN/mm (4 kip/in.)	0.9 kN/mm (5 kip/in.)

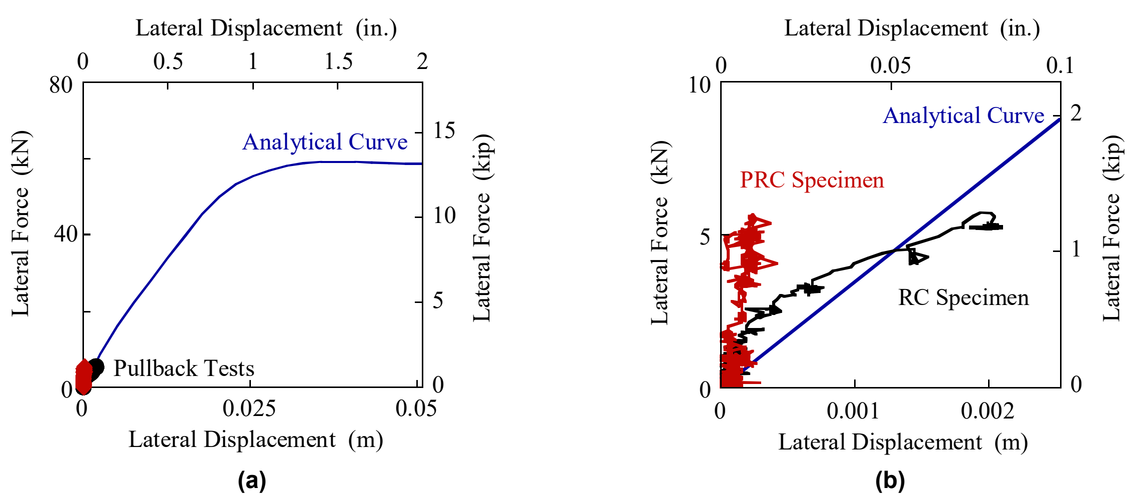

Figure 4.5 Initial stiffness obtained during pullback tests: (a) comparison with analytical curve; and (b) comparison between specimens.

4.2 PERFORMANCE OF EARTHQUAKE SIMULATOR

To assess the performance of the PRC specimen compared with that of the RC specimen, it is essential to determine how accurately the simulator reproduced the input signals. All documentation related to the performance of the simulator is summarized in Appendix E.

Figures 4.6 and 4.7 show time histories and Fourier spectra of the measured accelerations at the footing for selected tests of the RC specimen. Because the measured accelerations at the west and south faces have very similar characteristics, those measured at the west face are used to show accelerations in *X*-direction ("accel1" in Table 3.4), and those measured at the south face are used for *Y*-direction ("accel5" in Table 3.4). The measured accelerations contained high-frequency noise (see the time histories), and the spectra had large amplitude at several points over 20 Hz, especially for the yield-level test. Thus, the measured accelerations were low-pass filtered with a cutoff frequency of 20 Hz to remove the high-frequency noise. As shown in Figure 4.6, the accelerations had similar time histories even after being filtered.

Figure 4.8 shows displacement and acceleration time histories measured at the footing and response spectra for the design- and maximum-level tests. The response spectra were generated for the original non-filtered accelerations. The footing displacements (shown in Figure 4.8) were obtained as an average of the measurements of two linear potentiometers, which were placed at both sides at the west and south faces. Rotational movements of the table were negligible; see Appendix D, Figure D.4.

The figure shows that the simulator reproduced the signals with sufficient accuracy. Although the response spectra show that the simulator had difficulty in reproducing the high-frequency components, the simulator was able to reproduce natural periods over 0.5 sec, which was estimated to be the fundamental period of the specimens. More significantly, the simulator reproduced almost the same accelerations and displacements for tests of the RC specimen and the PRC specimen, which allowed for comparison of the performance between the two specimens.

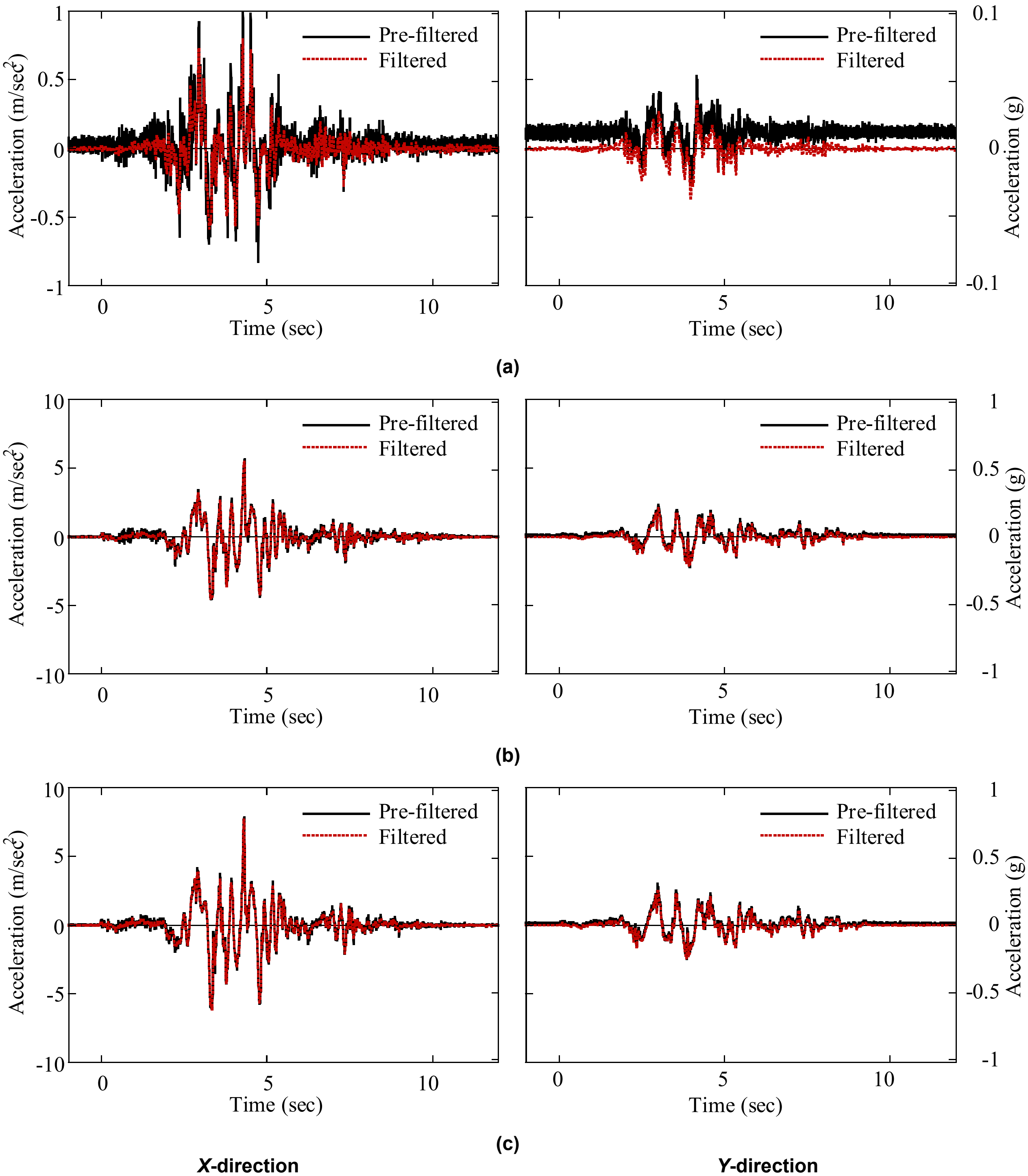

Figure 4.6 **Measured acceleration at footing: (a) yield-level test; (b) design-level test; and (c) maximum-level test.**

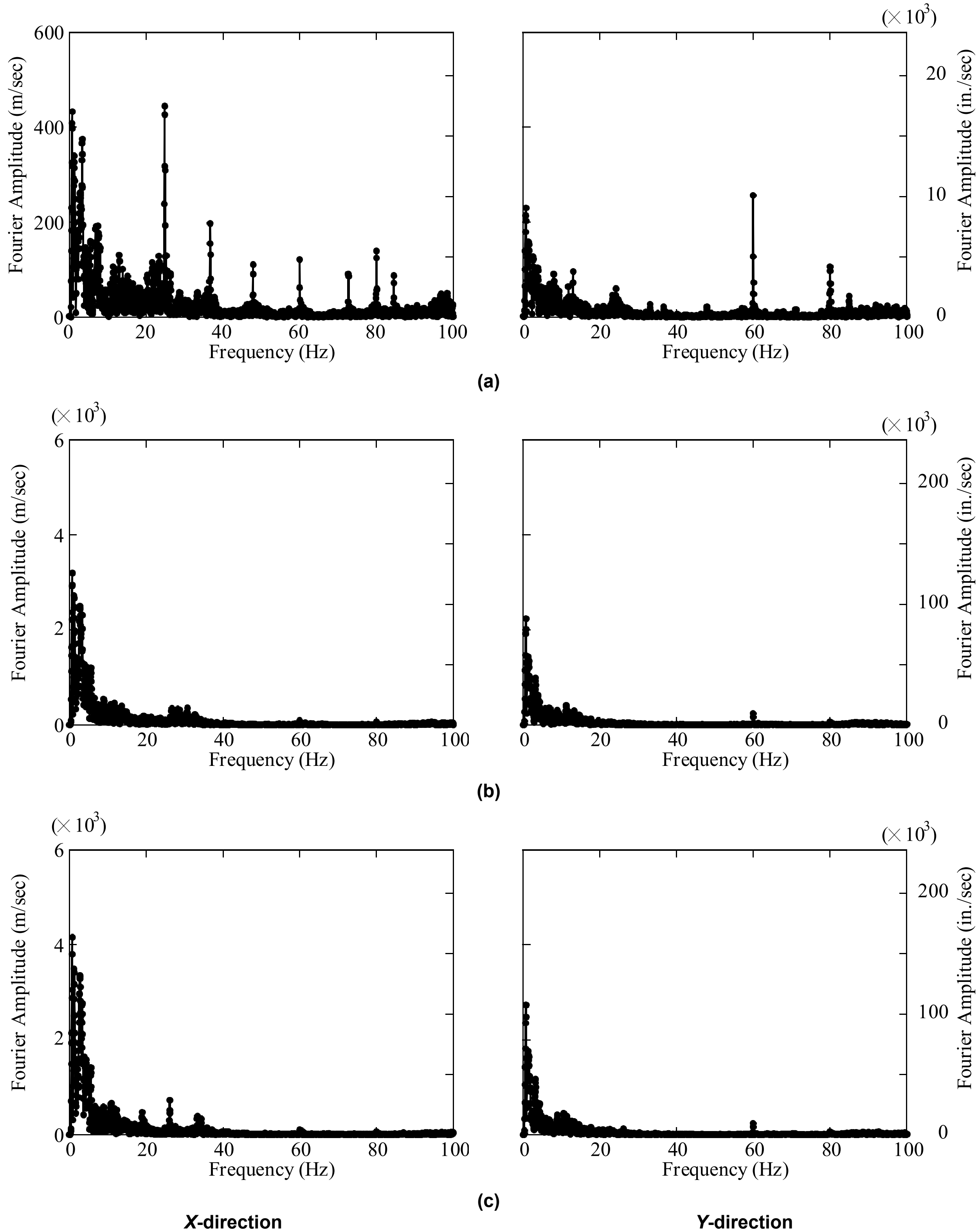

Figure 4.7 **Fourier spectra of footing accelerations: (a) yield-level test; (b) design-level test; and (c) maximum-level test.**

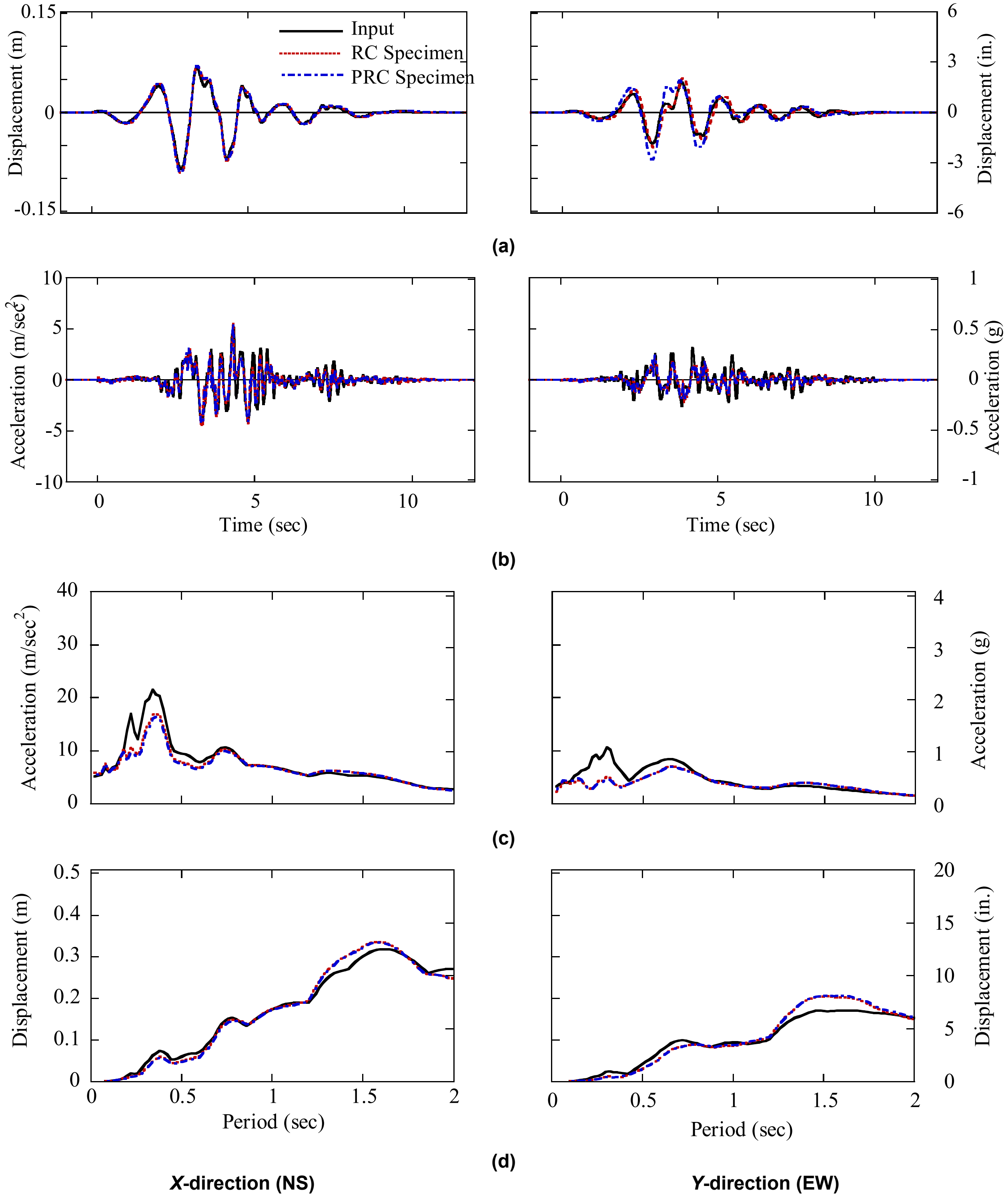

Figure 4.8(a) Performance of the earthquake simulator during the design-level test: (a) displacement measured at footing; (b) acceleration measured at footing; (c) acceleration response spectra; and (d) displacement response spectra.

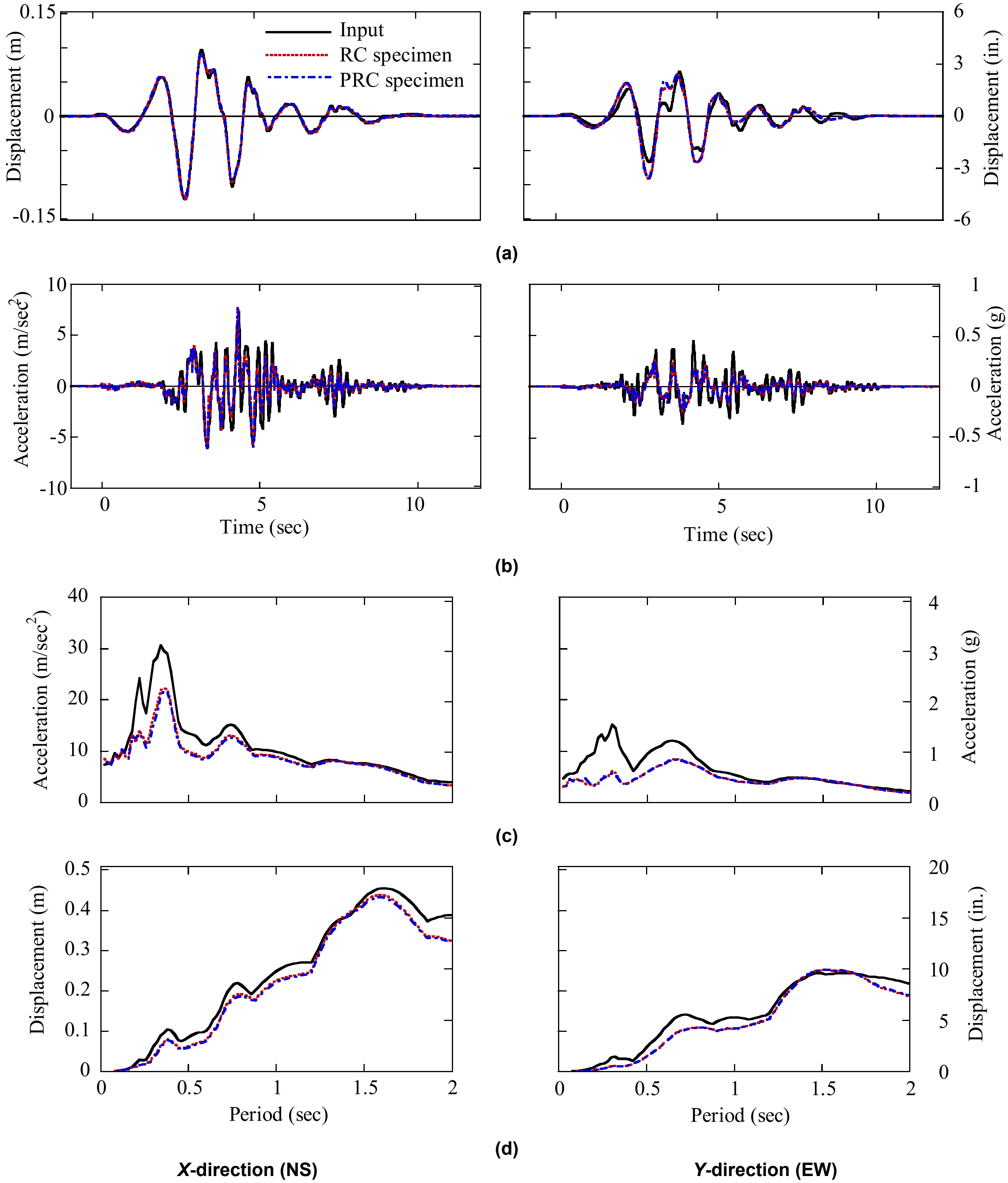

Figure 4.8(b) Performance of the earthquake simulator during the maximum-level test: (a) displacement measured at footing; (b) acceleration measured at footing; (c) acceleration response spectra; and (d) displacement response spectra.

4.3 LOW-LEVEL TESTS

4.3.1 Global Response

Before performing the actual earthquake simulation tests, two low-level tests were conducted to investigate the dynamic response properties of the specimens in the elastic range. The first test is referred to as an "elastic-level test": input signals were 7% of the filtered Los Gatos records. The amplitude increased up to 10% of the filtered Los Gatos records for the yield-level test (the second test). No visible damage including cracks was observed for either the RC or the PRC specimens during the tests.

Figure 4.9(a) and (b) shows acceleration and displacement response and lateral force–lateral displacement hysteresis at the center-of-gravity of the top blocks; Tables 4.3 and 4.4 summarize the maximum response. The measured accelerations were low-pass filtered with a cutoff frequency of 20 Hz. The displacements are shown as relative displacement to the footing, and no filtering was performed.

Larger response accelerations and displacements were observed in the *X*-direction (north–south) direction for both specimens during the stronger component of the signals. Although the maximum response accelerations during the yield-level tests were similar for both specimens, 1.12 m/sec^2 (0.11*g*) and 0.96 m/sec^2 (0.10*g*) for the RC and PRC specimens, respectively, the response displacement of the RC specimen was more than double that compared to the PRC specimen. The maximum displacements in the *X*-direction during the yield-level test were 0.02 m (0.79 in.) and 0.008 m (0.31 in.) for the RC and PC specimens, respectively. The difference of the initial natural periods of the specimens could have resulted in the difference found for the maximum response.

According to the lateral force–lateral displacement hysteresis, no significant nonlinear response was observed for either specimen during the low-level tests. The initial stiffness was approximately 2 kN/mm (11 kips/in.) and 5 kN/mm (29 kips/in.) for the RC and PRC specimens, respectively, which was similar to the stiffness estimated from the initial natural periods of the specimens; see Table 4.2.

The natural periods and damping properties of the specimens were investigated using a free-vibration portion of acceleration response. After the yield-level test, the natural periods were measured at 0.82 sec and 0.51 sec, and the damping ratios were 4.4% and 1.5 % for the RC and PRC specimens, respectively; see Table 4.1 and Figure 4.3.

Table 4.3 Maximum response accelerations.

	RC specimen		PRC specimen	
	***X*-direction**	***Y*-direction**	***X*-direction**	***Y*-direction**
Elastic-level test	0.86 m/sec^2 (0.09*g*)	0.35 m/sec^2 (0.04*g*)	0.68 m/sec^2 (0.07*g*)	0.46 m/sec^2 (0.05*g*)
Yield-level test	1.12 m/sec^2 (0.11*g*)	0.58 m/sec^2 (0.06*g*)	0.96 m/sec^2 (0.10*g*)	0.69 m/sec^2 (0.07*g*)
Design-level test	2.89 m/sec^2 (0.29*g*)	1.93 m/sec^2 (0.20*g*)	3.14 m/sec^2 (0.32*g*)	2.35 m/sec^2 (0.24*g*)
Maximum-level test	2.96 m/sec^2 (0.30*g*)	2.03 m/sec^2 (0.21*g*)	2.66 m/sec^2 (0.27*g*)	2.76 m/sec^2 (0.28*g*)

Table 4.4 Maximum response displacements.

	RC specimen		PRC specimen	
	***X*-direction**	***Y*-direction**	***X*-direction**	***Y*-direction**
Elastic-level test	0.014 m (0.54 in.)	0.006 m (0.22 in.)	0.005 m (0.20 in.)	0.003 m (0.10 in.)
Yield-level test	0.020 m (0.79 in.)	0.009 m (0.34 in.)	0.008 m (0.31 in.)	0.005 m (0.18 in.)
Design-level test	0.155 m (6.11 in.)	0.111 m (4.39 in.)	0.147 m (5.80 in.)	0.131 m (5.16 in.)
Maximum-level test	0.323 m (12.70 in.)	0.176 m (6.95 in.)	0.256 m (10.08 in.)	0.222 m (8.75 in.)

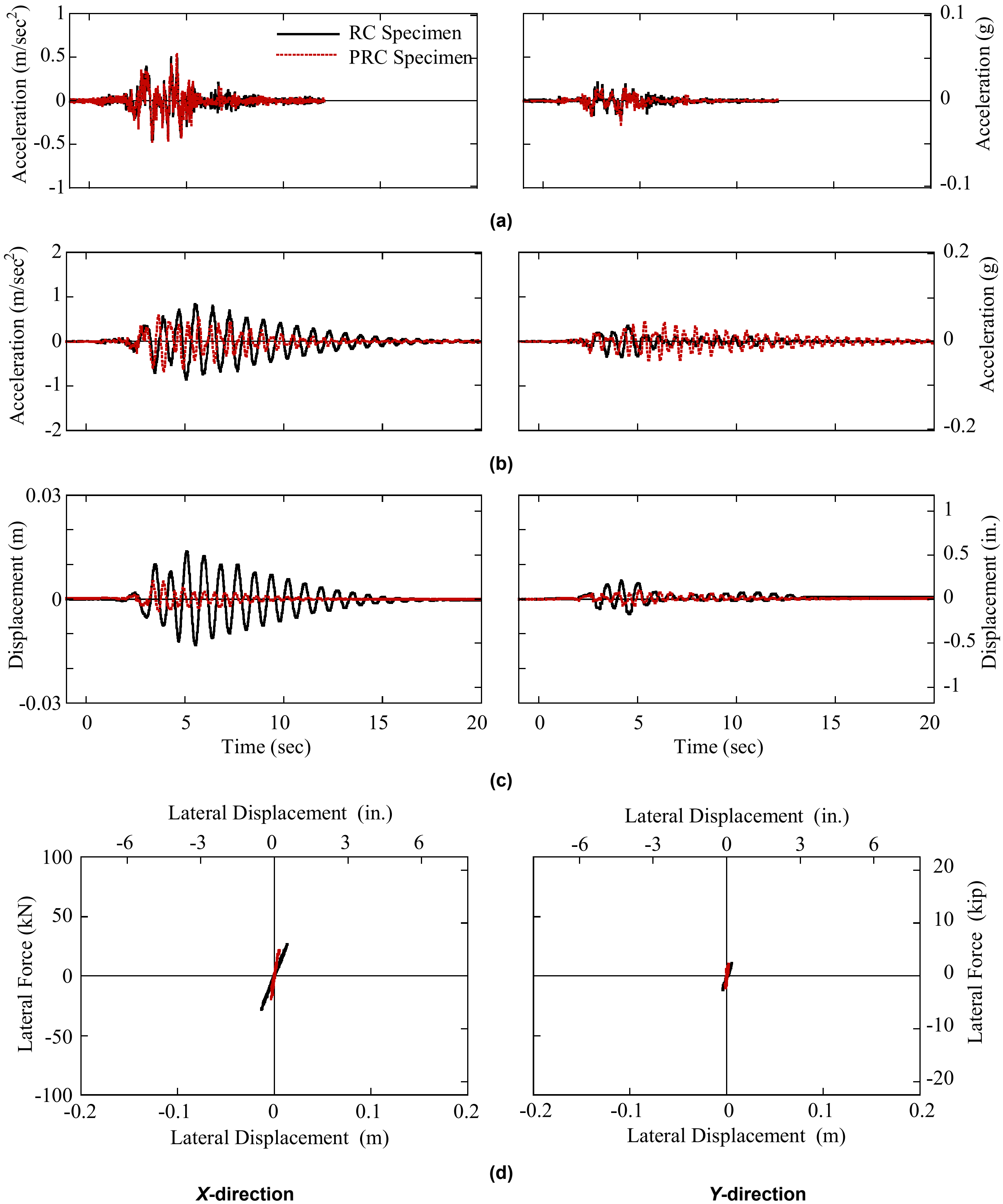

Figure 4.9(a) Global response of specimens during elastic-level tests: (a) displacement measured at footing; (b) acceleration measured at footing; (c) acceleration response spectral; and (d) displacement response spectra.

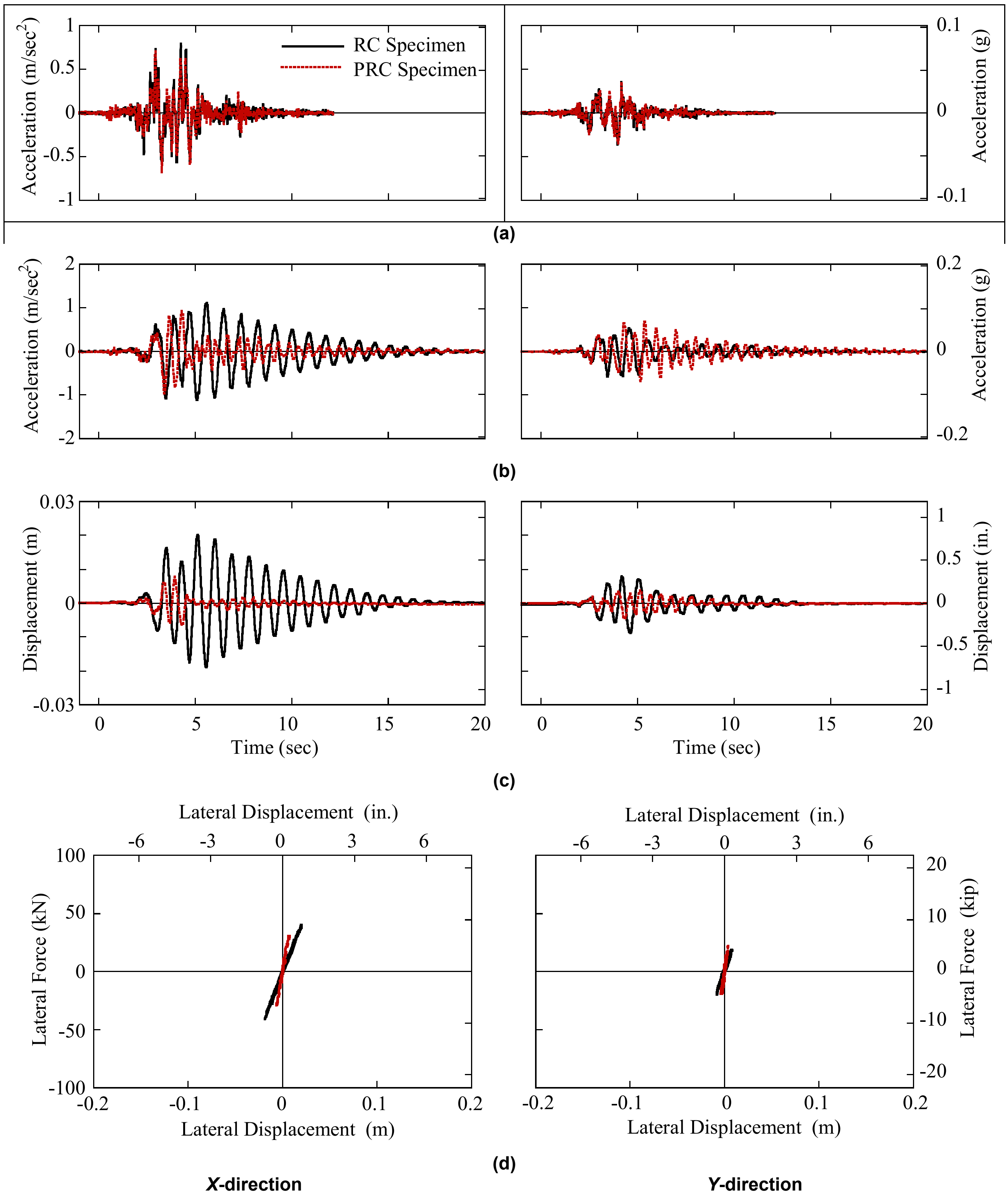

Figure 4.9(b) Global response of specimens during yield-level tests: (a) displacement measured at footing; (b) acceleration measured at footing; (c) acceleration response spectral and (d) displacement response spectra.

4.3.2 Local Response

Figure 4.10 shows strain time histories of the longitudinal reinforcing bars. No processing was performed for the measured strains. Because only one gauge was placed at the rebar surface facing outside at each location (see Section 3.4), measurements included both the axial strain and the flexural strain; thus, the measured strain can be larger than the pure axial strain. Note: the actual strain in the rebar must have been smaller in tension because the initial compressive strains induced in the rebar due to dead load of the weighted blocks were disregarded, and the strains were initialized to zero at the beginning of series of the tests. During the yield-level test of the RC specimen, strain that exceeded 0.005 was observed at the rebar located at the north and east sides around the bottom of the column; the maximum strain observed for the PC specimen was 0.0034.

The behavior of the tendon in the PRC specimen during the low-level tests is shown in Figure 4.11. The prestressing force and strains of the tendon at the beginning of the tests were set to the initial prestressing force and strain of the tendon measured prior to the tests. The initial prestressing force and strain were 379 kN (85 kips) and 0.0023, respectively. The initial stress is estimated to be 470 MPa (68 ksi), which is 40% of the ultimate strength of the tendon. During the yield-level test, the prestressing force as increased up to 382 kN (86 kips) as the specimen deformed, and decreased by 4 kN (1 kip) during the test.

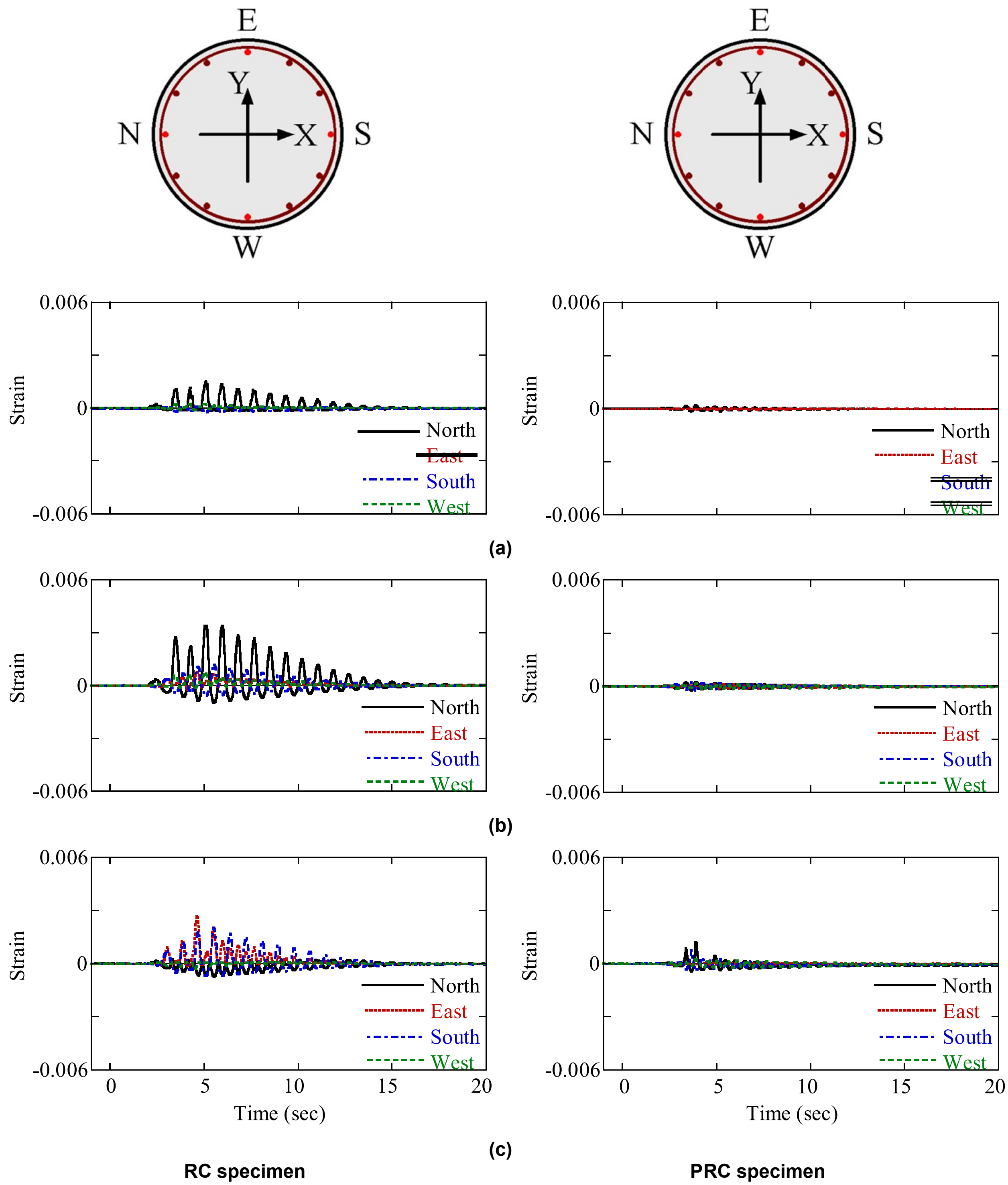

Figure 4.10(a) Strain of longitudinal reinforcement during elastic-level tests: (a) top of column 1.61 m from bottom of column; (b) 0.1 m from bottom of column; and (c) 0.01 m from bottom of column.

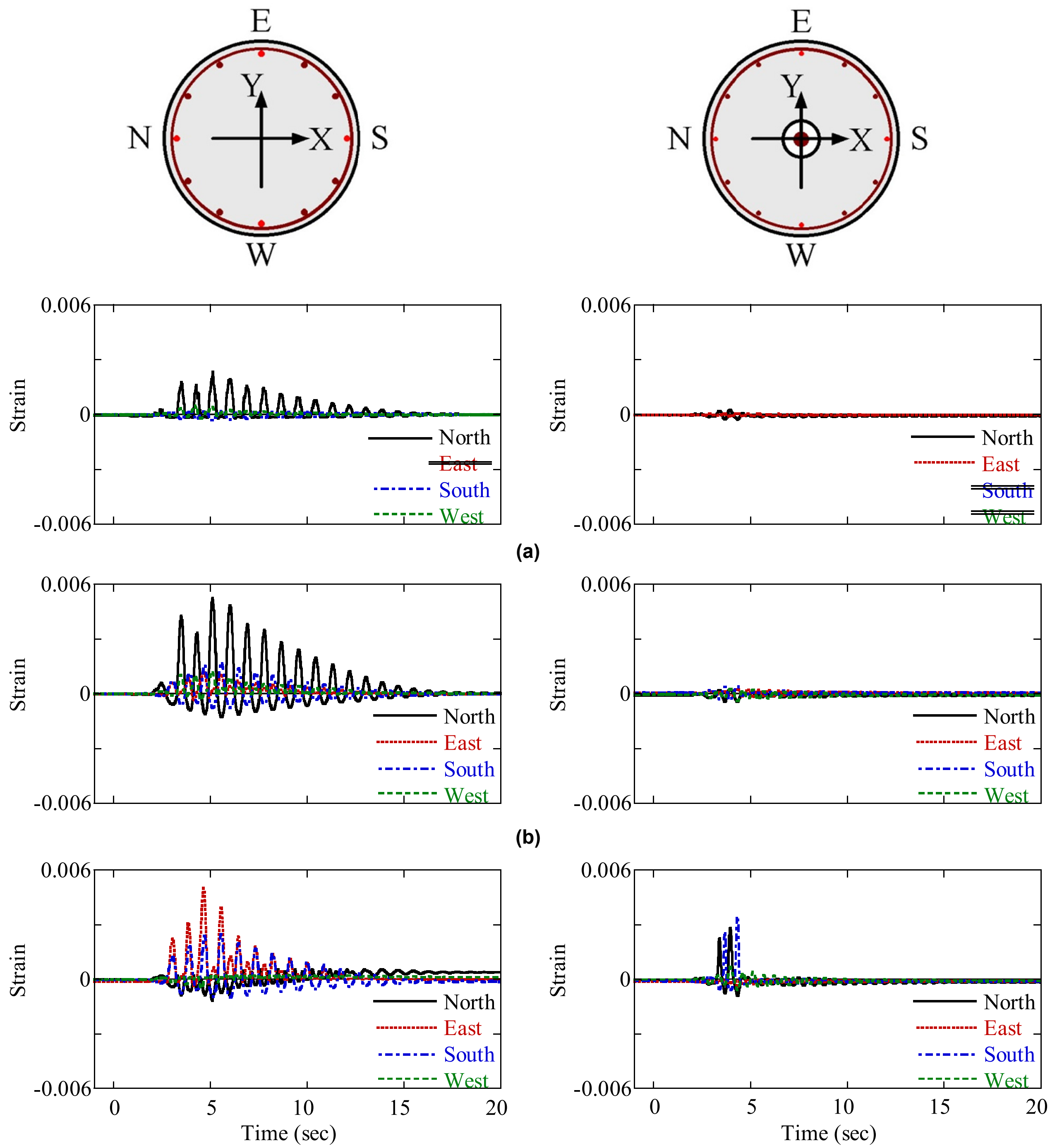

(c)

RC specimen

PRC specimen

Figure 4.10(b) Strain of longitudinal reinforcement during yield-level tests: (a) top of column 1.61 m from bottom of column; (b) 0.1 m from bottom of column; and (c) 0.01 m from bottom of column.

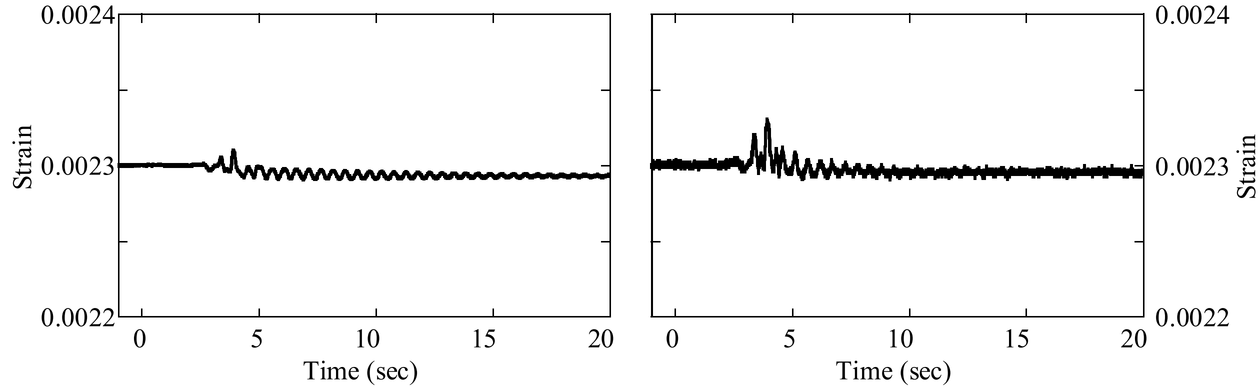

(a)

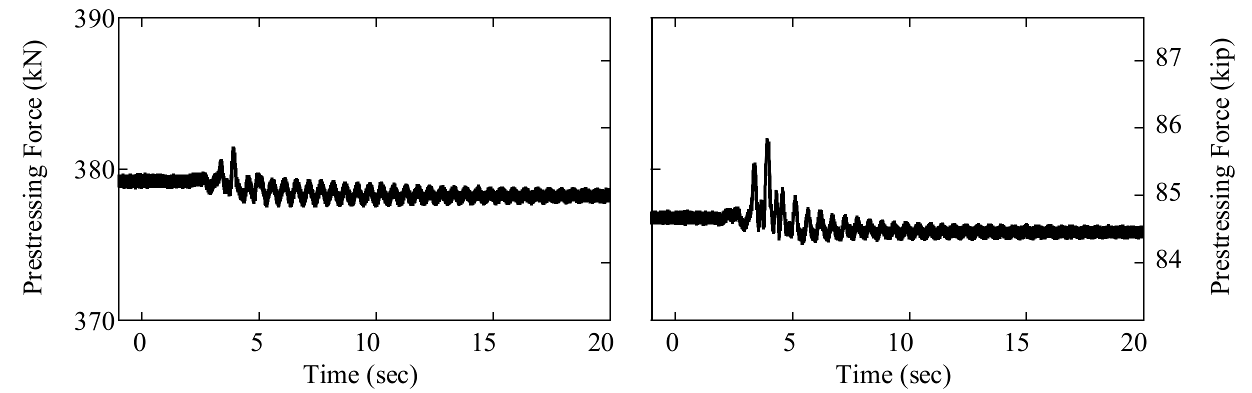

(b)

elastic-level test **yield-level test**

Figure 4.11 Behavior of tendon during elastic-level and yield-level tests: (a) strain and (b) prestressing force.

4.4 DESIGN-LEVEL TEST

4.4.1 Global Response

4.4.1.1 Damage Observations

Figure 4.12 shows the specimens after the design-level test. Note that the RC specimen is tilted to the northwest side, while the PRC specimen remained almost perpendicular. The tilt angle of the RC specimen is about 0.7° (1.3% in drift), and that of the PRC specimen is 0.2° (0.3% in drift). The large residual deformation experienced by the RC specimen most likely would render it non-functional and most likely demolished if this behavior had actually occurred in the field [Kawashima 2000].

Figure 4.13 shows damage experienced by the columns. Most of the cracks were concentrated below the mid-height, and the spalling of the cover concrete occurred largely below 305 mm (12 in.), as measured from the base of the column. The PRC specimen sustained slightly more damage than the RC specimen mainly because of larger compressive force due to the prestressing force. Note: evidence of spalling of the concrete cover at the northwest surface and southeast surface of the RC and PRC specimens, respectively. As shown in Figure 4.14, the local damage around the plastic regions for both specimens was similar.

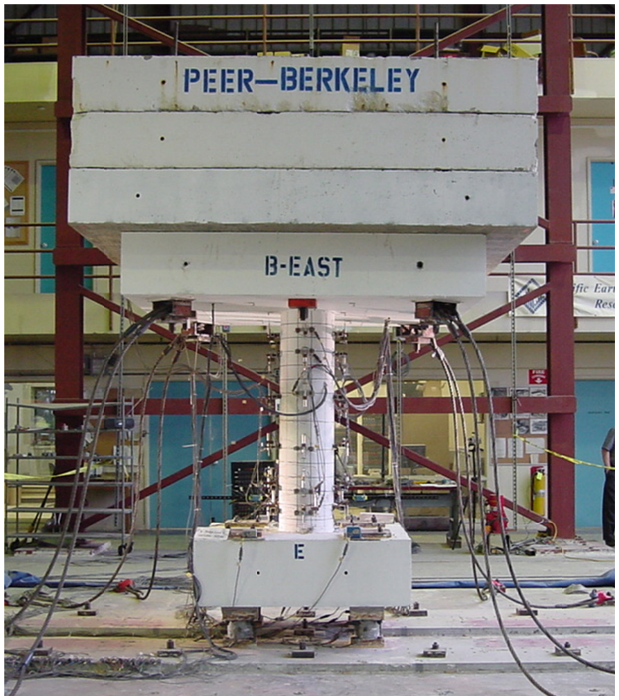

(a)

(b)

Figure 4.12 Specimens after the design-level test: (a) RC specimen and (b) PRC specimen.

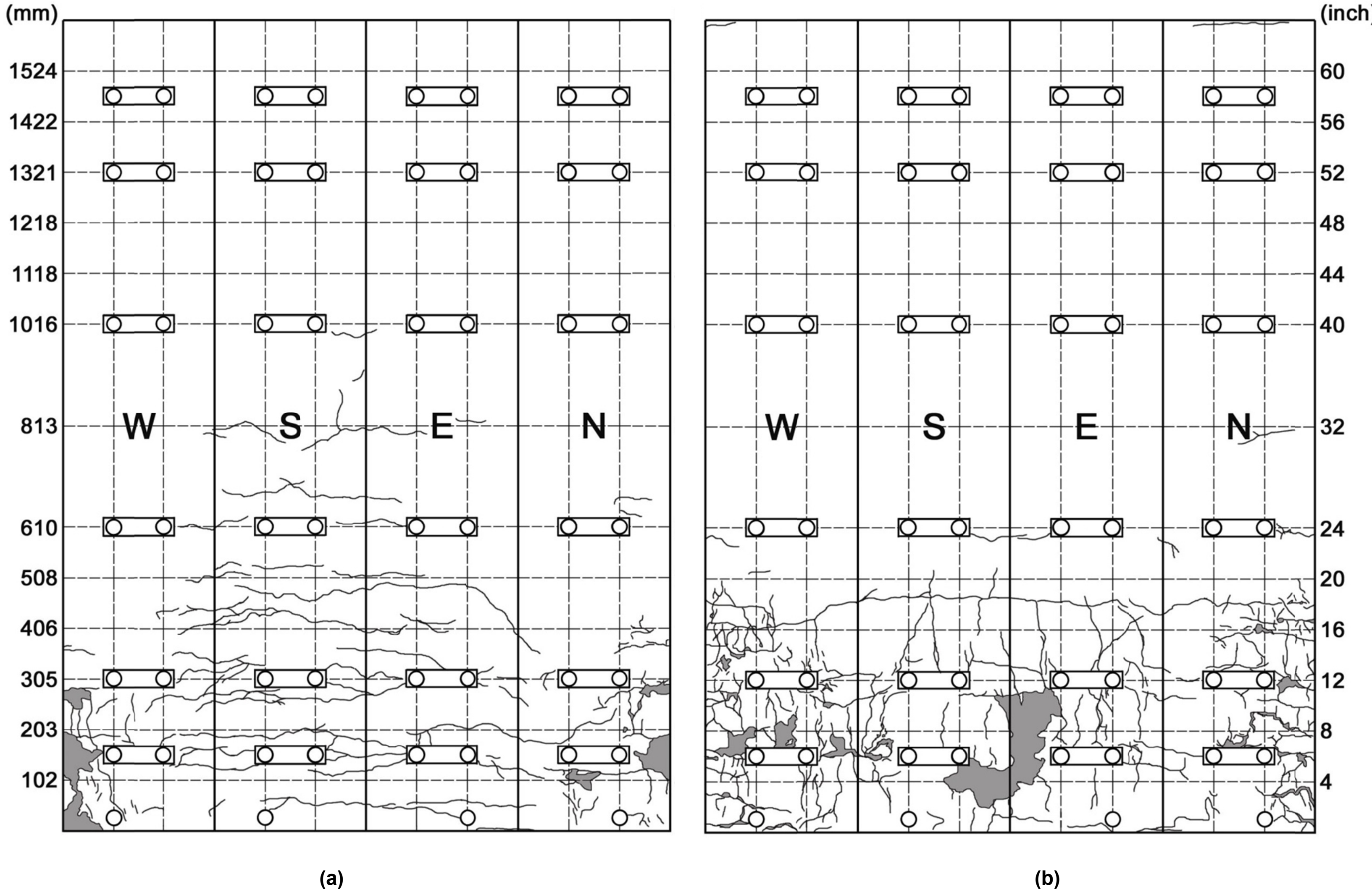

Figure 4.13 Damage of columns after the design-level test: (a) RC specimen and (b) PRC specimen.

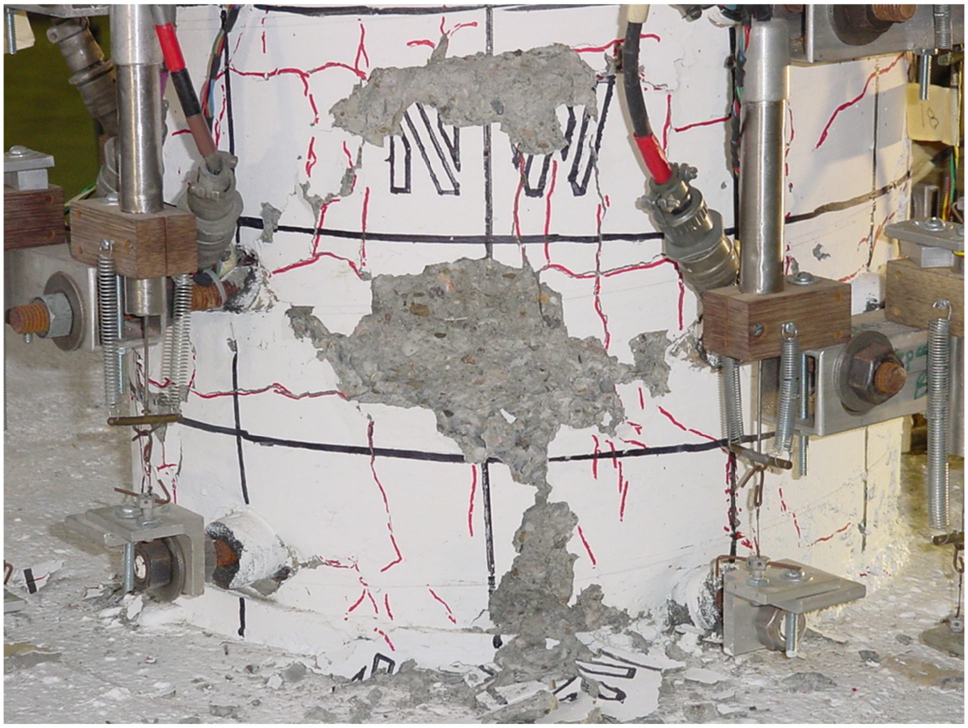

(a)

(b)

Figure 4.14 **Local damage at plastic-hinge region after design-level test: (a) RC specimen (NW corner); and (b) PRC specimen (SE corner).**

4.4.1.2 Acceleration Response

Figure 4.15 shows input signals and global response of the specimens during the design-level test. As mentioned in Section 4.2, the shaking table reproduced the input signals at a sufficiently accurate level for both specimens. The acceleration was low-pass filtered with a cutoff frequency of 20 Hz.

Although the specimens had different fundamental natural periods prior to the tests (0.82 sec and 0.51 sec for the RC and PRC specimens, respectively), the acceleration response shows a similar response during main pulse up to about 5 sec. The RC specimen had its maximum response acceleration at the center-of-gravity of the top blocks in the positive direction at 3 sec during the first strong pulse of the signals. The PRC specimen had its maximum acceleration at 3.8 sec during the first strong pulse in the negative direction. The maximum accelerations occurred in the *X*-directions for both specimens at 2.89 m/sec^2 (0.29*g*) and 3.14 m/sec^2 (0.32*g*) for the RC and PRC specimens, respectively. The maximum acceleration in the *Y*-direction occurred at 5 sec for both specimens. The response accelerations of the RC specimen had residual values during later part of the response because the specimen tilted during the test, thus, the accelerometers picked up the acceleration of gravity.

The damping properties and natural periods of the specimens were determined using the free-vibration portion of the acceleration response. The natural period of the RC specimen elongated from 0.82 sec to 1.14 sec in the *X*-direction during the design-level test, and the damping ratio was determined to be 4.2% at the end of the test (see Table 4.1 and Figure 4.3). The natural period of the PRC specimen also elongated by 50%, to 0.76 sec at the end of the test. The damping ratio of the PRC specimen was determined to be 2.9% and 4.6% for the *X*- and *Y*-directions, respectively.

4.4.1.3 Displacement Response

As shown in Figure 4.15(c), the RC specimen responded for a displacement -0.155 m (-6.1 in.) in the *X*-direction at 3.3 sec just after the first strong pulse was inputted. The response of the PRC specimen was 50% smaller compared to the RC specimen for the same time period. As described above, the RC specimen had a natural period of 0.82 sec, while the PRC specimen had a natural period of 0.51 sec prior to the test. The discrepancy in the natural periods is mostly likely the result of different responses of the specimens in the early stages of testing. A similar trend can be seen in the *Y*-direction as well.

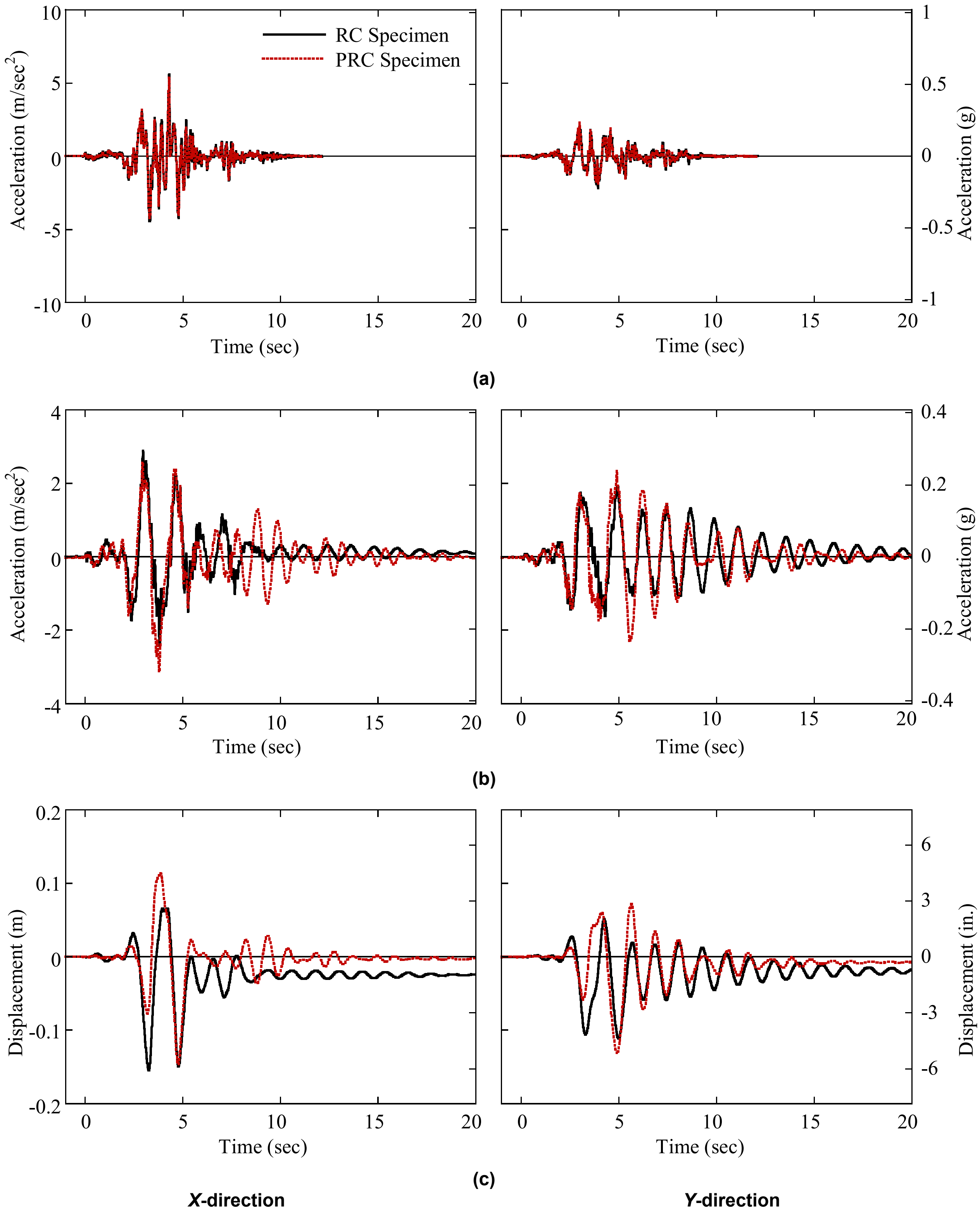

Figure 4.15 Global response of specimens during design-level test: (a) input signals (acceleration recorded at footing); (b) acceleration response at center-of-gravity of top blocks; and (c) displacement response at center-of-gravity of top blocks.

The response of the PRC specimen exceeded 0.1 m (4 in.) in the positive direction. The RC specimen had a positive peak at almost the same time, but the peak displacement was only 0.07 m (2.6 in.), which is 40% smaller than that of the PRC specimen. A comparison of the two specimens shows that the amplitudes of the response from the first negative peak to the first positive peak were similar: 0.22 m (8.7 in.) for the RC specimen and 0.19 (7.5 in.) for the PRC specimen, respectively.

Both specimens had similar peak displacements in the negative response in the *X*-direction at around 4.8 sec. The PRC specimen nearly returned to its original position and vibrated around this value for the rest of the response, including the free-vibration portion of the test; however, the RC specimen did not go back to its original position and a residual displacement remained, and the specimen vibrated around the value of the residual displacement.

The residual displacements in the *X*-direction were 0.025 m (0.97 in.) and 0.002 m (0.07 in.) for the RC and PRC specimens, respectively. In the *Y*-direction, the PRC specimen had a slightly larger peak [0.13 m (5.2 in.)]; at 5 sec the peak response of the RC specimen was 0.11 m (4.4 in.). After the main pulses, the PRC specimen had a final residual displacement of 0.008 m (0.3 in.), while the RC specimen had a final residual displacement of 0.019 m (0.76 in.); see Table 4.5.

Figure 4.16 shows magnitude and orbits of response displacements at the center-of-gravity of the top blocks. The specimens responded for the most part in the northwest–southeast direction. The maximum magnitudes of displacements were 0.187 m (7.4 in.) and 0.189 m (7.4 in.) for the RC and PRC specimens, respectively. The response ductility and drift were computed to be 7.2 and 7.7% for both specimens. The drift is defined as the ratio of lateral displacement to the specimen height [equal to 2.44 m (96.1 in.]. Magnitudes of the residual displacements were 0.031 m (1.2 in.) to the northwest direction for the RC specimen, and 0.008 m (0.3 in.) in the west–northwest direction for the PRC specimen. The ductility and drifts of residual displacements are 1.2 and 1.3%, and 0.3 and 0.3% for the RC and PRC specimens, respectively.

Table 4.5 Residual displacements.

	RC specimen		PRC specimen	
	***X*-direction**	***Y*-direction**	***X*-direction**	***Y*-direction**
Elastic-level test	0 m (0 in.)	0 m (0 in.)	0 m (0 in.)	0 m (0 in.)
Yield-level test	0 m (0 in.)	0 m (0 in.)	0 m (0 in.)	0 m (0 in.)
Design-level test	0.025 m (0.97 in.)	0.019 m (0.76 in.)	0.002 m (0.07 in.)	0.008 m (0.30 in.)
Maximum-level test	0.252 m (9.91 in.)	0.134 m (5.26 in.)	0.053 m (2.07 in.)	0.068 m (2.67 in.)

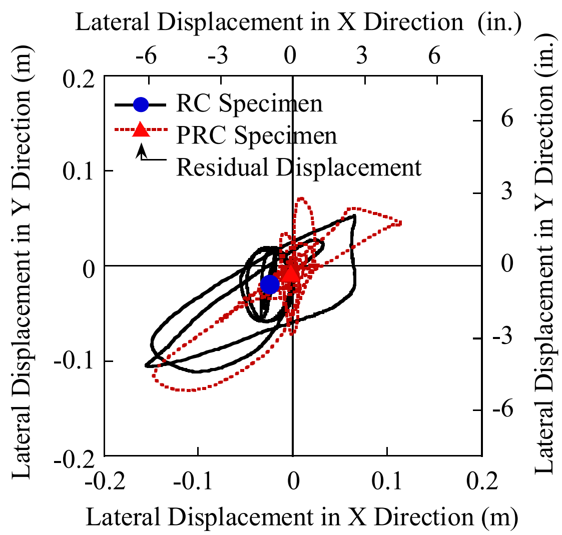

(a)

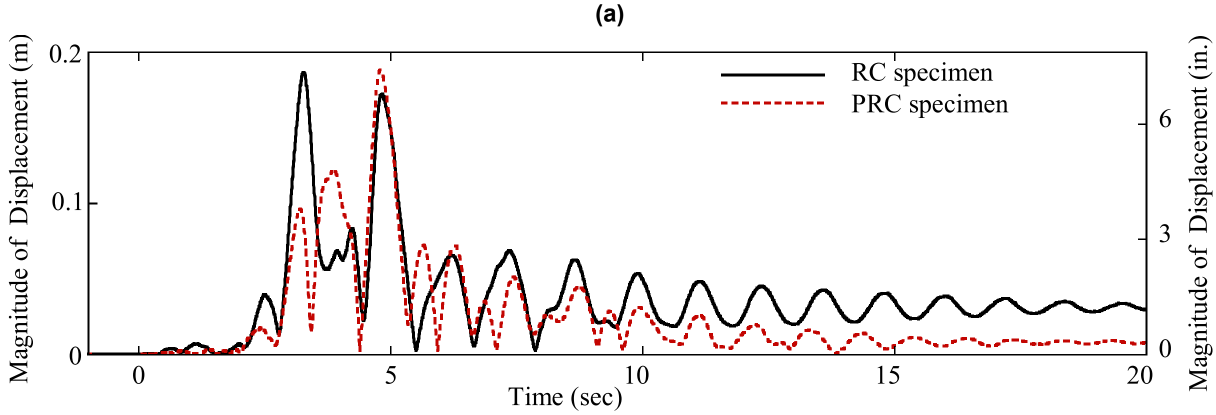

(b)

***X*-direction** ***Y*-direction**

Figure 4.16 Response displacement for design-level test: (a) orbit and (b) magnitude.

4.4.1.4 Lateral Force–Lateral Displacement Hysteresis

Figure 4.17 shows lateral force versus lateral displacement hysteresis at the center-of-gravity of the top blocks. As expected, (see Figure 2.32), both specimens exhibited similar skeleton curves as they moved away from their point of origin in the *X*-direction. Note, however, they had similar unloading curves as well. This is not the hysteresis expected according to the analyses, which show origin-oriented hysteresis for columns with unbonded prestressing tendons. In the *Y*-direction, the PRC specimen retained the origin-oriented hysteresis, although the hysteresis was smaller compared to the *X*-direction. The flexural strengths of the specimens were about 70 kN (16 kips).

Figure 4.18 shows inertia force versus lateral displacement hysteresis. The lateral forces computed from the load-cell measurements are shown in Figure 4.17. As shown in Figure 4.15(b), when the acceleration responses that were low-pass filtered were used, the hysteresis showed several sudden changes of tangential stiffness and forces; these hysteresis loops barely resemble those of standard RC members. If smaller cut-off frequencies are used, such as 2 Hz or 5 Hz, such sudden change of tangential stiffness can be eliminated, and the inertia force-lateral displacement hysteresis have better agreement with the lateral force–lateral displacement hysteresis.

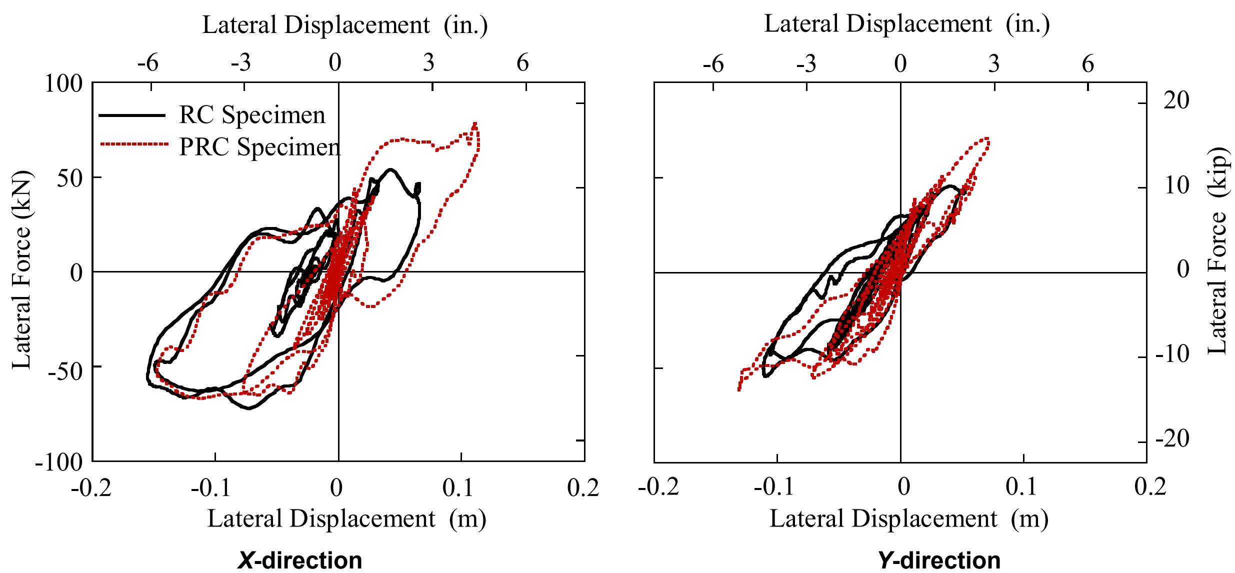

Figure 4.17 Lateral force–lateral displacement for the design-level test.

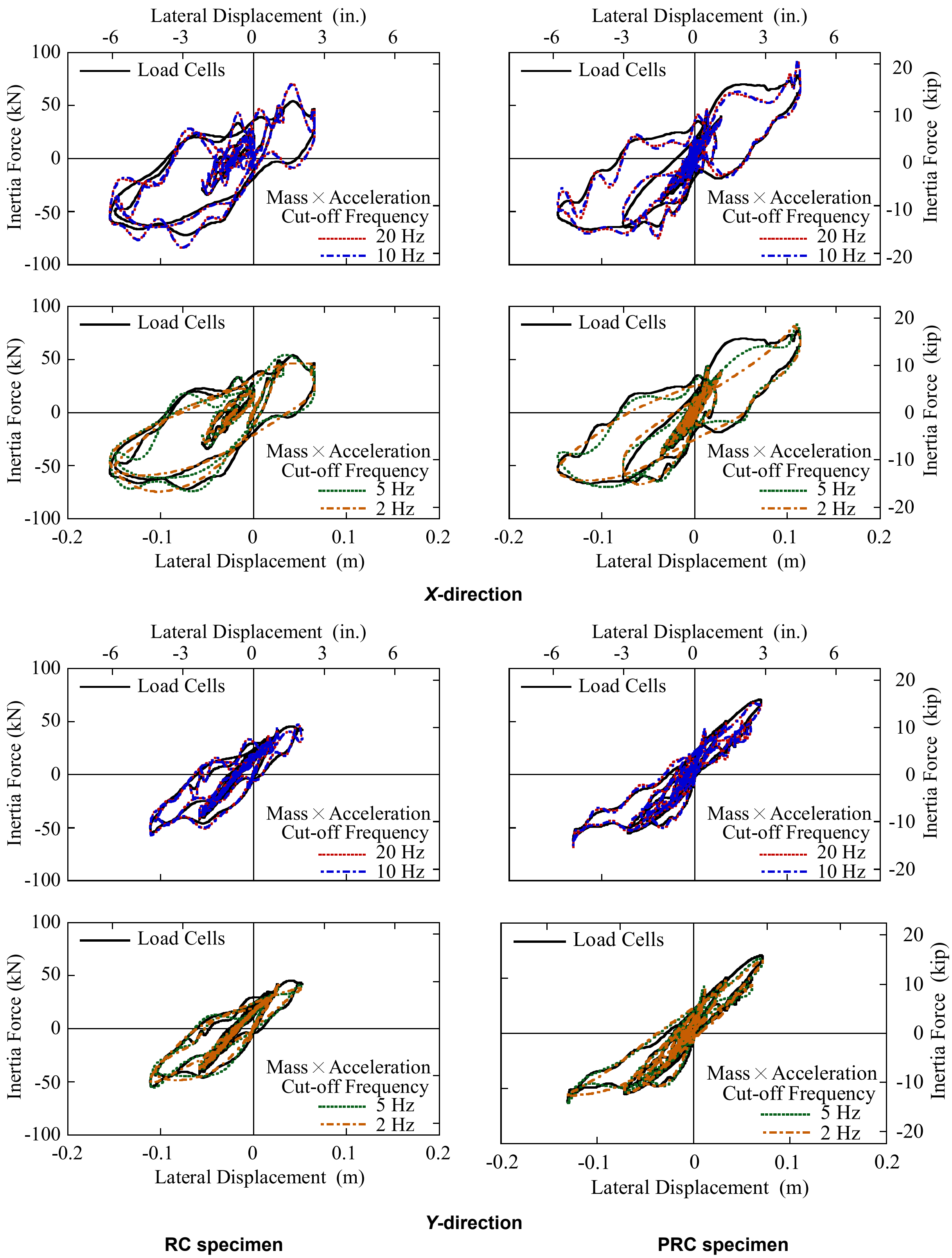

Figure 4.18 Inertia force–lateral displacement hysteresis for the design-level test.

4.4.1.5 Global Response during Main Pulses

As shown in Figure 4.17, the PRC specimen did not show an origin-oriented hysteresis as expected, prompting an investigation into the response during the main pulses. Figure 4.19 shows response displacement time histories, orbits at the center-of-gravity of the top blocks, and force versus displacement hysteresis from 2.5 to 6 sec during the main pulses. Eight points are marked in the figures: at Point A, the specimens reached the first peak in the positive *X*-direction; then, the lateral forces of the *X*-direction decreased to zero at Point B. Point C shows the positive peak in the following response, and then the forces returned to zero at Point D. Point E shows that when the response displacements reached the second peak in the positive direction, the forces went back to zero at Point F. Point G shows the positive peaks in the *Y*-direction in the subsequent response, and then again the forces went back to zero at Point H.

The hysteresis of the PRC specimen showed an origin-oriented tendency in the *Y*-direction during response between the Points A and B. Thus, the orbit of the PRC specimen shows that the response is directed to zero in both directions; however, during the response between Points C and D, in which the hysteresis shows no origin-oriented tendency, the response displacement increased in the *Y*-direction, although it decreased in the *X*-direction.

Between 4.4 and 6 sec, the same trend is observed. When the force decreased from Point E to F, in which the PRC specimen had a similar unloading path of the RC specimen and showed no origin-oriented tendency, the vector of displacement was not directed to the point of origin; however, in the response between Points G and H, the hysteresis of the PRC specimen had an origin-oriented hysteresis in the *Y*-direction, as the displacement vector was directed to the origin point.

These results suggest that when the displacement vector is not directed to the origin point, the PRC specimen will not show an origin-oriented hysteresis; when the displacement vector is directed to the origin point or near the origin point, the PRC specimen will show such hysteresis. While the response damped out in both directions after the specimen experienced the main pulses, the displacement vector of the PRC specimen is likely to be directed to the point of origin, and, therefore, the residual displacement tends to decrease. Thus, even though the hysteresis shown in Figure 4.17 does not show origin-oriented hysteresis, the PRC specimen had a smaller residual displacement than the RC specimen after being subjected to the earthquake excitation.

4.4.1.6 Global Response in 45°-Rotated Coordinate System

As shown in Figure 4.16, the specimens responded mostly in the northwest–southeast direction. Thus, the behaviors of the specimens were also investigated in a 45° rotated coordinate system; see Figure 4.20. The maximum displacements were 0.184 m (7.2 in.) and 0.188 m (7.4 in.) in the northwest direction for the RC and PRC specimens, respectively. The flexural strengths were 76 kN (17 kips) and 81 kN (18 kips), which were about 10% larger than those in the original coordinate system.

Figure 4.21 details the response of the specimens during the main pulses in this coordinate system. The tendency of the PRC specimen toward an origin-oriented hysteresis when the displacement vector is directed to the origin point or near the origin point can be also seen here. Furthermore, the hysteresis from Points C and E, which show no origin-oriented tendency in the original coordinate system, shows a slight origin-oriented tendency after the hysteresis passes Points D or F. From the orbits, the displacement vector is directed to the origin point or near the origin point after these points.

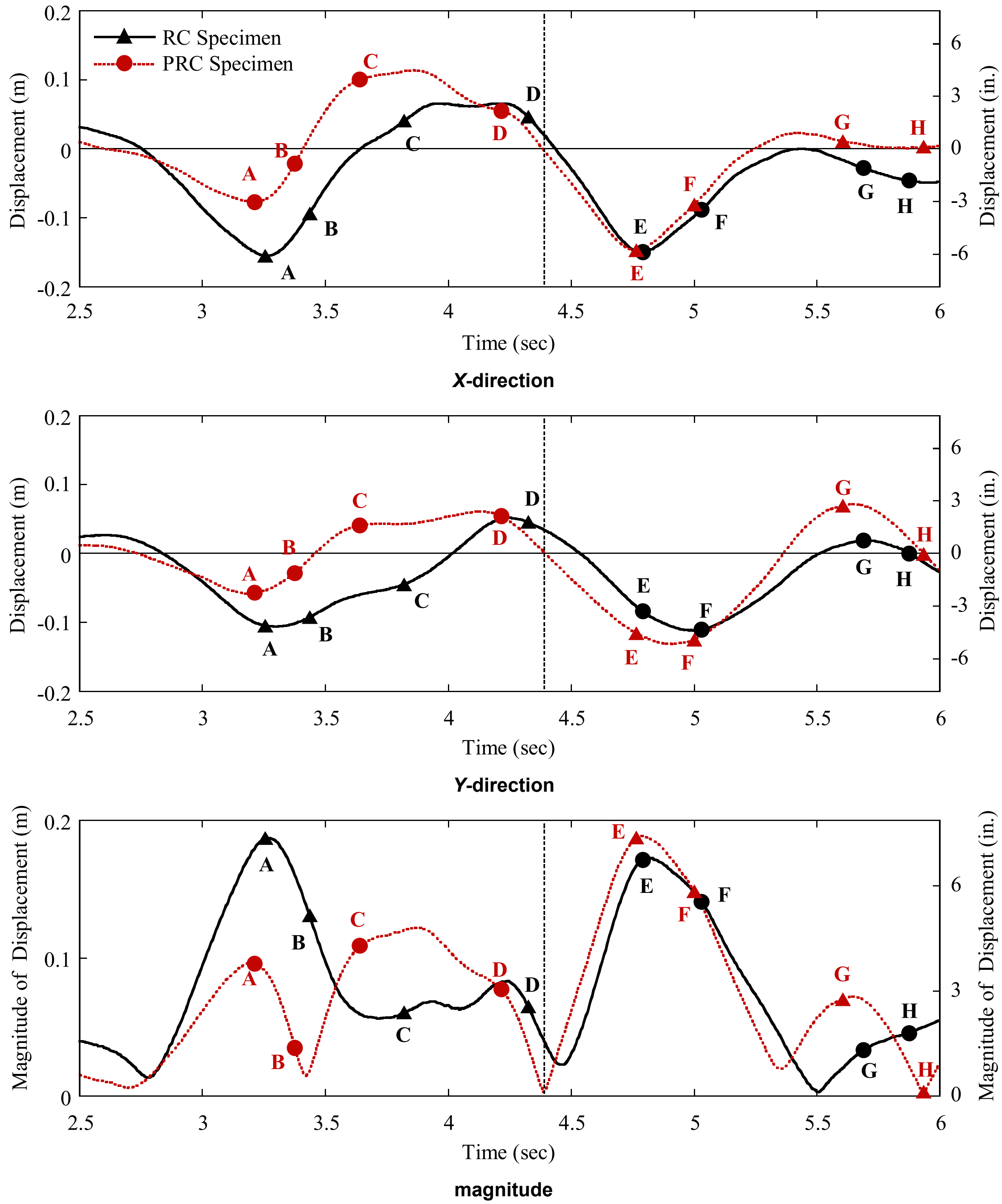

Figure 4.19(a) Response of specimens during main pulses for the design-level test: response displacement.

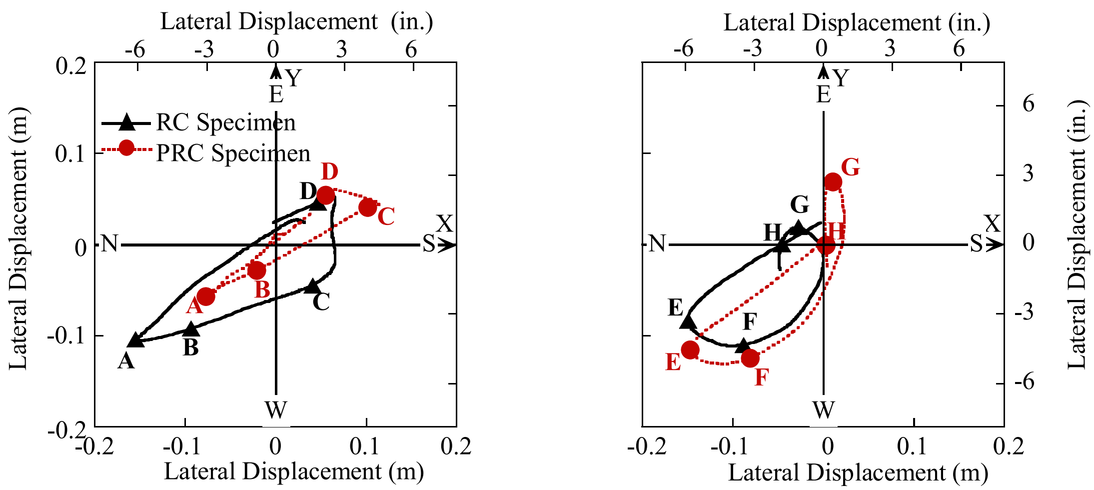

Figure 4.19(b) Response of specimens during main pulses for the design-level test: orbit of response displacement.

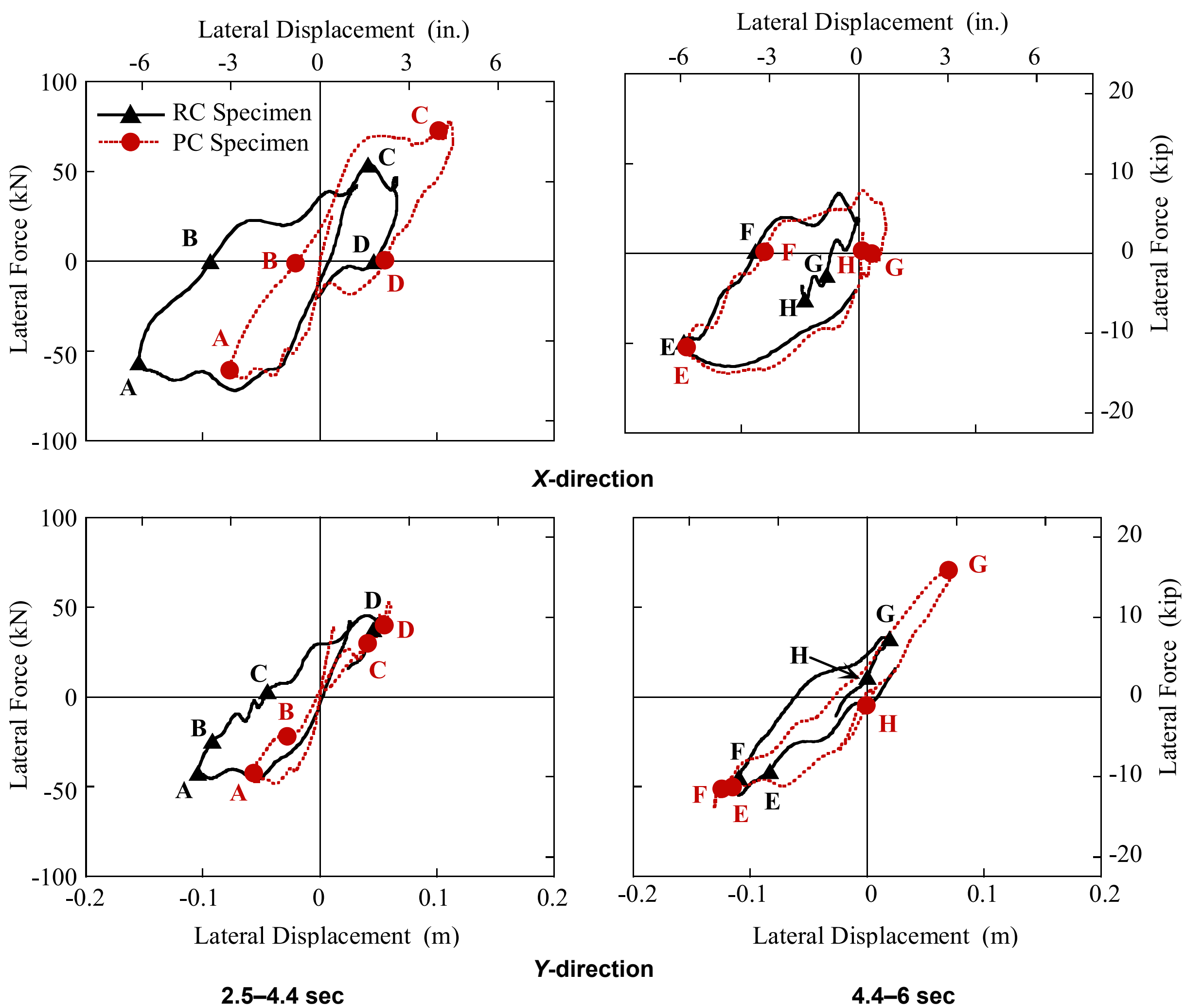

Figure 4.19(c) Response of specimens during main pulses for the design-level test: lateral force-lateral displacement hysteresis.

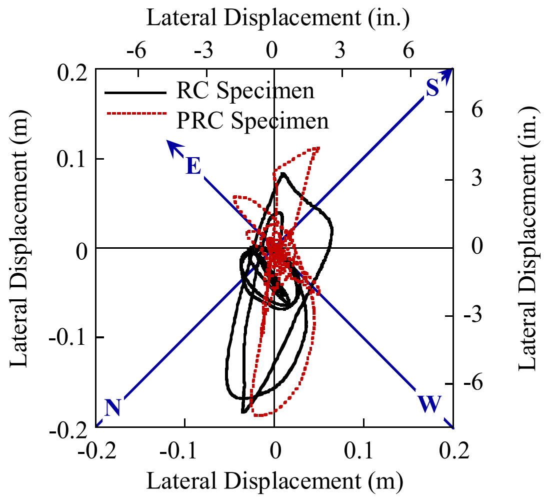

(a)

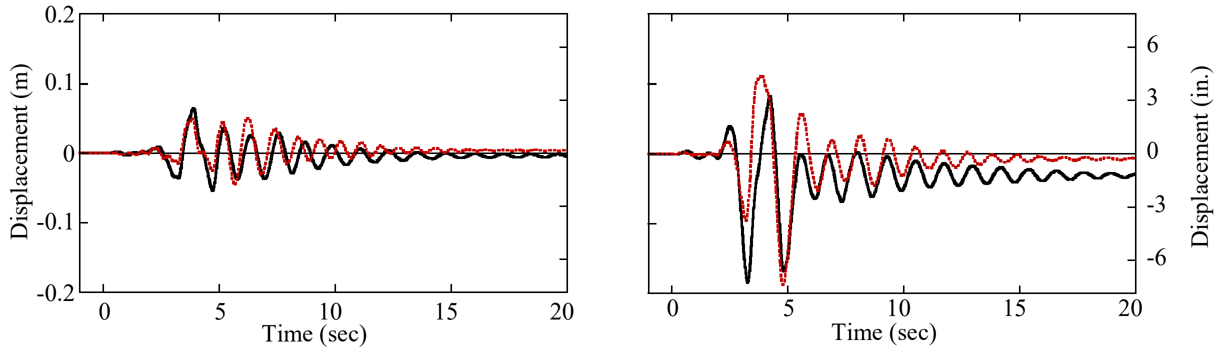

(b)

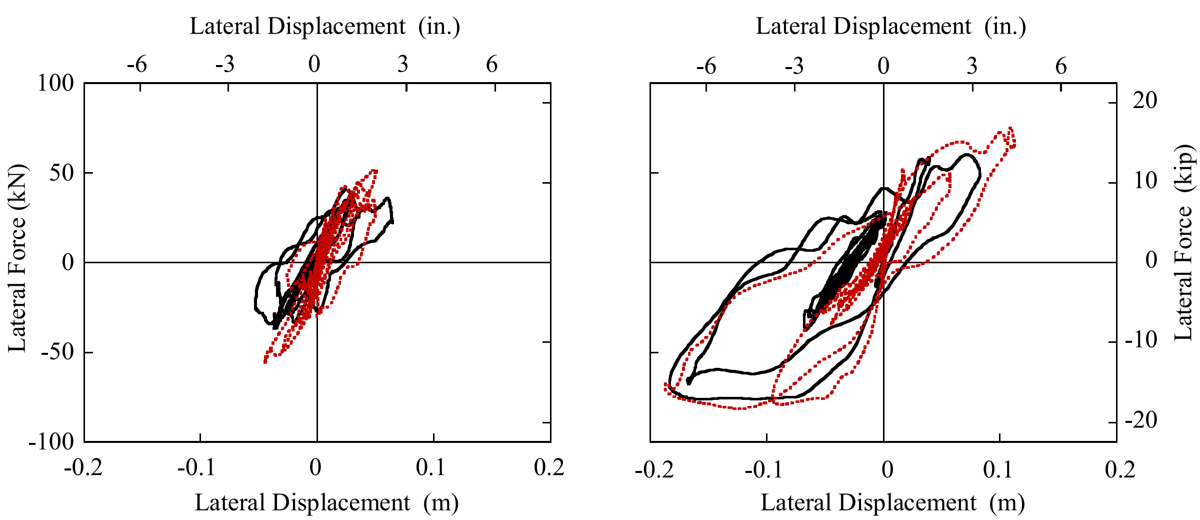

(c)

NW–SW direction **NW–SE direction**

Figure 4.20 **Response in 45° rotated coordinate system for the design-level test: (a) orbit of response displacement: (b) displacement response at center-of-gravity; and (c) lateral force–lateral displacement hysteresis.**

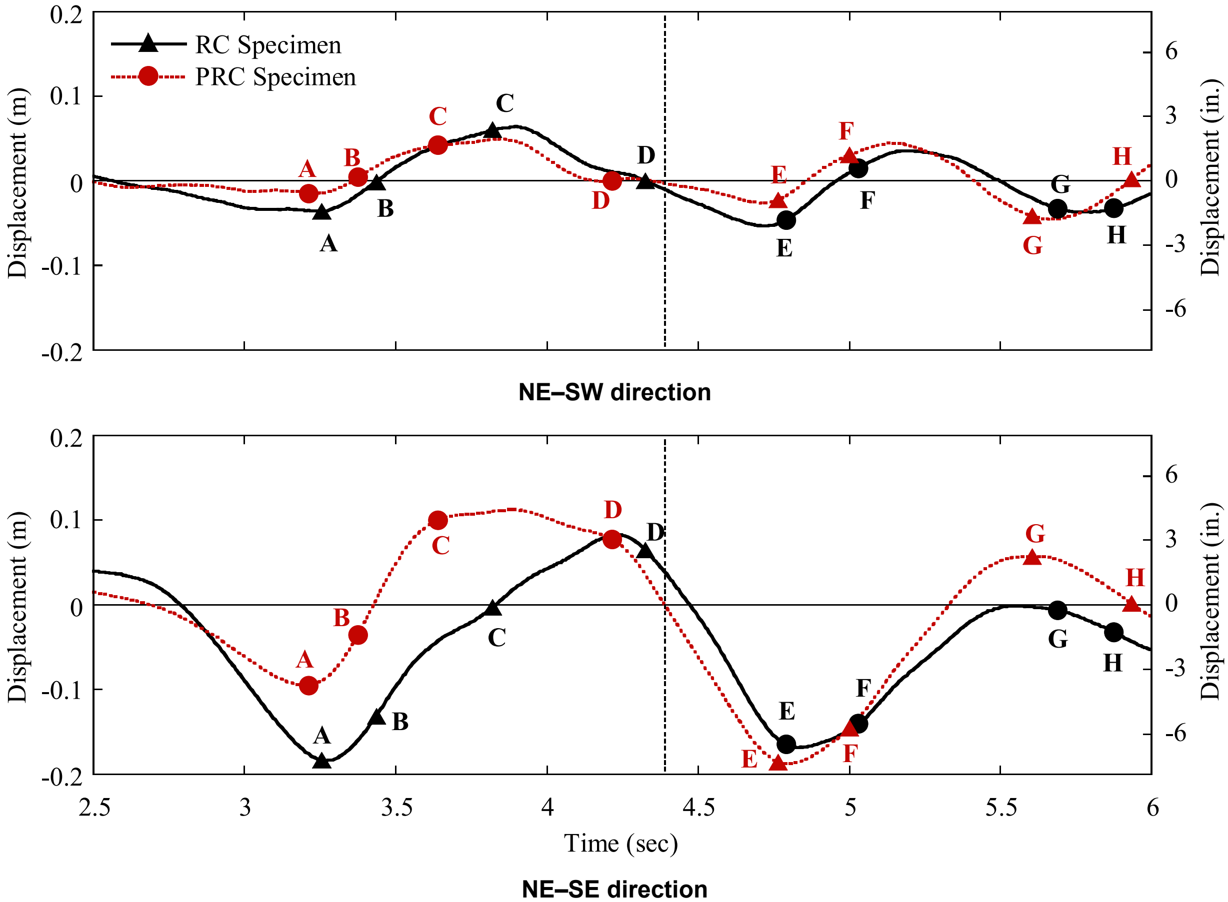

Figure 4.21(a) Response during main pulses in rotated coordinate system for the design-level test: response displacement.

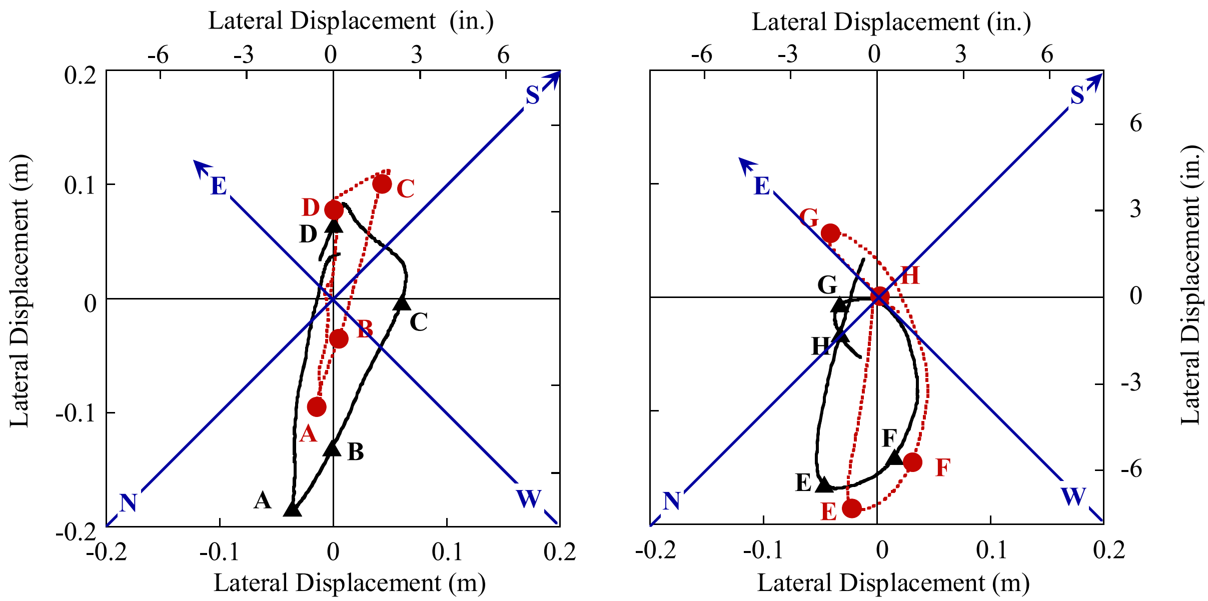

2.5–4.4 sec **4.4–6 sec**

Figure 4.21(b) Response during main pulses in rotated coordinate system for the design-level test: orbit of response displacement.

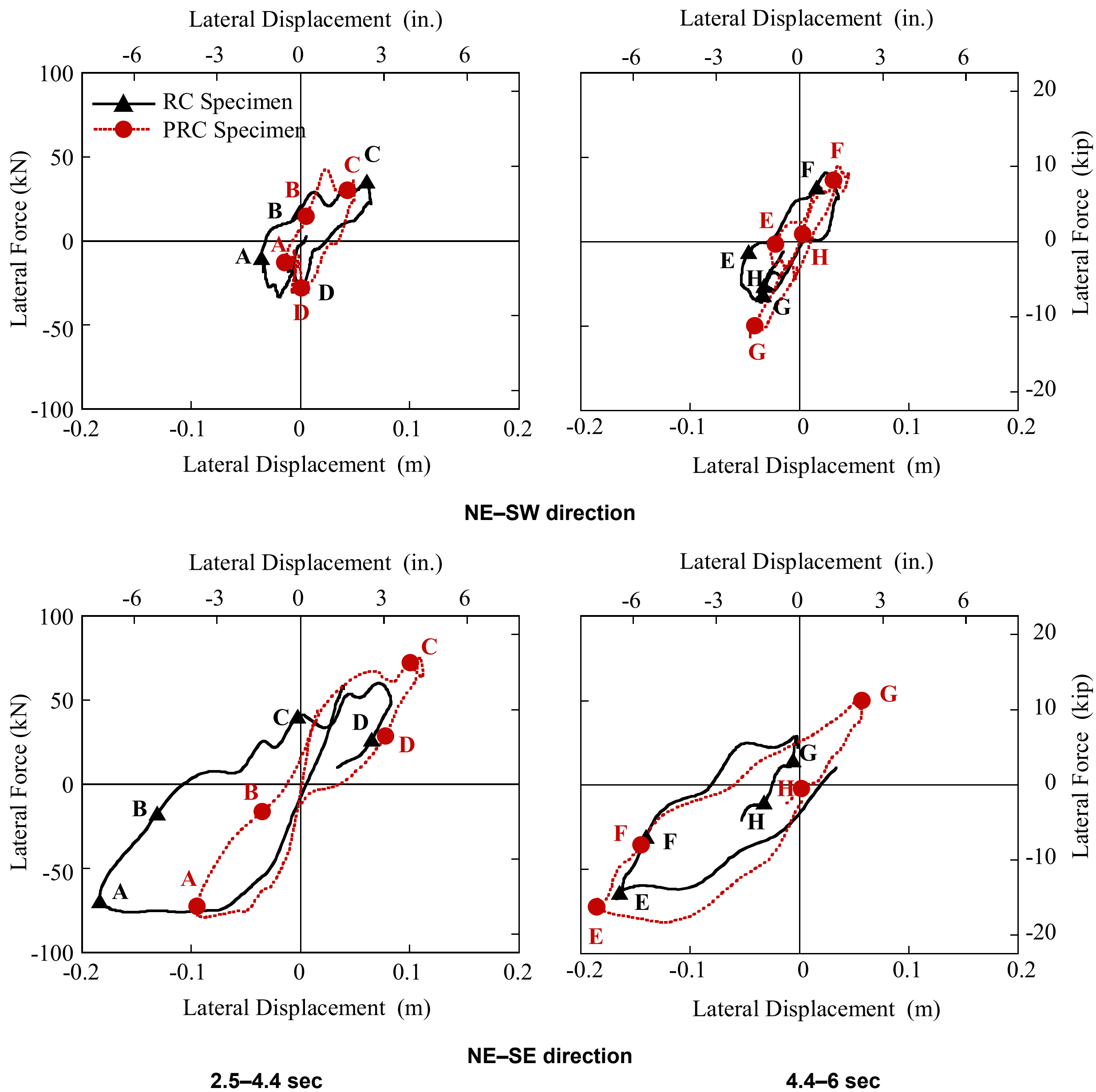

Figure 4.21(c) Response during main pulses in rotated coordinate system for the design-level test: lateral force–lateral displacement.

4.4.2 Local Response

4.4.2.1 Behavior of the Tendon

Figure 4.22 shows the behavior of the tendon installed in the PRC specimen during the design-level test. The pure axial strain of the tendon was obtained as an average of a pair of strain-gauge measurements at the opposite sides of the tendon surface around the bottom and top of the column. As expected, the axial strain obtained from the north and south gauges and the east and west gauges around the bottom of column show the same strain histories. Although the measurements obtained from the top strain gauges show strain beyond the gauge capacity at some points during the main pulses, the axial strain time histories are very similar to that obtained at the bottom gauges, demonstrating that the tendon behaved uniformly. No localized damage was observed in the tendon. The strain reached a maximum strain of 0.0037 at 4.8 sec.

The prestressing force increased up to 613 kN (138 kips) as the specimen deformed and then decreased by 39 kN (9 kips) during the test. As shown in Figure 4.22, the tendon force increased when the deformation of the specimen increased and decreased when the specimen returned to near the origin point. The maximum force occurred at 4.8 sec (Point E) when the column deformation reached the maximum, as shown in the orbit in Figure 4.21.

Figure 4.23 compares the stress–strain hysteresis of the tendon during the design-level test with the hysteresis obtained from the material test described in Section 2.4.3. The tendon remained in the elastic range during the test. The maximum stress was 65% of the ultimate strength of the tendon. Figure 4.24 shows the flexural strain of the tendon. The amplitude of flexural strain was about 0.0003, which is 10% smaller than the axial strain shown in Figure 4.22.

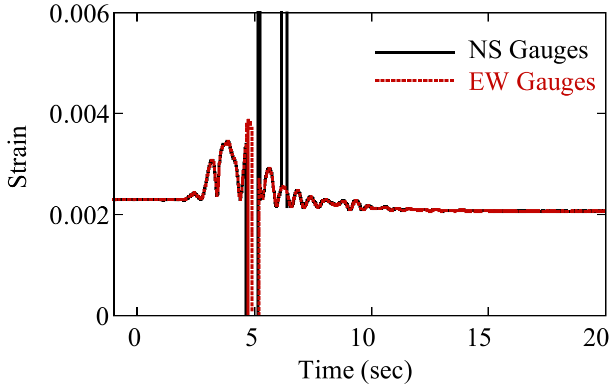

gauges at top of column

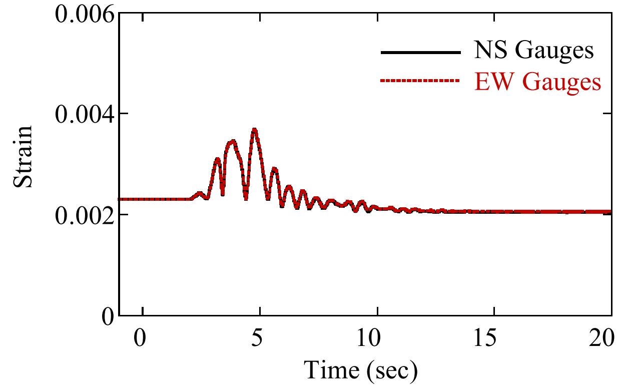

gauges at bottom of column

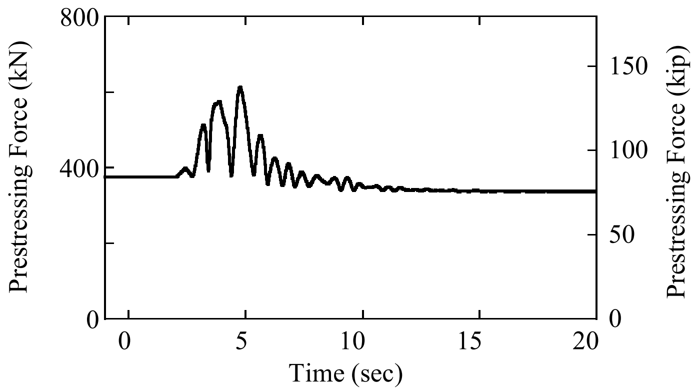

(b)

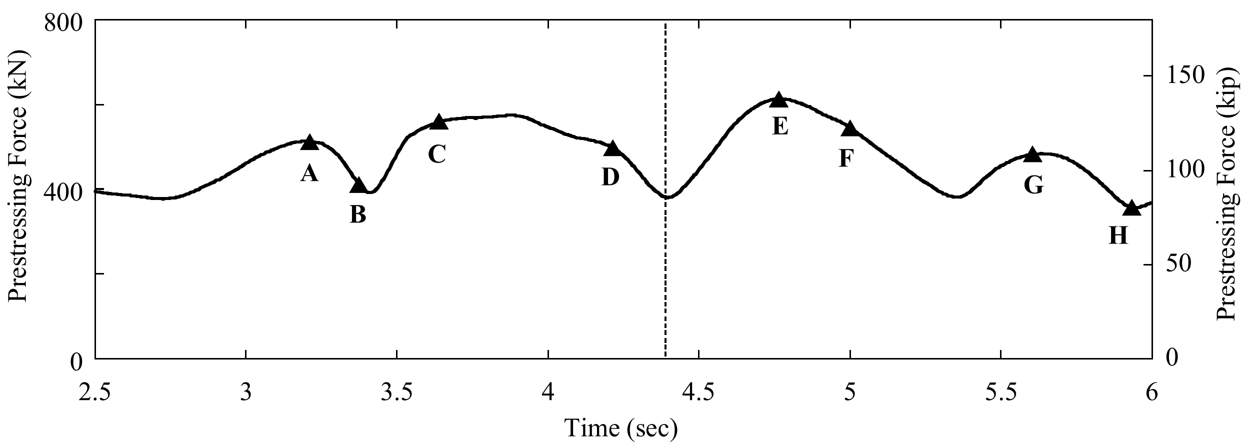

(c)

Figure 4.22 **Behavior of tendon during the design-level test: (a) axial strain; (b) prestressing force; and (c) variation of prestressing force during main pulses.**

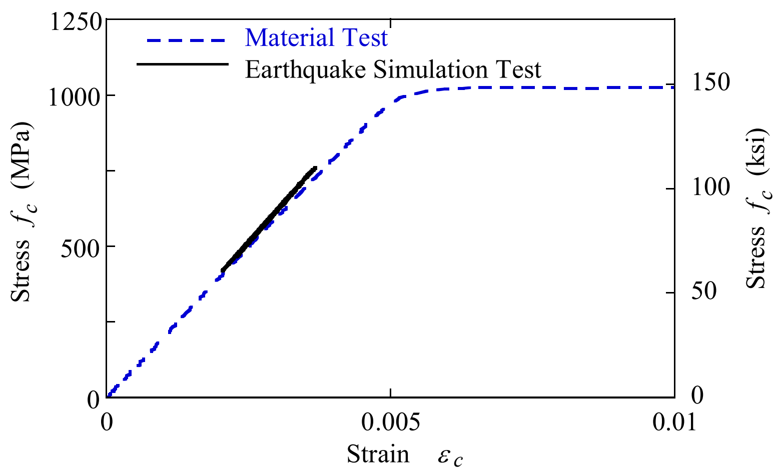

Figure 4.23 Stress–strain hysteresis of tendon during design-level test.

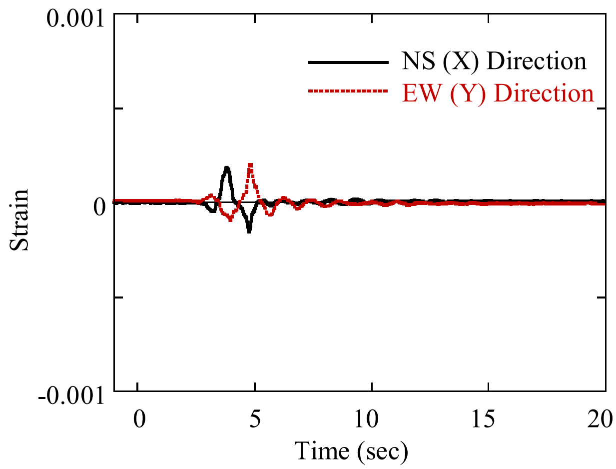

Figure 4.24 Flexural strain of tendon during the design-level test.

4.4.2.2 Strain of Reinforcement

Figure 4.25 shows strain time histories of the longitudinal reinforcing bars. During the main pulses, the longitudinal reinforcement around the bottom of the column yielded and exceeded the capacity of the gauges. Because almost all the gauges placed at the bottom of the columns were damaged, the strain of the reinforcement after the main pulses was not measured.

Figure 4.26 shows strain time histories of the spirals. Unfortunately, there is no legend available because the labels of the gauges placed on the spirals of the PRC specimen were lost during testing; however, the channel IDs are provided in the figure. The spirals experienced strains that exceed 0.01 during the main pulses.

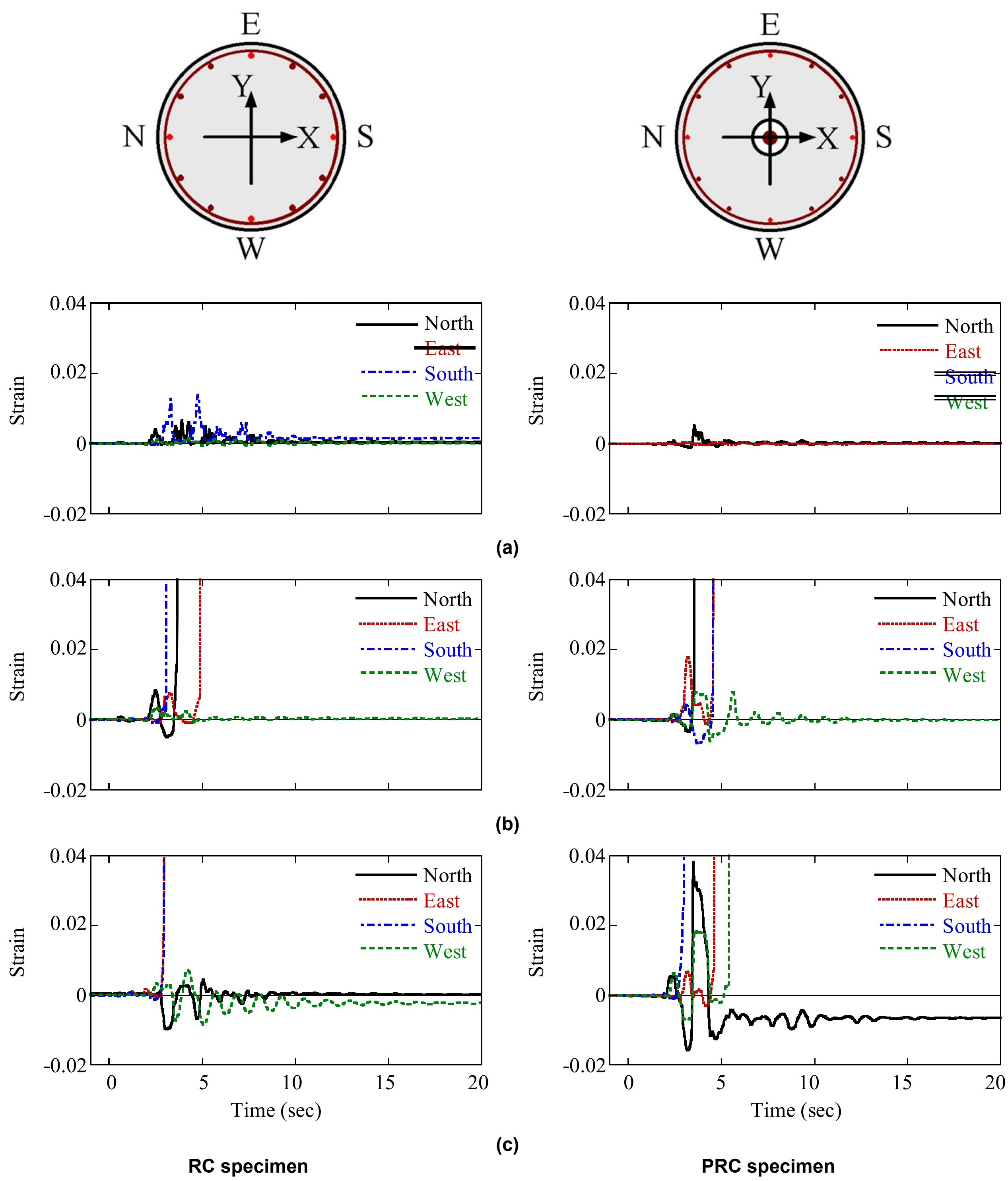

Figure 4.25 **Strain of longitudinal reinforcement for the design-level tests: (a) top of column (1.61 m from bottom of column): (b) 0.1 m from bottom of column; and (c) 0.01 m from bottom of column.**

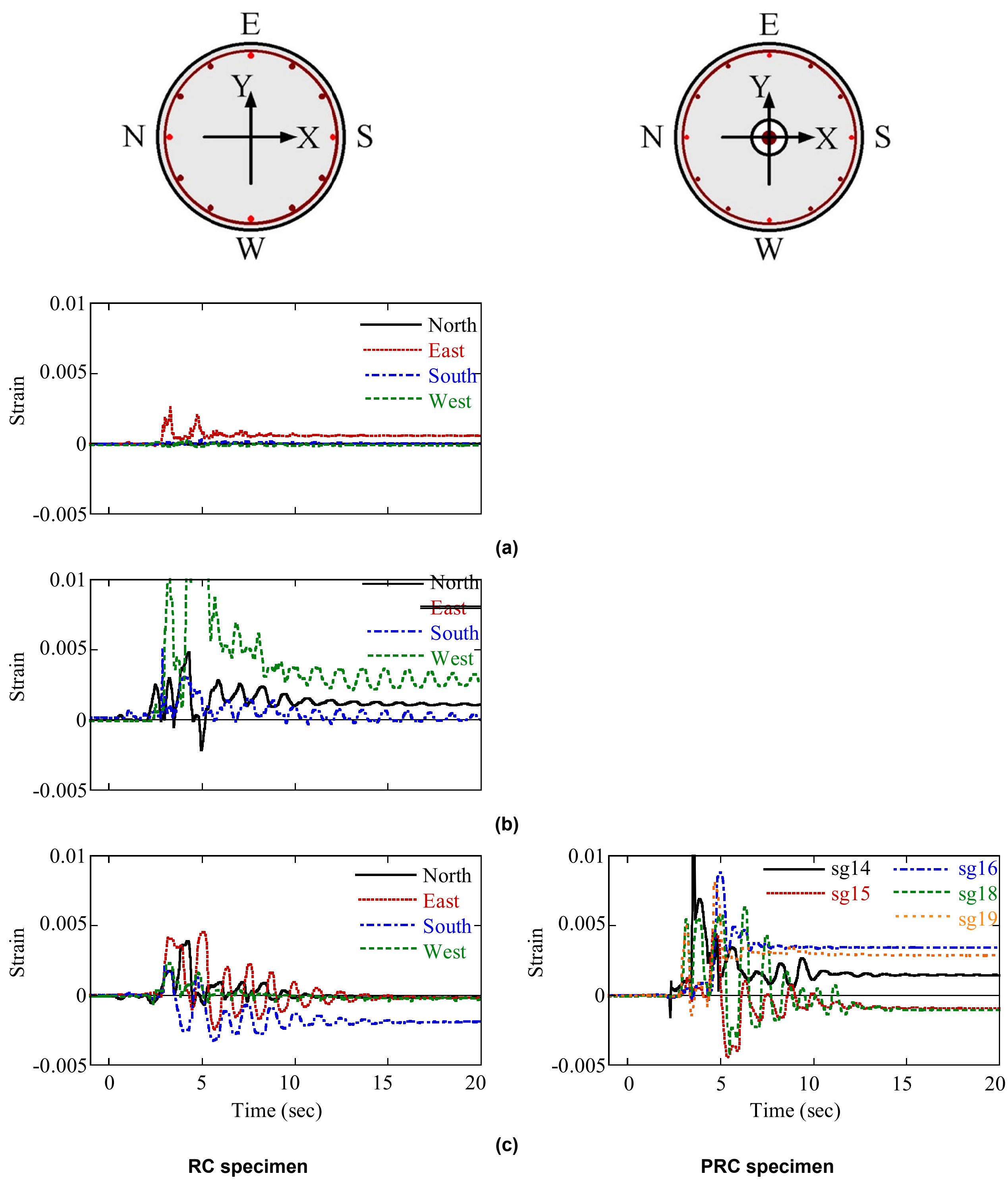

Figure 4.26 Strain of spirals for the design-level test for both the RC and PRC specimens: (a) top of column (1.61 m from bottom of column): (b) 0.1 m from bottom of column; and (c) 0.01 m from bottom of column.

4.4.2.3 Curvature of Columns

Figure 4.27 shows curvature time histories computed from measurements of the DCDTs, and Figure 4.28 shows moment versus curvature hysteresis of the columns. Figure 4.29 shows curvature distributions along the column at several peaks and at the end of the test. Measurements including the effect of strain penetration of reinforcement from the footing are not shown in the figures and will be discussed later. Nonlinear deformation occurred mainly at the bottom portion of the column between heights of 51 mm (2 in.) and 305 mm (12 in.) for both specimens. This correlates to the location of visible damage, such as cracks in the concrete cracks and spalling of the concrete cover. This portion is assumed to be a plastic-hinge region.

The specimens had almost the same negative peak in the *X*-direction at 4.8 sec with very similar curvature distributions, as shown in Figure 4.29. Therefore, reducing the amount of longitudinal reinforcement and applying an additional compressive force as prestressing force did not significantly affect formation of a plastic-hinge region, plastic-hinge length, or the magnitude of nonlinear curvature. As shown in Figure 4.29, the RC column had residual curvature of 0.4 m (16 in.) from the bottom of the column, while the PRC specimen had residual curvature only in 0.2 m (8 in.) from the bottom. The RC specimen had much larger residual curvature than the PRC specimen: 0.034 /m (8.6×10^{-4} /in.) and 0.012 /m (3.0×10^{-4} /in.) in the *X*-direction for the RC and PRC specimens, respectively.

Figure 4.30 shows curvature time histories obtained from the DCDTs placed around the bottom of the columns. Measurements by a pair of DCDTs placed between heights of 0 and 0.15 m (6 in.) potentially include the effect of strain penetration of reinforcement from the footing, as well as nonlinear deformation of the columns in the plastic-hinge region. The maximum curvatures due to strain penetration were evaluated to be about 0.06/m and 0.1/m for the RC and PRC specimens, respectively.

Figure 4.31 shows accuracy of curvature measurements and the contribution of strain penetration of the reinforcement to the lateral displacement at the top. The displacements at the center-of-gravity computed by integration of measured curvature along the column height were compared with the displacements directly measured by the linear potentiometers at the top. The integration of curvature measurements provided good agreement with the directly measured displacement responses. Contribution of the strain penetration to the response displacement at the top was estimated to be 10–20% for the RC specimen and 20–30% for the PRC specimen. This result bears some further study. Because the PRC specimen has smaller reinforcing bars, it was assumed that it would have smaller strain penetration, and, thus, smaller response displacement due to strain penetration.

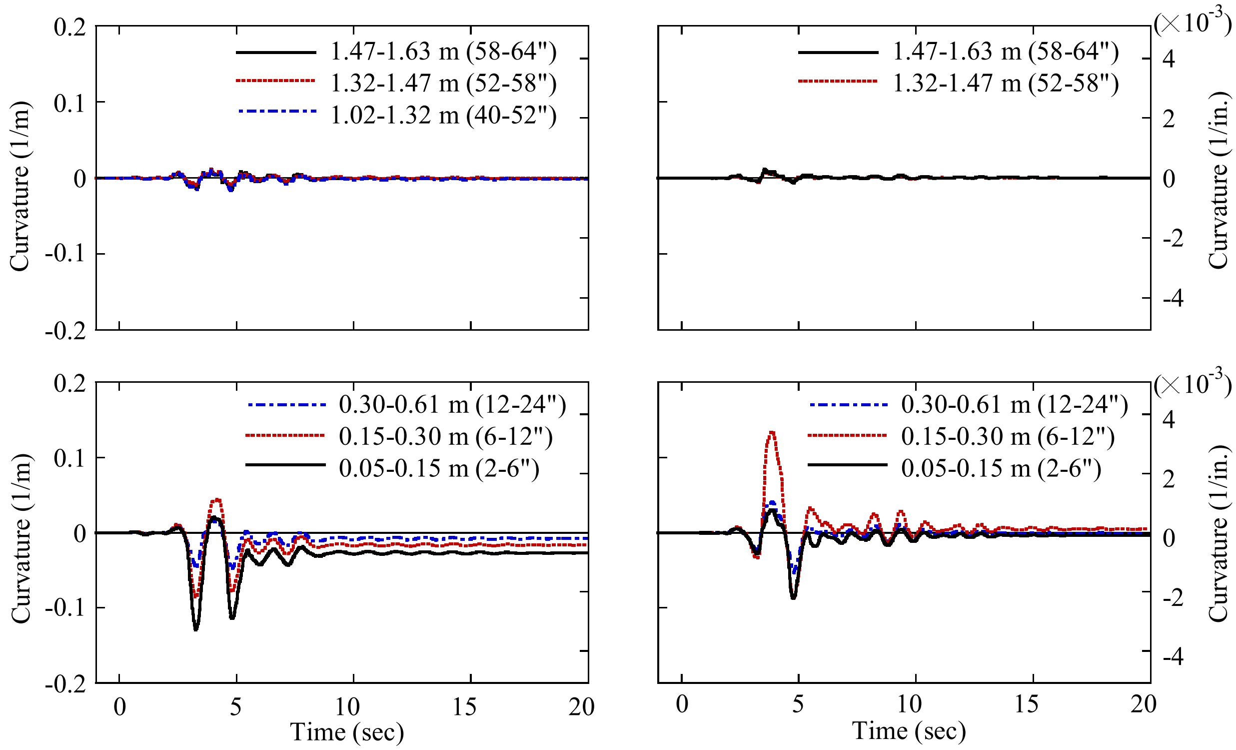

***X*-direction**

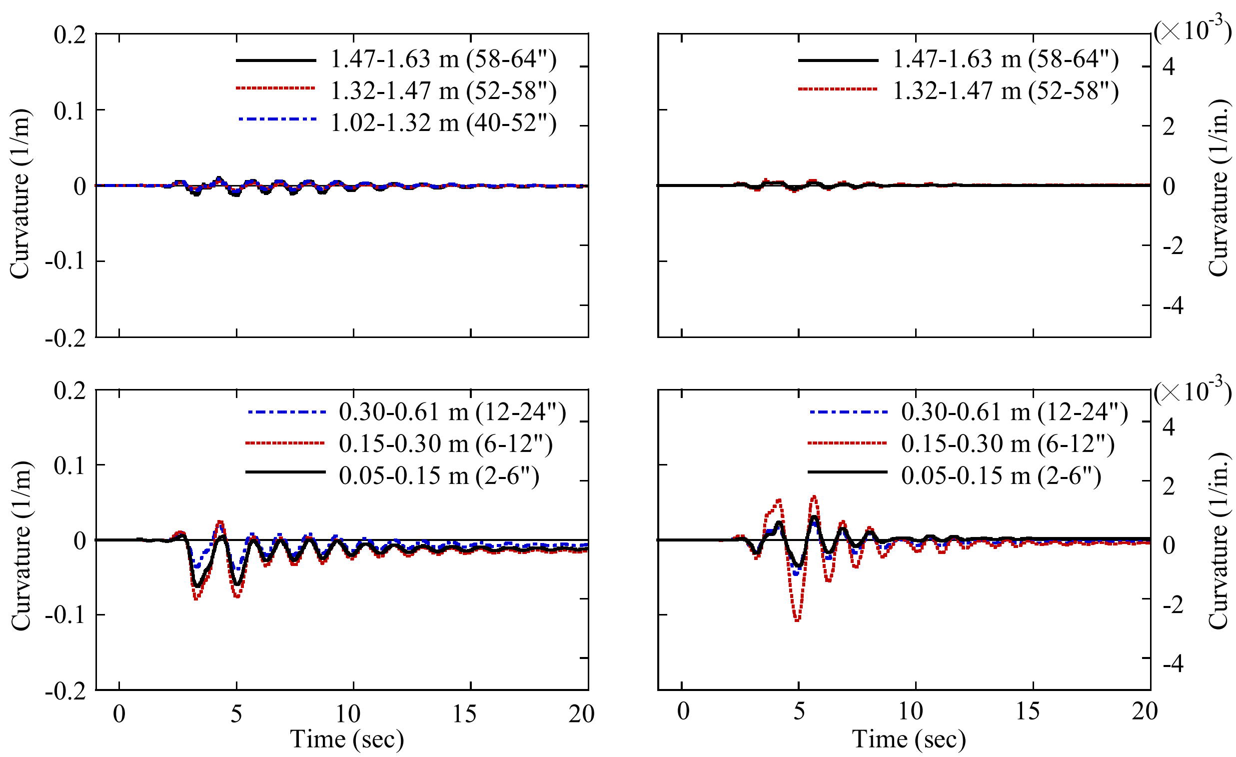

***Y*-direction**

RC specimen **PRC specimen**

Figure 4.27 Curvature of columns for the design-level tests.

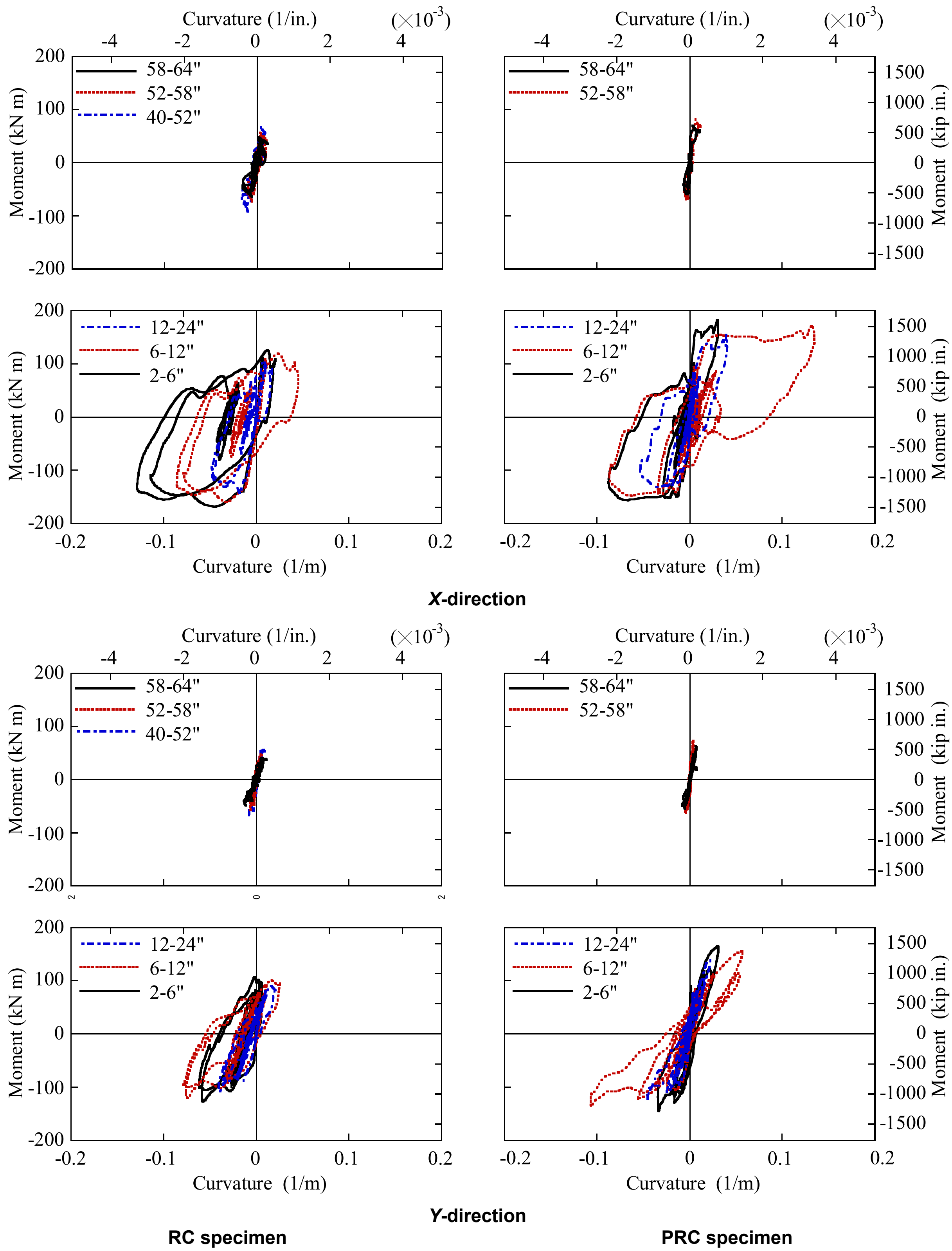

Figure 4.28 Moment curvature hysteresis for the design-level test for both the RC and PRC specimens.

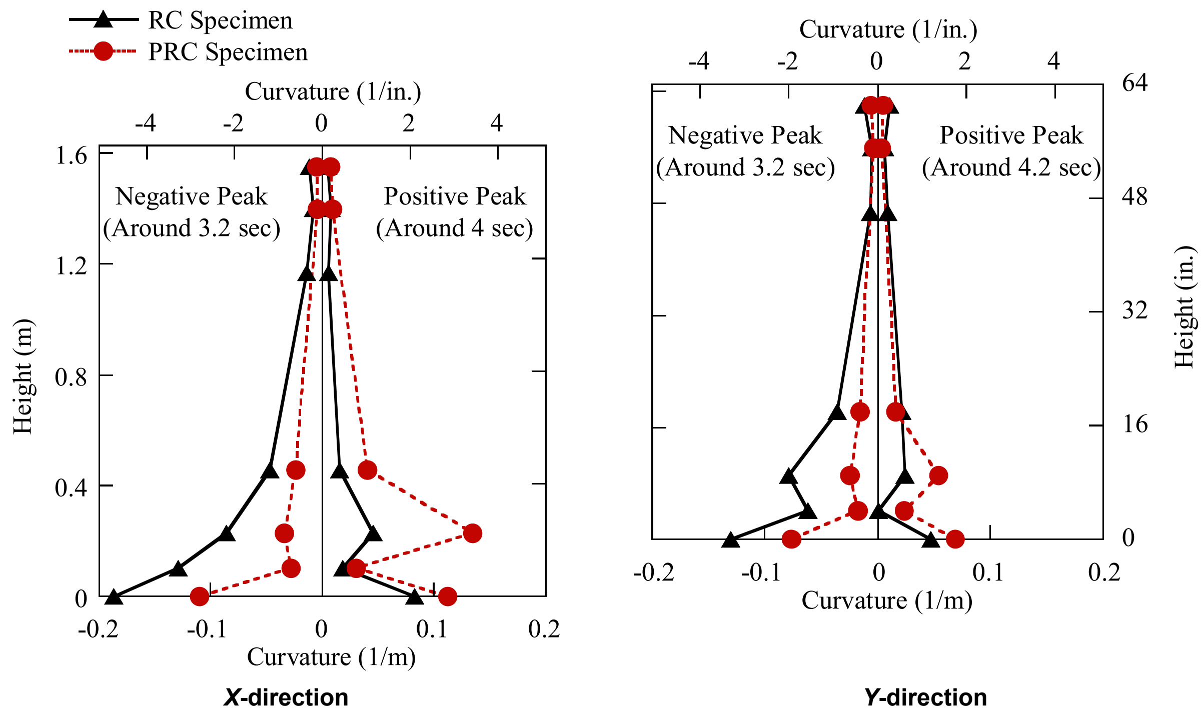

Figure 4.29(a) Curvature distribution along columns for the design-level test: first peaks.

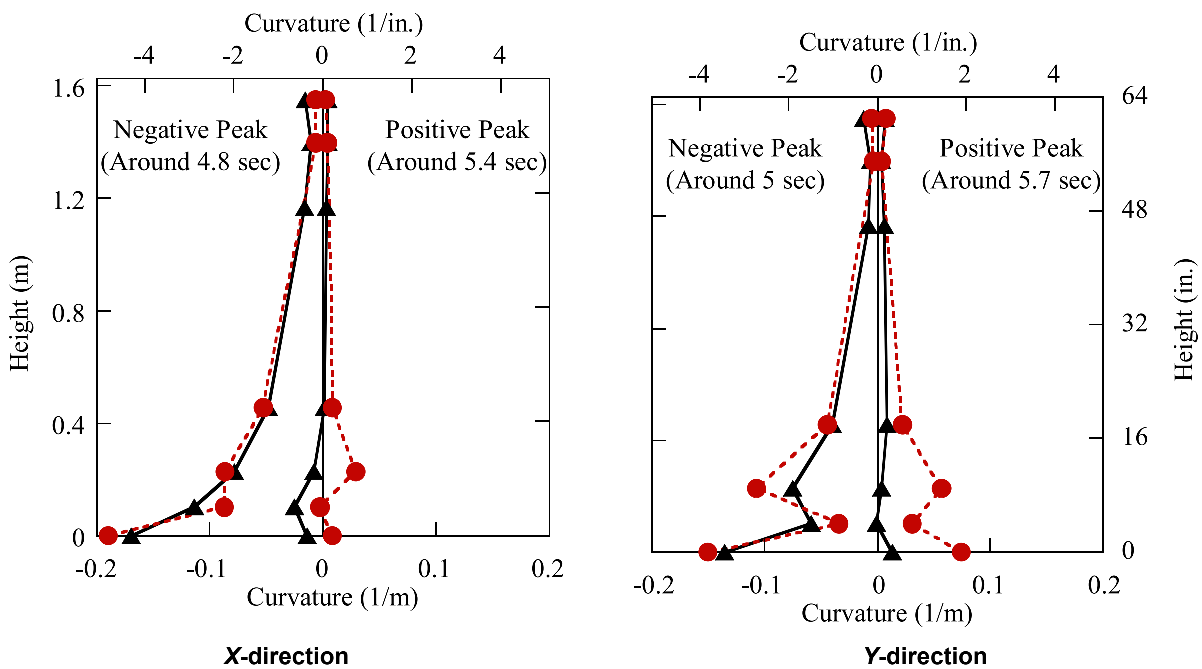

Figure 4.29(b) Curvature distribution along columns for the design-level test: second peaks.

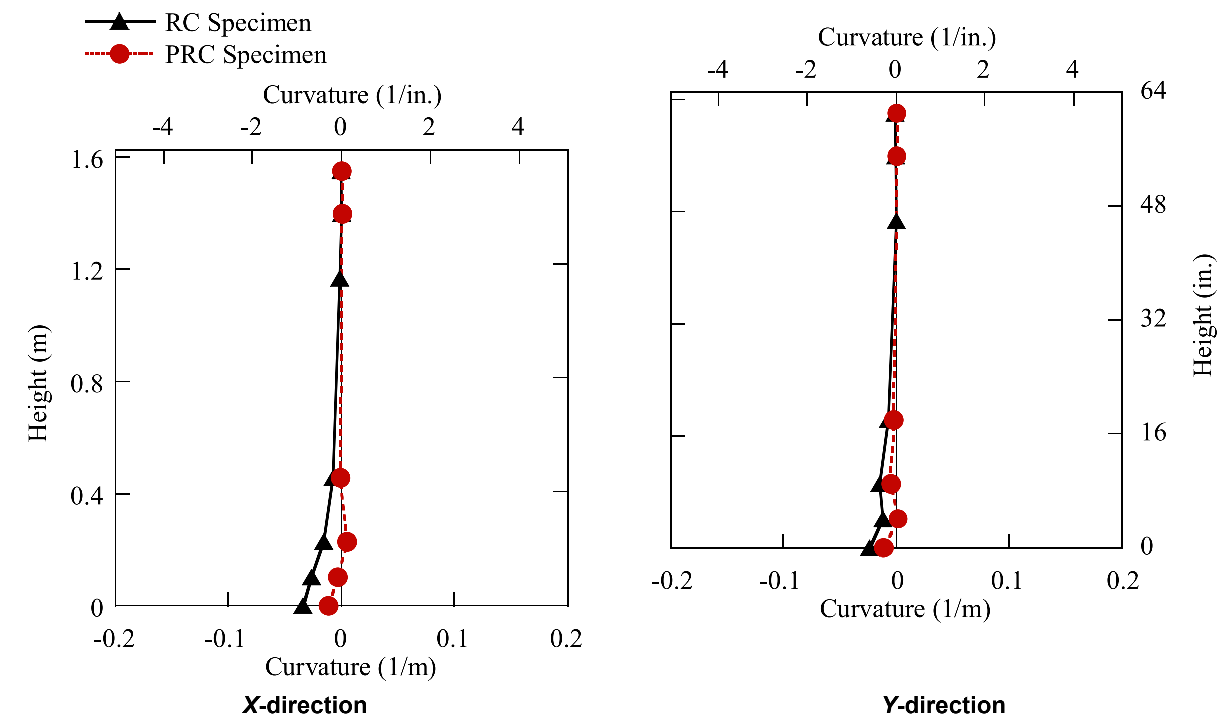

Figure 4.29(c) **Curvature distribution along columns for the design-level test: residual curvature.**

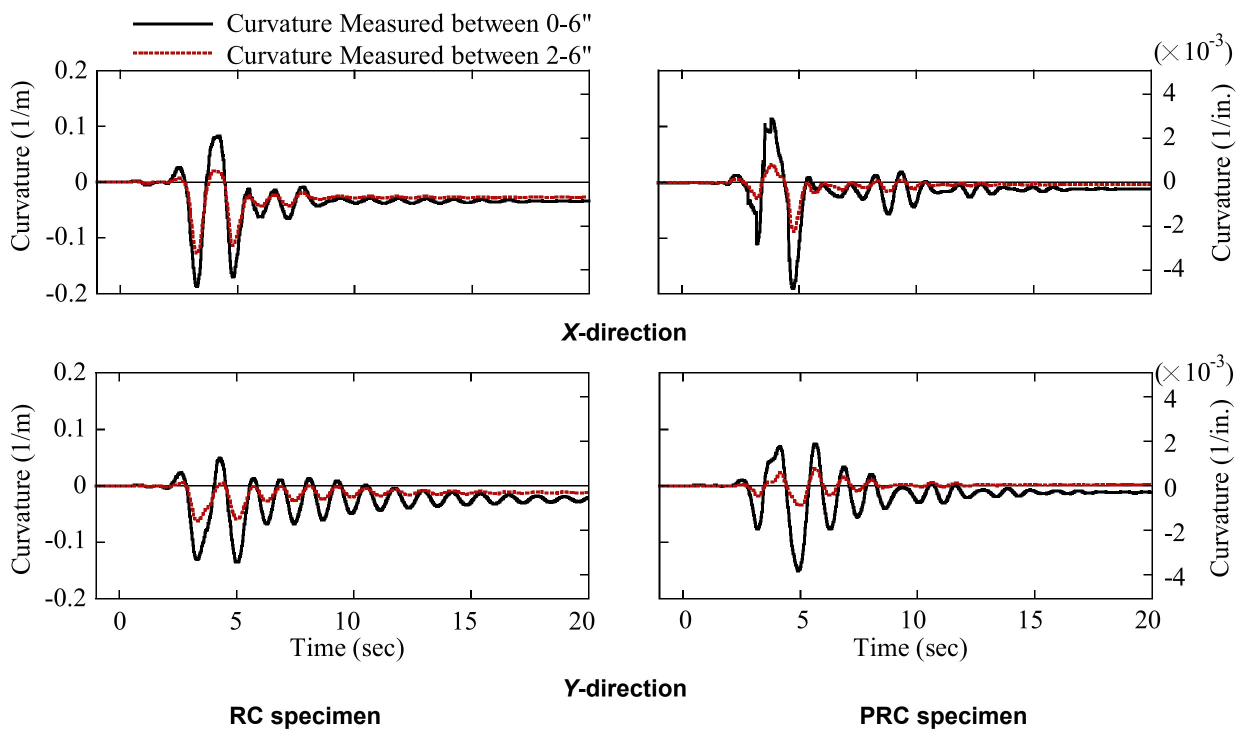

Figure 4.30 **Curvature due to strain penetration of reinforcement for the design-level tests.**

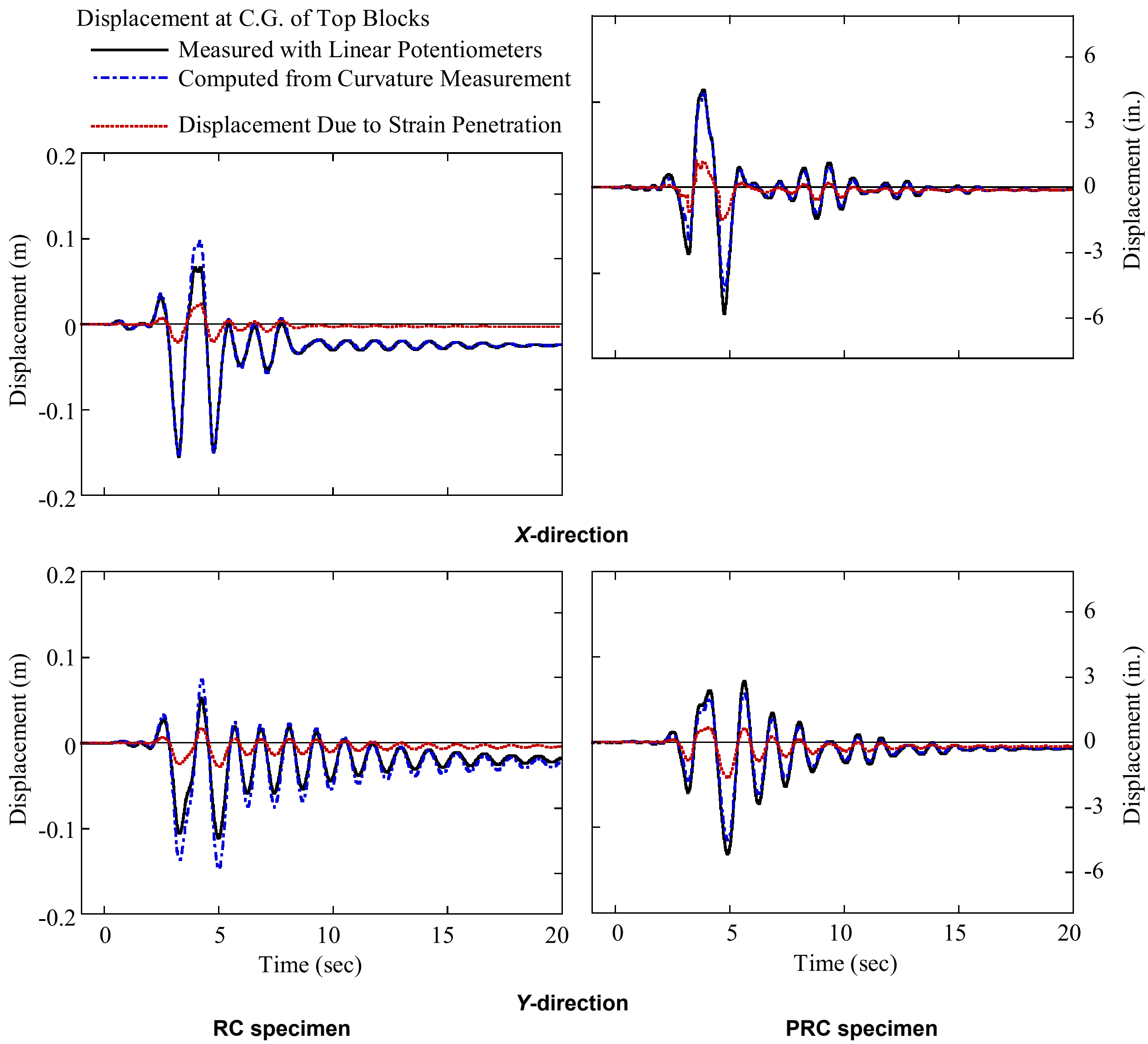

Figure 4.31 **Displacement computed with curvature measurements for the design-level tests.**

4.4.2.4 Deformation of Columns

Figure 4.32 shows displacement time histories measured at several heights along the columns, and Figure 4.33 shows deformation of the columns at several peaks and residual deformation; Figure 3.16 shows the locations of linear potentiometers. As expected, the response increased as the location of measurement goes up to the top of the column. The RC and PRC specimens had a similar deformation diagram and almost the same negative peaks at 4.8 sec, which again demonstrates incorporation of the prestressed tendon had no significant effect on the plastic-hinge region. The deformation diagrams for the residual deformation shows that the PRC specimen obviously had a smaller residual displacement than the RC specimen.

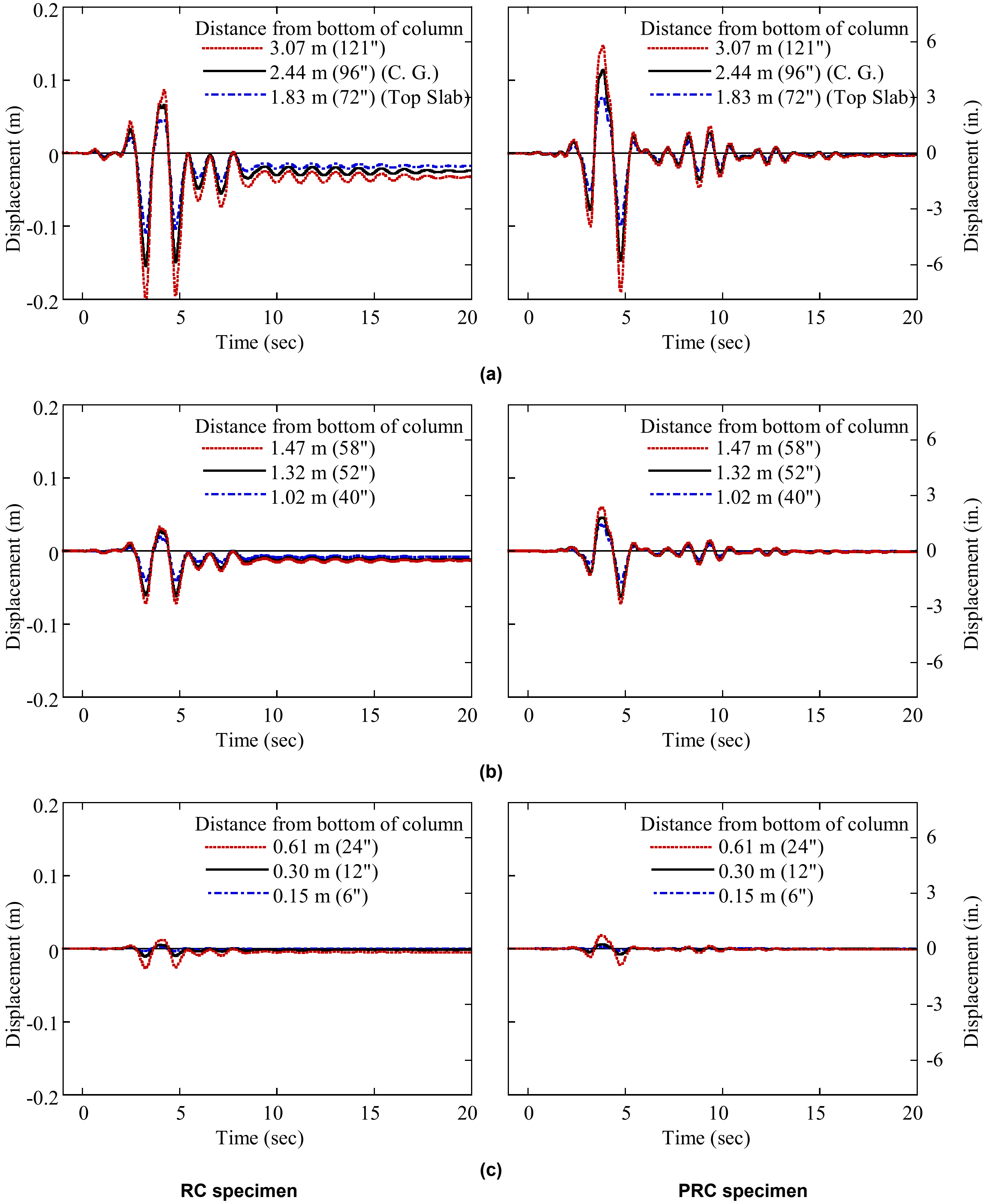

Figure 4.32(a) Response of displacement specimens for the design-level tests in the *X*-direction: (a) top blocks; (b) top portion of column; and (c) bottom portion of column.

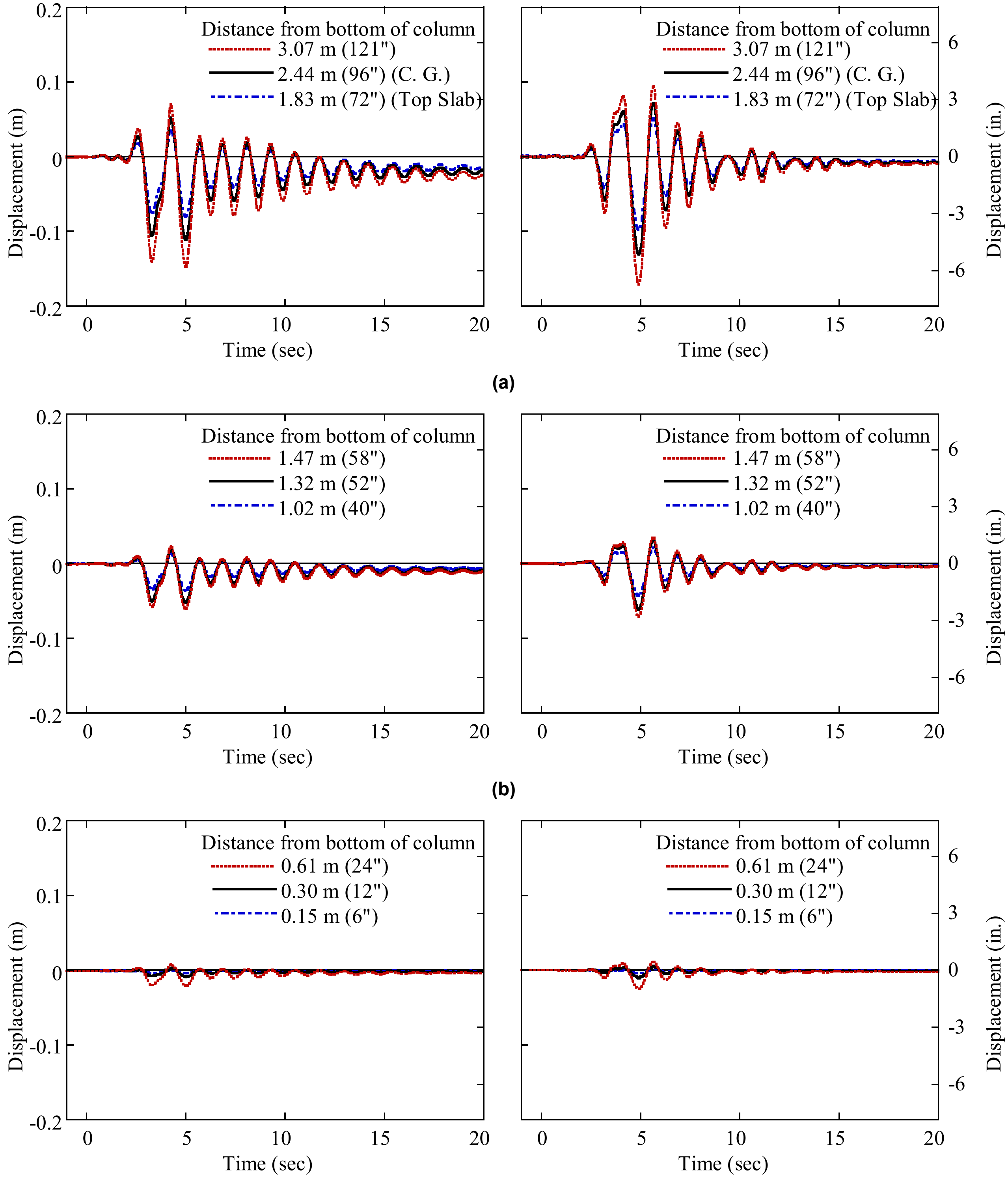

RC specimen **PRC specimen**

Figure 4.32(b) Response of displacement specimens for the design-level tests in the *Y*-direction: (a) top blocks; (b) top portion of column; and (c) bottom portion of column.

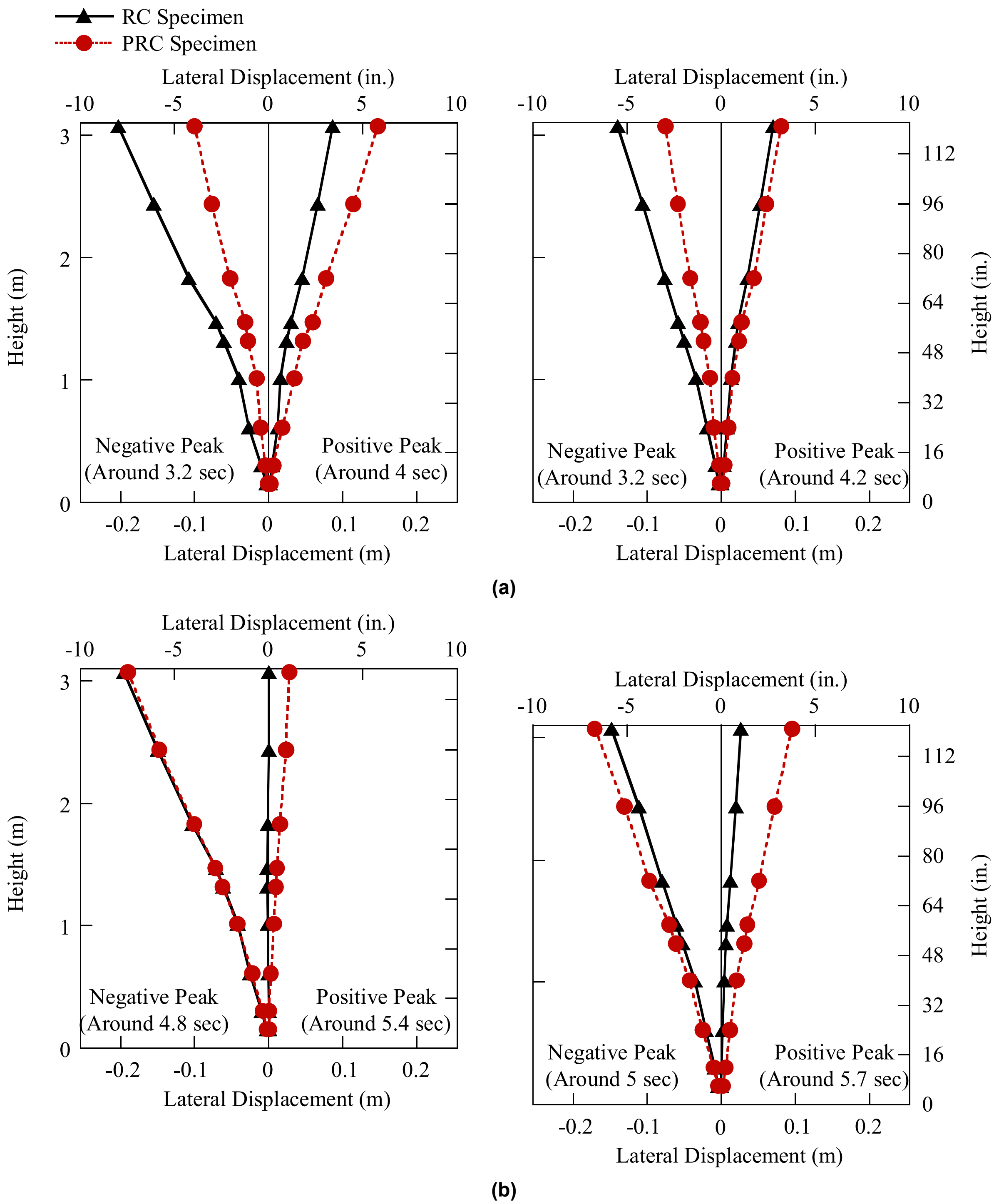

Figure 4.33(a) Column deformations for the design-level test: (a) first peaks and (b) second peaks; and (c) residual deformation.

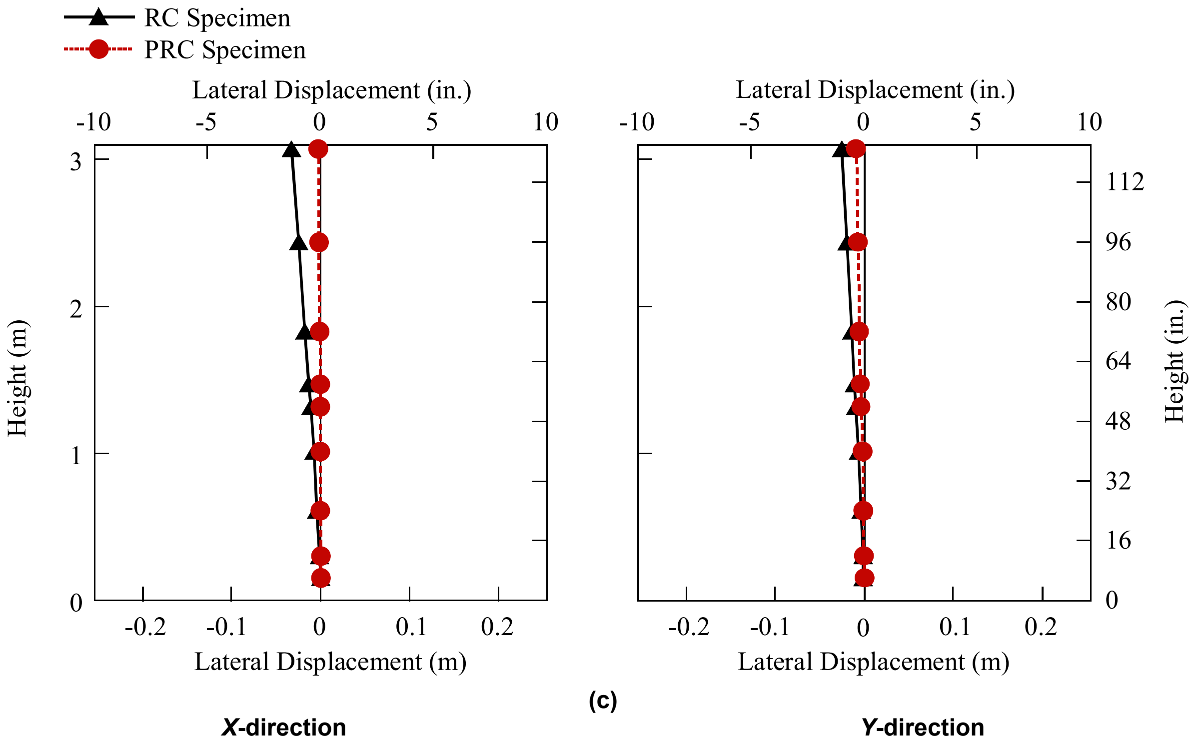

Figure 4.33(b) Column deformations for the design-level test (continued): (c) residual deformation.

4.5 MAXIMUM-LEVEL TEST

4.5.1 Global Response

4.5.1.1 Damage Observation

Figure 4.34 shows the specimens after the maximum-level test. The RC specimen tilted significantly in the northwest direction. The tilt angle of the specimen increased from 0.7° to 6.6°, which is 11.7% in drift after the maximum-level test. Even though the RC column did not collapse, it obviously lost its functionality as a bridge column. In comparison, even after being subjected to severe ground excitation the PRC specimen tilted just slightly to the west for a tilt angle of 2°, which corresponds to 3.5% drift.

Figures 4.35 and 4.36 show post-test damage to the columns. The RC specimen had cracks all over the column height on the south and east sides. Note the width of the cracks from the bottom through the mid-height because the specimen tilted severely to the northwest direction. A region where the spalling of cover concrete occurred extended to a height of 406 mm (16 in.). No major damage such as buckling or fracture of reinforcement or crushing of core concrete was observed even though the specimen was subjected to extreme ground excitation that resulted in large residual displacement.

A comparison of the observed damage of the PRC specimen versus the RC specimen shows that the PRC specimen had fewer cracks, which were limited to below the mid-height of the column. Spalling of the cover concrete occurred at the northwest surface; the region where the spalling occurred was similar in both specimens. No major damage such as buckling or fracture of reinforcement or crushing of core concrete was visible. According to the estimated natural period determined later, it is assumed that a few of longitudinal reinforcing bars fractured during the maximum-level test. The fracture could be the result of using smaller reinforcing bars.

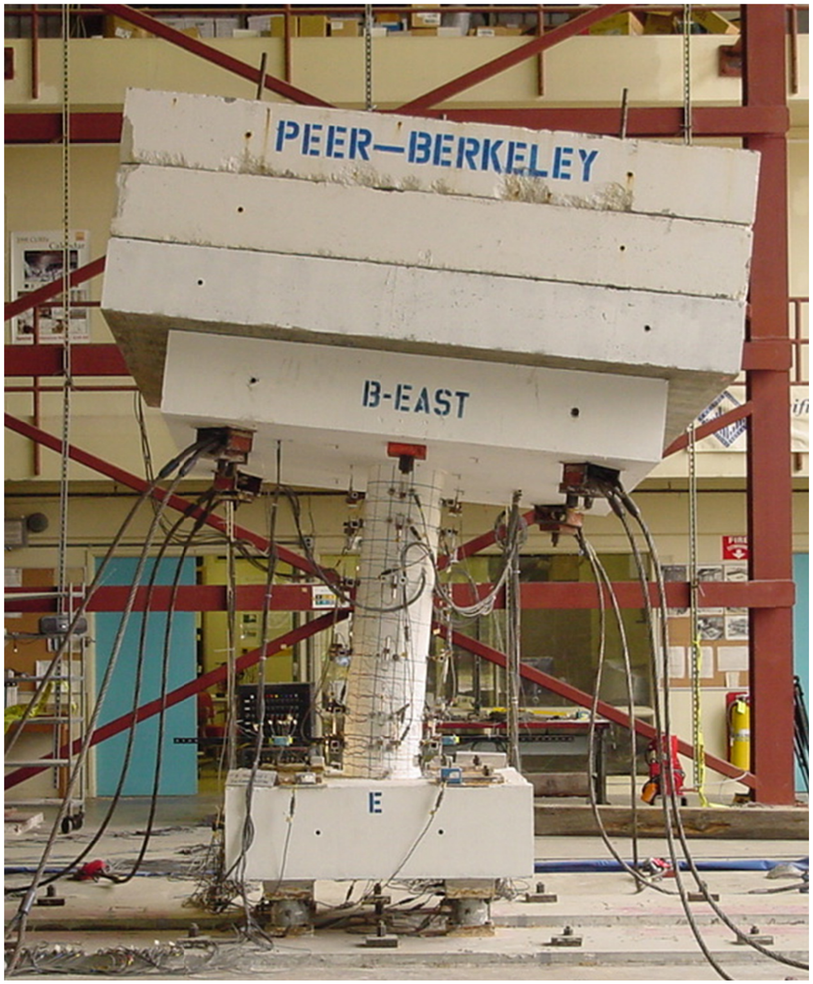

(a)

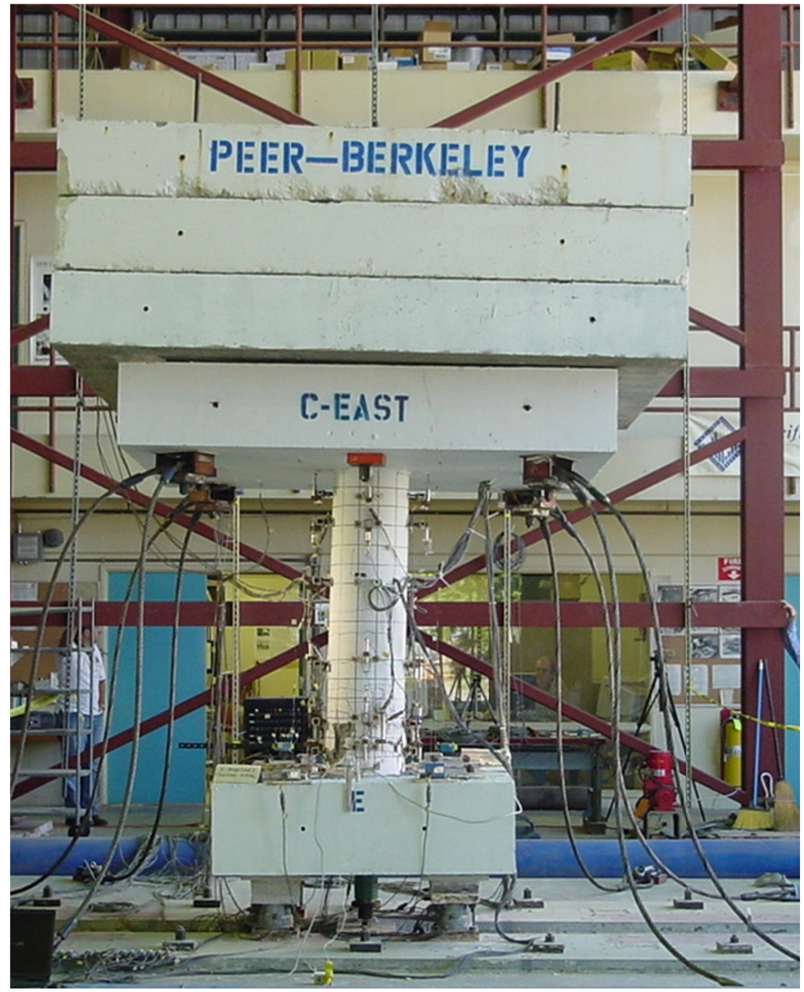

(b)

Figure 4.34(a) Specimens after the maximum-level test from the east side: (a) RC specimen and (b) PRC specimen.

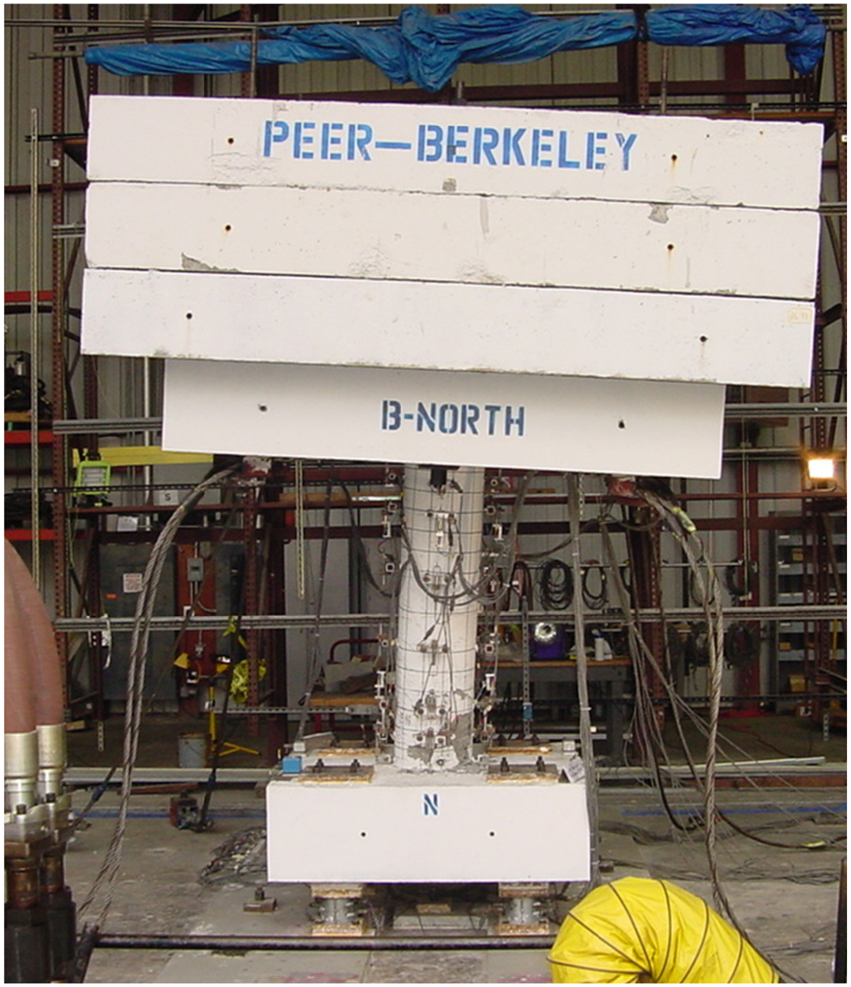

(a)

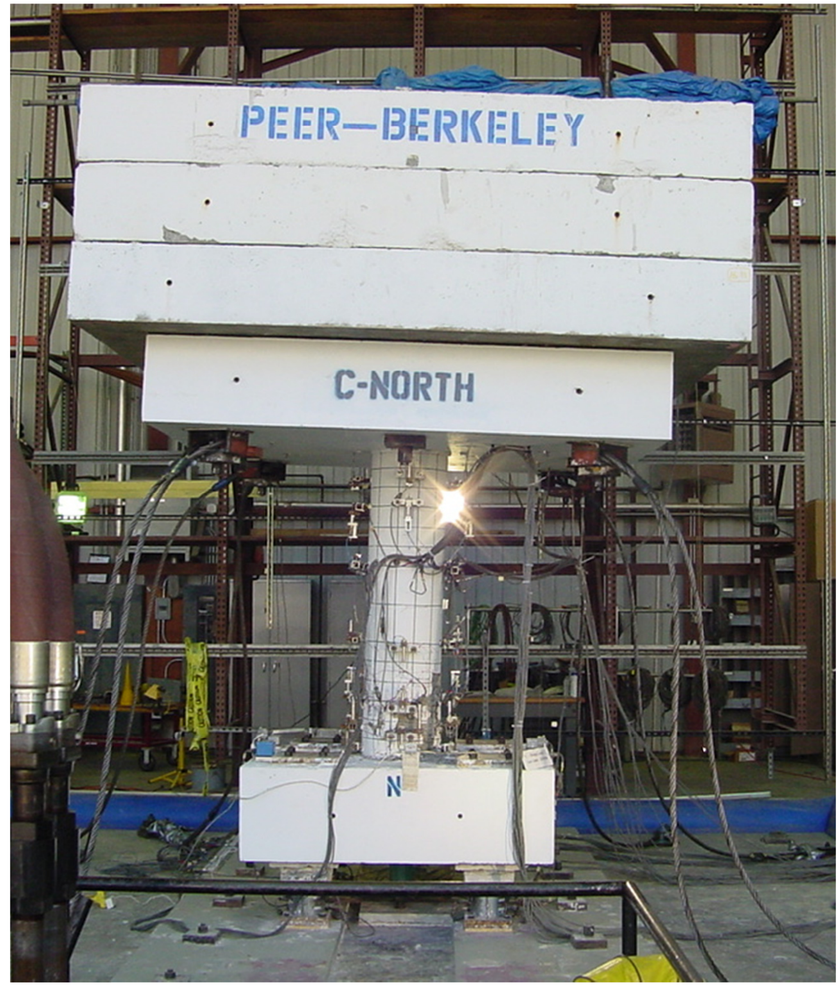

(b)

Figure 4.34(b) Specimens after the maximum-level test from the north side: (a) RC specimen and (b) PRC specimen.

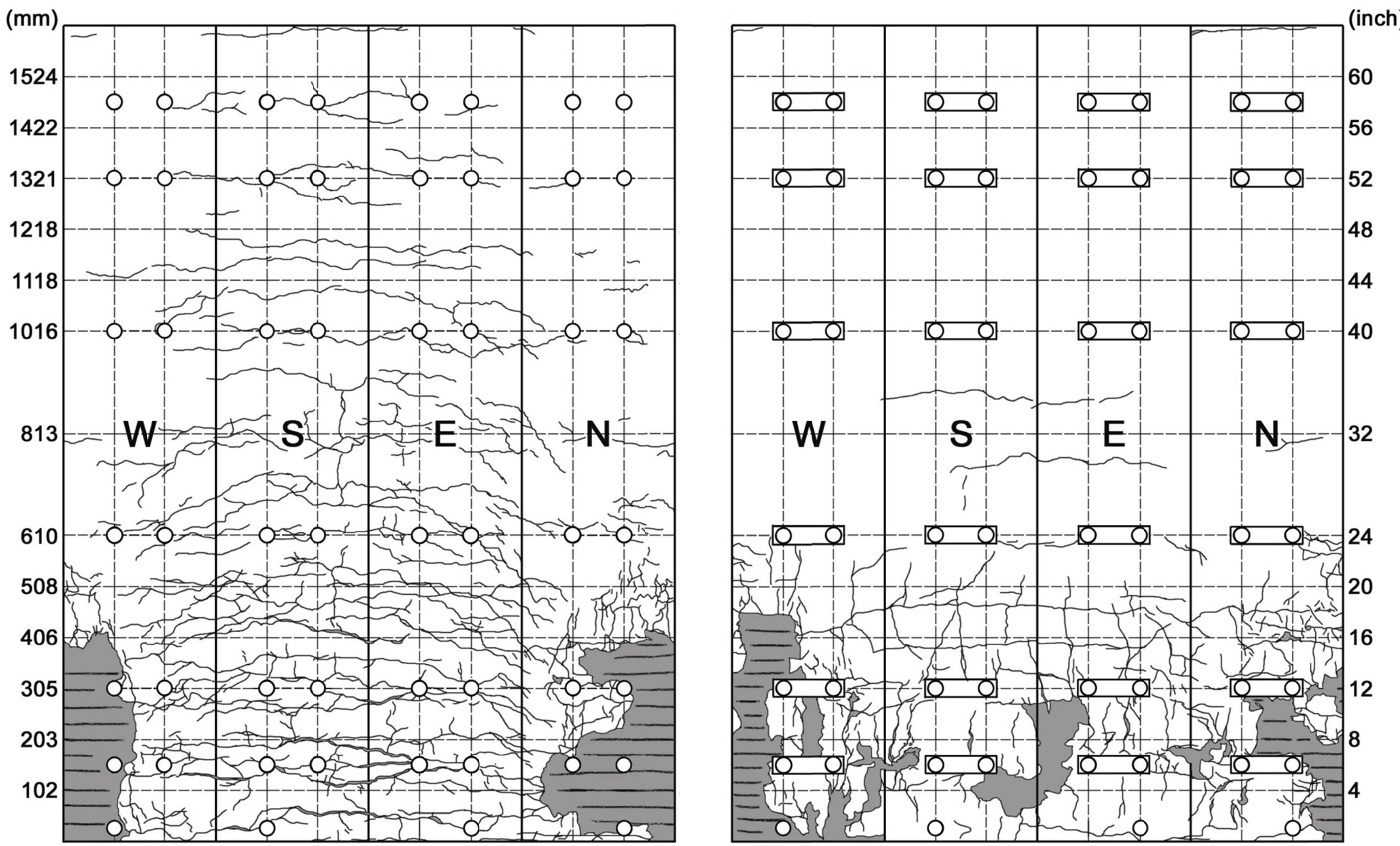

(a)

(b)

Figure 4.35 Damage of columns after the maximum-level test: (a) RC specimen and (b) PRC specimen.

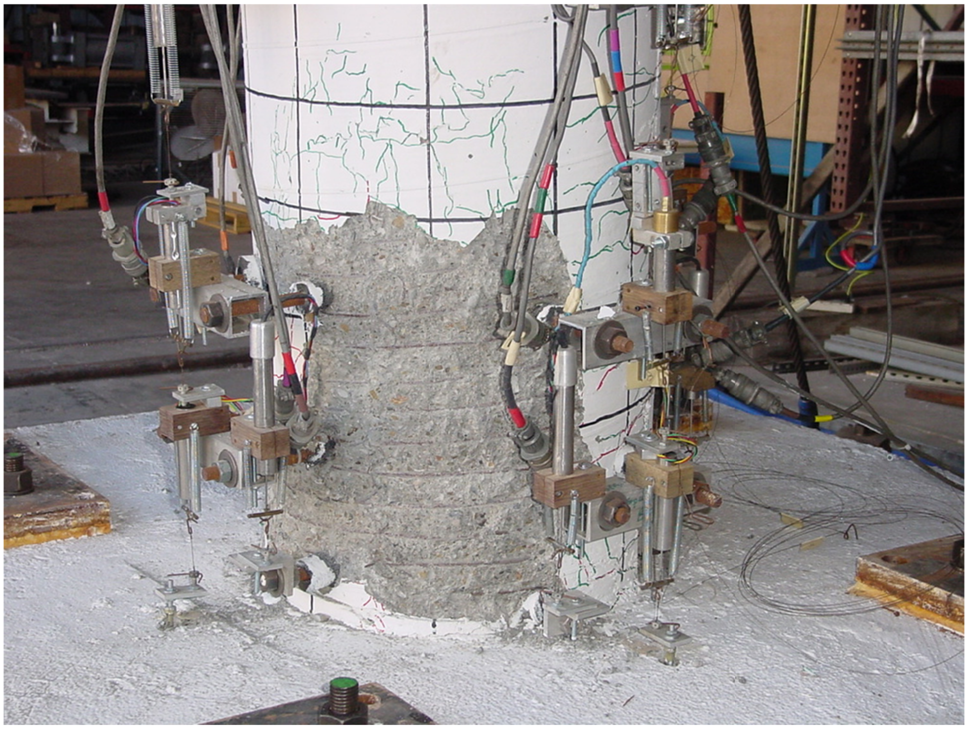

(a)

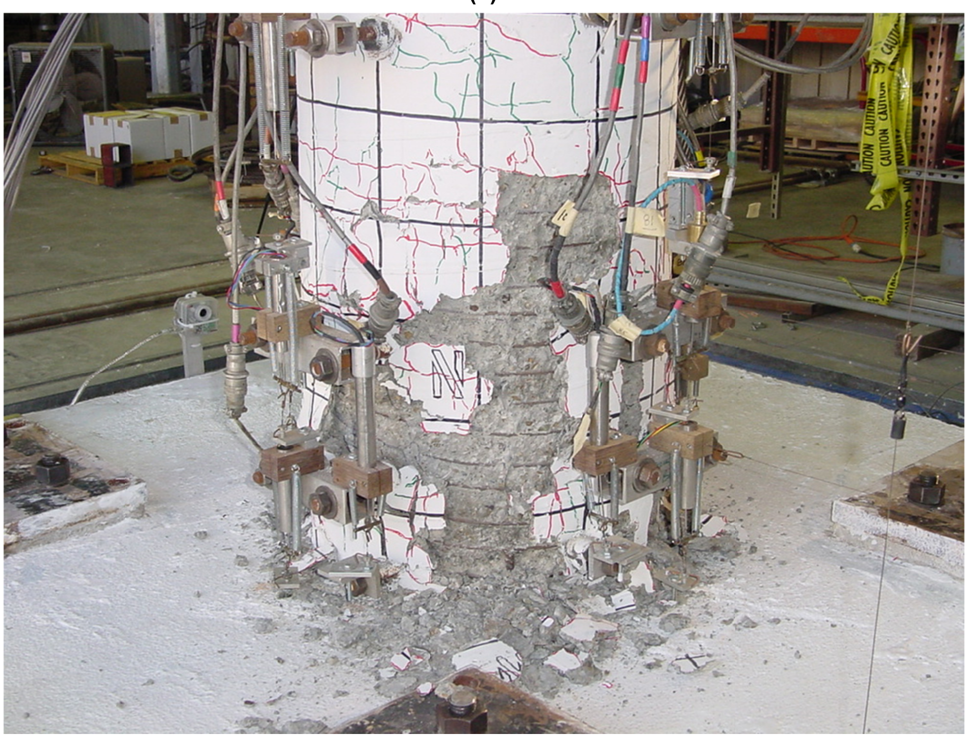

(b)

Figure 4.36 Local damage at plastic-hinge region after the maximum-level test: (a) RC specimen NW corner; and (b) PRC specimen NW corner.

4.5.1.2 Acceleration Response

Figure 4.37 shows the input signals and global response of the specimens during the maximum-level test. As mentioned in Section 4.2, during the tests the shaking table reproduced the input signals at a sufficient level of accuracy for both specimens.

Before the test, the specimens had different fundamental natural periods: 1.14 sec and 0.76 sec for the RC and PRC specimens, respectively. Despite this factor, the acceleration response of the specimens was similar during main pulse up to about 5 sec. The response accelerations of the specimens were evidence of the offsets, and the accelerometers showed acceleration of gravity due to tilting of the specimens.

Both specimens exhibited the maximum response acceleration at the center-of-gravity of the top blocks in the positive direction at 3 sec during the first strong pulse of the signals. The maximum accelerations occurred in the *X*-directions for both specimens: 2.96 m/sec^2 (0.3g) and 2.66 m/sec^2 (0.27 g) for the RC and PRC specimens, respectively. The maximum accelerations in the *Y*-direction occurred at 3.6 sec for both specimens.

The damping properties and natural periods of the specimens were investigated using the free-vibration portion of the acceleration response. The natural period of the RC specimen did not change from 1.14 sec in the *X*-direction during the test, and the damping ratio was 2.7% at the end of the test (see Table 4.1 and Figure 4.3). The natural period and the damping ratio decreased slightly in the *Y*-direction. Based on these observations, it is assumed that the RC specimen did not suffer any severe damage inside the column.

Despite no visible damage, it is assumed a few of the longitudinal reinforcing bars in the PRC specimen fractured as a result of the test because the natural period of the specimen was significantly elongated from 0.76 to 1.37 sec and 1.02 to 1.28 sec in the *X*- and *Y*-directions, respectively. The damping ratios of the PRC specimen were evaluated to be about 4.3% for both directions.

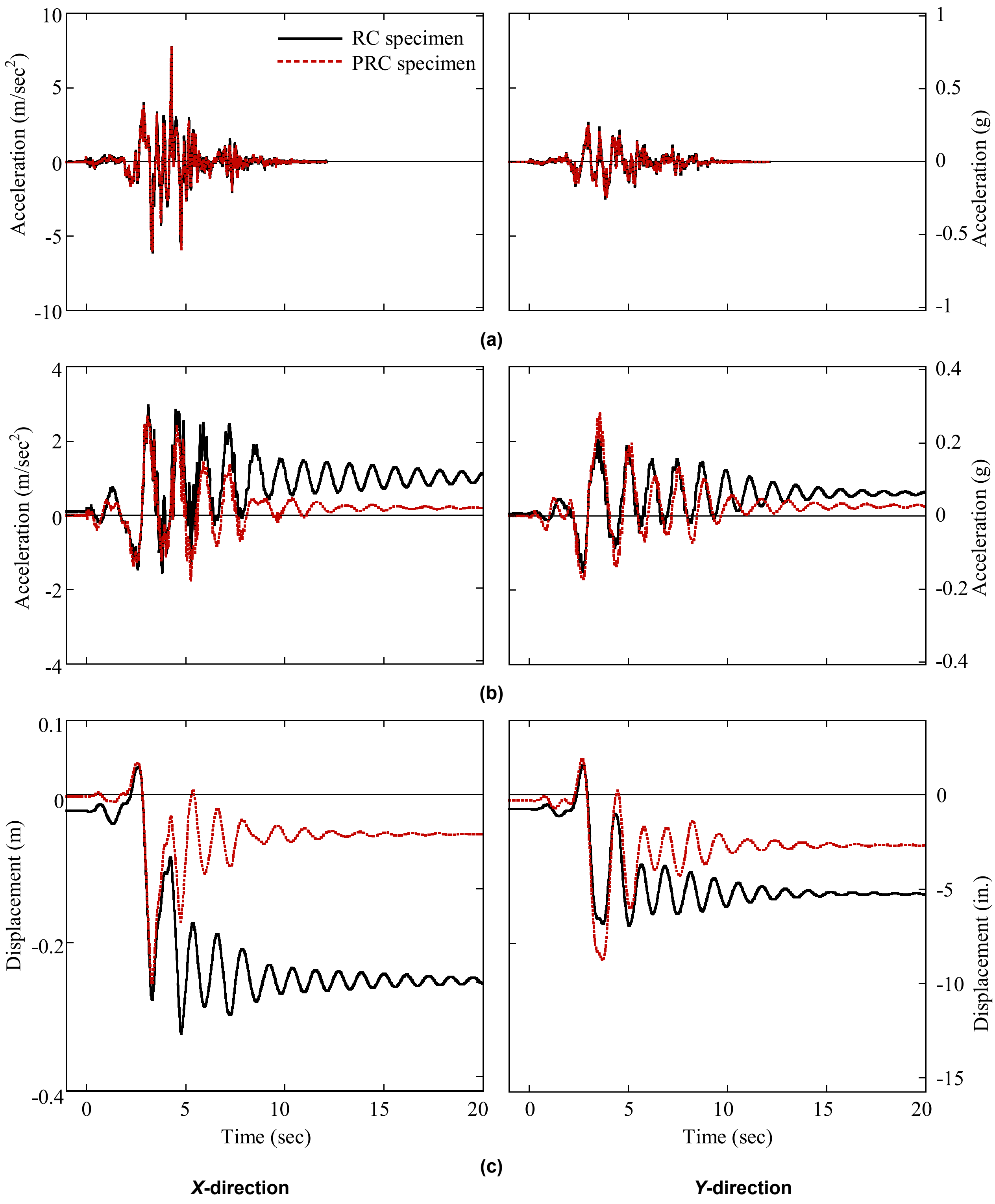

Figure 4.37 **Global response of specimens for the maximum-level test: (a) input signals (acceleration recorded at footing; (b) acceleration response at center-of-gravity of top blocks; and (c) displacement response at center-of-gravity of top blocks.**

4.5.1.3 Displacement Response

Both specimens had a similar peak response of about -0.25 m (-10 in.) at 3.4 sec [as shown in Figure 4.37(c)], even though the RC specimen had an offset of -0.025 m (-0.97 in.) and the PRC specimen exhibited no offset; this was the maximum response displacement of the PRC specimen. In the *Y*-direction, the PRC specimen had 30% larger response at 3.8 sec.

The response displacement in the *X*-direction of the PRC specimen decreased down to -0.029 m (-1.1 in.), while that of the RC specimen decreased to only -0.086 m (-3.4 in.). The RC specimen had a maximum response of -0.32 m (-12 in.) at 4.8 sec. The significant discrepancy in response between these two specimens resulted in the RC specimen showing a large offset, while the PRC specimen had a relatively small offset. The residual displacements in the *X*-direction are -0.252 m (-9.9 in.) and -0.053 m (-2.1 in.) for the RC and PRC specimens, respectively.

Figure 4.38 shows magnitude and orbits of response displacements at the center-of-gravity of the top blocks. The specimens responded mostly in the northwest-southeast direction. Magnitudes of the maximum displacements were 0.349 m (13.7 in.) and 0.323 m (12.7 in.) for the RC and PRC specimens, respectively. The response ductility and drift were computed to be 13.4 and 14.3% for the RC specimen and 12.4 and 13.2% for the PRC specimen. Magnitudes of the residual displacements were 0.285 m (11.2 in.) and 0.107 m (4.2 in.) for the RC and PRC specimens, respectively. The ductility and drift of the residual displacements were 10.9 and 11.7%, and 4.1 and 4.4% for the RC and PRC specimens, respectively.

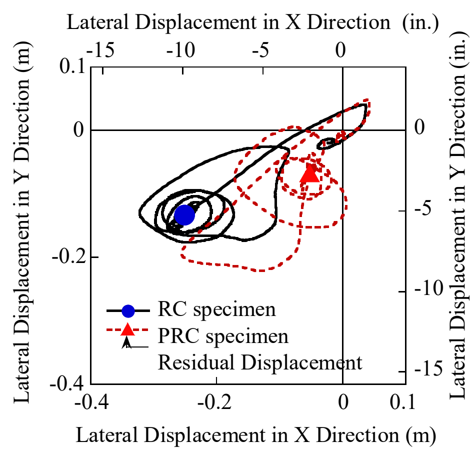

(a)

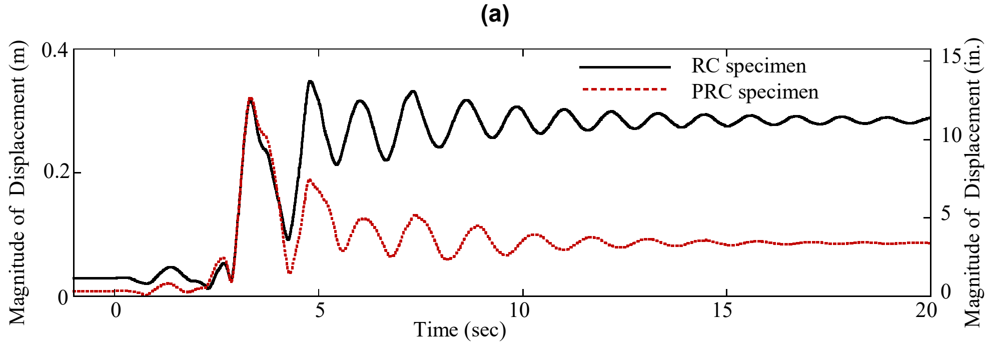

(b)

Figure 4.38 Response displacement for the maximum-level test: (a) orbit and (b) magnitude.

4.5.1.4 Lateral Force-Lateral Displacement Hysteresis

Figure 4.39 shows lateral force versus lateral displacement hysteresis at the center-of-gravity of the top blocks, and Figure 4.40 shows inertia force versus lateral displacement hysteresis. As seen in the responses during the design-level tests, both specimens had similar unloading curves and skeleton curves. The hysteresis computed from inertia force show similar trends to that seen during the design-level tests.

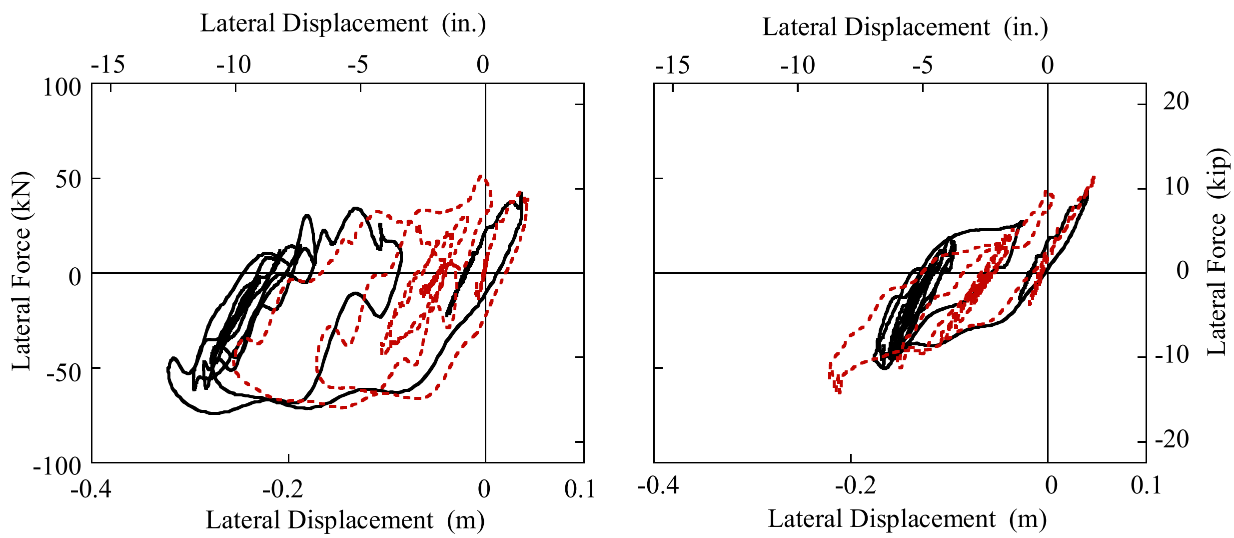

(a)

***X*-direction** ***Y*-direction**

Figure 4.39 Lateral force–lateral displacement hysteresis for the maximum-level test.

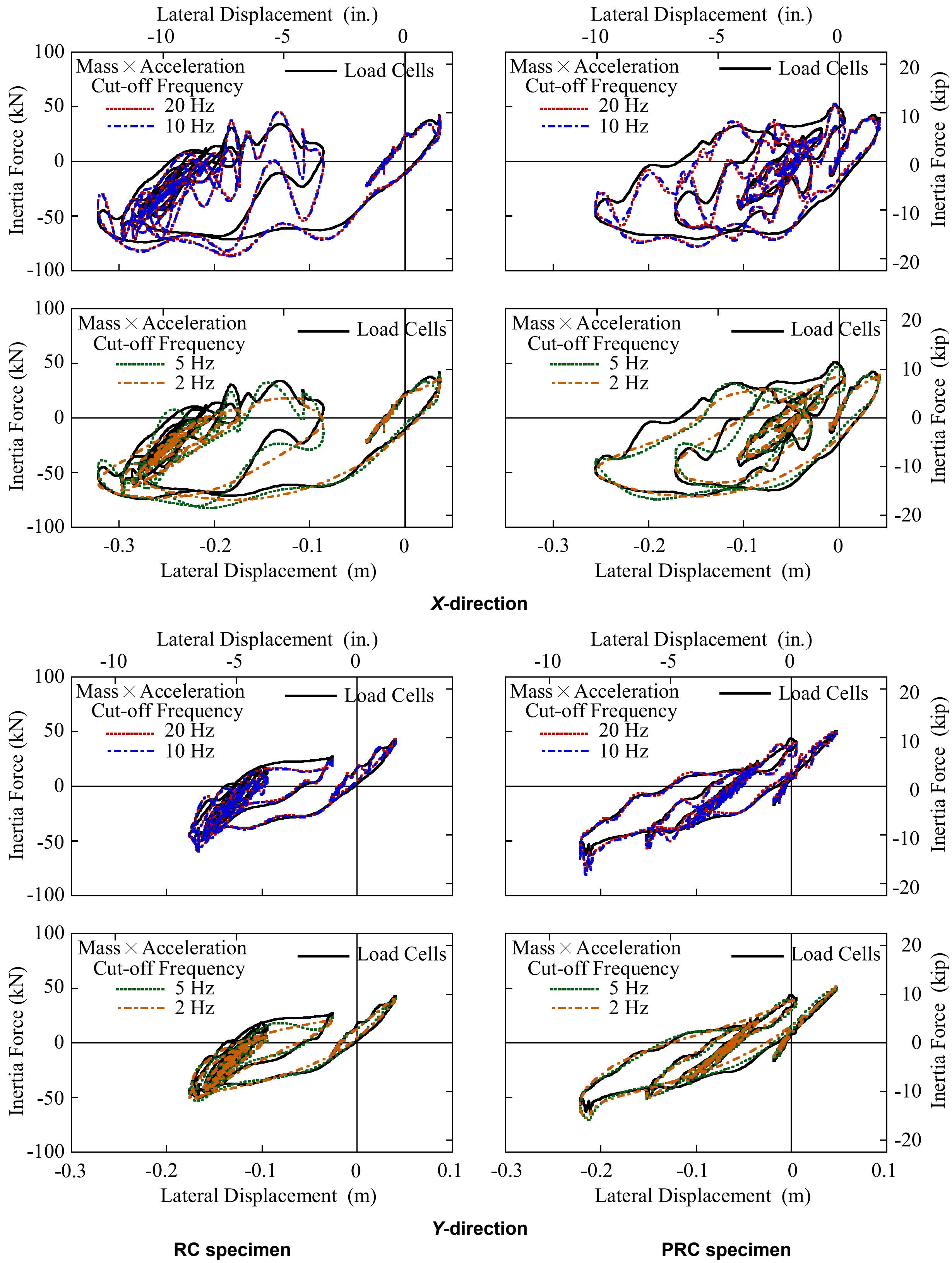

Figure 4.40 Inertia force–lateral displacement hysteresis for the maximum-level tests.

4.5.1.5 Global Response during Main Pulses

Figure 4.41 shows the response displacement time histories and orbits at the center-of-gravity of the top blocks and force versus displacement hysteresis from 2.5 to 6 sec during the main pulses. Eight points are marked in the figures; at Point A, the specimens reached the first peaks in the positive *X*-direction. Point B shows the negative peaks during the first pulse; the forces decreased to zero at Point C. Point D shows the response displacements at the smallest displacement in the subsequent response. The displacements reached the second peaks at Point E; the forces decreased to zero at Point F. The displacements reached zero for the PRC specimen and a peak for the RC specimen at Point G.

Both specimens showed similar response from Points A to C in the *X*-direction, including the unloading curves. Although the loading curves from Points A to B are similar in the *Y*-direction, the PRC specimen had smaller tangential stiffness in the unloading curve from Point C, thus showing the effect of incorporating the unbonded prestressing tendon. Even though the PRC specimen had a slightly larger response displacement at Point C, the force reached zero at almost the same displacement on the unloading path. The orbit of the PRC specimen shows an origin-oriented path from Point C, proving that the specimen had an origin-oriented hysteresis when the displacement vector directs to the origin. Because the displacement vector of the PRC specimen does not show origin-oriented loop, the PRC specimen does not show origin-oriented tendency between 4.4 and 6 sec.

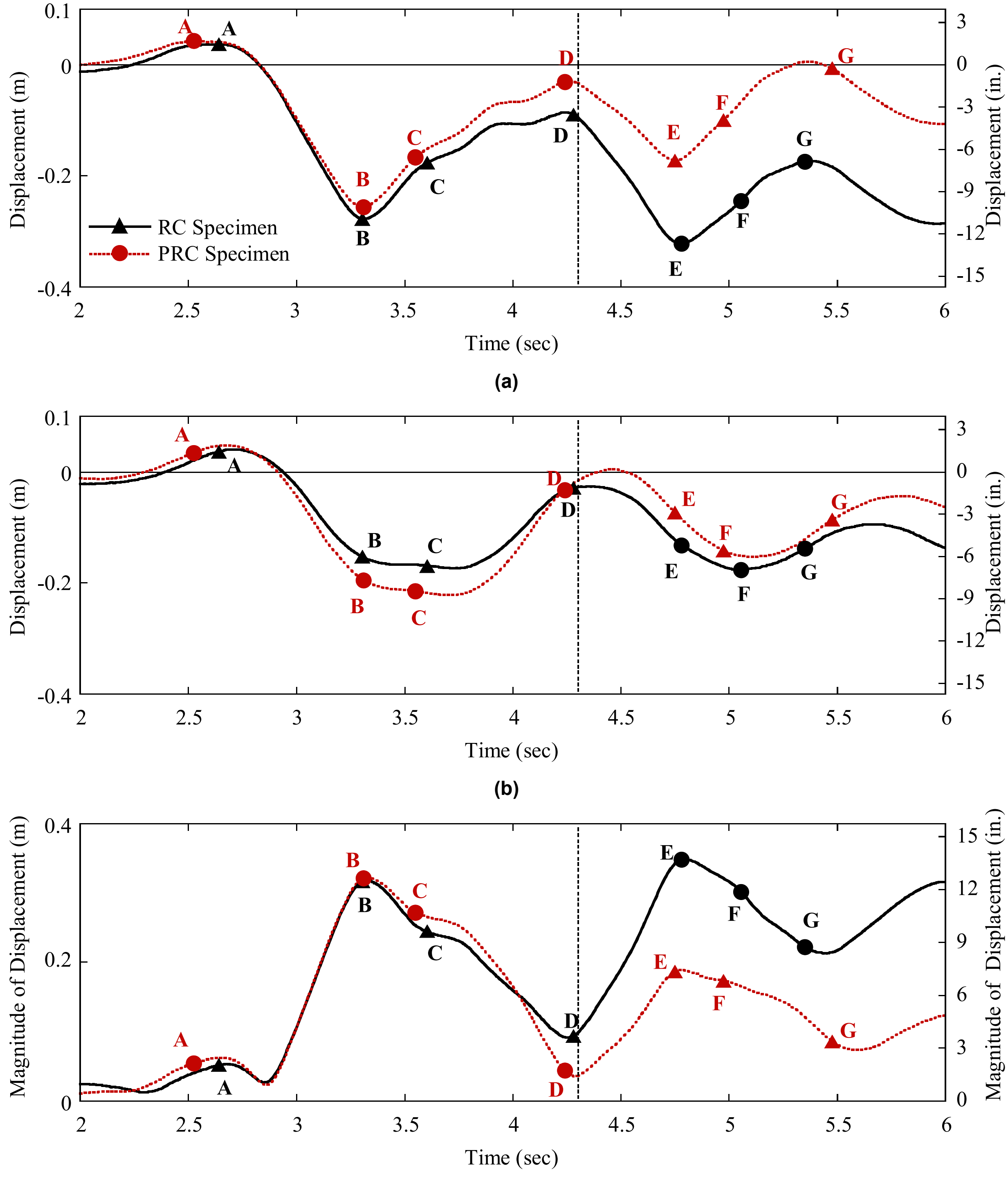

Figure 4.41(a) Response displacement of specimens during the main pulses for the maximum-level test: (a) *X*-direction; (b) *Y*-direction; and (c) magnitude.

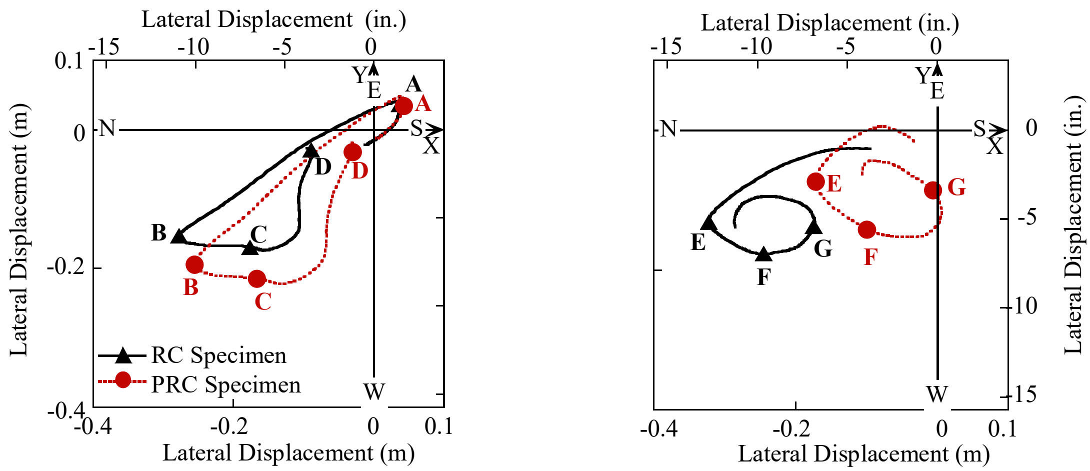

Figure 4.41(b) Orbit of response displacement of specimens during the main pulses for the maximum-level test.

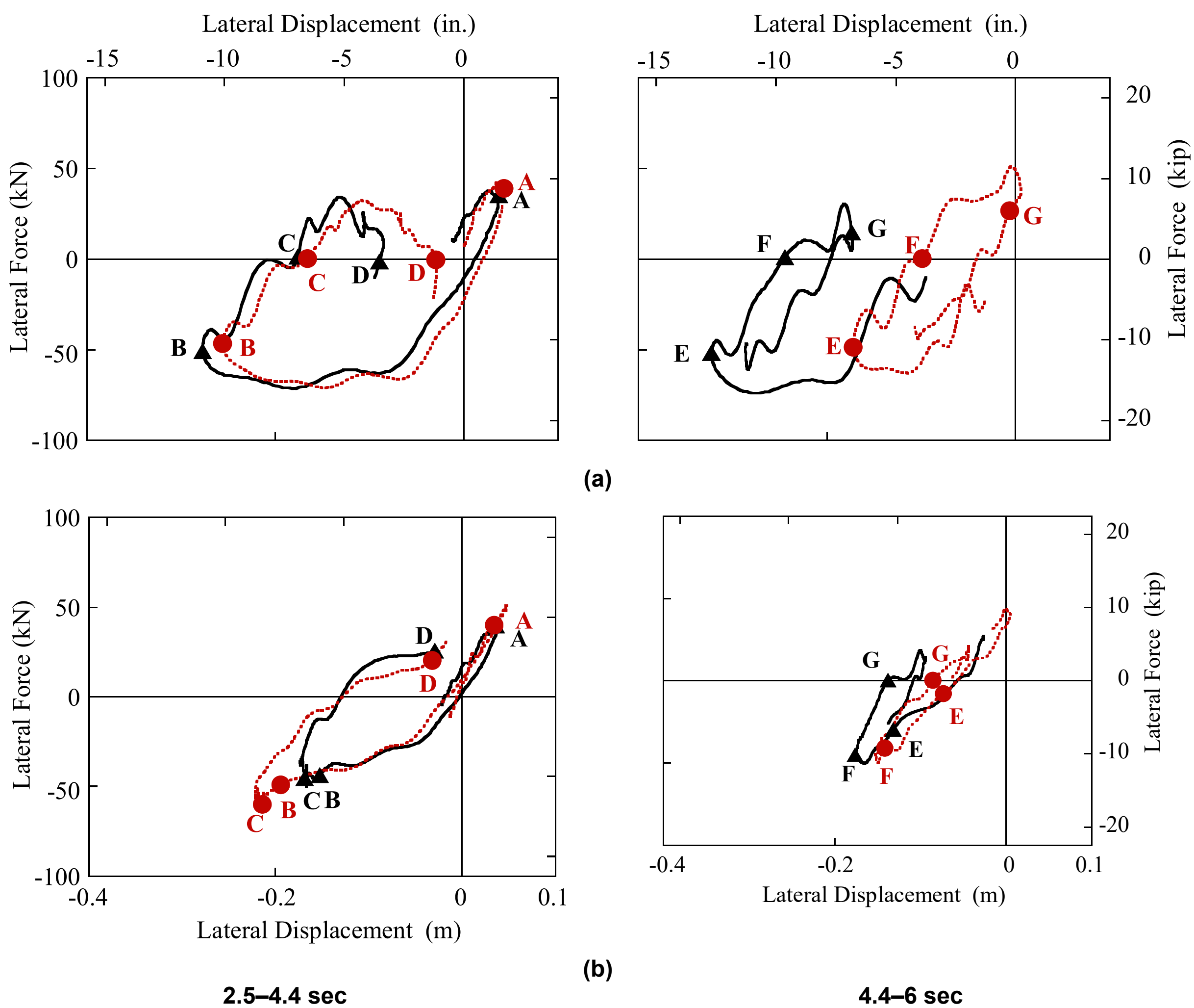

Figure 4.41(c) Lateral force–lateral displacements of specimens during the main pulses for the maximum-level test.

4.5.1.6 Global Response in 45°-Rotated Coordinate System

Figure 4.42 shows response of the specimens in a 45° rotated coordinate system. The maximum displacements were 0.325 m (12.8 in.) and 0.321 m (12.6 in.) in the northwest direction for the RC and PRC specimens, respectively. Figure 4.43 shows details of the response during the main pulses in this coordinate system. Again, the PRC specimen shows an origin-oriented hysteresis when the displacement vector is directed to the origin or near the origin point.

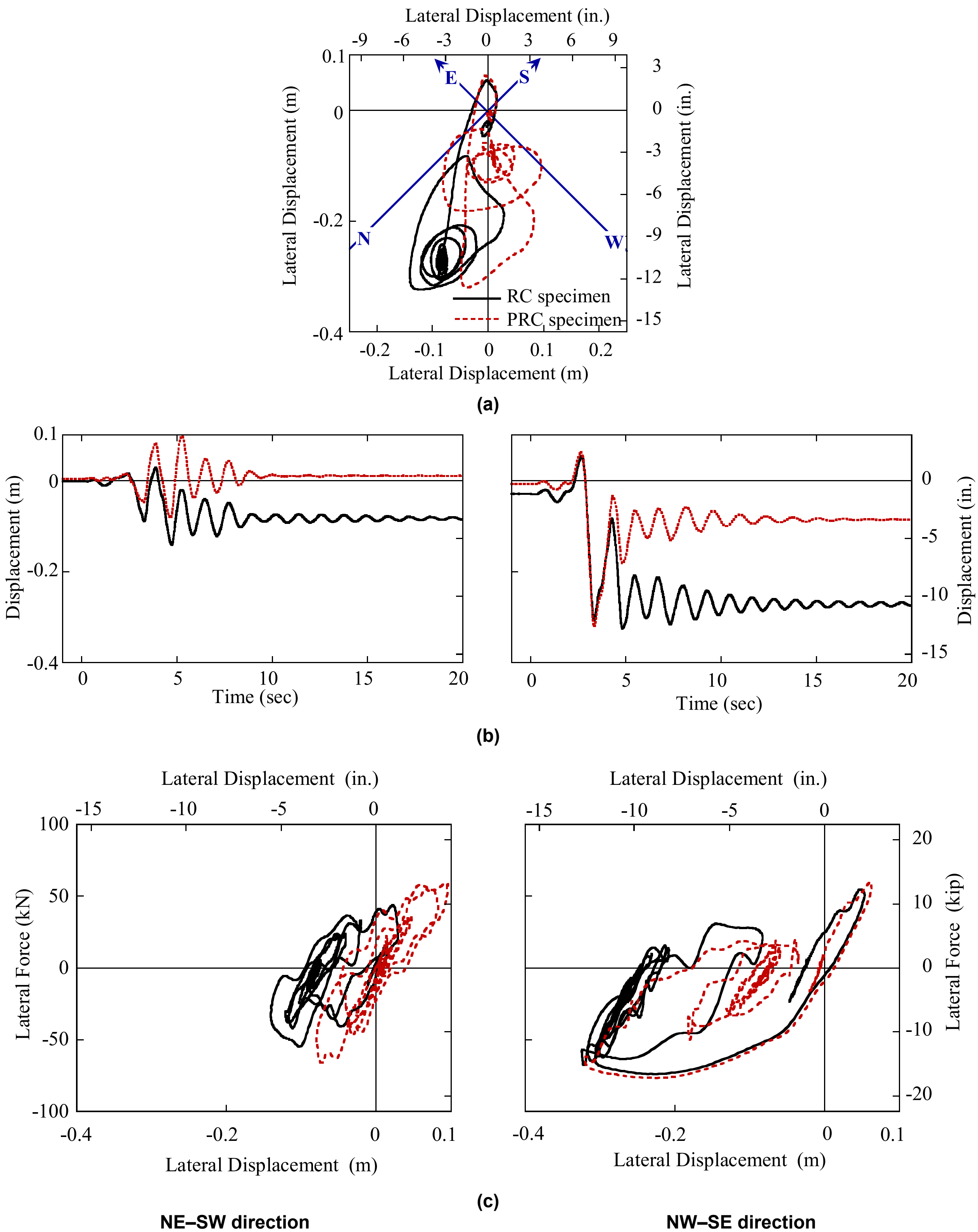

Figure 4.42 **Response in 45° rotated coordinate system for the maximum-level test: (a) orbit of response displacement; (b) displacement response at center-of-gravity; (c) lateral force–lateral displacement hysteresis.**

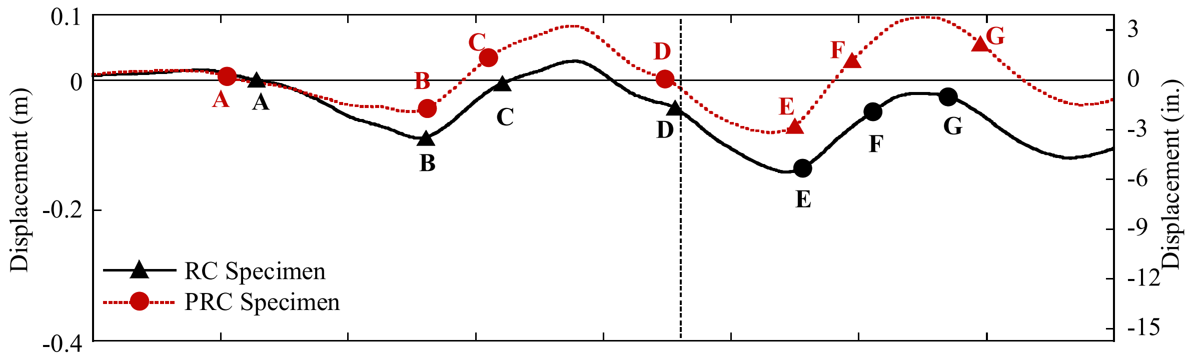

(a)

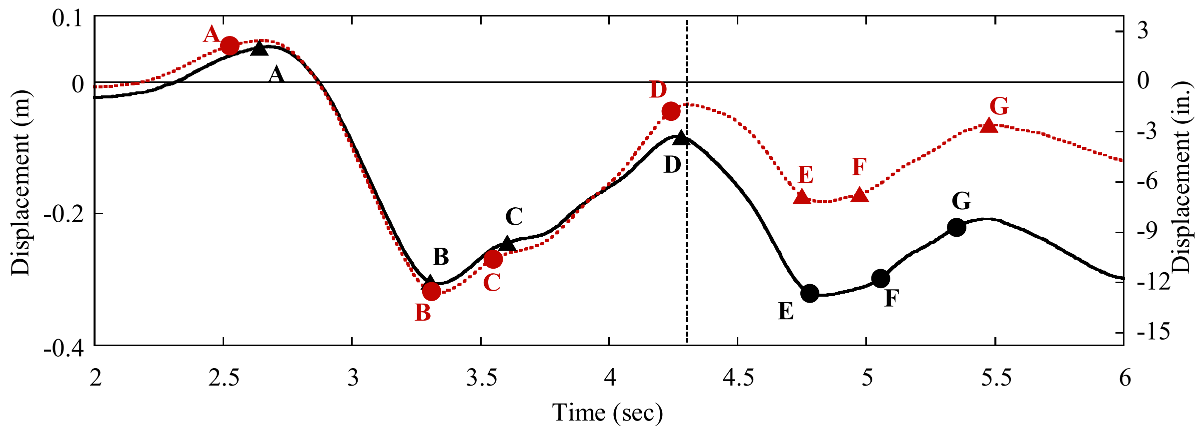

(b)

Figure 4.43(a) Response displacement during main pulses in rotated coordinate system for the maximum-level test: (a) NE–SW direction and (b) NE–SE direction.

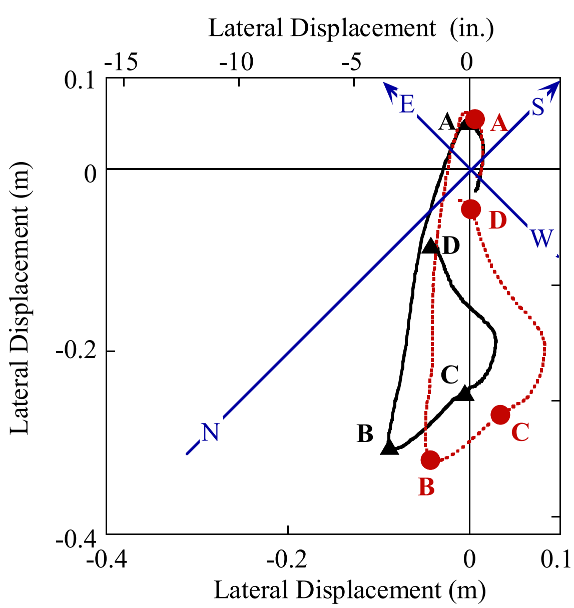

2.5–4.4 sec

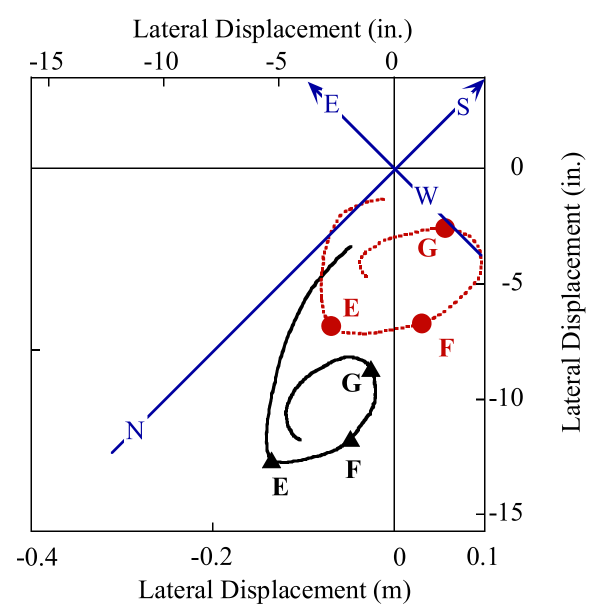

4.4–6 sec

Figure 4.43(b) Orbit of response displacement during main pulses in rotated coordinate system for the maximum-level test.

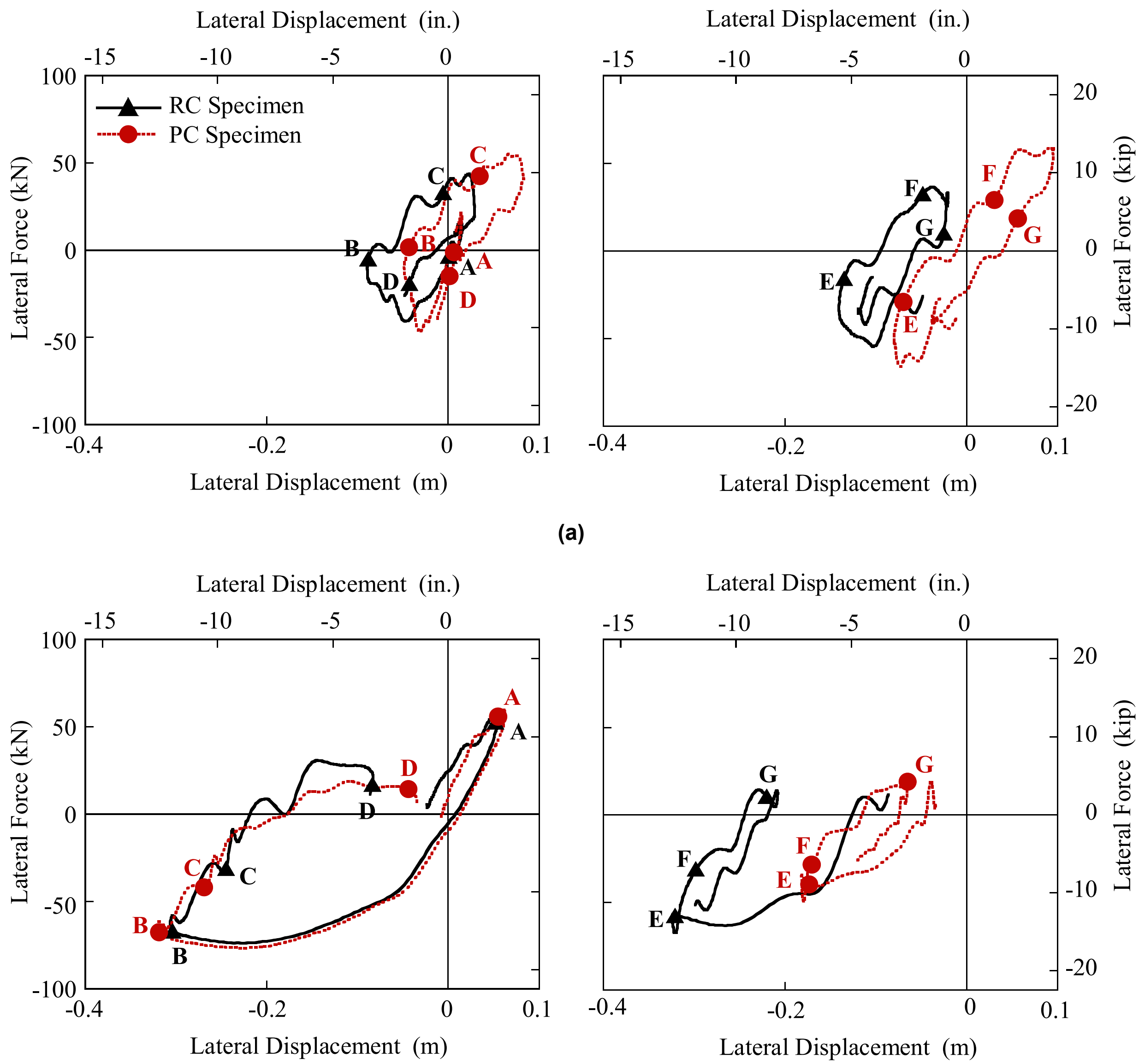

(b)

2.5–4.4 sec **4.4–6 sec**

Figure 4.43(c) Lateral force–lateral displacement hysteresis for the maximum-level test: (a) NE–SW direction and (b) NE–SE direction.

4.5.2 Local Response

4.5.2.1 Behavior of Tendon

Figure 4.44 shows the behavior of the tendon installed in the PRC specimen during the maximum-level test. Because the gauges placed around the top of the column did not measure strain during the test, only the measurements of the bottom gauges are shown here. The strain exceeded 0.004 at 4.8 sec.

The prestressing force increased up to 675 kN (152 kips) as the specimen deformed, and decreased by 6% [to 320 kN (72 kips)] during the test. As shown in Figure 4.44(c), the tendon force reached the maximum during the first pulse and decreased when the specimen returned to near its origin point. Figure 4.45 shows the stress–strain hysteresis of the tendon during the maximum-level test compared with the hysteresis obtained from the material test described in Section 2.4.3. The tendon remained in the elastic range during the test. The maximum stress was 72% of the ultimate strength of the tendon. Figure 4.46 shows the flexural strain of the tendon. The amplitude of flexural strain increased up to 0.00066, but was still smaller than 20% of the axial strain described above.

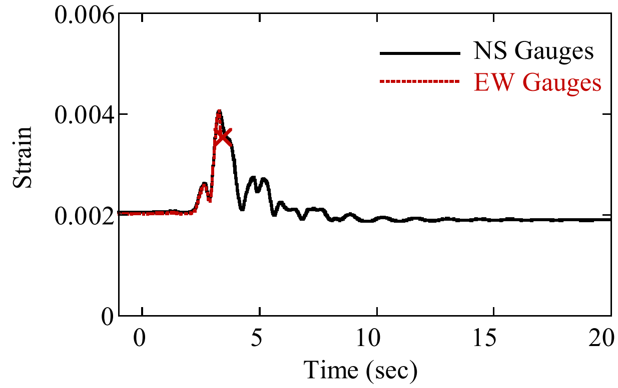

(a)

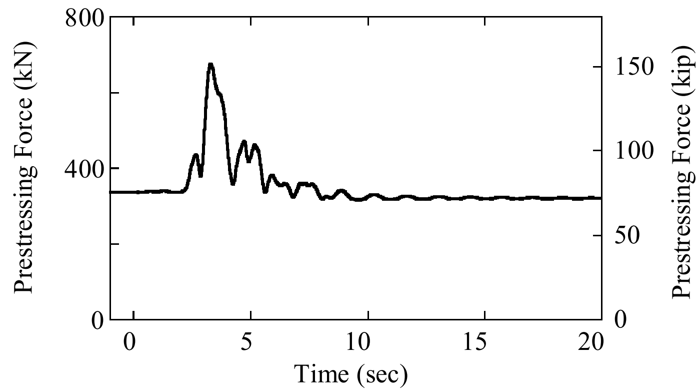

(b)

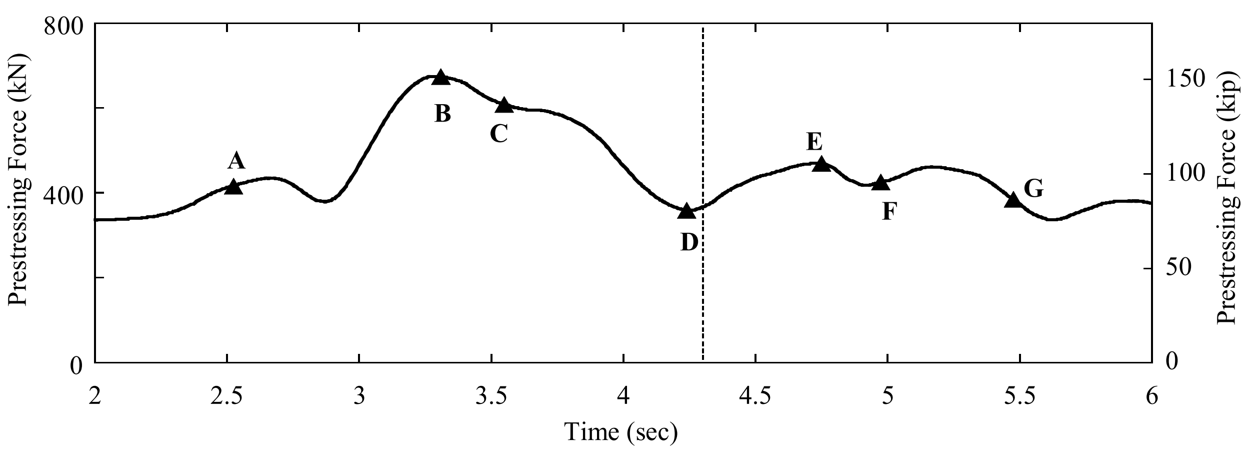

(c)

Figure 4.44 Behavior of tendon during the maximum-level test: (a) axial strain (gauges at bottom of column); (b) prestressing force; and (c) variation of prestressing force during main pulses.

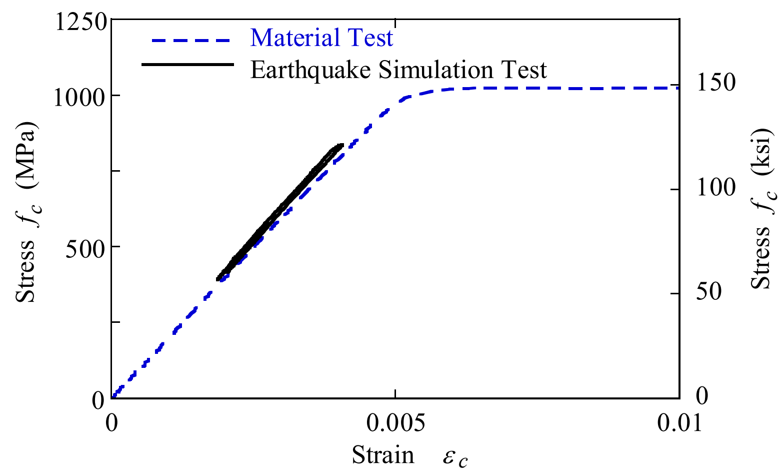

Figure 4.45 Stress–strain hysteresis of tendon during the maximum-level test.

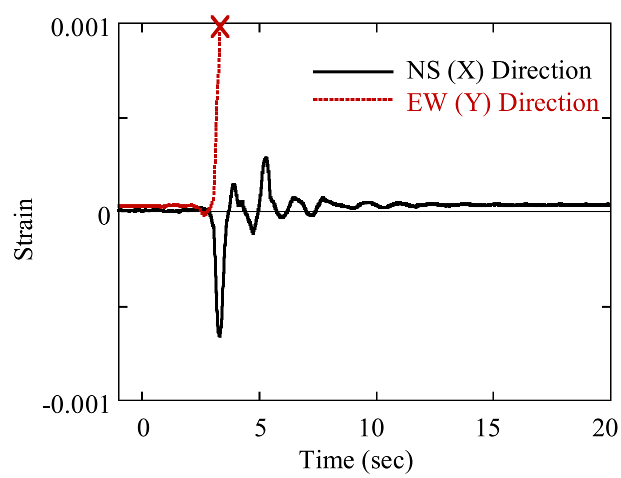

Figure 4.46 Flexural strain of tendon during the maximum-level test.

4.5.2.2 Strain of Reinforcement

No data was obtained during the maximum-level tests because almost all the gauges were damaged.

4.5.2.3 Curvature of Column

Figure 4.47 shows curvature time histories computed from measurements of the DCDTs, and Figure 4.48 shows moment versus curvature hysteresis of the columns. Figure 4.49 shows curvature distributions along the column at several peaks and at the end of the test. The effect of pullout of reinforcement from the footing is not shown in the figures and will be discussed later. Regions where nonlinear deformation mainly occurred around the bottom of the column were between heights of 51 mm (2 in.) and 457 mm (18 in.) for both specimens, which match those areas where the damage is most visible.

Residual curvature mostly occurred below a height of 457 mm (18 in.) for both specimens. Note, however, that the RC specimen had about a 9 times larger residual curvature at the bottom of the specimen.

Figure 4.50 shows curvature time histories obtained from the DCDTs placed around the bottom of the columns. Measurements by a pair of DCDTs measuring vertical deformation of the columns between heights of 0 and 0.15 m (6 in.) included the effect of strain penetration of reinforcement from the footing, as well as nonlinear deformation of the columns in the plastic hinge region. The curvatures due to strain penetration were evaluated to be about 0.1/m for both specimens.

Figure 4.51 shows accuracy of curvature measurements and the contribution of strain penetration of reinforcement to the lateral displacement at the top. The displacements at the center-of-gravity computed by integration of measured curvature along column height were compared with the displacements directly measured by the linear potentiometers at the same location. The integration of curvature measurements provided good agreements with the directly measured displacement responses, especially in the *X*-direction for the RC specimen and in the *Y*-direction for the PRC specimen. As a whole, the curvature measurement was relatively accurate during the maximum-level test. Contribution of the strain penetration to the response displacement was estimated to be about 15% for the RC specimen and 25% for the PRC specimen.

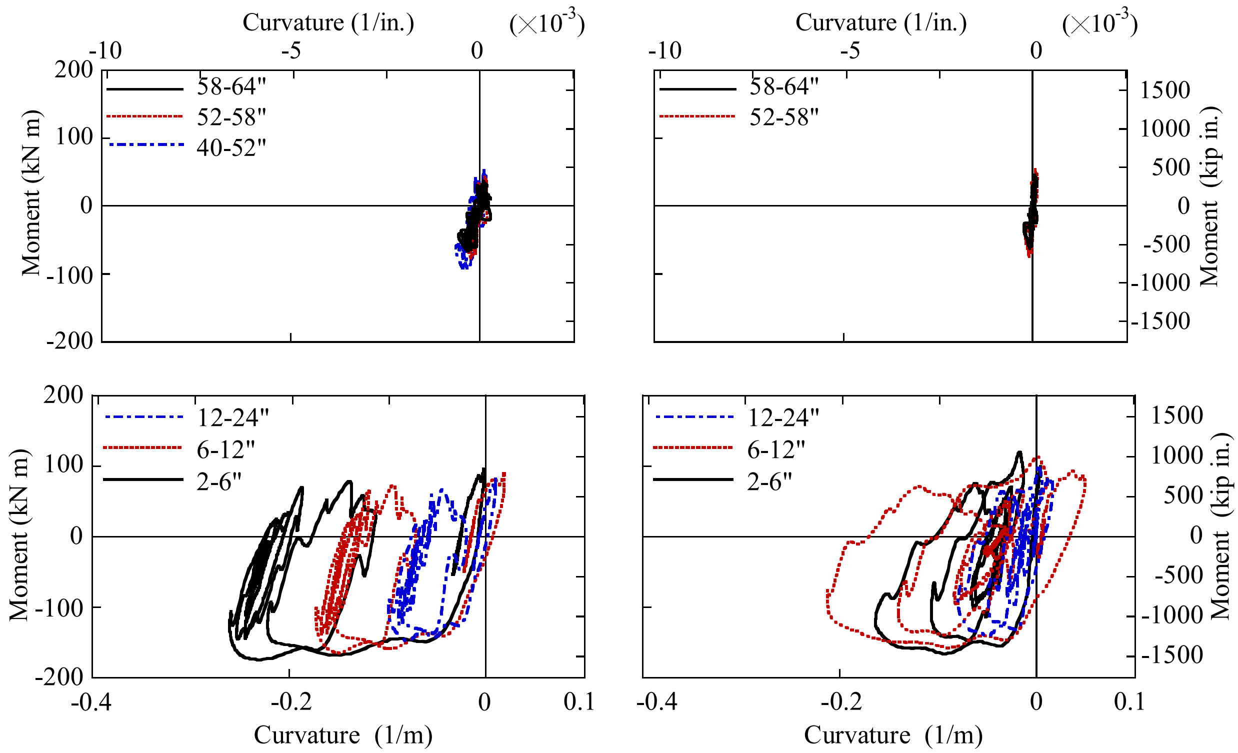

(a)

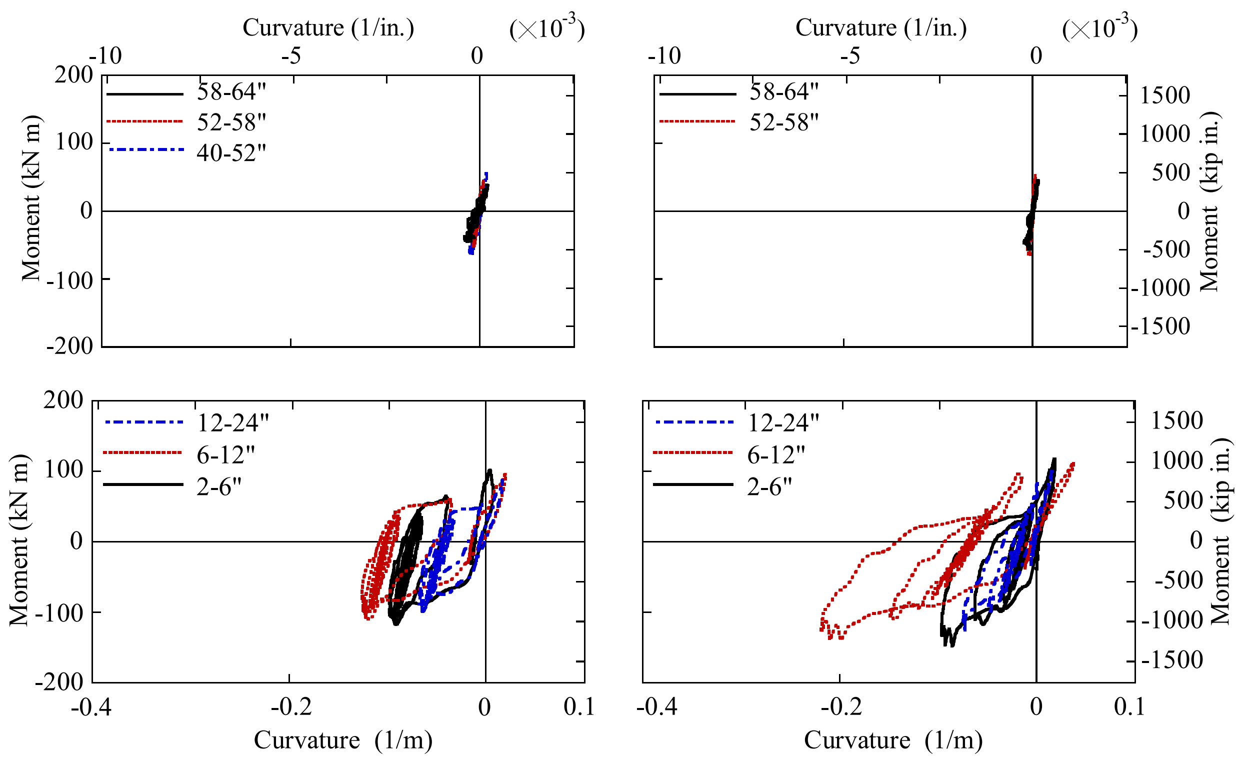

(b)

RC specimen **PRC specimen**

Figure 4.47 Curvature of columns for the maximum-level test: (a) *X*-direction and (b) *Y*-direction.

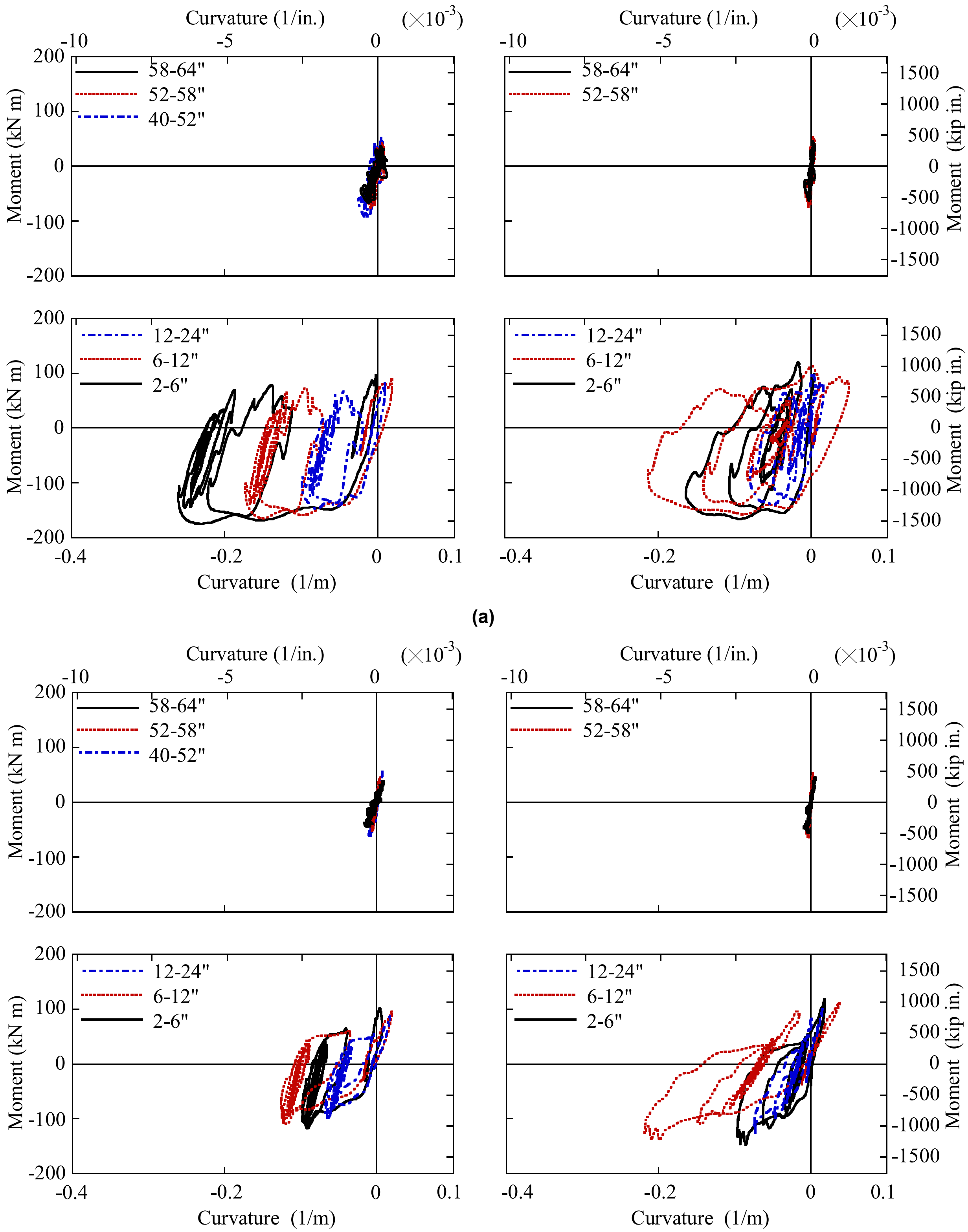

(a)

(b)

RC specimen **PRC specimen**

Figure 4.48 Moment curvature hysteresis for the maximum-level test: : (a) *X*-direction and (b) *Y*-direction.

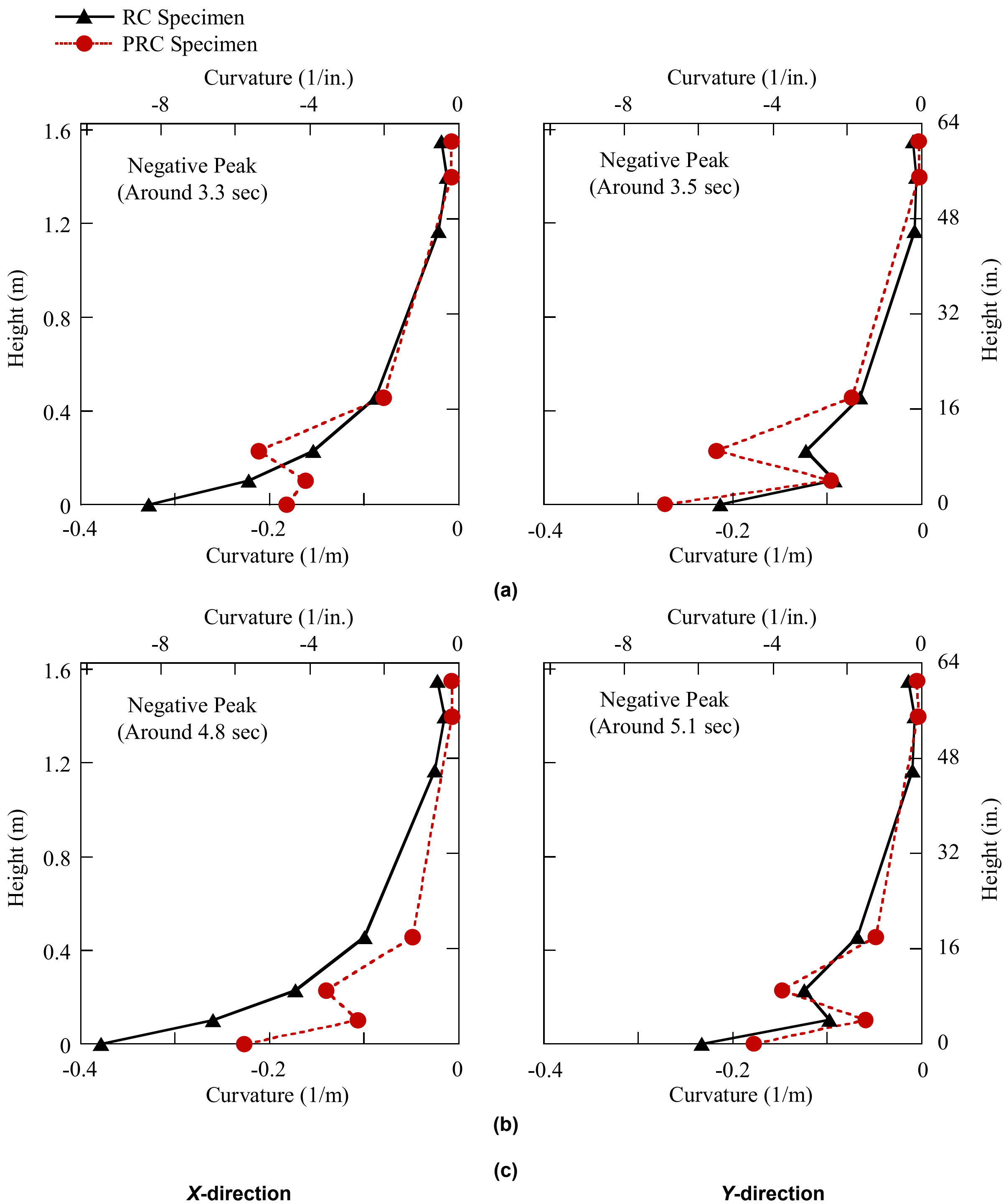

Figure 4.49(a) Curvature distribution along columns for maximum-level test: (a) first peaks and (b) second peaks.

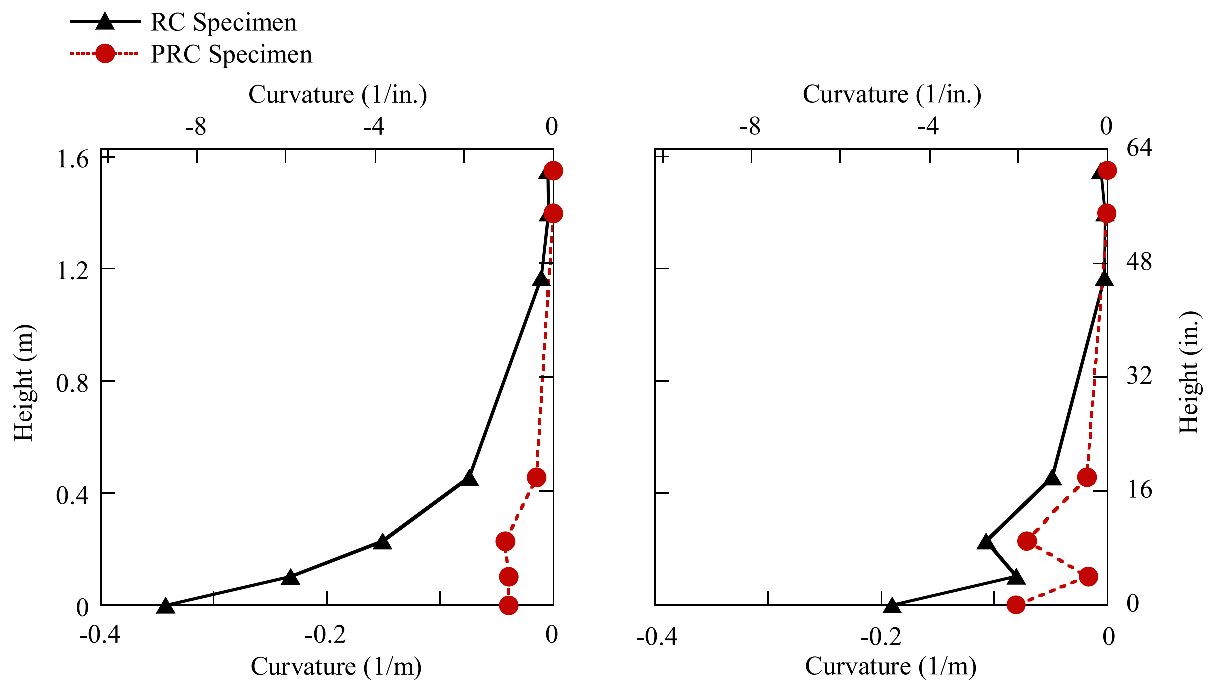

(c)

X-direction | *Y*-direction

Figure 4.49(b) Curvature distribution along columns for maximum-level test: (c) residual curvature.

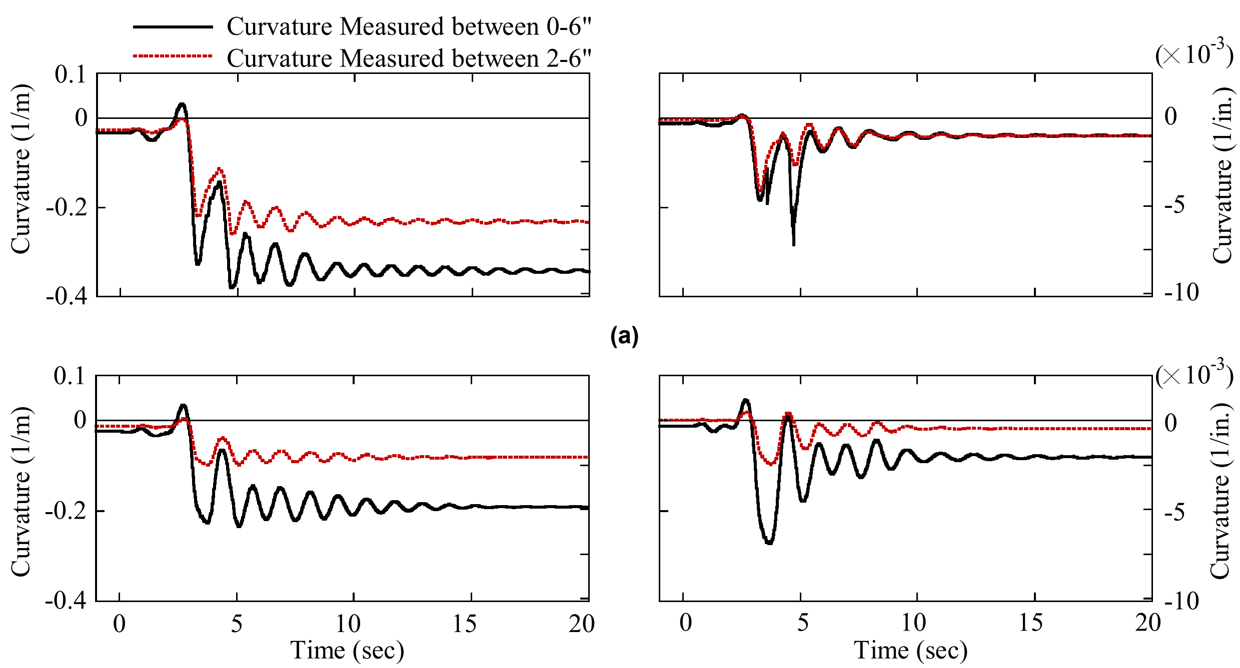

(b)

RC specimen | PRC specimen

Figure 4.50 Curvature due to strain penetration of reinforcement for the maximum-level test: (a) *X*-direction and (b) *Y*-direction.

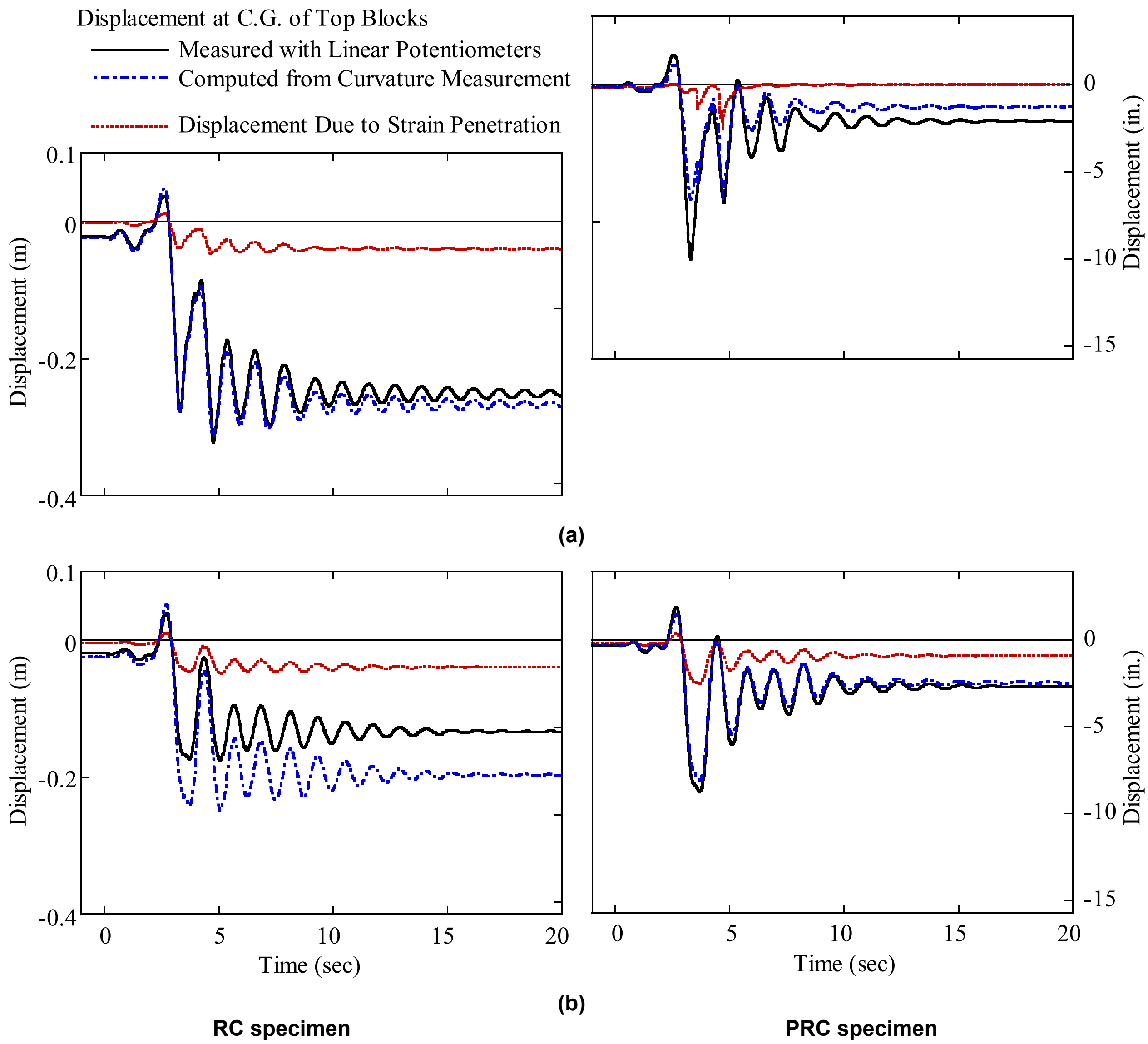

Figure 4.51 **Displacement computer with measured curvature for the maximum-level test: (a) *X*-direction and (b) *Y*-direction**

4.5.2.4 Deformation of Column

Figure 4.52 shows displacement time histories measured at several heights along the columns, and Figure 4.53 shows deformation of the columns at several peaks and residual deformation. The RC and PRC specimens had a similar deformation diagram with almost the same negative peaks at 3.3 sec. Again, the PRC specimen shows no significant effect on the plastic-hinge region. Comparing the deformation diagrams for the residual deformation shows that the PRC specimen obviously had a smaller residual displacement than the RC specimen.

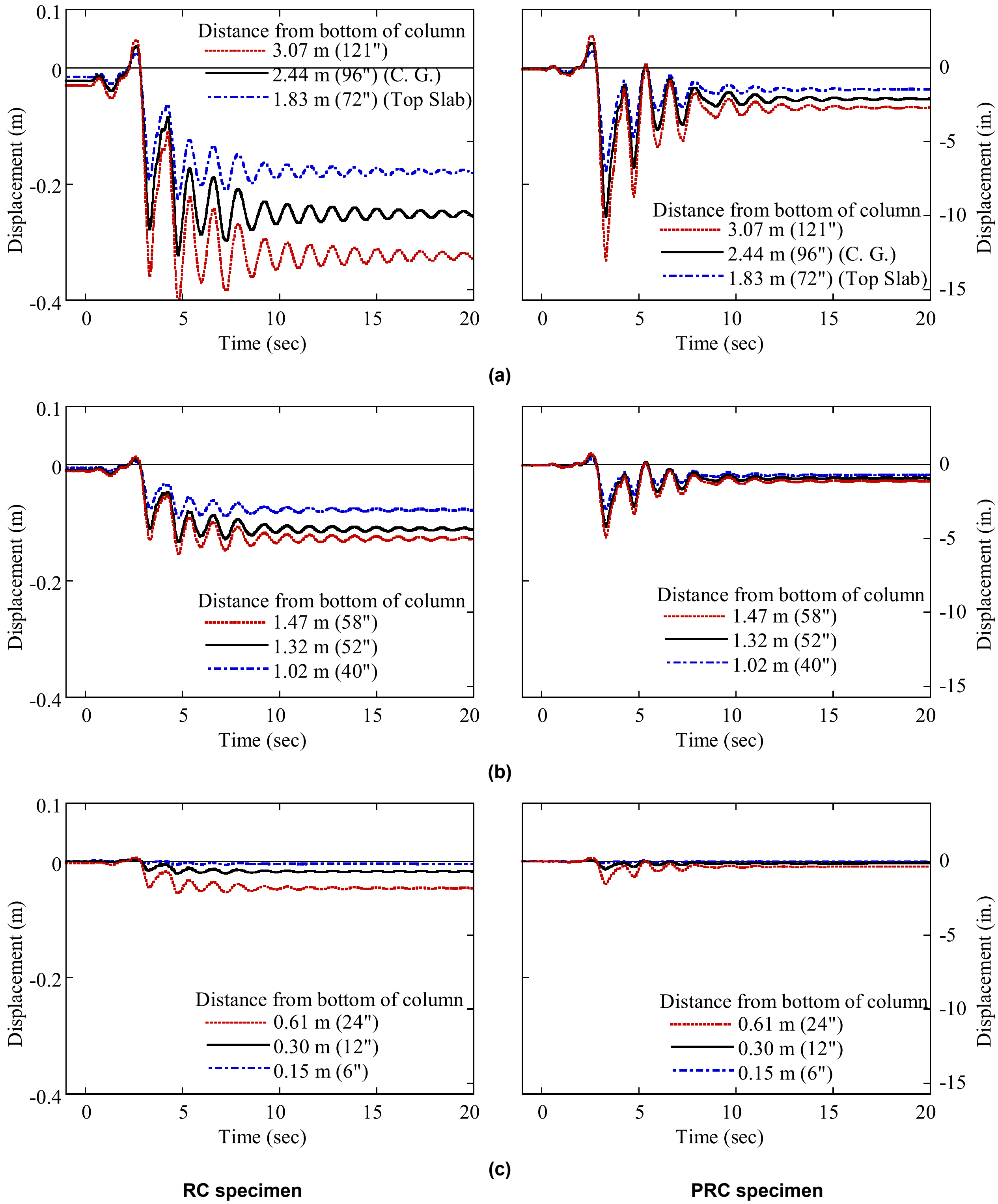

Figure 4.52(a) Response of displacement of RC and PRC specimens for the maximum-level test in the *X*-direction: (a) top blocks; (b) top portion of column; and (c) bottom portion of column.

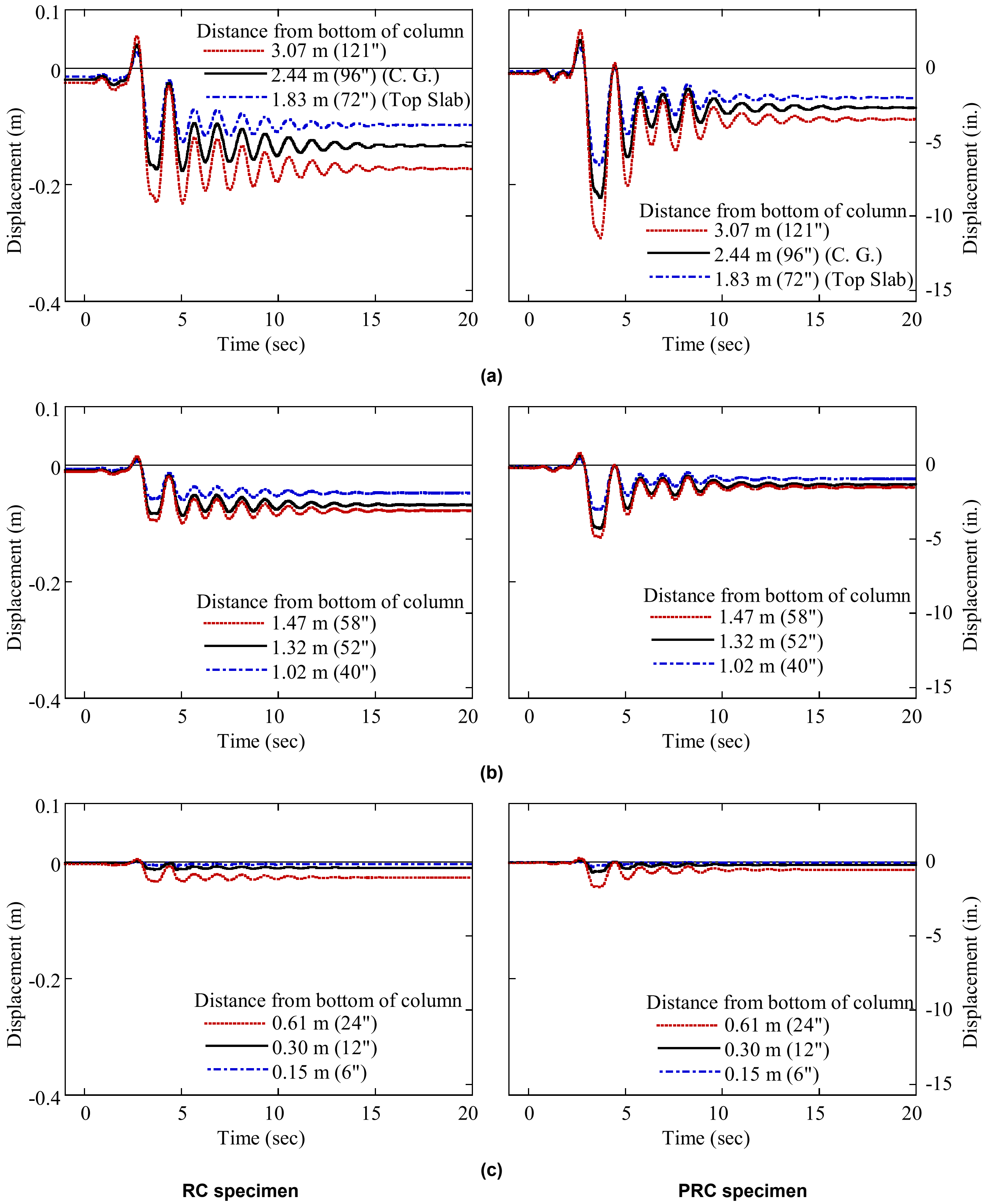

Figure 4.52(b) Response of displacement of RC and PRC specimens for the maximum-level test in the *Y*-direction: (a) top blocks; (b) top portion of column; and (c) bottom portion of column.

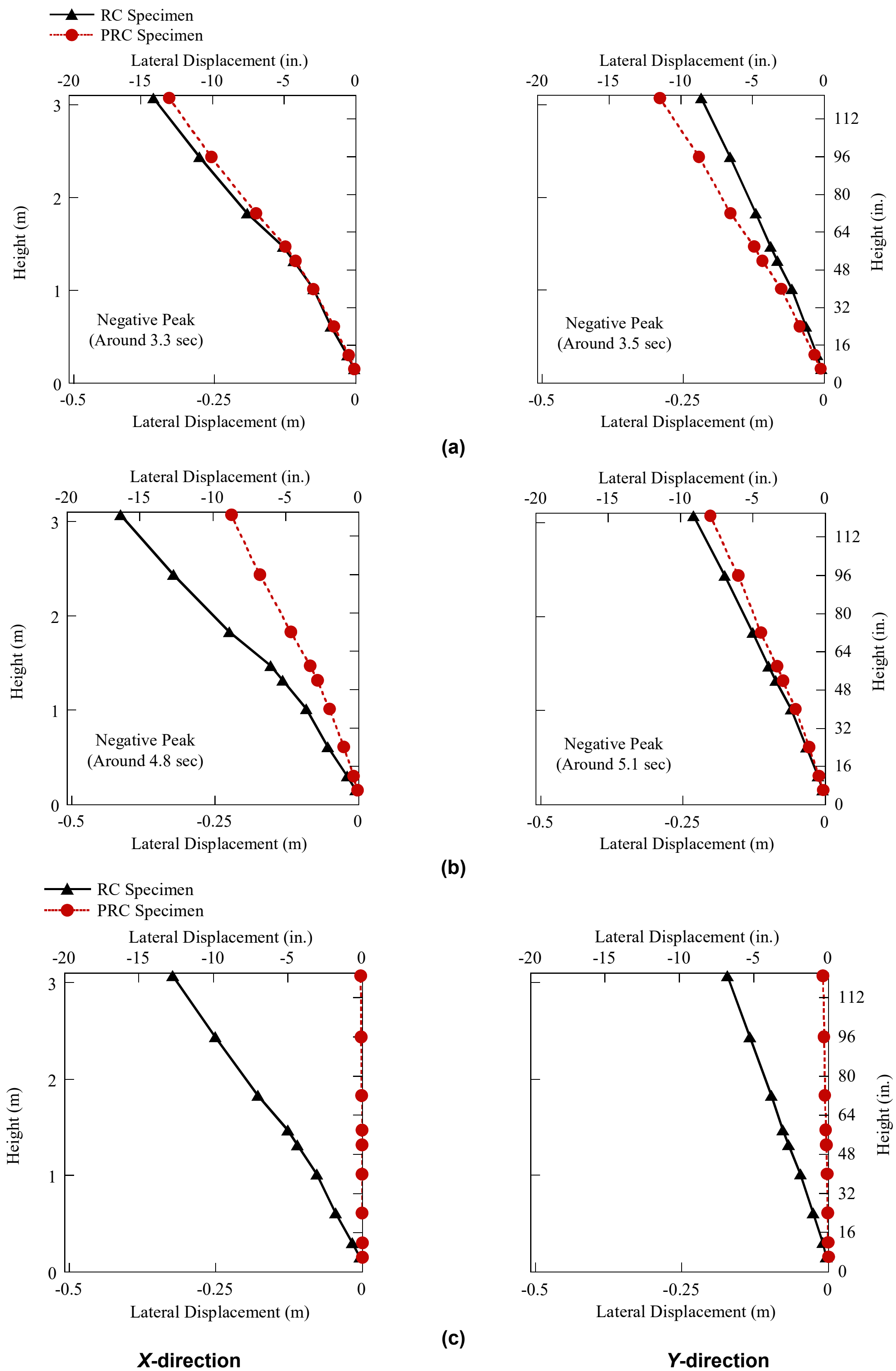

Figure 4.53 Column deformation for the maximum-level test): (a) first peaks; (b) second peaks; and (c) residual deformation.

4.6 EFFECT OF AFTERSHOCKS

4.6.1 Ground Motion Intensity for Tests for Aftershocks

As described above, the PRC specimen did not show severe damage or large residual deformation after the maximum-level tests. Thus, two more tests were performed on the PRC specimen to investigate the effect of aftershocks and final failure mode. No more tests were performed for the RC specimens because of safety concerns. First a low-level test was conducted, which was followed by a high-level test. Seven percent of the modified Los Gatos record was inputted for the low-level test, and then the intensity of the ground motion was increased to 70% of the modified Los Gatos record for the high-level test.

4.6.2 Second Elastic-Level Test

Figure 4.54 shows the response of the PRC specimen during the second elastic-level test. The response during the first elastic-level test is also shown in the figure for comparison. The specimen vibrated around the residual displacement resulting from the previous test, and the residual displacement did not change during the test. As the natural period of the specimen increased from 0.51 sec to 1.37 sec (see Table 4.1 and Figure 4.3), the PRC specimen shows larger tangential stiffness during the second elastic-level test, and, thus, larger response displacement.

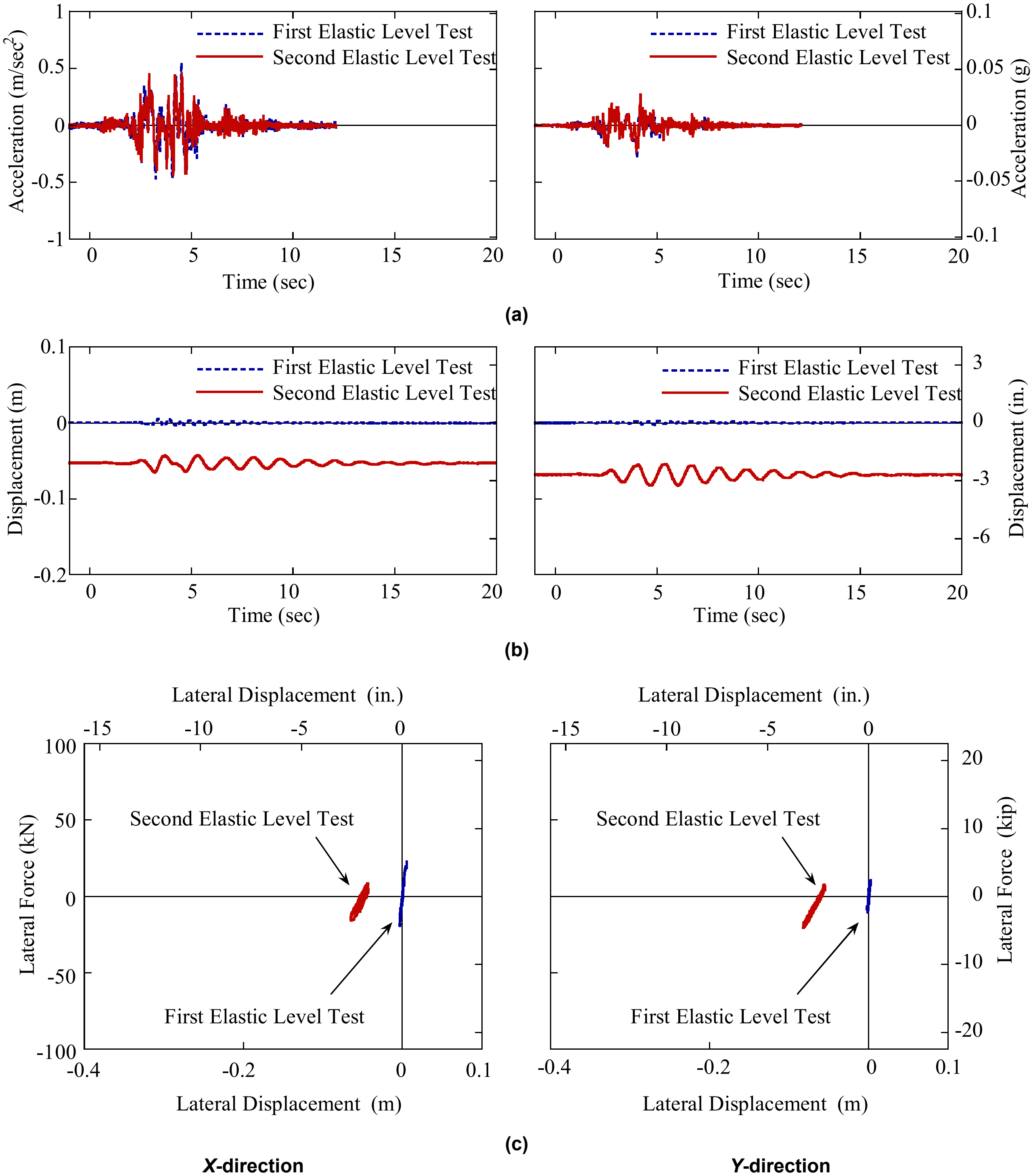

Figure 4.54 **Response during second elastic-level test: (a) input signals (acceleration recorded at footing); (b) displacement response at center-of-gravity of top blocks; and (c) lateral force–lateral displacement hysteresis.**

4.6.3 Second Design-Level Test

Figure 4.55 shows the final failure mode of the PRC specimen after the second design-level test. Because of *P*-delta effects to the northwest side, the specimen collapsed during the second main pulse at around 7 sec. Figure 4.56 shows local damage of the specimen. Note fracture of 6 of 12 longitudinal reinforcing bars on the southeast side, which could have resulted in a significant loss of flexural capacity of the column. The core concrete was crushed, and several spirals were fractured at the northwest side.

Figures 4.57 and 4.58 show response displacement and force-displacement hysteresis recorded during the test. During the first pulse, the displacement of the specimen was 0.252 m (9.9 in.), which is similar to the experienced maximum displacement of the specimen; the response displacement then decreased. During the second pulse, however, the response increased again to the northwest direction, and the specimen become unstable due to the *P*-delta effects. It is at this point that the safety cables stopped the specimen from collapsing.

It is assumed that the main cause of this total collapse was the fracture of some of the longitudinal bars. The smaller bars that were used in the PRC specimen to reduce the amount of mild reinforcement could have resulted in premature fractures. Thus, unbonding of mild reinforcement could be implemented to reduce the risk of total failure; however, total collapse might have been prevented if a smaller number of larger size bars had been used. The failure mode of this specimen should be studied to that other specimen models are designed and constructed to avoid unexpected or undesirable failure mode.

(a)

(b)

Figure 4.55 Collapse of PRC specimen during second design-level test: (a) from east side and (b) from north side.

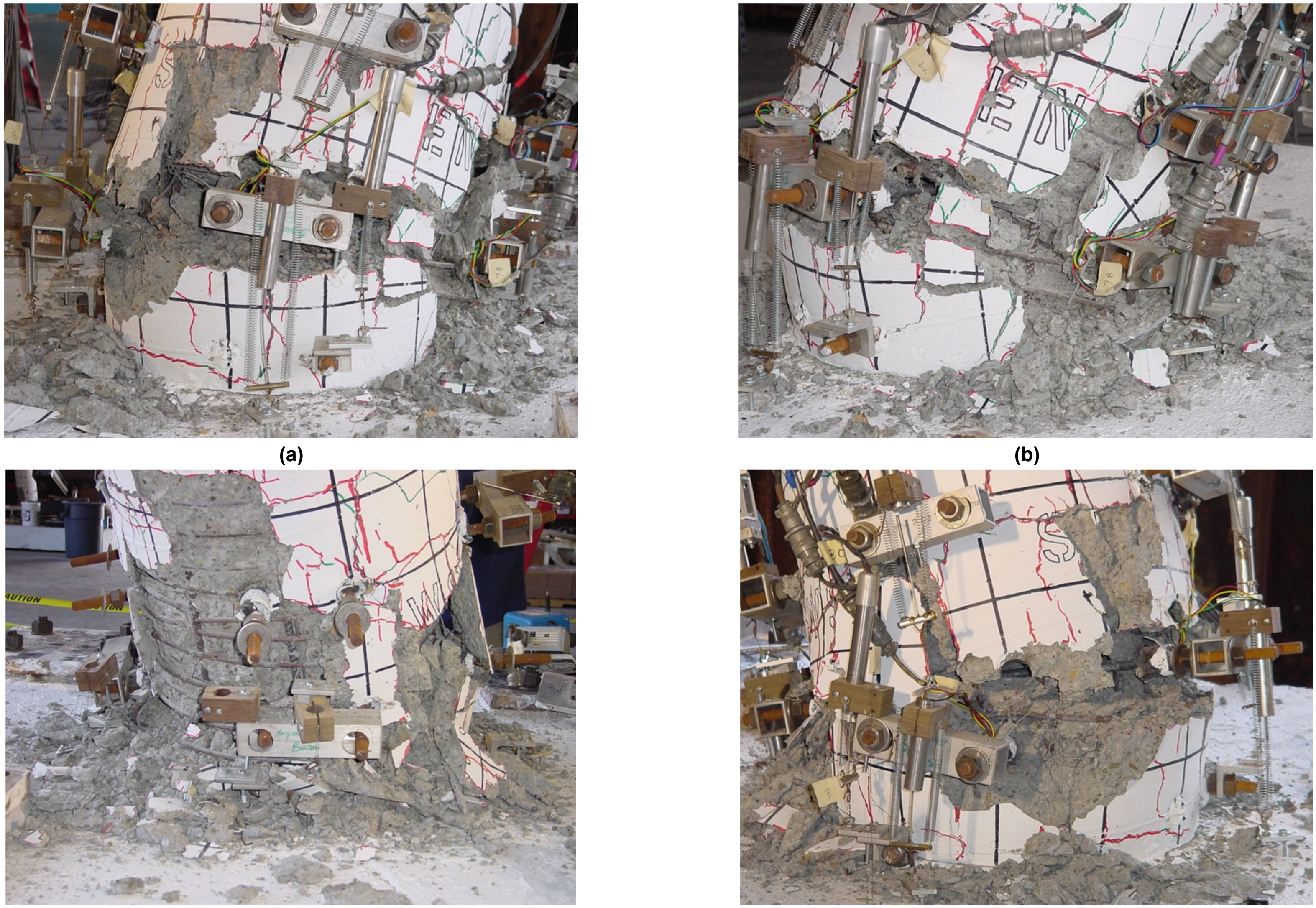

(a) (b) (c) (d)

Figure 4.56 Local damage of PRC specimen after second design-level test: (a) east face; (b) north face; (c) west face; and (d) south face.

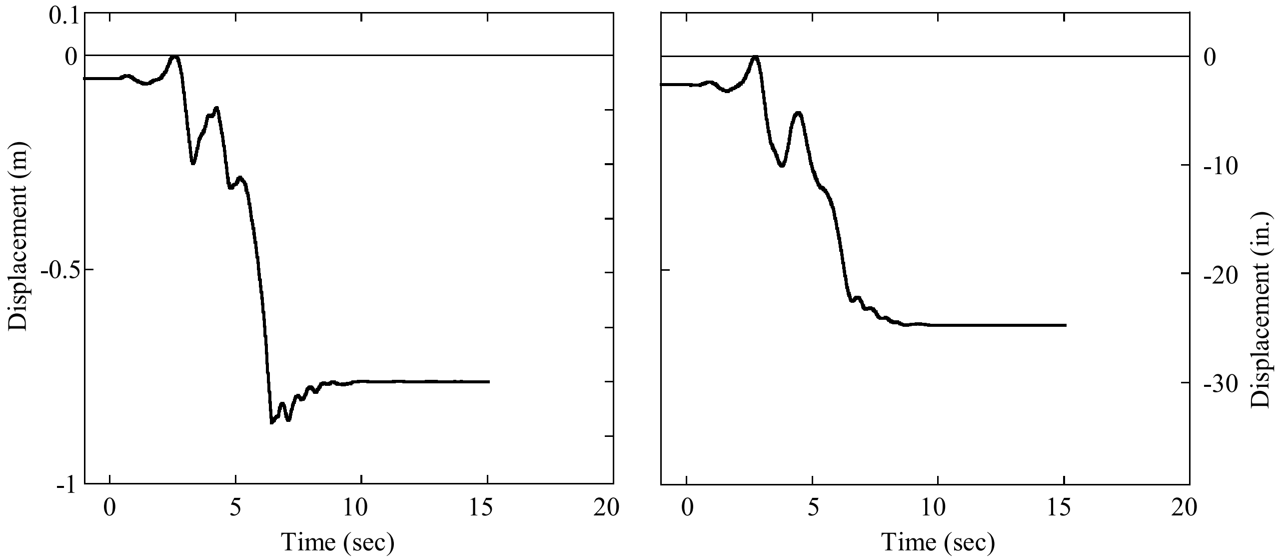

(a)

***X*-direction** **_Y_-direction**

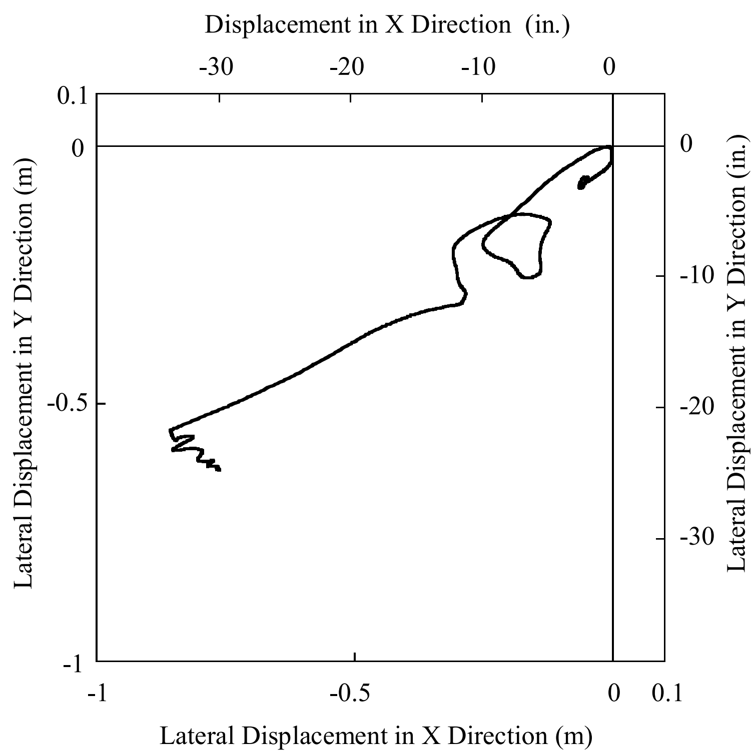

(b)

Figure 4.57 Response displacement for the second design-level test: (a) displacement response at center-of-gravity of top blocks; and (b) displacement response orbit.

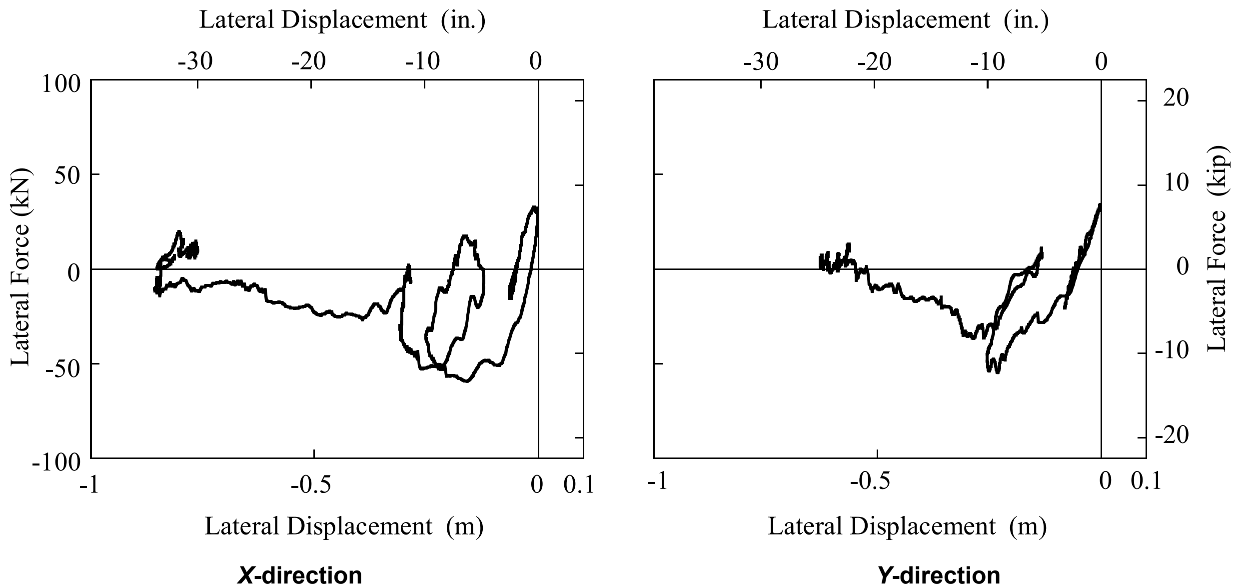

Figure 4.58 **Lateral force–lateral displacement hysteresis for the second design-level test.**

5 Analytical Simulation of the Dynamic Behavior of the Columns

5.1 ANALYTICAL MODELS AND INPUT GROUND MOTIONS

5.1.1 Analytical Models

To further understand the dynamic behavior of the specimens during the earthquake simulation tests, a series of nonlinear dynamic analyses was performed. The analytical model shown in Figure 2.7(b) was used to analyze the PRC specimen. The same model was used for the RC specimen without incorporating the spring element representing an unbonded tendon. Actual material properties detailed in Section 2.4 were incorporated, and the Mander model and the Sakai-Kawashima models were used for stress–strain hysteresis of concrete and reinforcing bars. P-Delta effects due to the dead load of the top slab and weighted blocks were included; P-delta effects due to the prestressing force of the tendon were disregarded.

5.1.2 Damping Assumptions

Damping properties of the analytical models were idealized using Rayleigh damping. Measured natural periods and damping ratios were used for determining damping properties of the models. Natural periods of 0.8 and 0.5 sec for the RC and PRC specimens, respectively, which were measured prior to the series of earthquake simulation tests as shown in Table 4.1, were used for the natural period of the first mode when determining Rayleigh damping.

To determine Rayleigh damping, two sets of natural period and damping ratios are required; however, there is no appropriate way to determine the second natural period for Rayleigh damping. Based on an Eigenvalue analysis of a model assuming cracked stiffness properties for the reference RC column, the first, second, and third modes were determined to have periods of 0.74, 0.09, and 0.02 sec, respectively, suggesting that the second natural period can be taken an order of 1% to 10% of that of the first mode. Thus, 10%, 5%, and 1% were assumed for the first mode, and the effects of damping assumption were explored for the RC specimen. As described later, the effect on the analytical response was minor, so 5% of the natural period of the first mode was used to analyze the PRC specimen.

As shown in Table 4.1, the damping ratio varied from 2.7% to 6% for the RC specimen, presenting difficulties in determining the damping properties for the analyses. Thus, three damping ratios (4% prior to the test in *X*-direction, 6% prior to the test in *Y*-direction, and 2.7%, which is the smallest value), were assumed, and the results were compared to the observed response during the tests. For the PRC specimen, the damping ratio varied from 1.5% to 4.4%.

As described later, the smaller damping ratio provided larger response and better prediction of the test results. Thus, a damping ratio of 2% was assumed for the dynamic analysis of PRC specimen. The same damping ratios were assumed for both the first and the other modes.

Figure 5.1 shows the damping ratio versus natural period relation based on Rayleigh damping. If a smaller second natural period is assumed, the damping ratio in shorter natural period range decreases, while damping ratios in longer natural period range have a similar damping ratio. Smaller damping ratio assumed for the first and second natural periods resulted in a smaller damping ratio for entire natural period range.

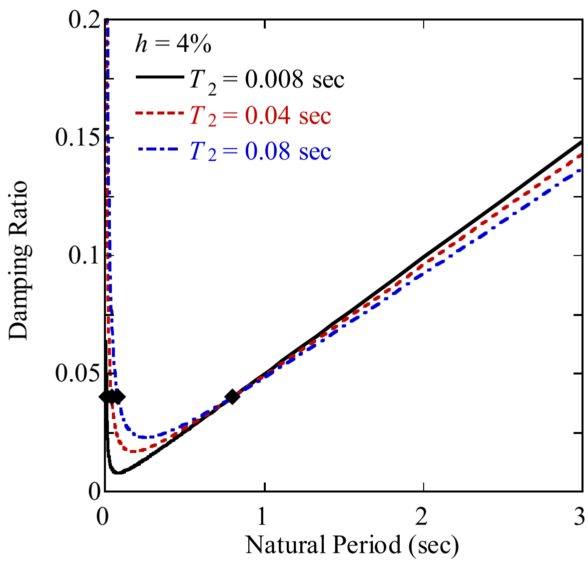

(a)

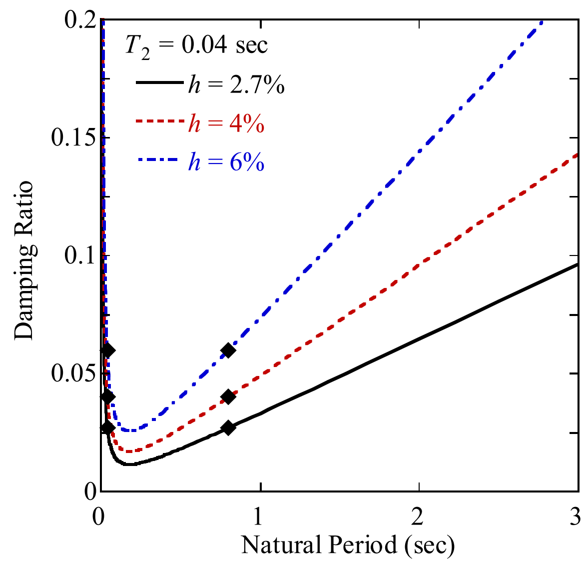

(b)

Figure 5.1 **Rayleigh damping: (a) effect of assumption of second natural period; and (b) effect of damping ratio.**

5.1.3 Input Motions Used

Figure 5.2 shows ground motions used for the analyses. The recorded accelerations at the footing were input. The accelerations recorded at the west surface are used for the *X*-direction while those recorded at the south surface are used for the *Y*-direction. The accelerations were low-pass filtered with a cutoff frequency of 20 Hz. Zeros for about fifteen sec were added after the records to provide enough intervals between the tests to ensure that the response damped out before another record was input, and combined records from four levels of the tests together to form one 120-sec long input acceleration record were used in the analyses.

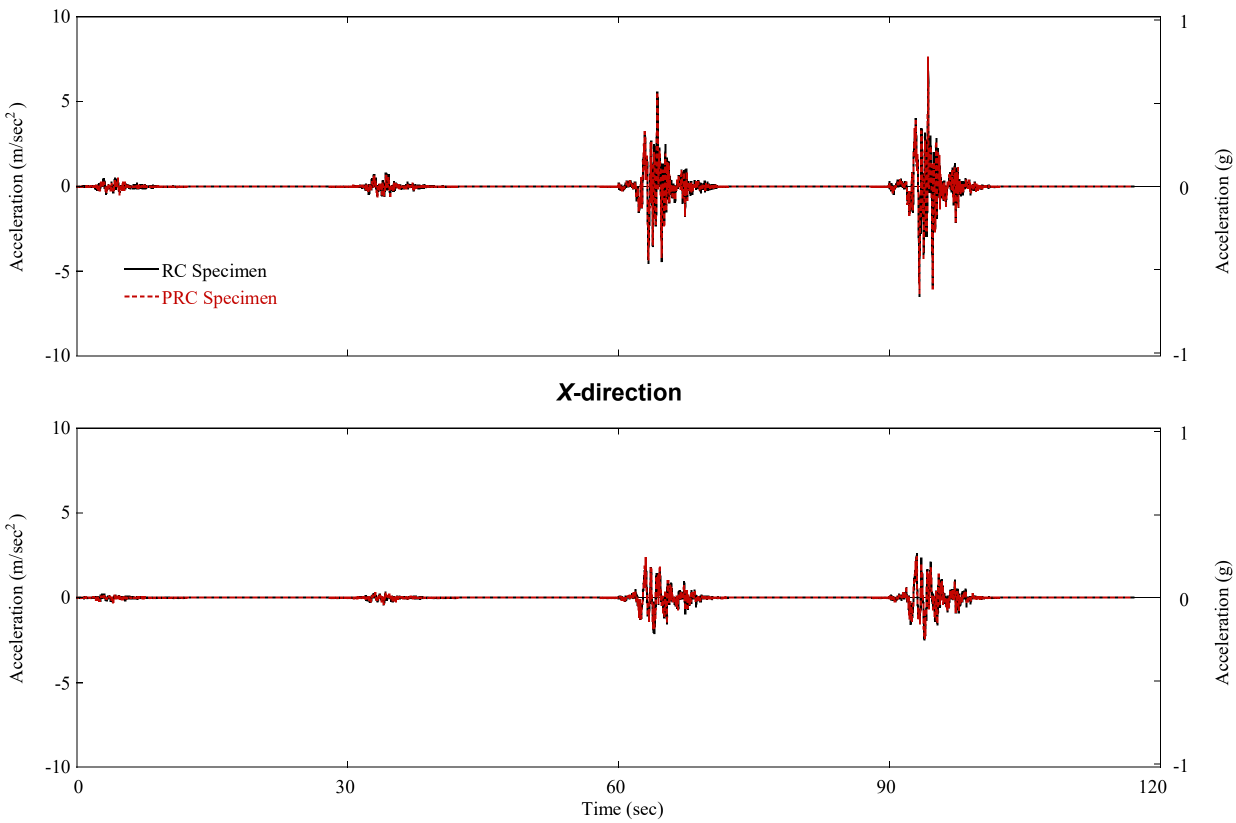

***Y*-direction**

Figure 5.2 Input acceleration for dynamic analyses.

5.2 ANALYTICAL SIMULATION OF DYNAMIC BEHAVIOR OF RC SPECIMEN

Table 5.1 and Figure 5.3 show the effect of damping assumption on the analytical response displacement of the columns; in addition, the test results are compared. The analyses predict 20%–50% smaller maximum response no matter how the damping assumptions are determined. The analytical residual displacements were only about 5%–20% of the observed response.

Varying the second natural period had minor effects, although the smaller second natural period resulted in a smaller damping ratio in the shorter natural period range, resulting in a larger response. Changing the magnitude of damping ratio for the first and second natural periods proved to be a little more sensitive. When a smaller damping ratio was assumed, the analytical maximum and residual displacement increased.

Table 5.1 Analytical response displacement of RC specimen; damping assumed to be 4%.

Damping level assumed to be 4%

Maximum displacement

	Elastic level		**Yield level**		**Design level**		**Maximum level**	
	$d_{x\cdot\max}$ (m)	$d_{y\cdot\max}$ (m)	$d_{x\cdot\max}$ (m)	$d_{y\cdot\max}$ (m)	$d_{x\cdot\max}$ (m)	$d_{y\cdot\max}$ (m)	$d_{x\cdot\max}$ (m)	$d_{y\cdot\max}$ (m)
Test T_2 = 0.08 sec	0.014	0.006	0.020	0.009	0.155	0.111	0.323	0.176
T_2 = 0.04 sec	0.010 (74%)	0.005 (79%)	0.015 (77%)	0.007 (83%)	0.085 (55%)	0.074 (66%)	0.173 (54%)	0.122 (69%)
T_2 = 0.008 sec	0.010 (74%)	0.005 (79%)	0.015 (77%)	0.007 (83%)	0.093 (60%)	0.081 (73%)	0.186 (58%)	0.130 (74%)

Residual displacement

	Design level		**Maximum level**	
	$dr_{x\cdot\max}$ (m)	$dr_{y\cdot\max}$ (m)	$dr_{x\cdot\max}$ (m)	$dr_{y\cdot\max}$ (m)
Test	0.025	0.019	0.252	0.134
T_2 = 0.08 sec	0.0024 (9%)	0.0033 (17%)	0.0095 (4%)	0.0083 (6%)
T_2 = 0.04 sec	0.0031 (12%)	0.0037 (19%)	0.0113 (4%)	0.0093 (7%)
T_2 = 0.008 sec	0.0019 (7%)	0.0025 (13%)	0.0154 (6%)	0.0119 (9%)

T_2 is assumed to be 0.04 sec

Maximum displacement

	Elastic level		**Yield level**		**Design level**		**Maximum level**	
	$d_{x\cdot\max}$ (m)	$d_{y\cdot\max}$ (m)	$d_{x\cdot\max}$ (m)	$d_{y\cdot\max}$ (m)	$d_{x\cdot\max}$ (m)	$d_{y\cdot\max}$ (m)	$d_{x\cdot\max}$ (m)	$d_{y\cdot\max}$ (m)
Test	0.014	0.006	0.020	0.009	0.155	0.111	0.323	0.176
h = 6%	0.009 (64%)	0.004 (69%)	0.013 (66%)	0.007 (74%)	0.079 (51%)	0.066 (60%)	0.162 (50%)	0.113 (64%)
h = 4%	0.010 (74%)	0.005 (79%)	0.015 (77%)	0.007 (83%)	0.093 (60%)	0.081 (73%)	0.186 (58%)	0.130 (74%)
h = 2.7%	0.012 (83%)	0.005 (88%)	0.017 (86%)	0.008 (92%)	0.106 (68%)	0.094 (84%)	0.204 (63%)	0.144 (82%)

Residual displacement

	Design level		**Maximum level**	
	$dr_{x\cdot\max}$ (m)	$dr_{y\cdot\max}$ (m)	$dr_{x\cdot\max}$ (m)	$dr_{y\cdot\max}$ (m)
Test	0.025	0.019	0.252	0.134
h = 6%	0.0023 (9%)	0.0028 (15%)	0.0083 (3%)	0.0071 (5%)
h = 4%	0.0031 (12%)	0.0037 (19%)	0.0113 (4%)	0.0093 (7%)
h = 2.7%	0.0033 (13%)	0.0041 (21%)	0.0196 (8%)	0.0145 (11%)

Note: ratio of analytical values to experimental values are shown in parentheses.

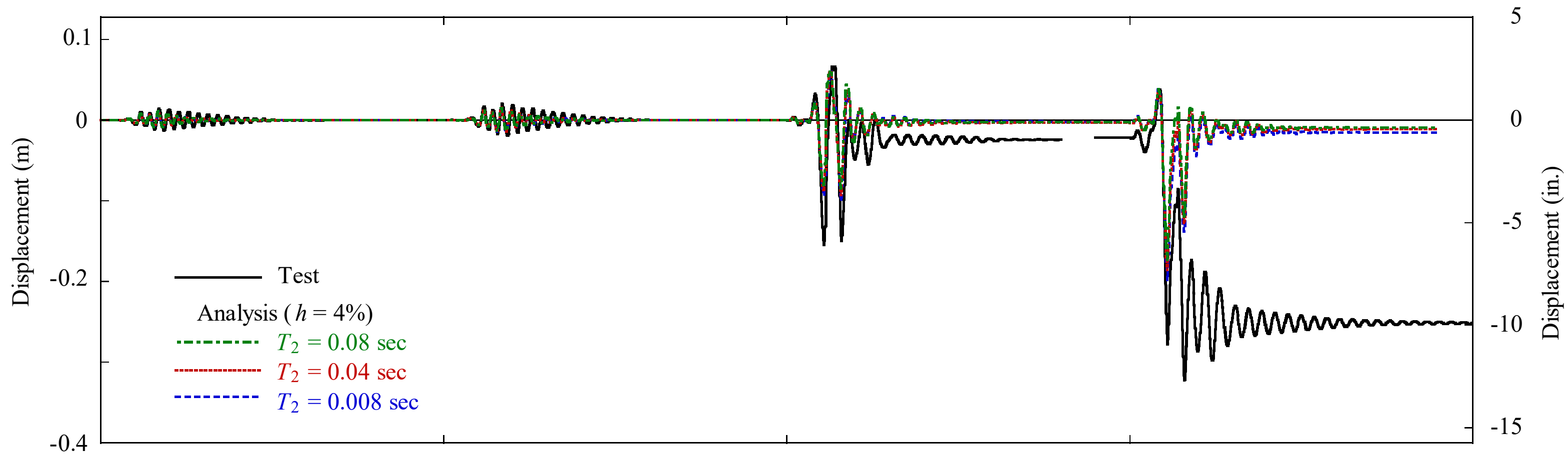

***X*-direction**

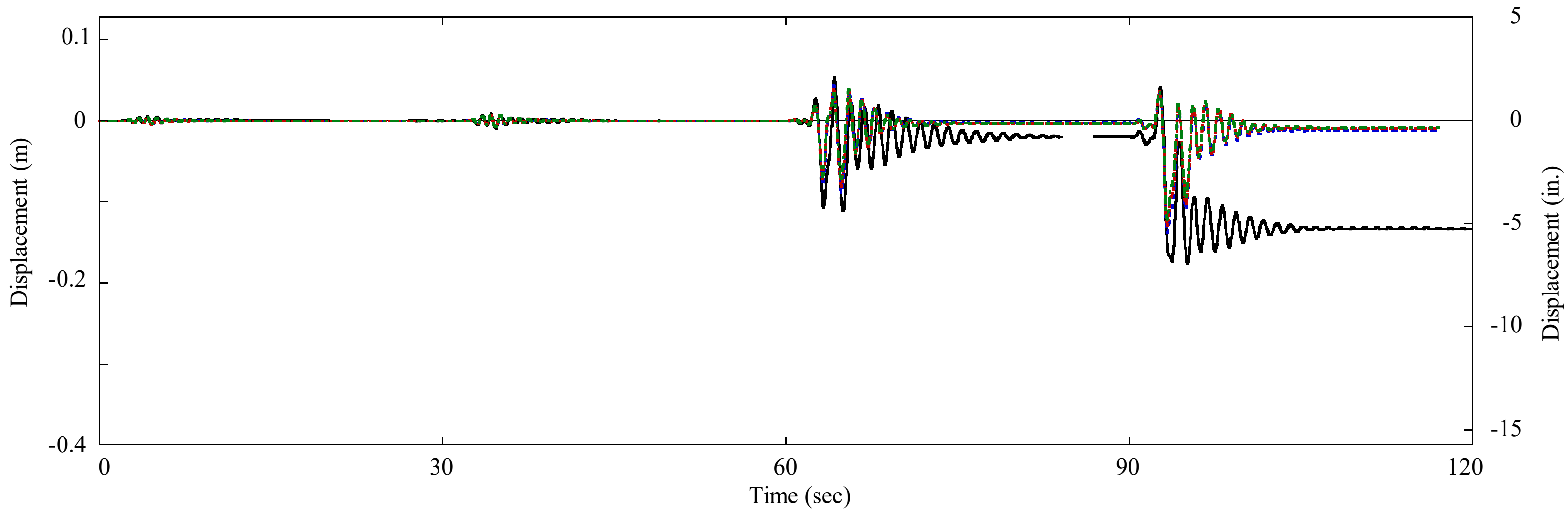

***Y*-direction**
(a)

Figure 5.3(a) Analytical response displacement at center-of-gravity of top blocks of RC specimen: effect of assumption of second natural period.

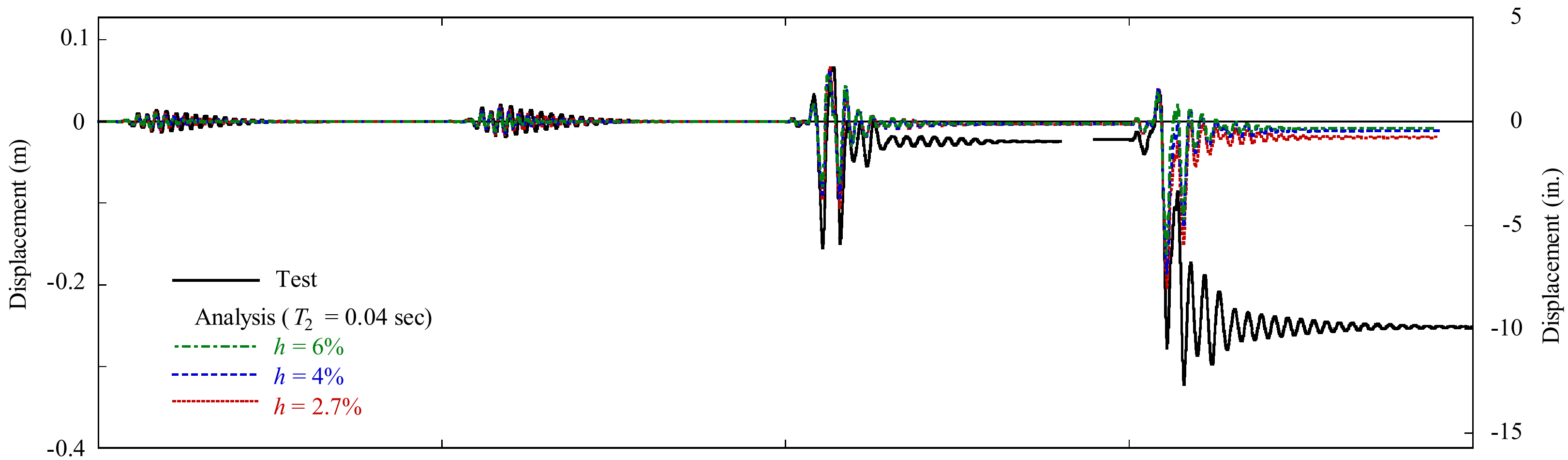

***X*-direction**

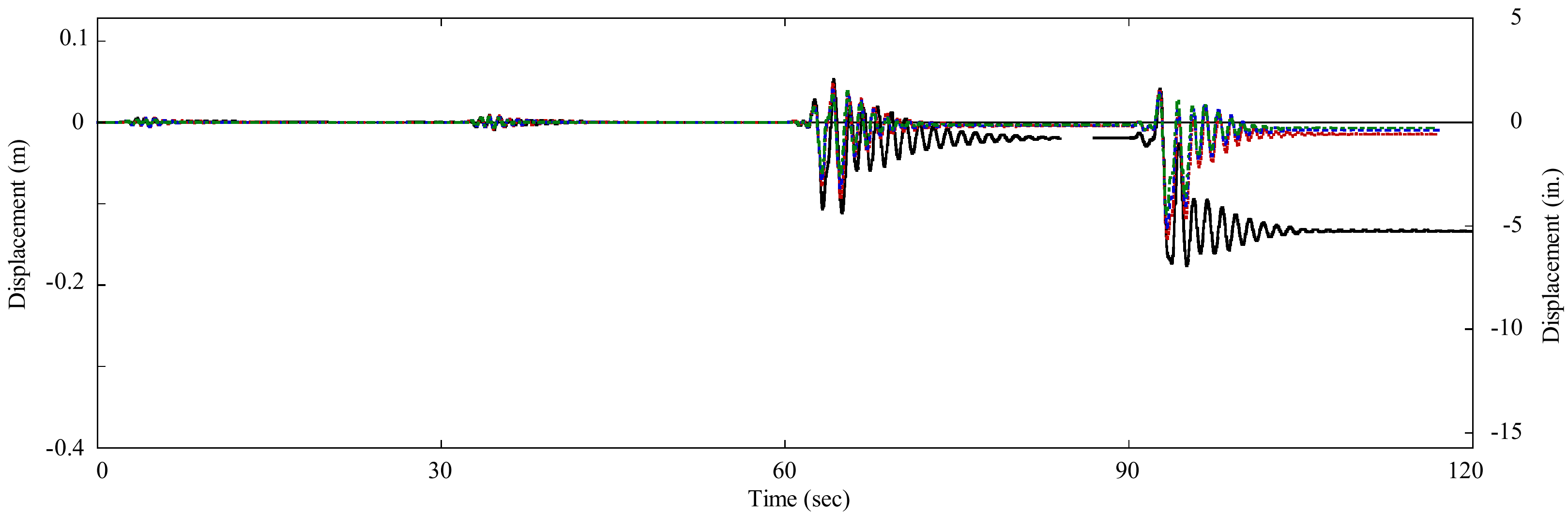

***Y*-direction**
(b)

Figure 5.3(b) Analytical response displacement at center-of-gravity of top blocks of RC specimen (continued): effect of damping ratio.

An assumed damping ratio of 2.7% and a second natural period of 0.04 sec (T_2=0.05T_1) provided the best agreement with the test results among the conditions considered here. Huge discrepancies still exist between the analytical maximum displacements of the test results in the *X*- and *Y*-directions during the maximum-level test (63% and 82%, respectively), and those of the residual displacements were only about 10% after the maximum-level test.

Figure 5.4 compares lateral force versus lateral displacement hysteresis between the actual test results and analysis. The results for a damping ratio of 2.7%, and a second natural period of 0.04 sec are shown here. The initial stiffness results from low-level tests are in good agreement between the tests and analysis. For the high-level tests, the analysis fails to predict both flexural strength and the hysteresis. The flexural strength obtained from the analysis is 55 kN (12 kip), which is 75% of that observed during the test. This might be because the analytical hysteresis clearly shows negative post-yield stiffness due to P-delta effects and bi-lateral loading effects, while the test results do not show such a trend. In general, a larger post-yield stiffness tends to decrease the maximum and residual response, and these results show a totally opposite trend. Additional analysis should be conducted to accurately predict the dynamic behavior of the column.

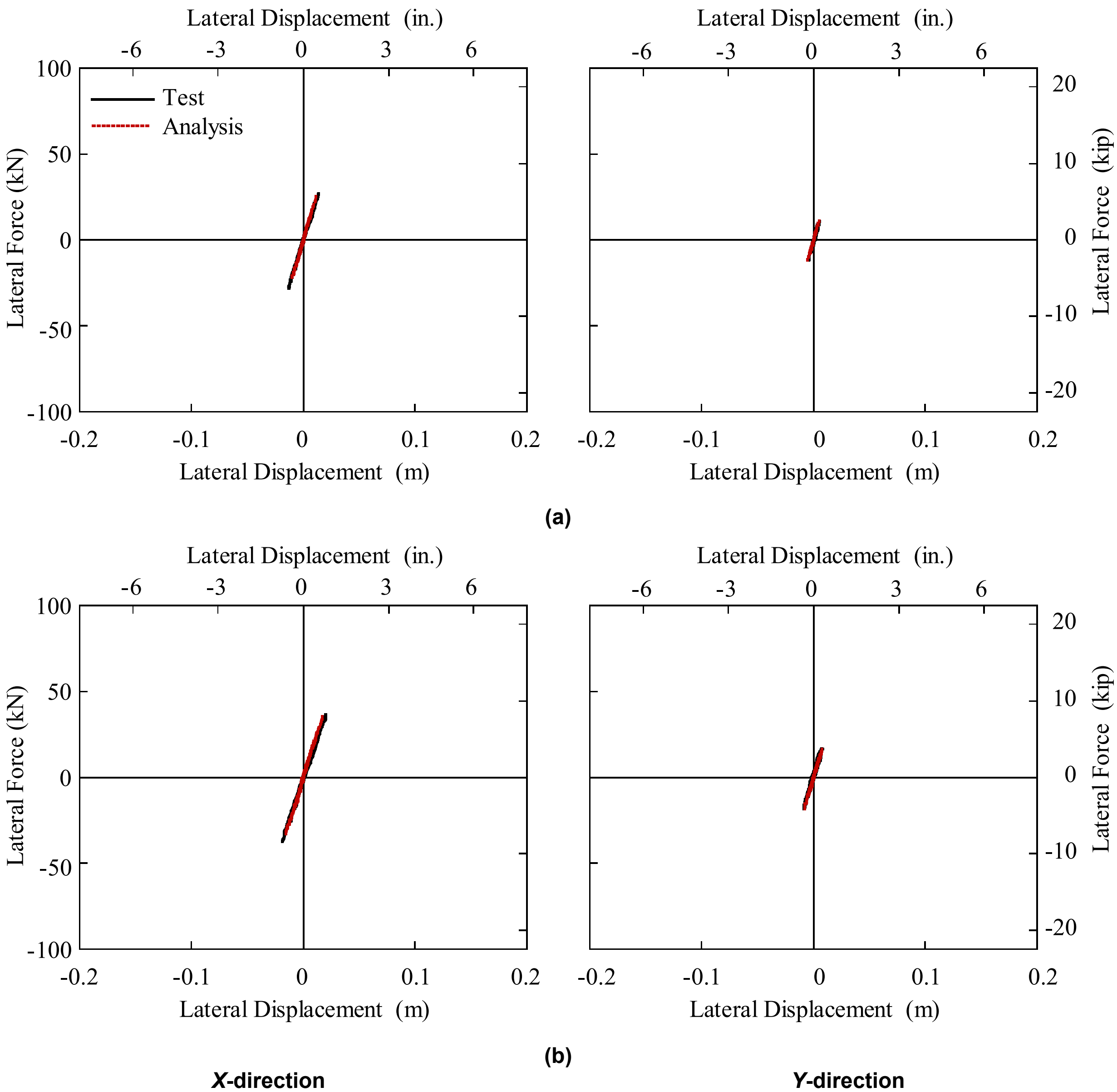

Figure 5.4(a) **Analytical lateral force–lateral displacement hysteresis of the RC specimen: (a) elastic-level test and (b) yield-level test.**

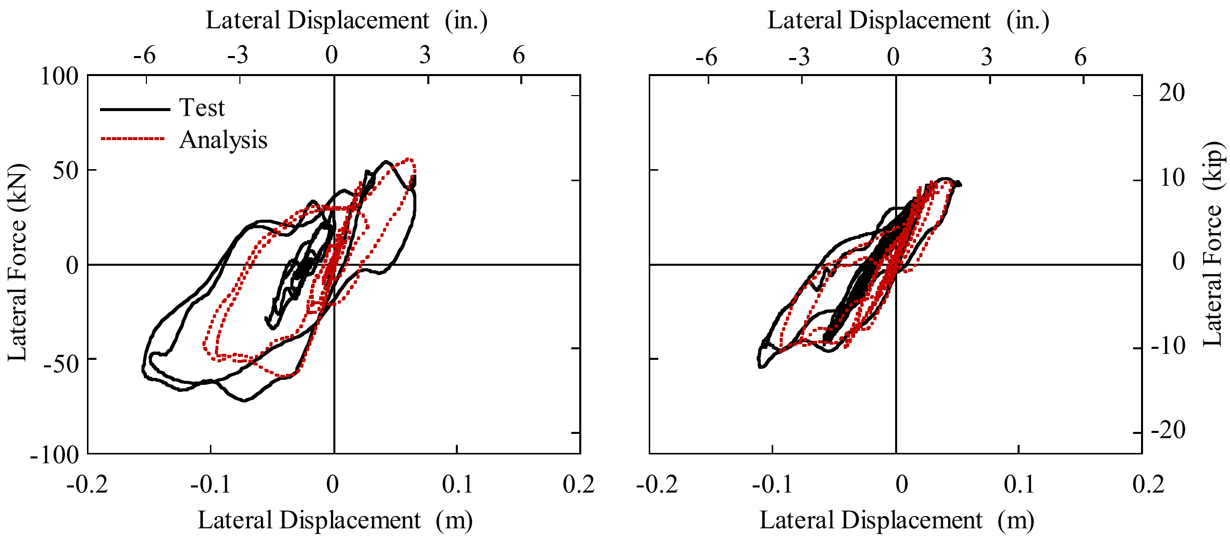

(c)

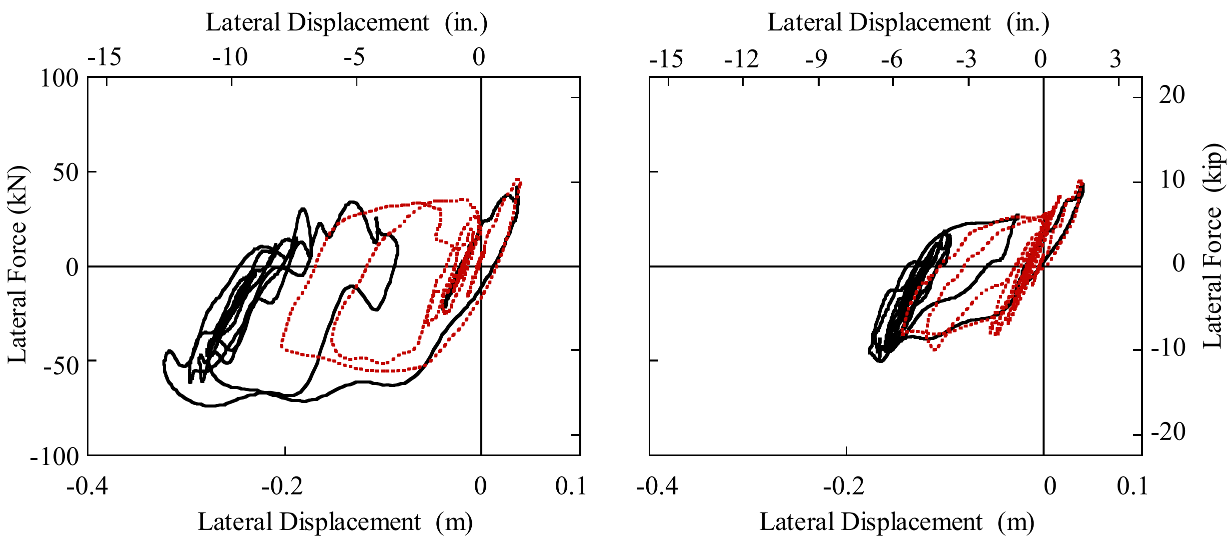

(d)

***X*-direction** ***Y*-direction**

Figure 5.4(b) Analytical lateral force–lateral displacement hysteresis of the RC specimen (continued): (c) design-level test and (d) maximum-level test.

5.3 ANALYTICAL SIMULATION OF DYNAMIC BEHAVIOR OF PRC SPECIMEN

Table 5.2 and Figure 5.5 compare the response displacement at the center-of-gravity of the top of the specimen. The analysis provided much better prediction than for the RC specimen; the analytical maximum displacements were 80% and 100% of the test in the *X*- and *Y*-directions, respectively, during the design-level test. The residual displacements were also predicted with sufficient accuracy. During the maximum-level test, the analysis predicted adequately the response up to the second big pulse; however, the response did not return to the point of origin and displacements twice as large as what occurred during the test results were predicted.

Figure 5.6 shows lateral force versus lateral displacement hysteresis. For the low-level tests, the analysis provided larger initial stiffness than the test results, which resulted in a larger restoring force and response displacement.

Even though the analysis provides a good agreement in terms of response displacement for high-level tests, the predicted flexural strength was 30% smaller than that of the test results, and again negative post-yield stiffness was shown, similar to the analysis for the RC specimen. The analysis cannot predict internal hysteresis loops and residual displacement. A refined model should be developed to accurately predict the response of the PRC column.

Figure 5.7 shows fluctuation of the prestressing force during the tests and its prediction by the analysis. The analysis provides very good agreement with the test results, suggesting that using spring element would be appropriate to represent an unbonded prestressing tendon in the column.

Table 5.2 Analytical response displacement of PRC specimen.

	Elastic level		**Yield level**		**Design level**		**Maximum level**	
	$d_{x\cdot\max}$ (m)	$d_{y\cdot\max}$ (m)	$d_{x\cdot\max}$ (m)	$d_{y\cdot\max}$ (m)	$d_{x\cdot\max}$ (m)	$d_{y\cdot\max}$ (m)	$d_{x\cdot\max}$ (m)	$d_{y\cdot\max}$ (m)
Test	0.005	0.003	0.008	0.005	0.147	0.131	0.256	0.222
Analysis (ratio)	0.011 (230%)	0.005 (181%)	0.017 (218%)	0.009 (188%)	0.114 (78%)	0.129 (98%)	0.206 (80%)	0.199 (90%)

Residual displacement

	Design level		**Maximum level**	
	$dr_{x\cdot\max}$ (m)	$dr_{y\cdot\max}$ (m)	$dr_{x\cdot\max}$ (m)	$dr_{y\cdot\max}$ (m)
Test	0.002	0.008	0.053	0.068
Analysis (ratio)	0.0032 (158%)	0.0072 (90%)	0.119 (224%)	0.143 (210%)

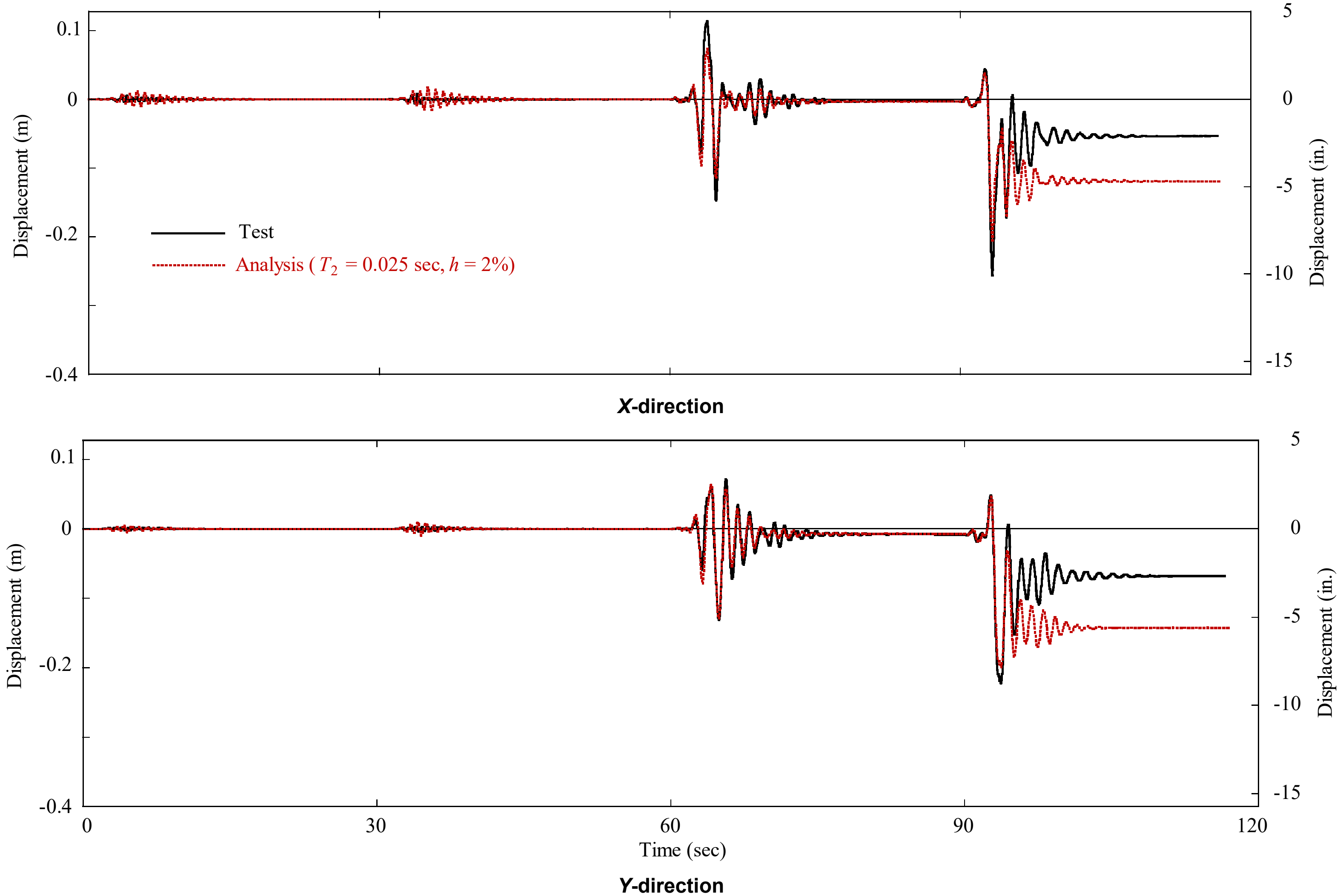

Figure 5.5 Analytical response displacement at center-of-gravity of top blocks of PRC specimen.

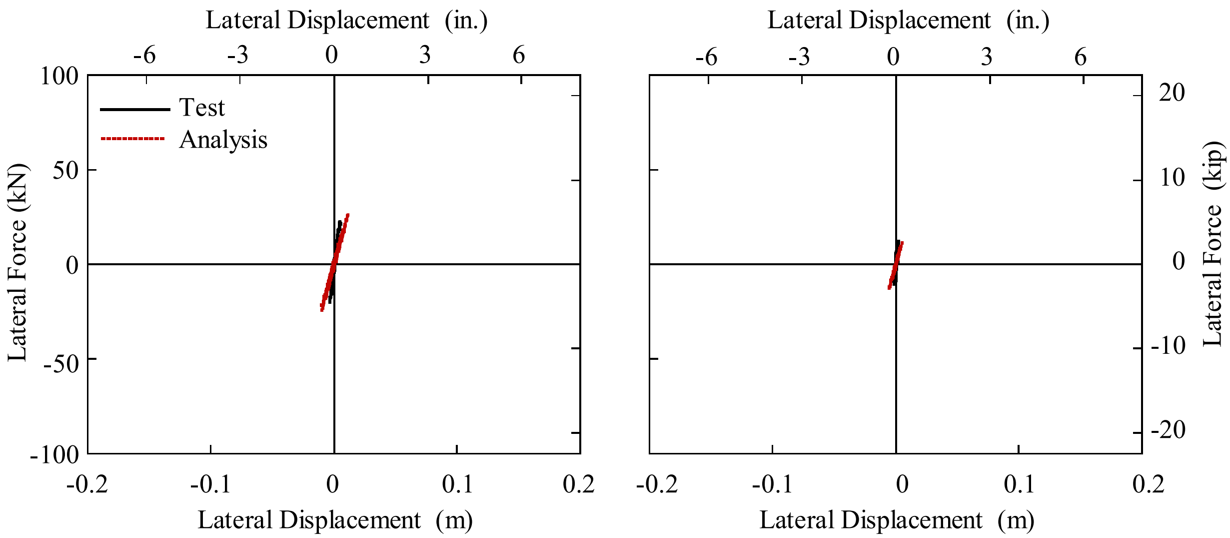

(a)

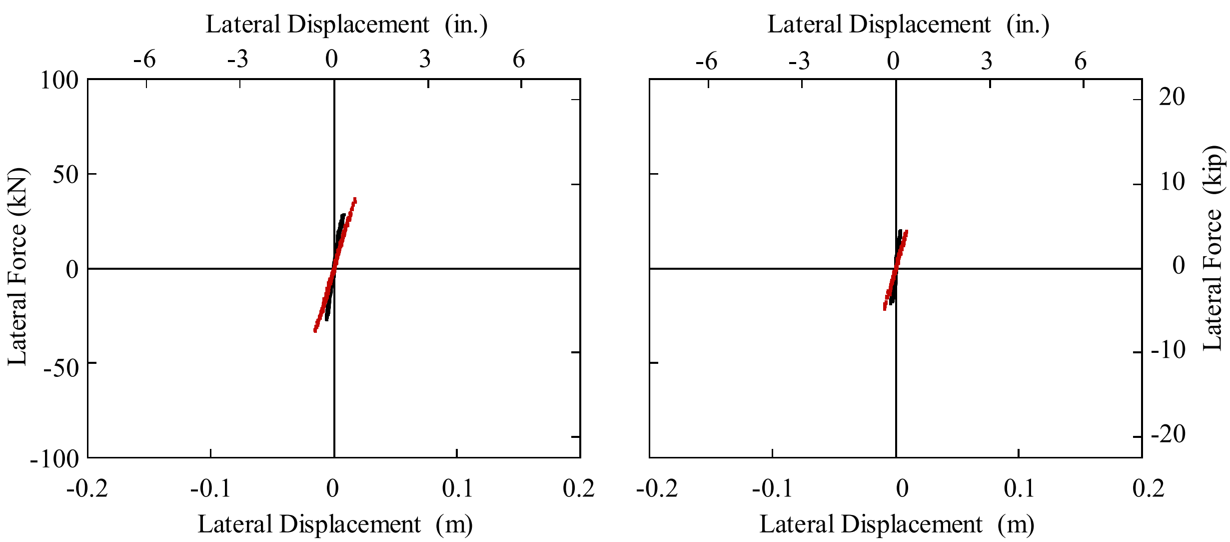

***X*-direction** ***Y*-direction**

(b)

Figure 5.6(a) Analytical lateral force–lateral displacement hysteresis of PRC specimen: (a) elastic-level test and (b) yield-level test.

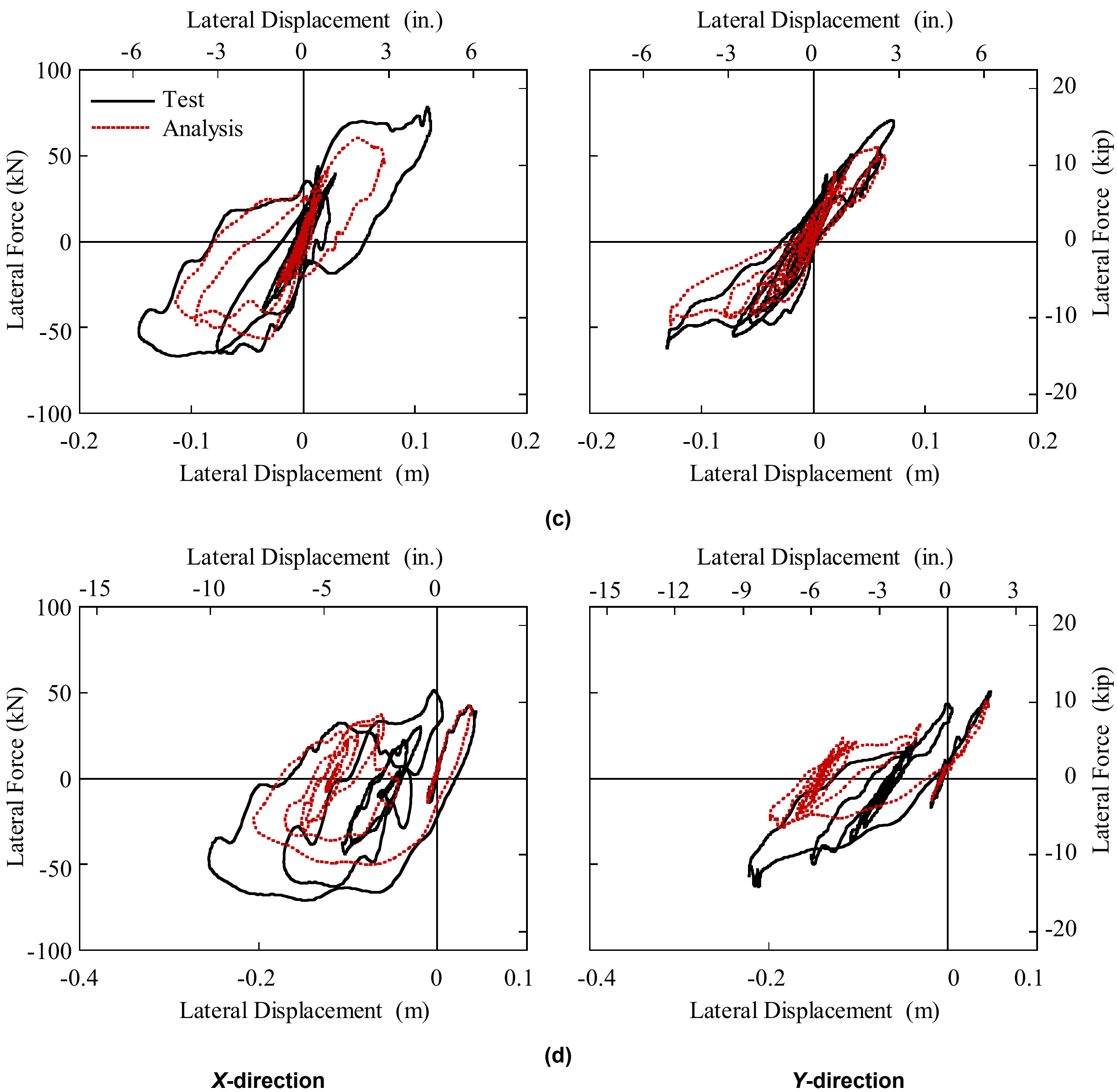

Figure 5.6(b) Analytical lateral force–lateral displacement hysteresis of PRC specimen (continued): (c) design-level test and (d) maximum-level test.

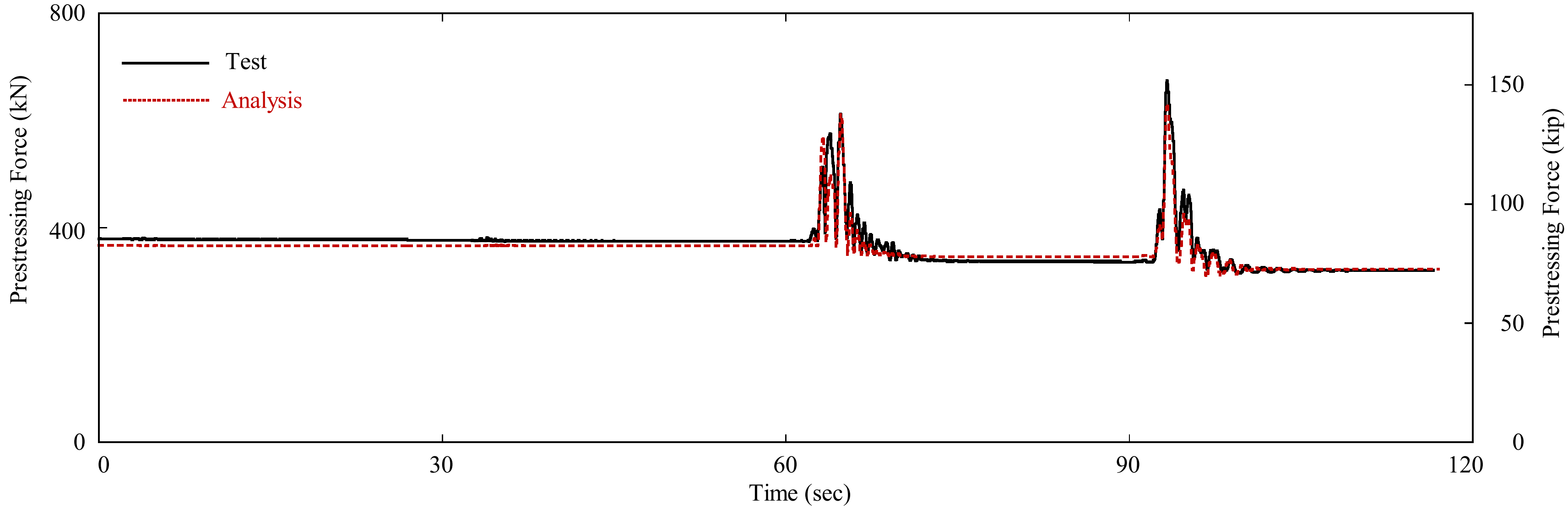

Figure 5.7 Fluctuation of prestressing force obtained by dynamic analyses.

6 Conclusions

A large ductility capacity is generally required of bridge columns located in regions of high seismicity to ensure economical designs that provide adequate protection against collapse. However, conventionally designed bridge columns that develop high ductility demands tend to retain large permanent displacements after an extreme earthquake. To minimize such residual displacements in RC columns, a design was proposed whereby longitudinal post-tensioning strands replaced some of usual longitudinal mild reinforcing bars. A series of earthquake simulation tests were conducted to validate the effectiveness of providing unbonded prestressing strands in lightly reinforced concrete columns to reduce residual displacements under near-field strong ground motion.

Two column specimens were designed and constructed; one represented a conventionally designed RC column, referred to as the RC specimen, and the other represented a lightly reinforced concrete column with unbonded prestressed tendon, referred to as the PRC specimen. Both specimens had a diameter of 0.406 m (16 in.) and an aspect ratio of 6. For the PRC specimen, about a half of the longitudinal reinforcement of the RC specimen was replaced with a 32 mm (1 1/4 in.)-diameter tendon, and 380 kN (85 kip) of a prestressing force was induced in the column. These design parameters were determined based on a series of analyses conducted prior to the tests.

The specimens were tested under two horizontal ground excitations; modified Los Gatos records from the 1989 Loma Prieta, California, earthquake were used as input ground motions. The ground motion intensity was increased in four steps: an elastic- (7% as a scaling factor), a yield- (10%), a design- (70%) and a maximum- (100%) level tests.

A series of nonlinear dynamic analyses was also conducted. Fiber elements and a nonlinear spring element were used to represent hysteretic behavior of the RC and unbonded tendon.

The conclusions determined from the earthquake simulation tests are as follows:

1. In response to the design-level tests, both specimens had similar maximum response displacements of about 0.15 m (6 in.) for a ductility of 6 in the direction of the stronger component of the ground motion. During the maximum-level tests, the maximum response displacements increased up to about 12 and 10 in ductility for the RC and PRC specimens, respectively. Although providing an unbonded prestressed tendon reduced the capacity for energy dissipation, this did not have a significant effect the on maximum response displacement under near-field ground motions.

2. Residual displacements after the tests were 0.025 m (1 in.) and 0.008 m (0.3 in.) for the RC and PRC specimens, respectively. After the design-level test, there was an increase up to 0.25 m (10 in.) and 0.07 m (2.7 in.) at the end of the maximum-level test, demonstrating that the unbonded prestressed tendon effectively reduced the residual displacement after strong ground excitation.
3. Both specimens showed similar lateral force versus lateral displacement hysteresis. The PRC specimen, however, did not show an expected origin-oriented hysteresis. The PRC specimen showed origin-oriented hysteresis only when a displacement vector was directed to the origin or near the origin.
4. Observed local damage of the specimens after the design-level tests were similar. After experiencing a response ductility of 6, no core concrete crushing, buckling of longitudinal reinforcement, or fracture of longitudinal and spiral reinforcement were observed. The new configuration did not affect the formation of plastic hinges or a plastic-hinge region; however, after the maximum-level tests, some of longitudinal rebar of the PRC specimen was presumed fractured even though the RC specimen did incur such damage.
5. The tendon remained elastic during the tests while the specimen experienced a response ductility of 10. The prestressing force increased up to 613 kN (138 kip) as the specimen deformed and decreased by 39 kN (9 kip) at the end of the design-level test. During the maximum-level test, the prestressing force increased up to 675 kN (152 kip).
6. During the aftershocks, the PRC specimen totally collapsed. The main cause of this total collapse was fracture of some of the longitudinal bars.

Below are the conclusions determined from the nonlinear dynamic analyses:

1. The analyses predicted 20–50% smaller maximum response of the RC specimen. The predicted residual displacements were only 10% of the test results.
2. The analyses provide better prediction of the PRC specimen. However, larger residual displacements were predicted.
3. The analyses predicted the tendon behavior with sufficient accuracy. Using a spring element was determined to be appropriate in idealizing an unbonded prestressing tendon in the PRC column.

Further research in the following areas is necessary:

1. The effects of unbonding of mild longitudinal reinforcement should be investigated. This can prevent the localization of strain and thus premature fracture of the reinforcement, which is presumed to the main cause of the total collapse of the PRC specimen.
2. A refined model should be developed that can predict dynamic behavior of RC columns, especially the residual displacement.

REFERENCES

Caltrans (2001). *Seismic Design Criteria*, Ver. 1.2, California Department of Transportation, Sacramento, CA.

Dodd L.L., Cooke N. (1992). The dynamic behavior of reinforced-concrete bridge piers subjected to New Zealand seismicity, *Res. Rep. 92-04*, Department of Civil Engineering, University of Canterbury, Christchurch, New Zealand.

Hachem M.M., Mahin S.A., Moehle J.P. (2003). Performance of circular reinforced concrete bridge columns under bidirectional earthquake loading, *Report No. 2003/06,* Pacific Earthquake Engineering Research Center, University of California, Berkeley, CA.

Hewes J.T., Priestley M.J.N. (2001). Experimental testing of unbonded post-tensioned precast concrete segmental bridge columns, *Proceedings, 6th Caltrans Seismic Research Workshop, No. 02-104*, Division of Engineering Services, California Department of Transportation, Sacramento, CA.

Iemura H., Takahashi Y., Sogabe, N. (2002). Innovation of high-performance RC structure with unbonded bars for strong earthquakes, Japan Society of Civil Engineers, *J. Struct. Mech. Earthq. Eng*., 710/I-60: 283–296. (in Japanese).

Ikeda S. (1998). Seismic behavior of reinforced concrete columns and improvement by vertical prestressing, *Proceedings, XIIIth FIP Congress*, 1: 879–884, Balkema Rotterdam, Netherlands.

Kawashima K. (2000). Seismic design and retrofit of bridges, *Proceedings, 12th World Conference on Earthquake Engineering*, CD-ROM No. 2828, New Zealand Society for Earthquake Engineering, Auckland, New Zealand.

Kowalsky M.J., Priestley M.J.N., Seible F. (1997). Dynamic shake table testing of lightweight concrete bridges, *Proceedings, National Seismic Conference on Bridges and Highways*, Sacramento, CA.

Krawinkler H., Moncarz P.D. (1982). Similitude requirements for dynamic models, American Concrete Institute, *Dynamic Modeling of Concrete Structures SP 73-1*, pp. 1–22, Detroit, MI.

Laplace P.N., Sanders D.H., Saiidi M. (2001). Experimental and analytical study of circular flexural retrofitted columns subjected to shake table loading, *Proceedings, 6th Caltrans Seismic Research Workshop, No. 02-103,* California Department of Transportation, Sacramento, CA.

Mander J.B., Priestley M.J.N., Park R. (1988). Theoretical stress-strain model for confined concrete, ASCE, *J. Struct. Eng*., 114(8): 1804–1826.

McCormac J.C. (1986). *Design of Reinforced Concrete*, 2nd ed., Harper & Row, Publishers, Inc.

Mehta P.K., Monteiro P.J.M. (1993). *Concrete: Structure, Properties, and Materials*, 2nd ed., Prentice Hall.

PEER (2000–2004). Pacific Earthquake Engineering Research Center, *http://peer.berkeley.edu/Research/facilities.html*.

Park S.W., Yen W.P., Cooper J.D., Unjoh S., Terayama T., Otuska H. (2003). A comparative study of U.S.-Japan seismic design of highway bridges: II. Shake-table model tests, *Earthq. Spectra*, 19(4) 933–958.

Priestley M.J.N., Seible F., Calvi G.M. (1996). *Seismic Design and Retrofit of Bridges*, John Wiley & Sons, Inc.

PEER (2000). Strong motion database, Pacific Earthquake Engineering Research Center, *http://peer.berkeley.edu/smcat/.*

Somerville P., Smith N. Punyamurthula S., Sun, J. (1997). Development of ground motion time histories for phase 2 of the FEMA/SAC steel project, *Report No. SAC/BD-97/04*, SAC Joint Venture, *http://nisee.berkeley.edu/data/strong_motion/sacsteel/motions/nearfault.html*.

Sakai J., Kawashima K. (2000). An unloading and reloading stress-strain model for concrete confined by tie reinforcement, *Proceedings, 12th World Conference on Earthquake Engineering,* CD-ROM No. 1431, New Zealand Society for Earthquake Engineering, Auckland, New Zealand.

Sakai J., Kawashima K. (2003). Modification of the Giuffre, Menegotto and Pinto model for unloading and reloading paths with small strain variations, Japan Society of Civil Engineers, *J. Struct. Mech. Earthq. Eng*., 738/I-64: 159–169. (in Japanese).

Sakai J., Kawashima, K. (2006). Unloading and reloading stress-strain model for confined concrete, ASCE, *J. Struct. Eng*., ASCE, 132(1): 112–122.

Sakai J., Mahin S.A. (2004). Analytical investigations of new methods for reducing residual displacements of reinforced concrete bridge columns, *Report No. 2004/02*, Pacific Earthquake Engineering Research Center, University of California, Berkeley, CA.

Yen W.P., Cooper J.D., Park S.W., Unjoh S., Terayama T., Otuska H. (2003). A comparative study of U.S.-Japan seismic design of highway bridges: I. Design methods, *Earthq. Spectra*, 19(4): 913–932.

Zatar W.A., Mutsuyoshi H. (2000). Reduced residual displacements of partially prestressed concrete bridge piers, *Proceedings, 12th World Conference on Earthquake Engineering*, CD-ROM No. 1111, New Zealand Society for Earthquake Engineering, Auckland, New Zealand.

Appendix A Quasi-Static Behavior of the PRC Specimens

This appendix shows the quasi-static behavior of partially prestressed reinforced concrete (PRC) specimens with various tendon sizes and prestressing force described in Section 2.2.3. Variables considered are shown in Table 2.3, and the seismic performances of the specimens are summarized in Table 2.4. The hysteresis after the columns reached the ultimate state are shown by the dotted line.

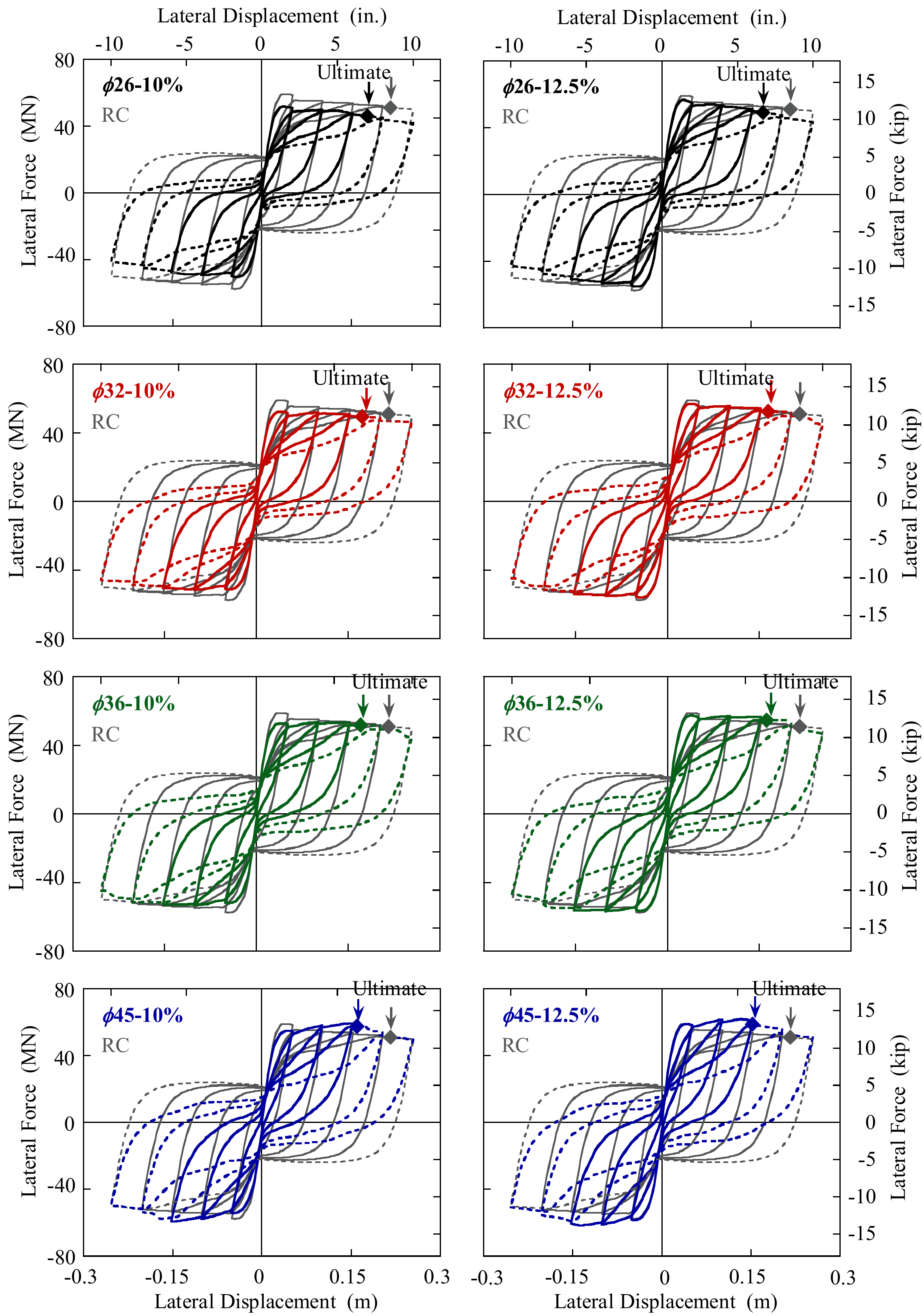

Figure A.1(a) Hysteretic behaviors of PRC specimens: total axial force ratio = 10%' and total axial force ratio = 12.5%

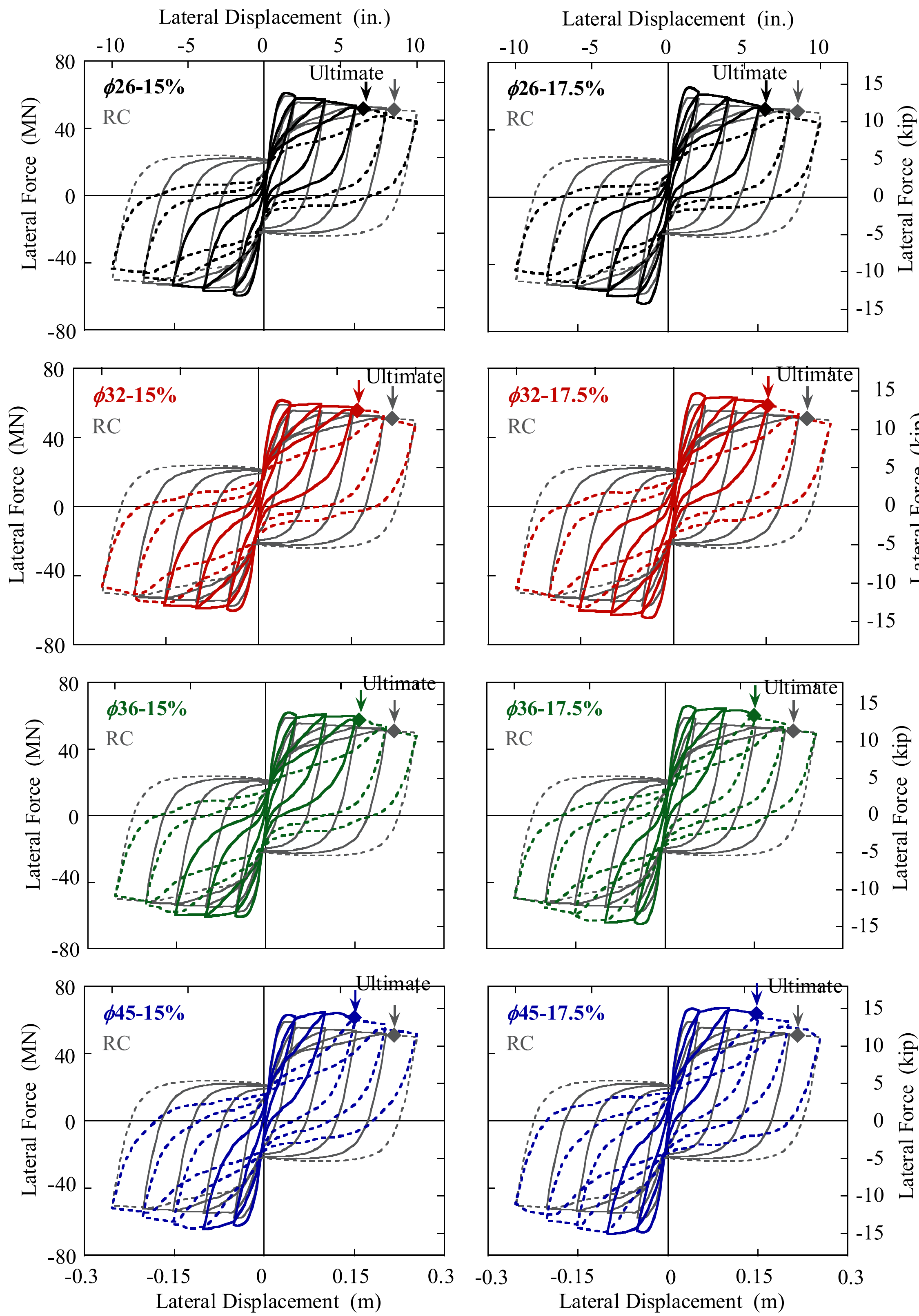

Figure A.1(b) Hysteretic behaviors of PRC specimens: total axial force ratio = 15% and total axial force ratio = 17.5%.

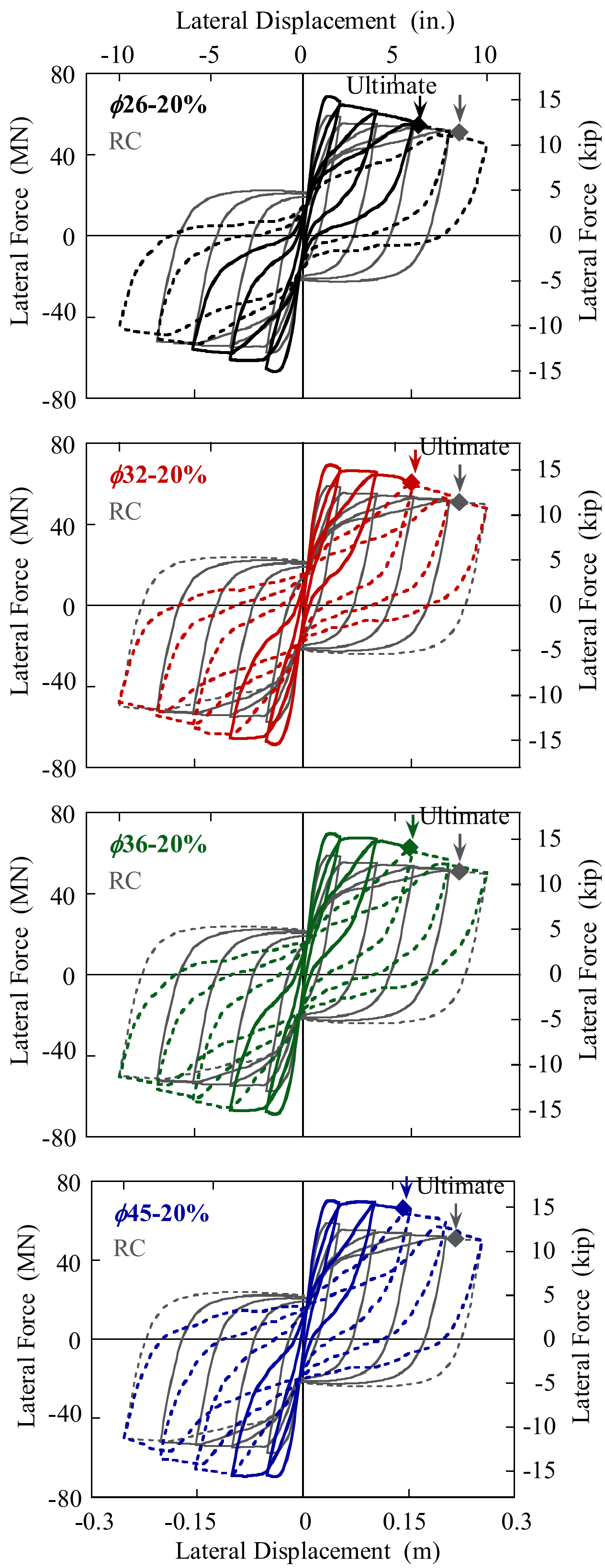

Figure A.1(c) Hysteretic behaviors of PRC specimens: total axial force ratio = 20%.

Appendix B Response Spectra of Strong-Ground Motions

This appendix shows the response acceleration, velocity, and displacement spectra of strong ground motions considered in Section 2.5. The scale factor for the specimen is taken into account when computing the spectra, with an assumed damping ratio of 5%. The lists of ground motions are summarized in Table 2.10. The fundamental natural period of the specimen (= 0.67 sec.) is shown in the figures.

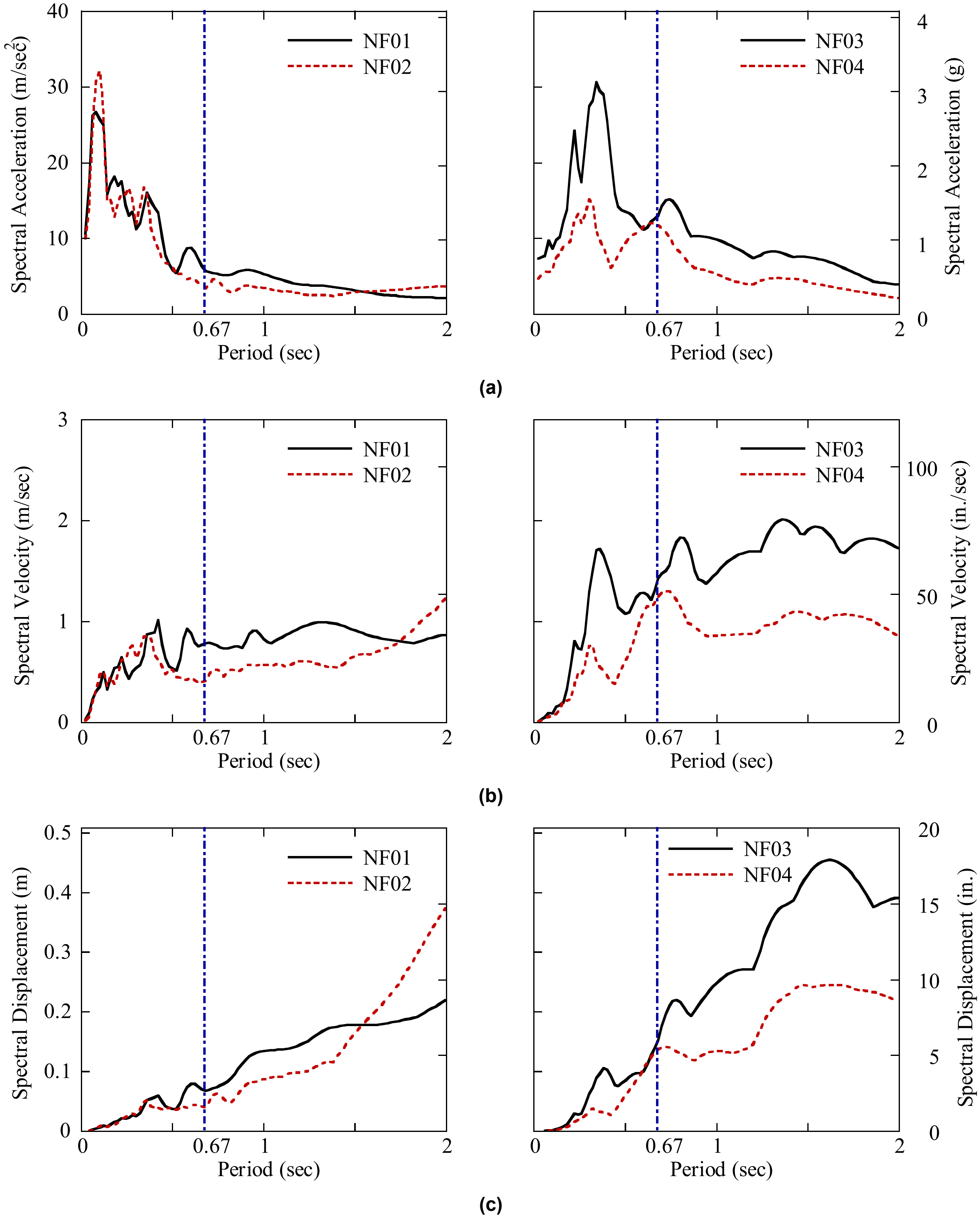

Modified Tabas records **Modified Los Gatos records**

Figure B.1 **Response spectra (5% damping) for the modified Tabas records and the modified Los Gators records: (a) acceleration response spectra; (b) velocity response spectra; and (c) displacement response spectra.**

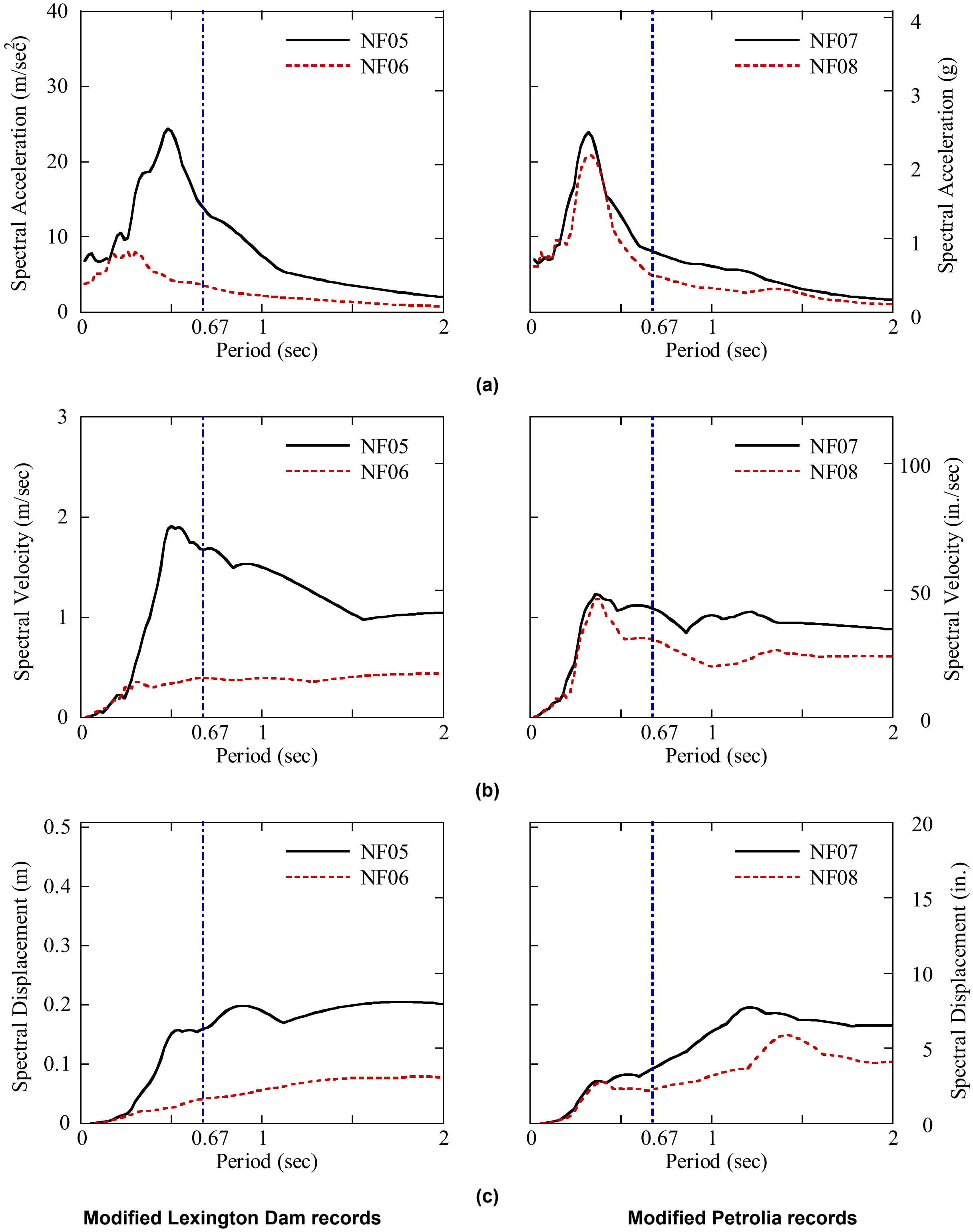

Figure B.2 **Response spectra (5% damping) for the modified Lexington Dam records and the modified Petrolia records: (a) acceleration response spectra; (b) velocity response spectra; and (c) displacement response spectra.**

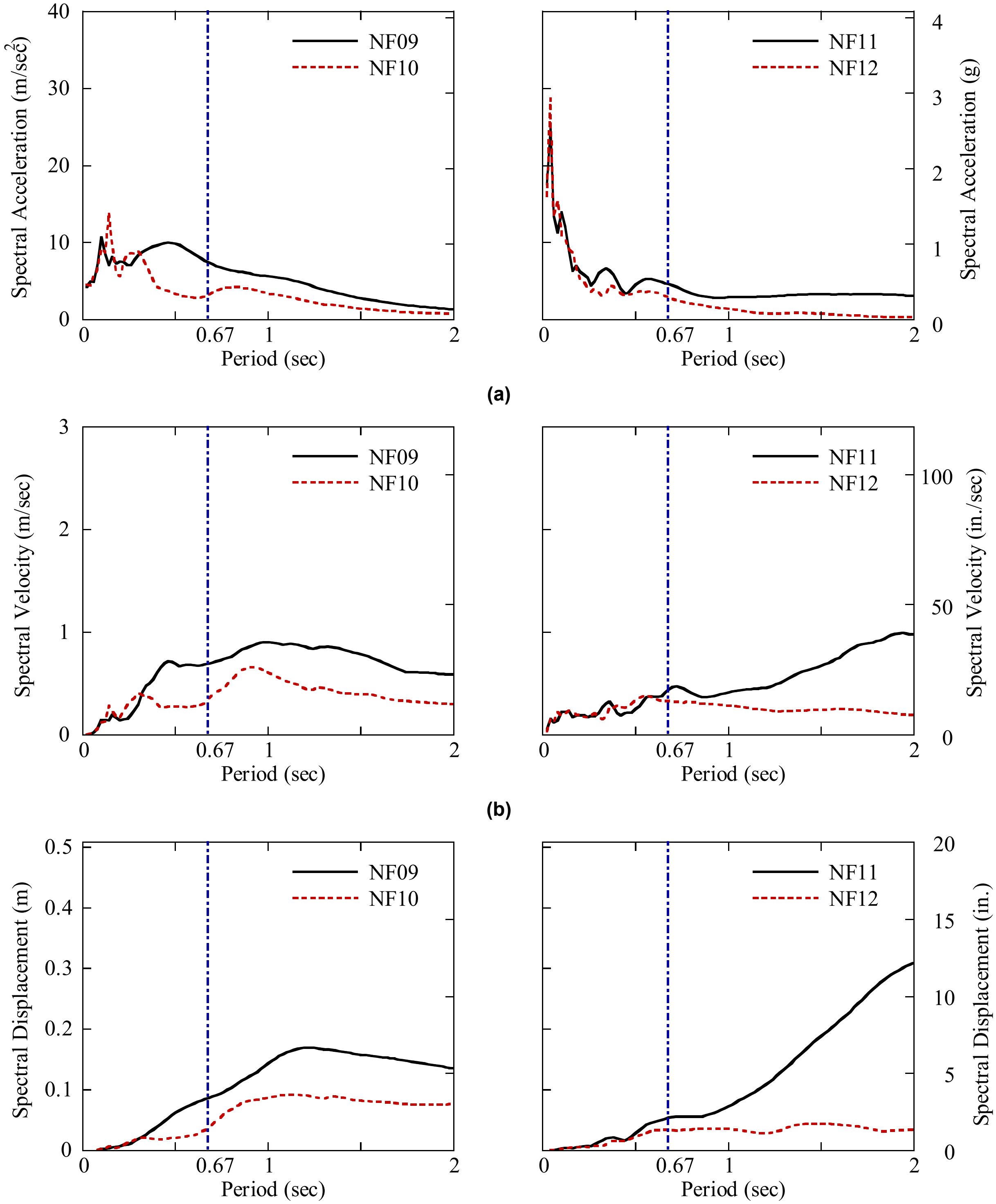

(c)

Modified Erzincan records | Modified Landers records

Figure B.3 **Response spectra (5% damping) for the modified Erzincan records and the modified Landers records: (a) acceleration response spectra; (b) velocity response spectra; and (c) displacement response spectra.**

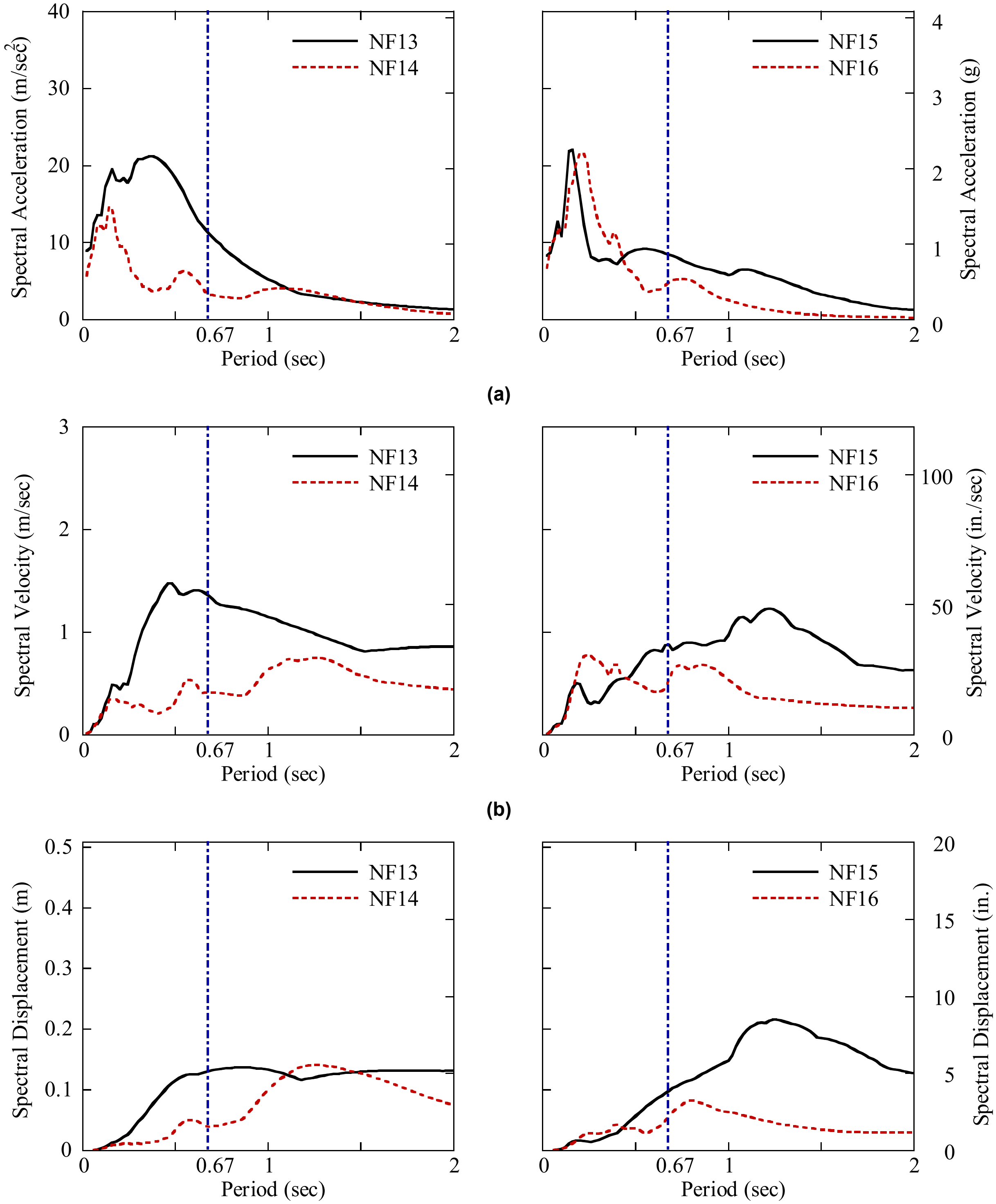

Modified Rinaldi records
Modified Olive View records

Figure B.4 **Response spectra (5% damping) for the modified Rinaldi records and the modified Olive View records: (a) acceleration response spectra; (b) velocity response spectra; and (c) displacement response spectra.**

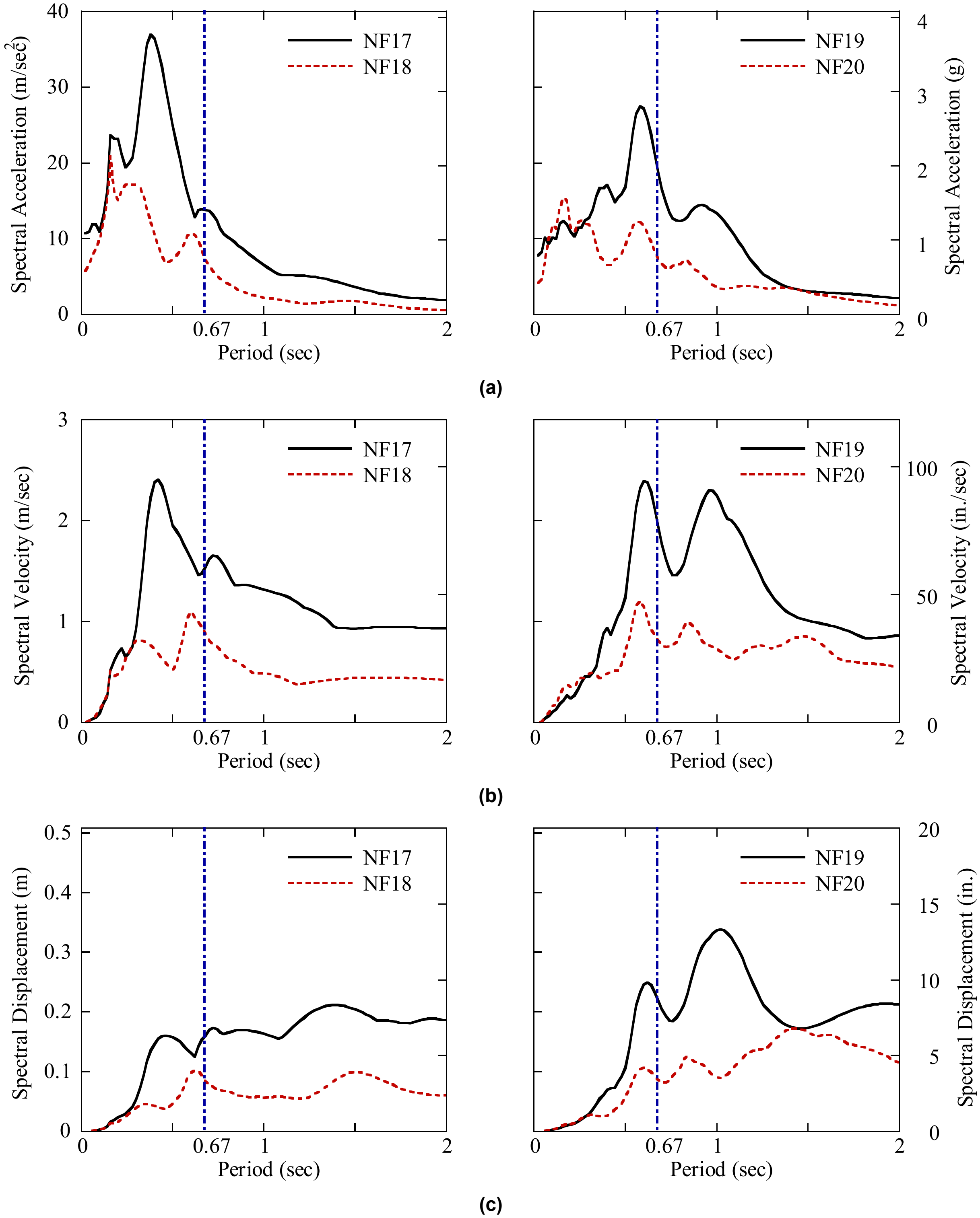

Modified JMA Kobe records Modified Takatori records

Figure B.5 Response spectra (5% damping) for the modified JMA Kobe records and the modified Takatori records: (a) acceleration response spectra; (b) velocity response spectra; and (c) displacement response spectra.

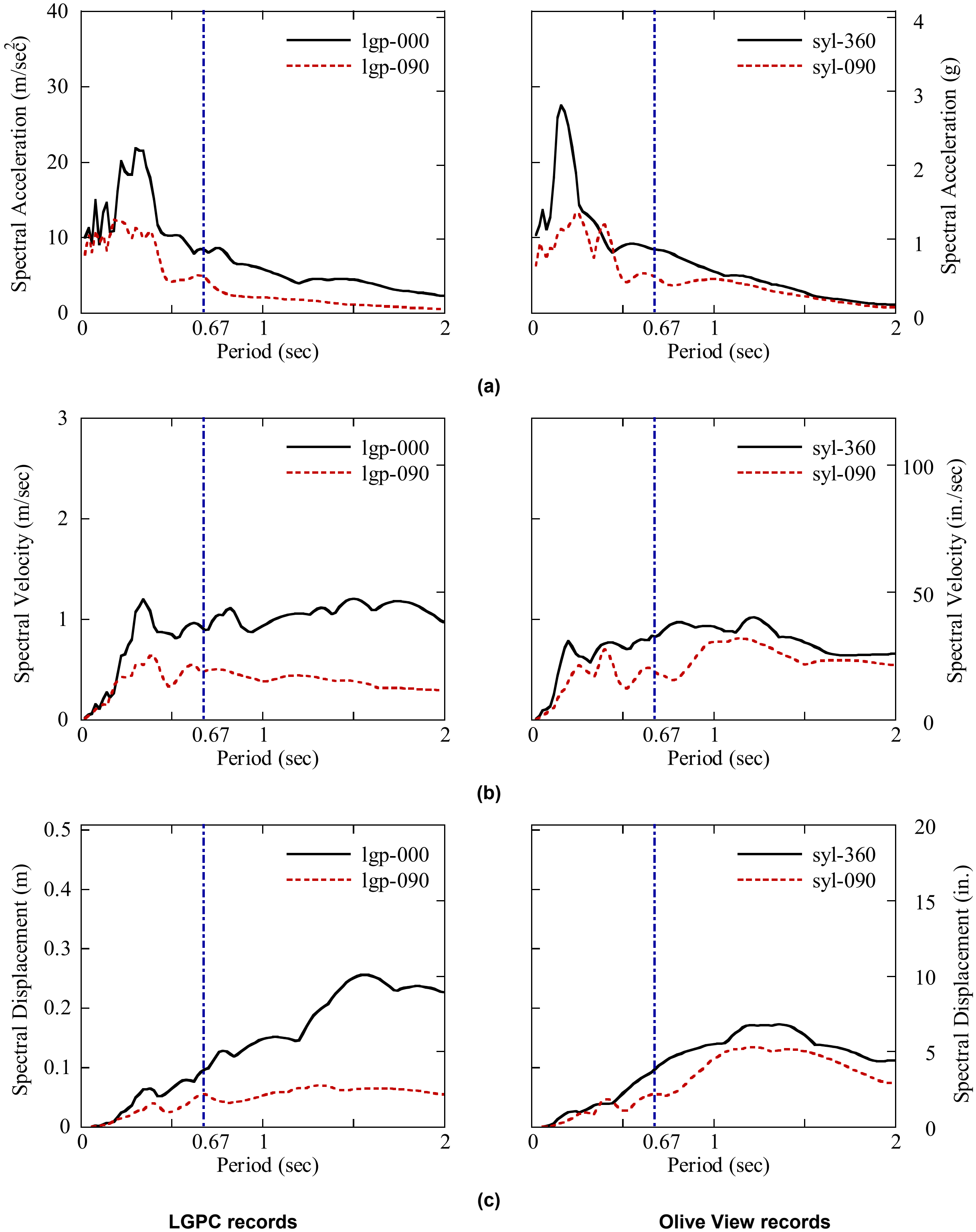

Figure B.6 Response spectra (5% damping) for the LGPC records and the Olive View records: (a) acceleration response spectra; (b) velocity response spectra; and (c) displacement response spectra.

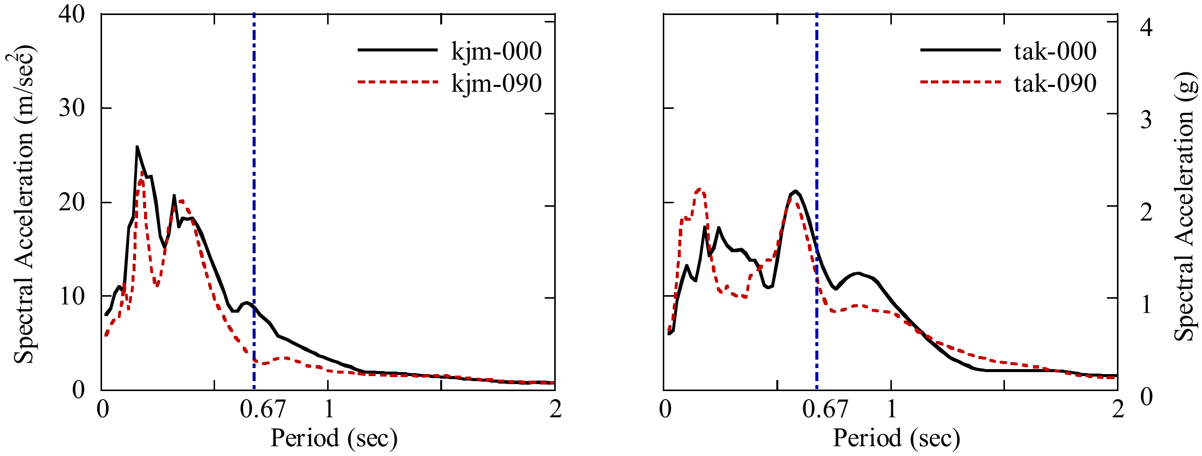

(a)

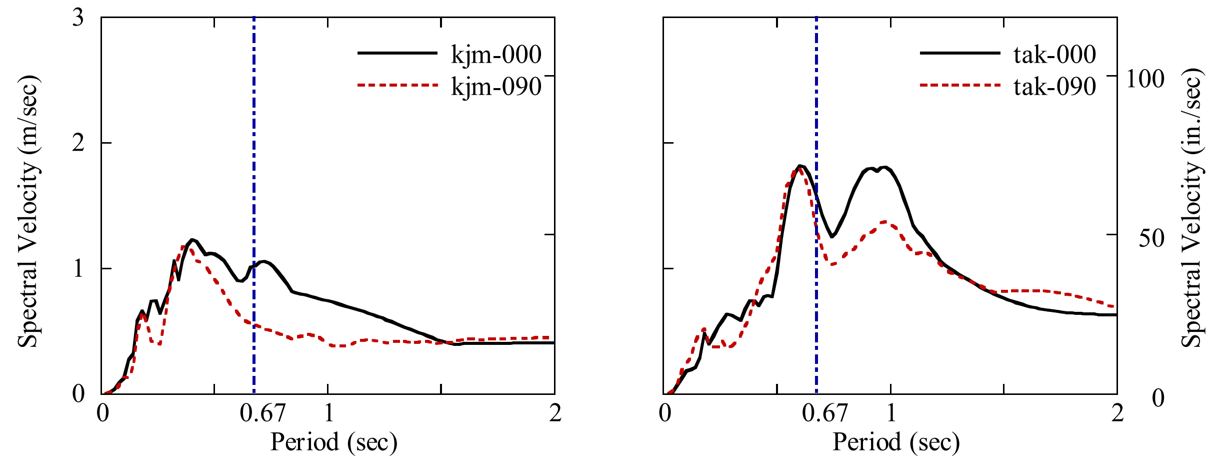

(b)

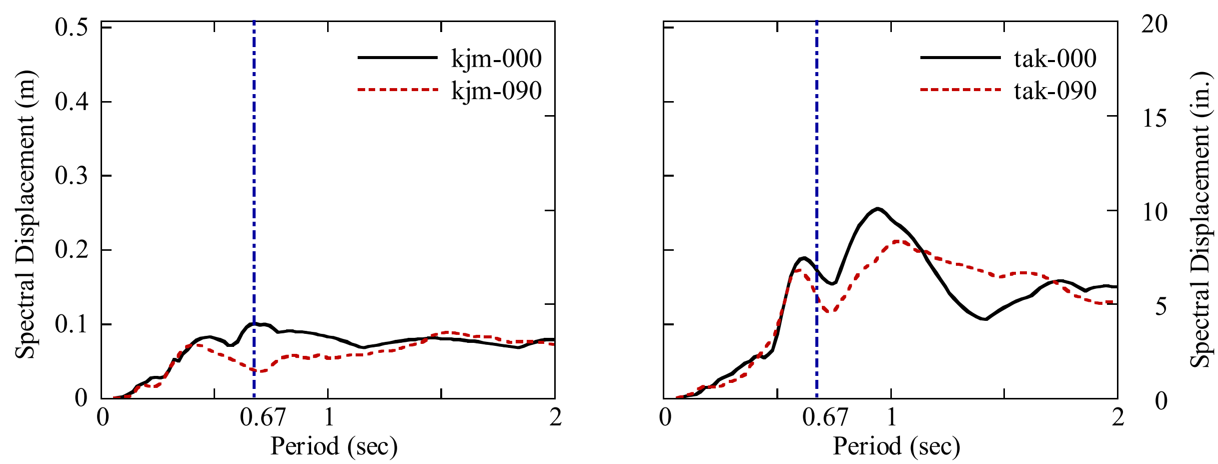

(c)

JMA Kobe records **Takatori records**

Figure B.7 Response spectra (5% damping) for the JMA Kobe records and the Takatori records: (a) acceleration response spectra; (b) velocity response spectra; and (c) displacement response spectra.

Appendix C Analytical Dynamic Response of RC Specimen

This appendix shows response displacement time histories, orbits of response displacements, and lateral force versus lateral displacement hysteresis of the conventionally designed reinforced concrete (RC) specimen obtained from a series of dynamic response analyses described in Section 2.5. Based on the analytical results, the modified Los Gatos records were selected for the earthquake simulation tests.

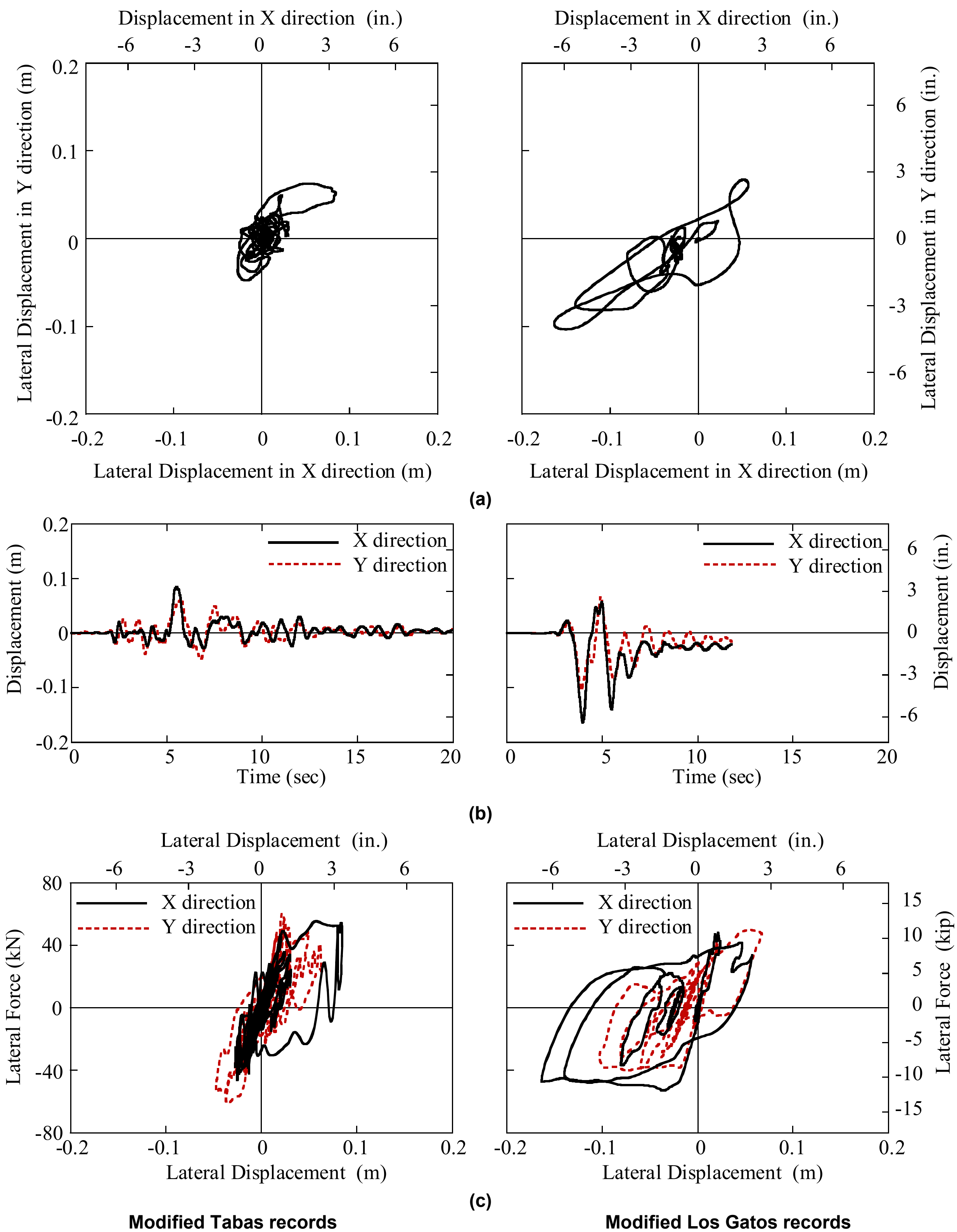

Figure C.1 Analytical dynamic response of RC specimen: (a) orbit of lateral displacements; (b) response displacement at center-of-gravity of weighted blocks; and (c) lateral force–lateral displacement hysteresis.

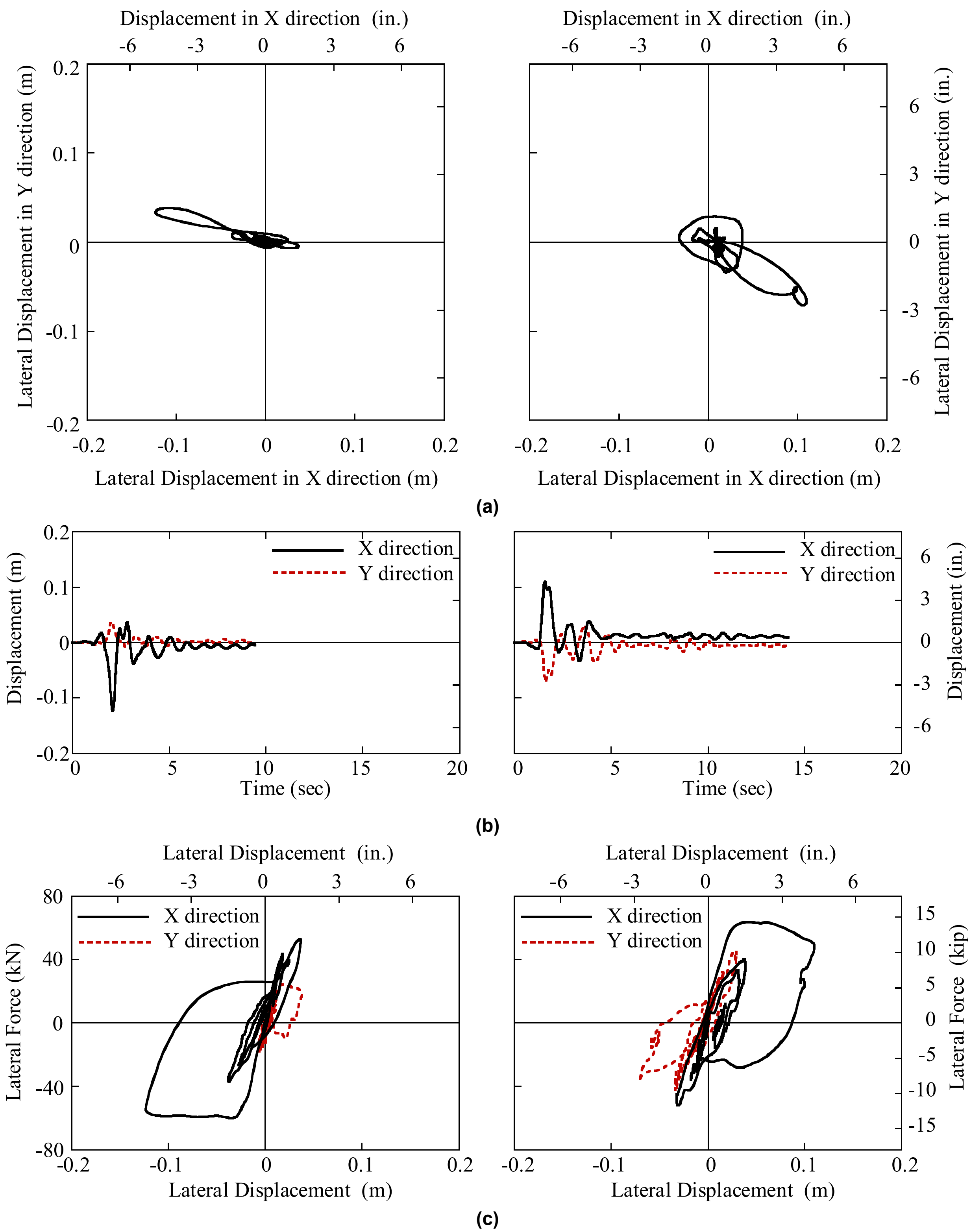

Modified Lexington Dam records **Modified Petrolia records**

Figure C.2 **Analytical dynamic response of RC specimen: (a) orbit of lateral displacements; (b) response displacement at center-of-gravity of weighted blocks; and (c) lateral force–lateral displacement hysteresis.**

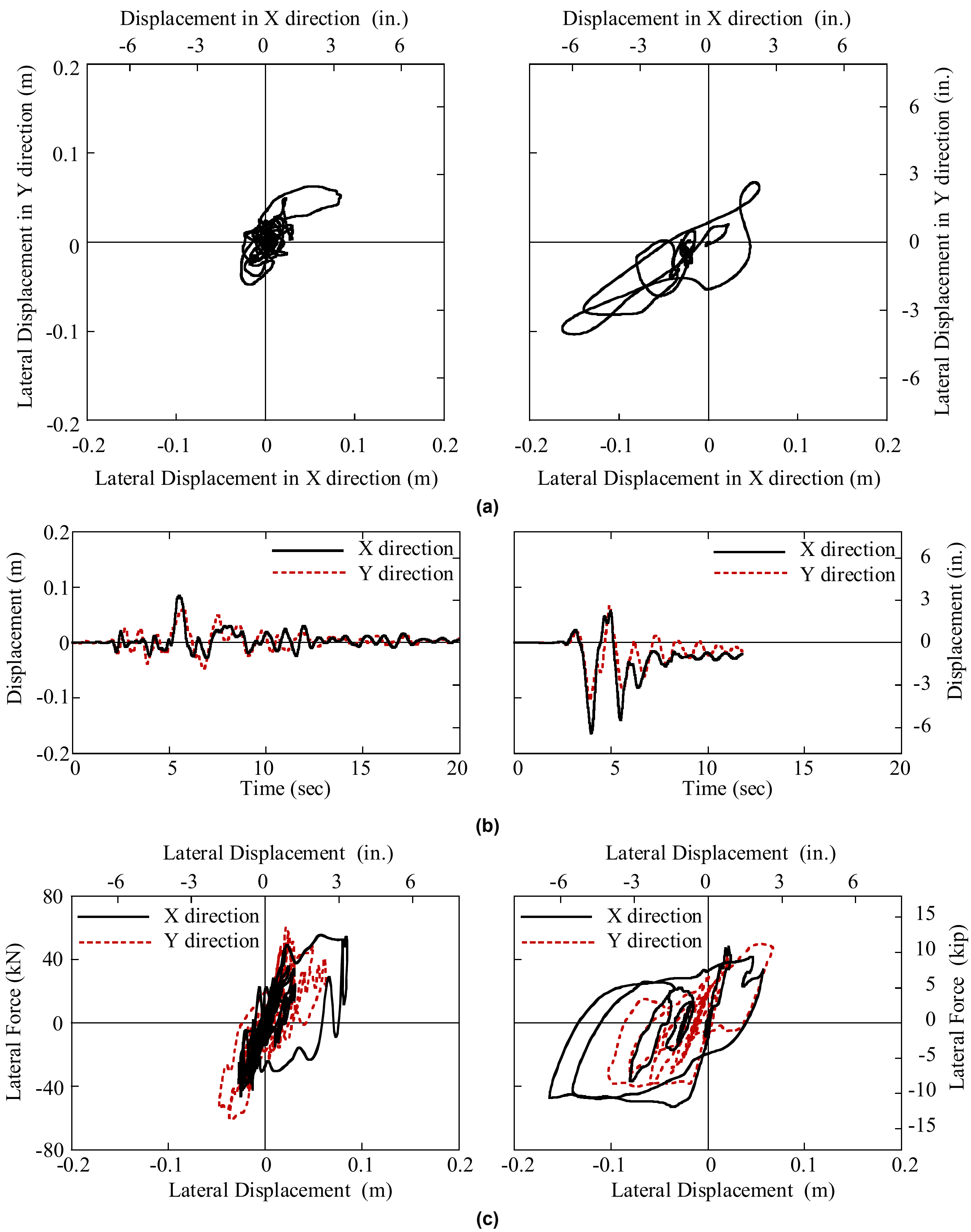

Modified Tabas records **Modified Los Gatos records**

Figure C.2 **Analytical dynamic response of RC specimen: (a) orbit of lateral displacements; (b) response displacement at center-of-gravity of weighted blocks; and (c) lateral force–lateral displacement hysteresis.**

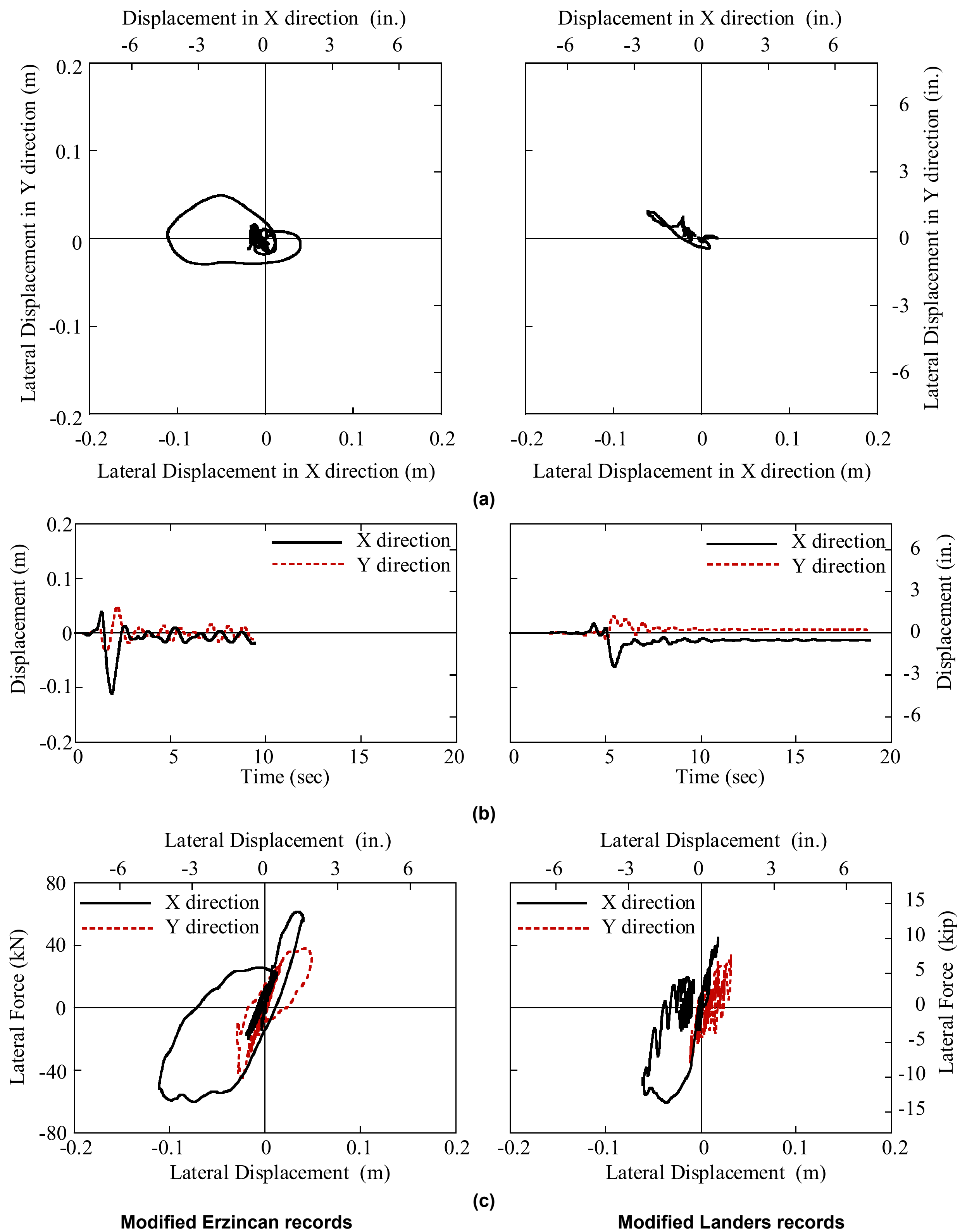

Figure C.3 Analytical dynamic response of RC specimen for the modified Erzincan records and the modified Landers records: (a) orbit of lateral displacements; (b) response displacement at center-of-gravity of weighted blocks; and (c) lateral force–lateral displacement hysteresis.

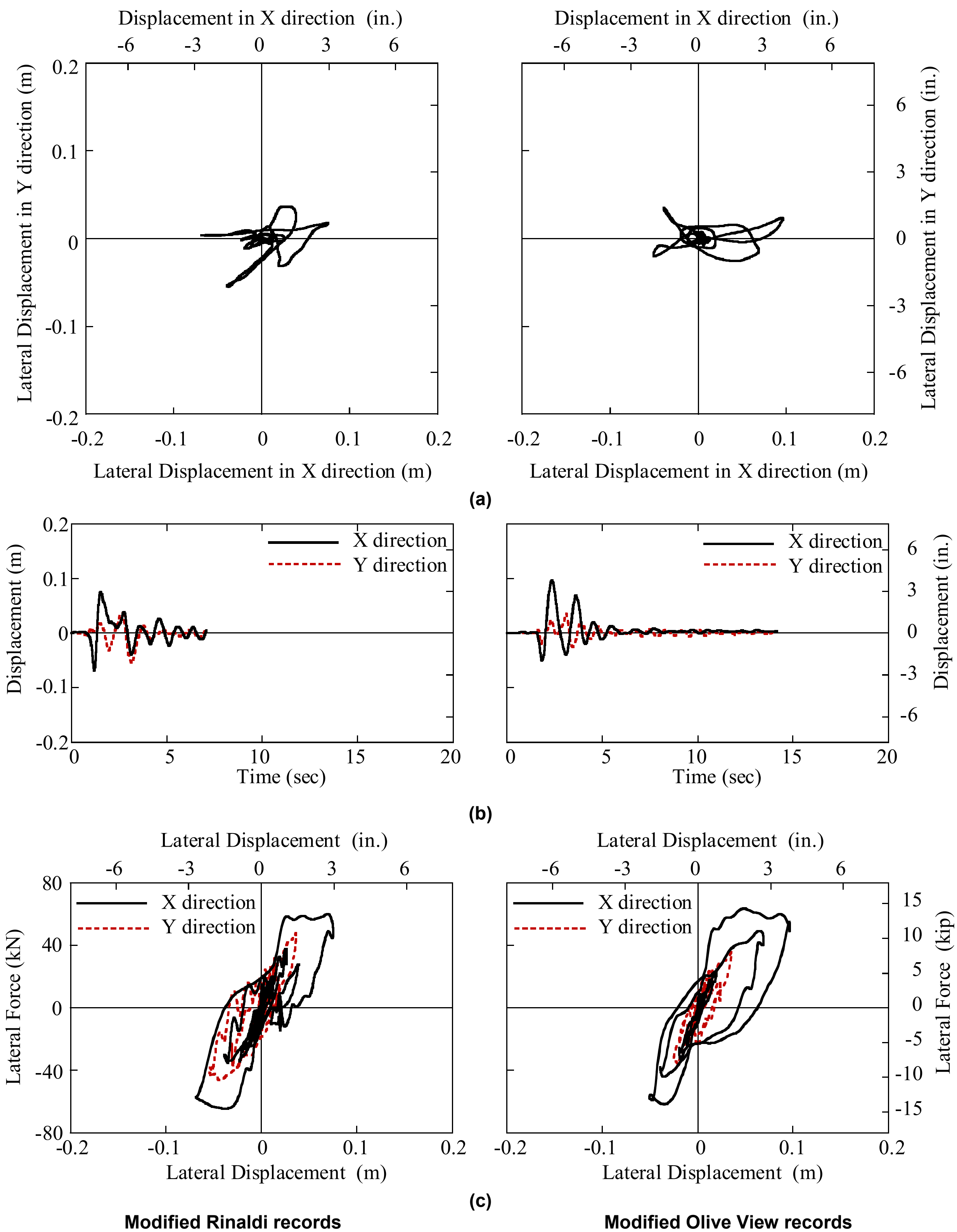

Figure C.4 **Analytical dynamic response of RC specimen for the modified Rinaldi records and the modified Olive View Records: (a) orbit of lateral displacements; (b) response displacement at center-of-gravity of weighted blocks; and (c) lateral force–lateral displacement hysteresis.**

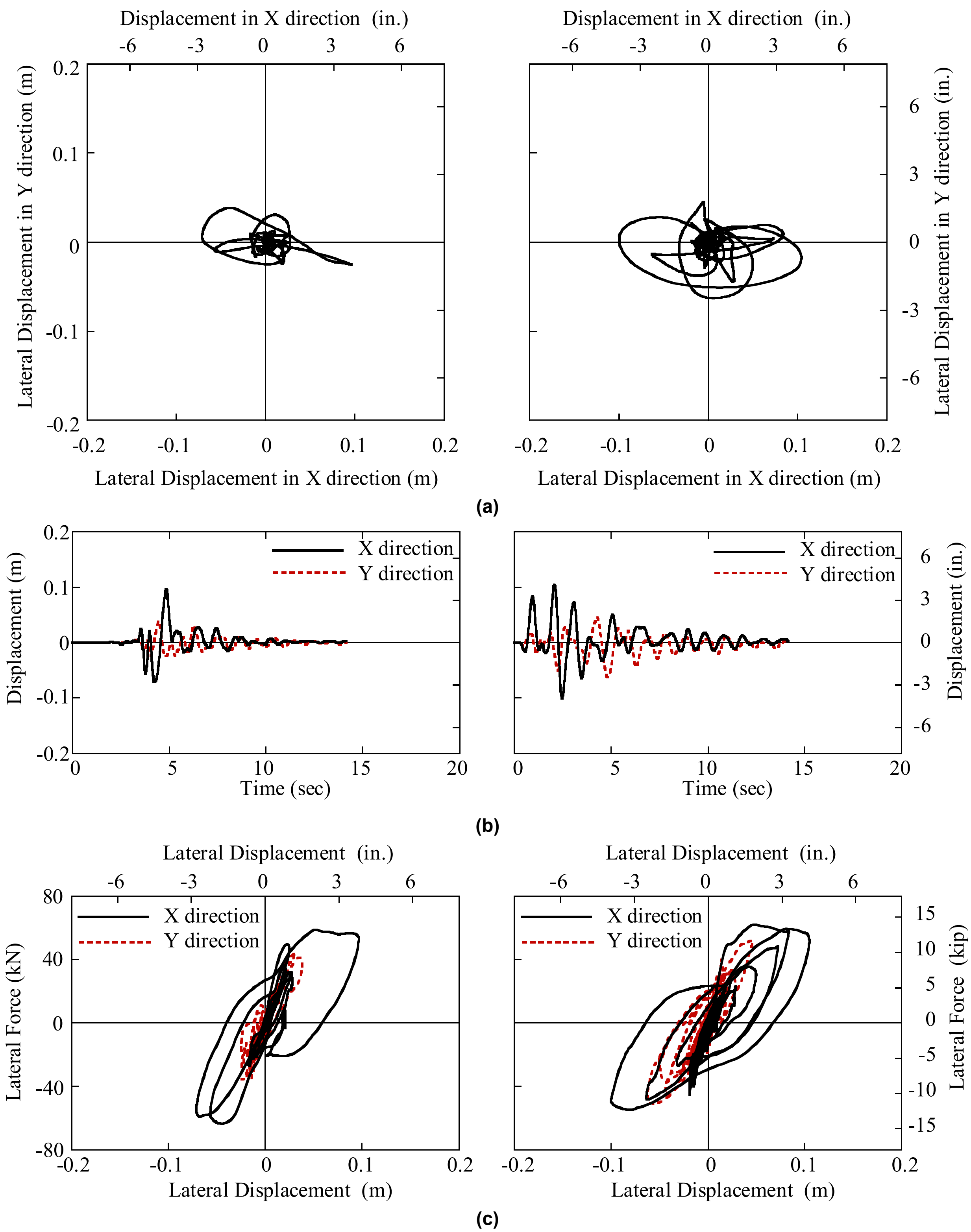

Modified JMA Kobe records **Modified Takatori records**

Figure C.5 Analytical dynamic response of RC specimen for modified JMA Kobe records and the modified Takatori records: (a) orbit of lateral displacements; (b) response displacement at center-of-gravity of weighted blocks; and (c) lateral force–lateral displacement hysteresis.

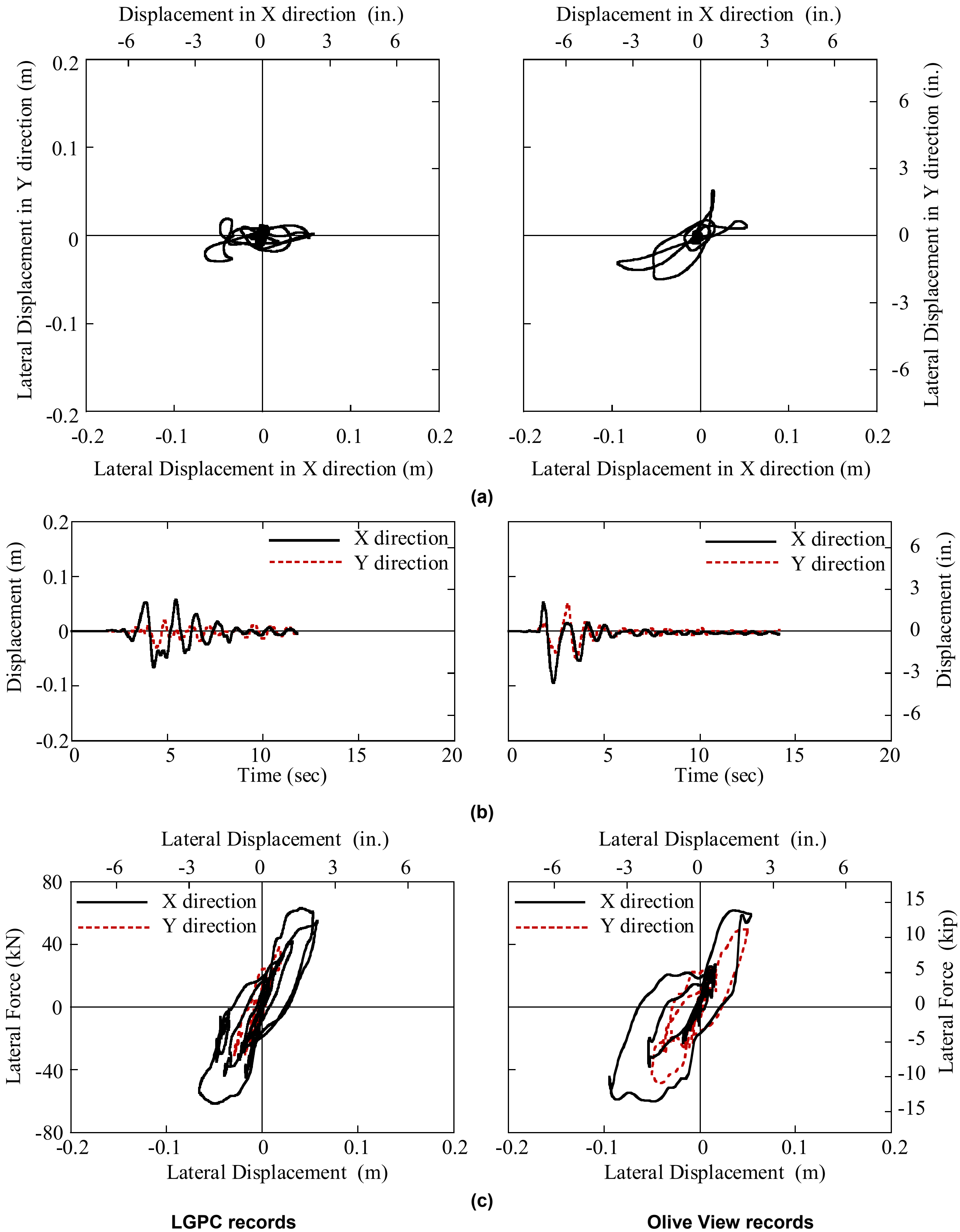

Figure C.6 Analytical dynamic response of RC specimen for the LGPC records and the Olive View records: (a) orbit of lateral displacements; (b) response displacement at center-of-gravity of weighted blocks; and (c) lateral force–lateral displacement hysteresis.

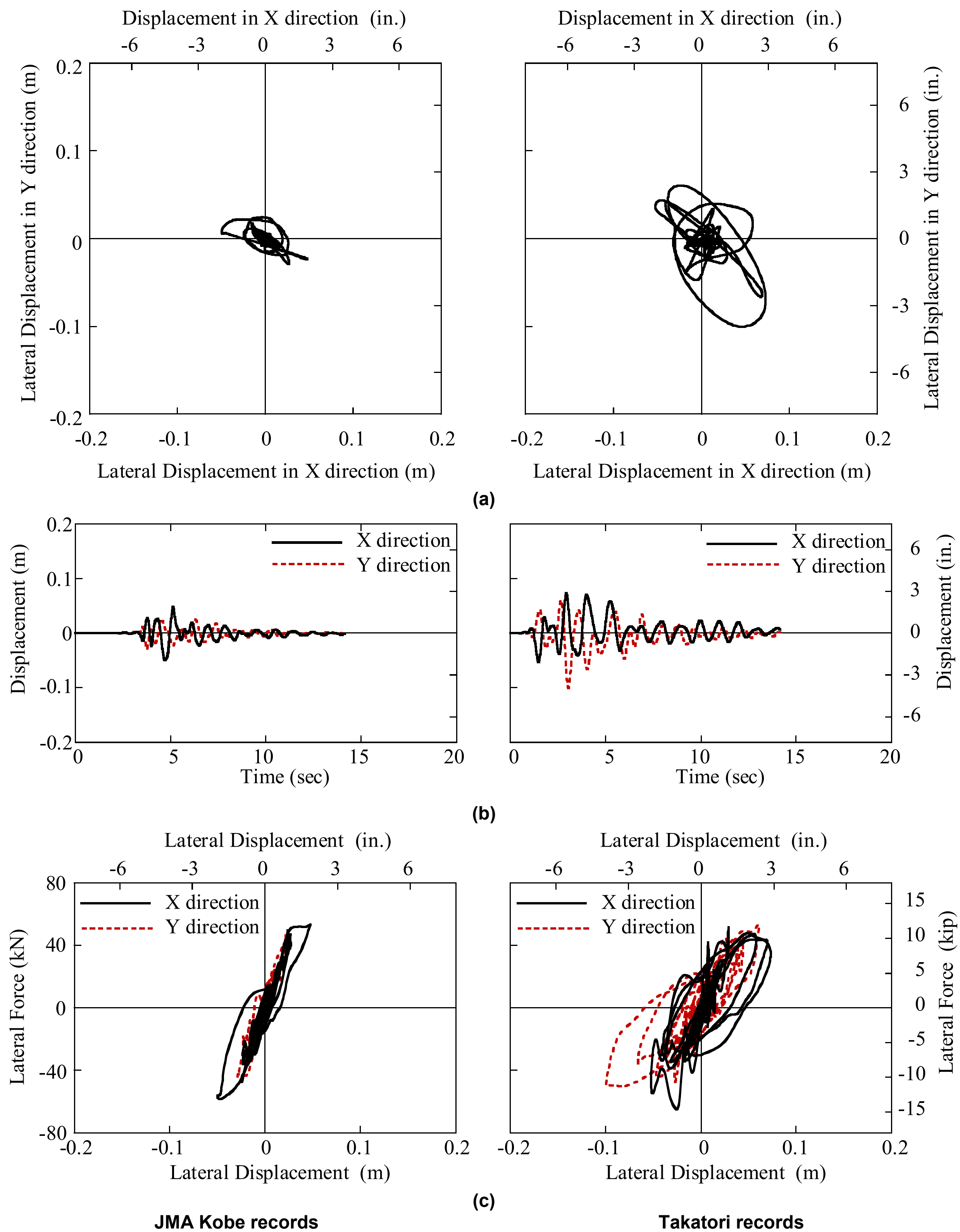

Figure C.7 **Analytical dynamic response of RC specimen for the JMA Kobe records and the Takatori records: (a) orbit of lateral displacements; (b) response displacement at center-of-gravity of weighted blocks; and (c) lateral force–lateral displacement hysteresis.**

Appendix D: Effect of Bi-Directional Movement of Specimens on Measured Lateral Displacement Response

This appendix shows the effects of bi-directional movement of specimens on measured lateral displacement response. The displacements measured by the instruments do not exactly represent an actual movement in each direction under bi-directional excitation. As shown in Figure D.1, the measured lateral displacements include the effects of movement in the other direction.

The actual and measured lateral displacements have the following geometric relation:

$$\left(D_{x\cdot m}+L_x\right)^2 = D_{y\cdot r}{}^2 + \left(D_{x\cdot r}+L_x\right)^2 \tag{D.1}$$

$$\left(D_{y\cdot m}+L_y\right)^2 = D_{x\cdot r}{}^2 + \left(D_{y\cdot r}+L_y\right)^2 \tag{D.2}$$

where $D_{x\cdot r}$ and $D_{y\cdot r}$ are the actual lateral displacements in the *X*- and *Y*-directions, respectively; $D_{x\cdot m}$ and $D_{y\cdot m}$ are the measured lateral displacements in the *X*- and *Y*-directions; and L_x and L_y are the initial length of the wires of the linear potentiometers. Here L_x and L_y are 2.18 m (86 in.) and 4.42 m (174 in.), respectively, in the test setup used in this study.

Based on these relation, the actual lateral displacements, $D_{x\cdot r}$ and $D_{y\cdot r}$ can be obtained from the following equations;

$$D_{x\cdot r} = a\,D_{y\cdot r} + b \tag{D.3}$$

$$D_{y\cdot r} = \frac{-\left(ab+L_y\right) \pm \sqrt{\left(a+L_y\right)^2 - \left(1+a^2\right)\left(b^2 - D_{y\cdot m}{}^2 - 2L_y D_{y\cdot m}\right)}}{1+a^2} \tag{D.4}$$

where

$$a = L_y / L_x \tag{D.5}$$

$$b = \frac{D_{x\cdot m}{}^2 + 2L_x D_{x\cdot m} - \left(D_{y\cdot m}{}^2 + 2L_y D_{y\cdot m}\right)}{2L_x} \tag{D.6}$$

(D.6)

Figure D.2 compares the actual and measured lateral displacement of the RC specimen during the design- and the maximum-level tests. There was an insignificant discrepancy between the actual and measured lateral displacements during the design-level test; only 0.0025 m (0.1 in.) at the most. There was some discrepancy during the maximum-level test of the lateral displacement in the *Y*-direction due to large displacement in the other direction; however, this still remained only less than 0.01 m (0.4 in.). Given that the effects of the lateral movement of the specimens on the measured lateral displacement were minor, the measured lateral displacements were used in discussion of dynamic behavior of the specimens in Chapter 4.

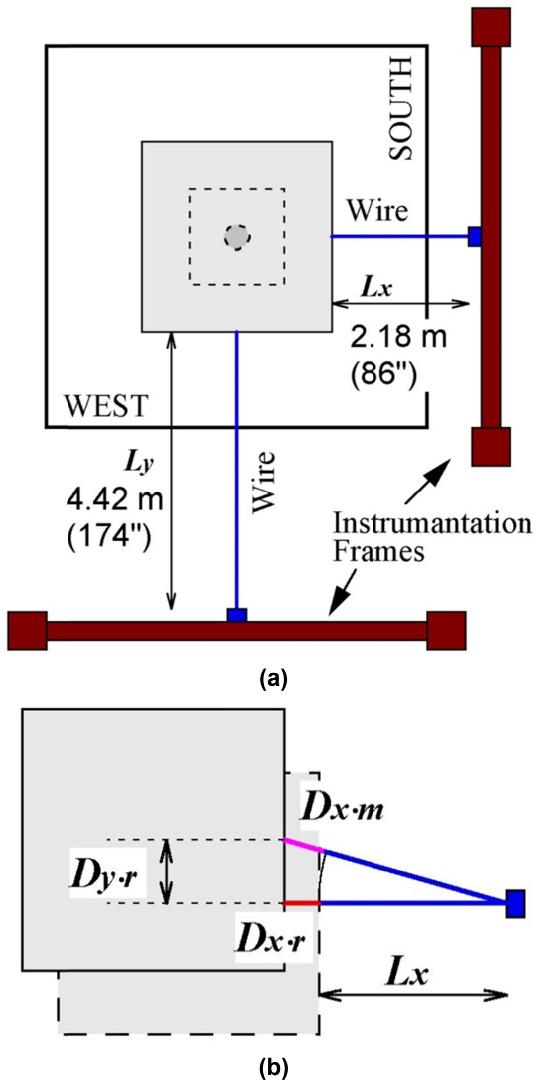

Figure D.1 Measurement of lateral displacement response: (a) locations of linear potentiometers and length of wires; and (b) relation between actual and measured lateral displacement.

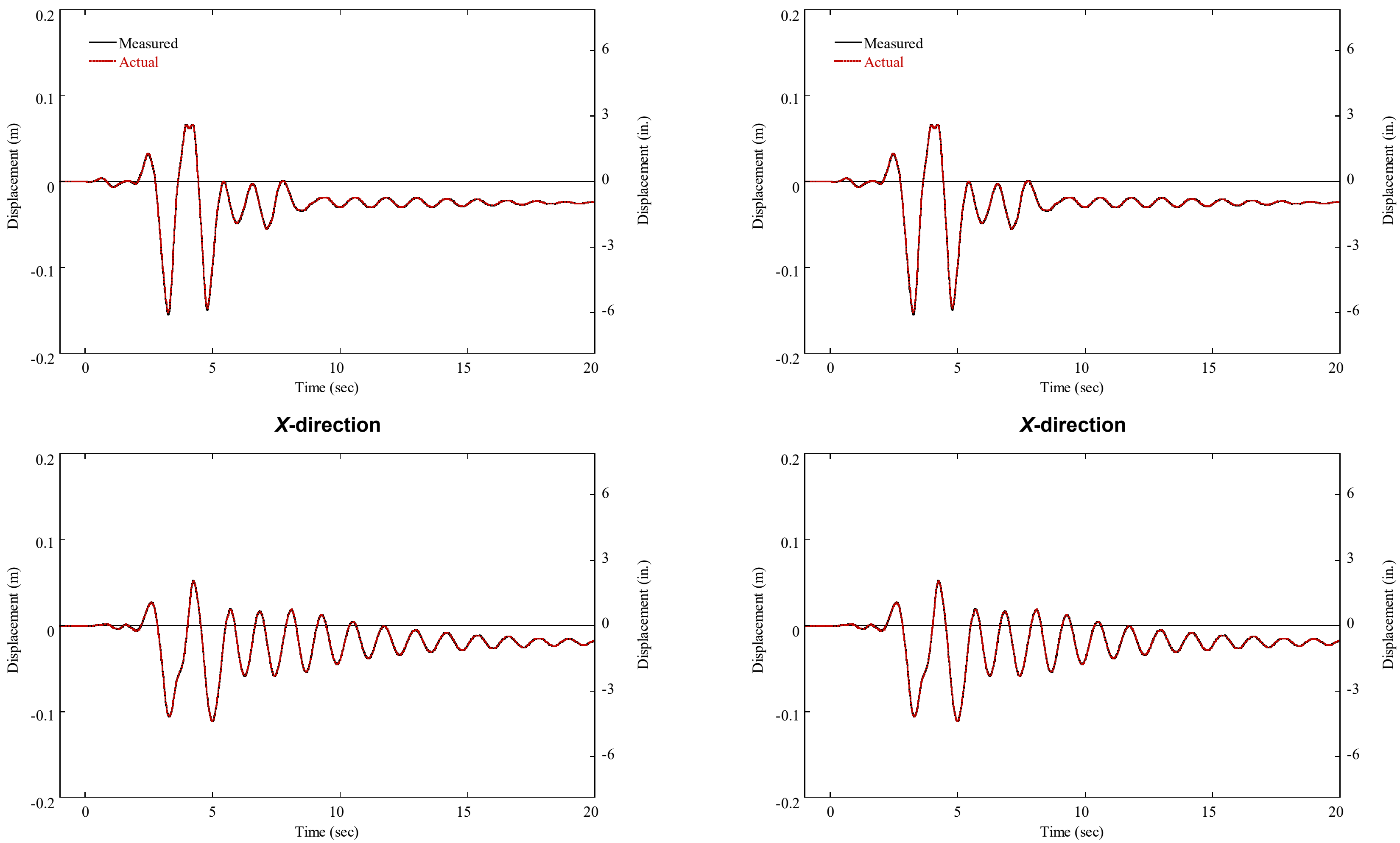

***X*-direction**

***X*-direction**

***Y*-direction**
(a)

***Y*-direction**
(b)

Figure D.2 Actual and measured response displacement for (a) the design-level test and (b) the maximum-level test.

Appendix E: Performance of Earthquake Simulator

This appendix shows the performance of earthquake simulator. Fourier spectra, acceleration time histories, and response spectra were generated from accelerations measured at the footing to show how the simulator re-produced the input signals. Comparisons between the footing displacements and input signals show not only the re-product ability of the simulator, but also how large undesirable rotational movements of the simulator developed.

Figure E.1 shows the locations of instruments of the footing. Accelerations measured at the west face are used to show accelerations in *X*-direction (accel1 in Table 3.4), and ones measured at the south face are used for *Y*-direction (accel5 in Table 3.4). The measured accelerations at the west and south faces have very similar characteristics.

As described in Section 4.1, the measured accelerations were low-pass filtered with a cutoff frequency of 20 Hz to remove high-frequency noise; the measured displacements were not filtered. Footing displacements are obtained as an average of measurements of two of three linear potentiometers that were placed at both sides at each face because the center one did not work properly in some of the tests.

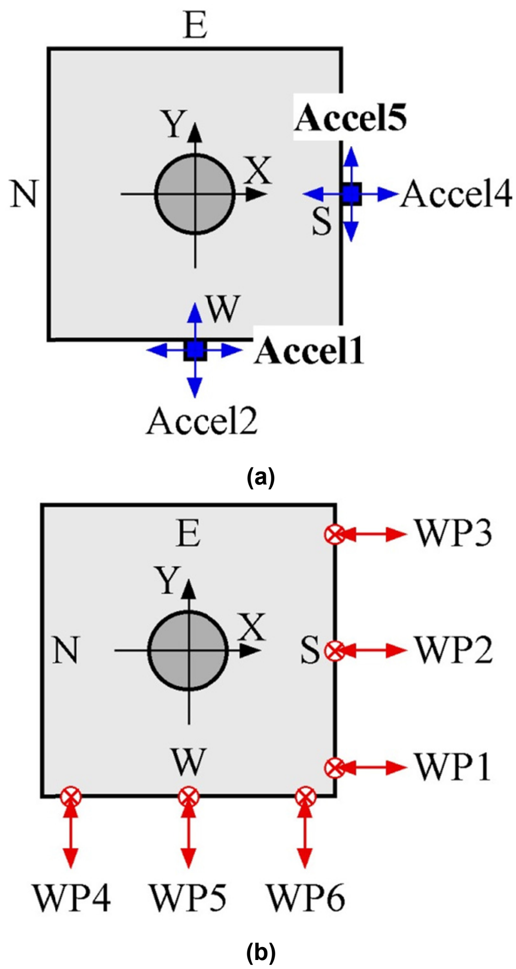

Figure E.1 Locations of instruments of footing: (a) accelerometers and (b) linear potentiometers (wire pods).

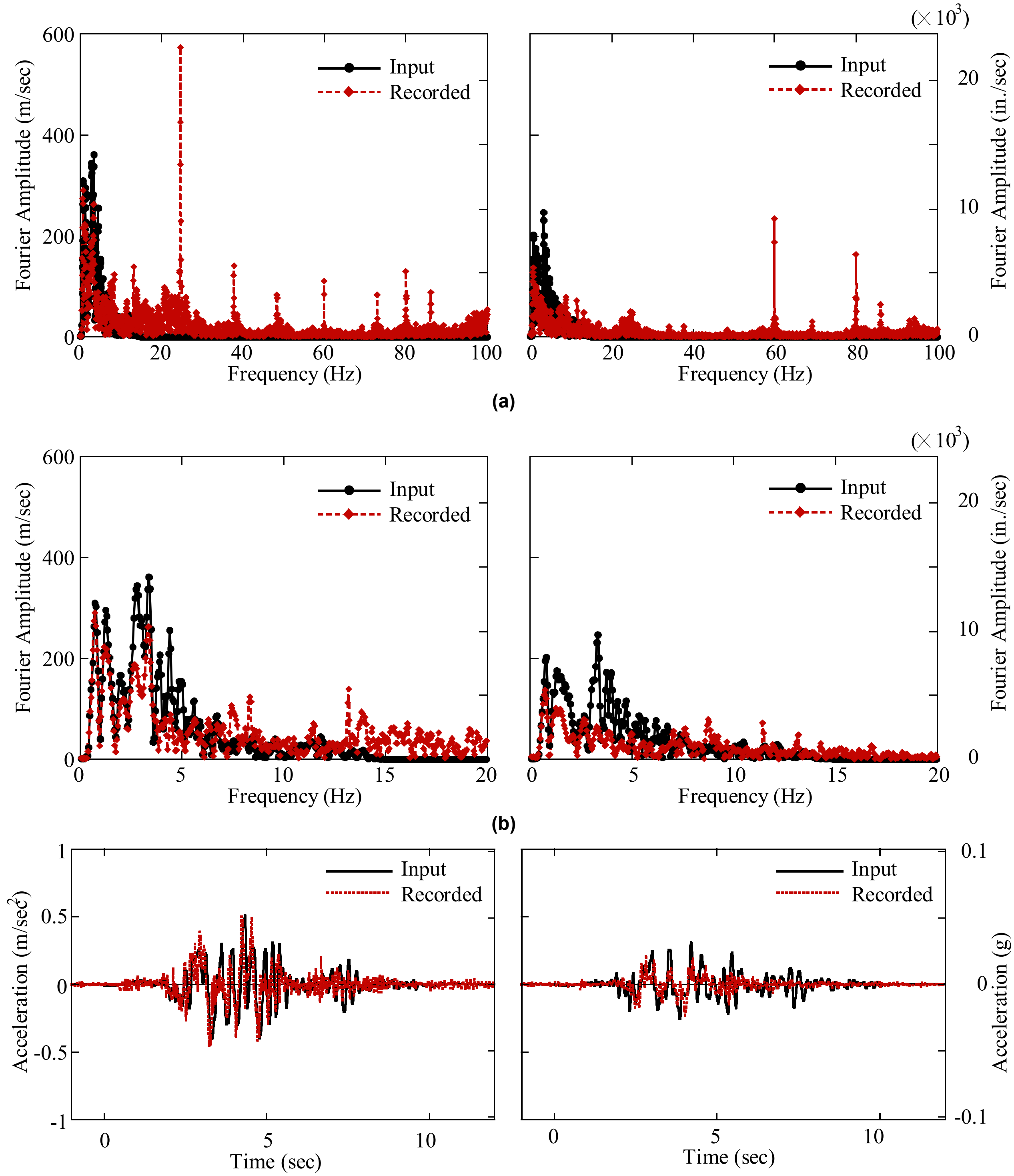

(c)

***X*-direction (NF03)** **_Y_-direction (NF04)**

Figure E.2(a) Fourier spectra and acceleration time histories for the elastic-level test for conventional reinforced concrete column specimen (B-3-14); (a) Fourier spectra for entire range; (b) Fourier spectra under 20 Hz; and (c) acceleration measured at footing.

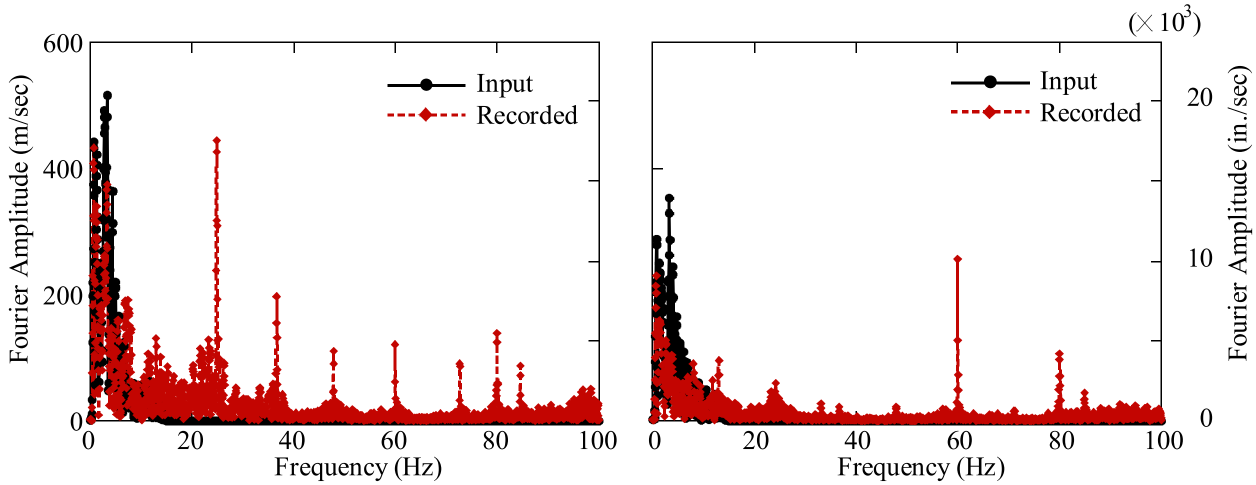

(a)

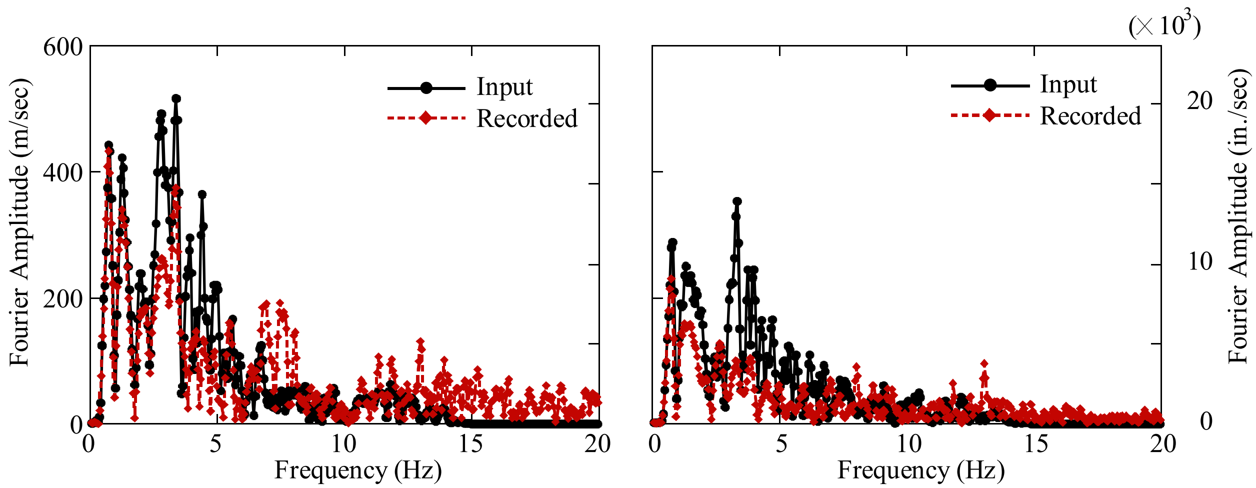

(b)

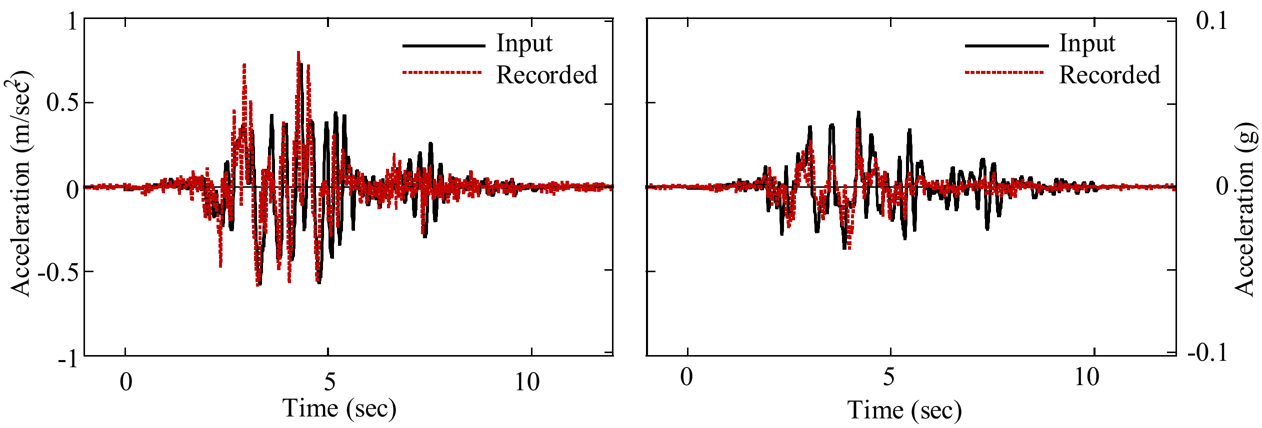

(c)

***X*-direction (NF03)** ***Y*-direction (NF04)**

Figure E.2(b) **Fourier spectra and acceleration time histories for the yield-level test for conventional reinforced concrete column specimen (B-3-15); (a) Fourier spectra for entire range; (b) Fourier spectra under 20 Hz; and (c) acceleration measured at footing.**

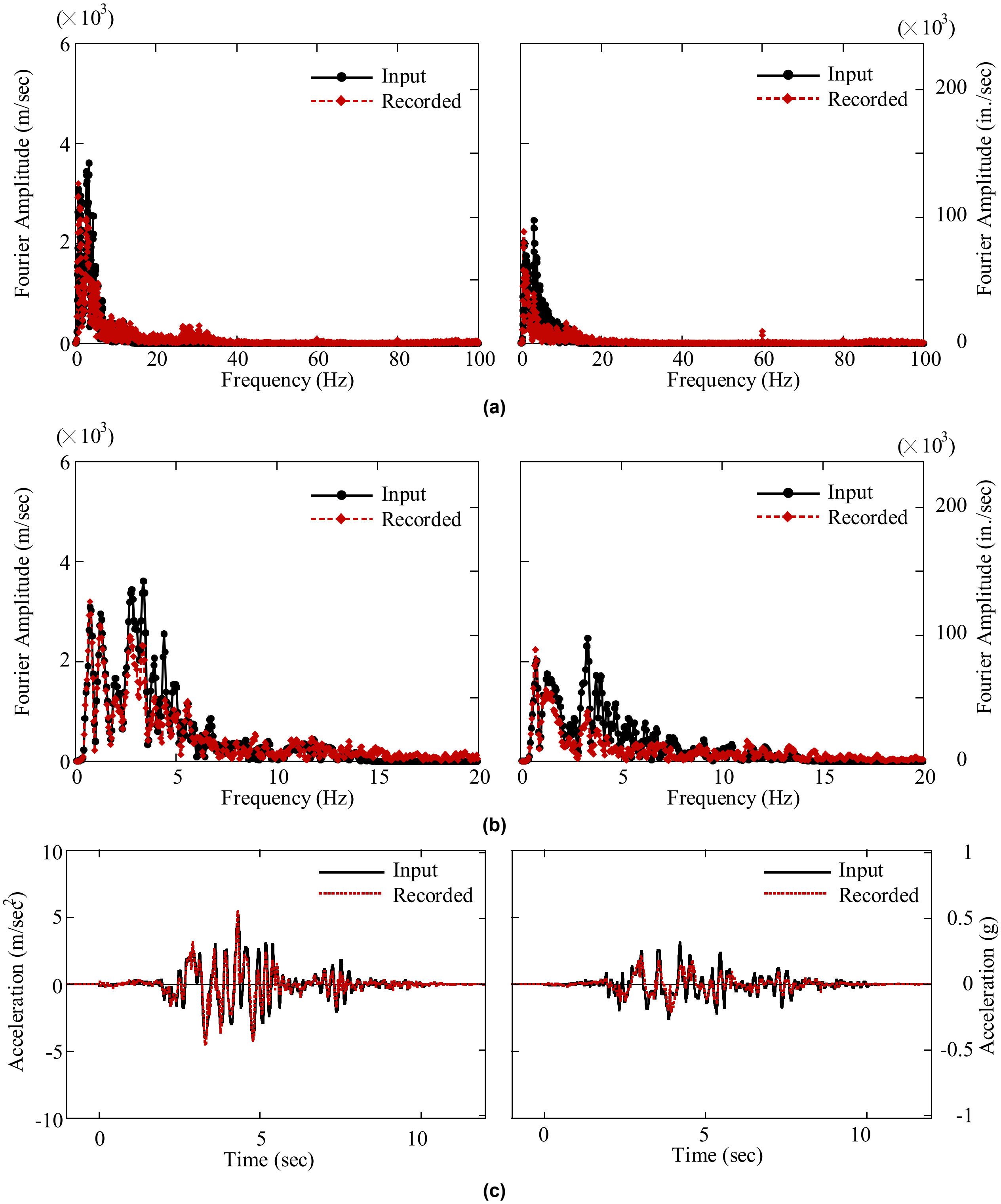

***X*-direction (NF03)** ***Y*-direction (NF04)**

Figure E.2(c) Fourier spectra and acceleration time histories for the design-level test for conventional reinforced concrete column specimen (B-3-19); (a) Fourier spectra for entire range; (b) Fourier spectra under 20 Hz; and (c) acceleration measured at footing.

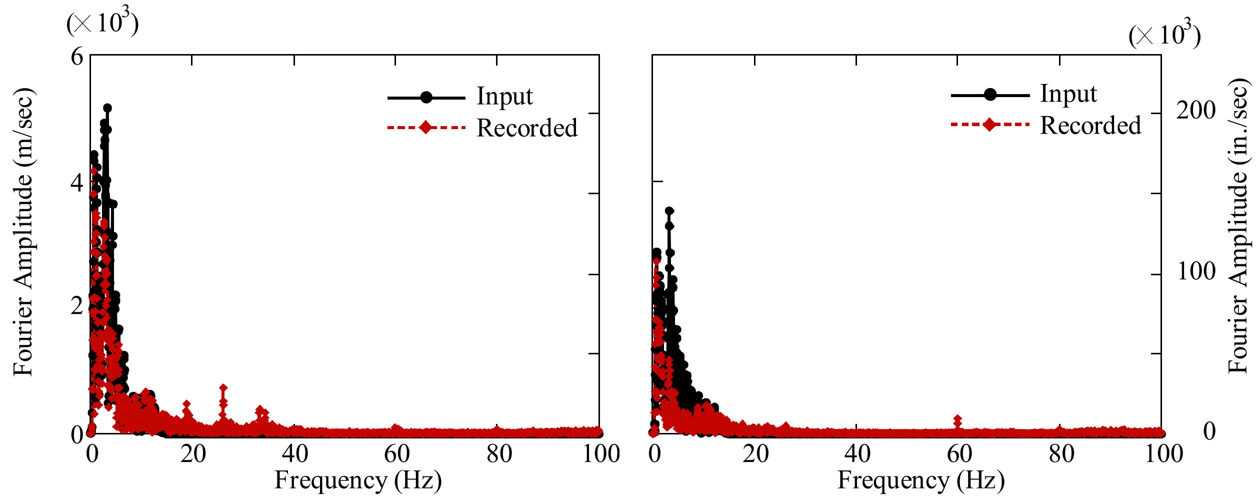

(a)

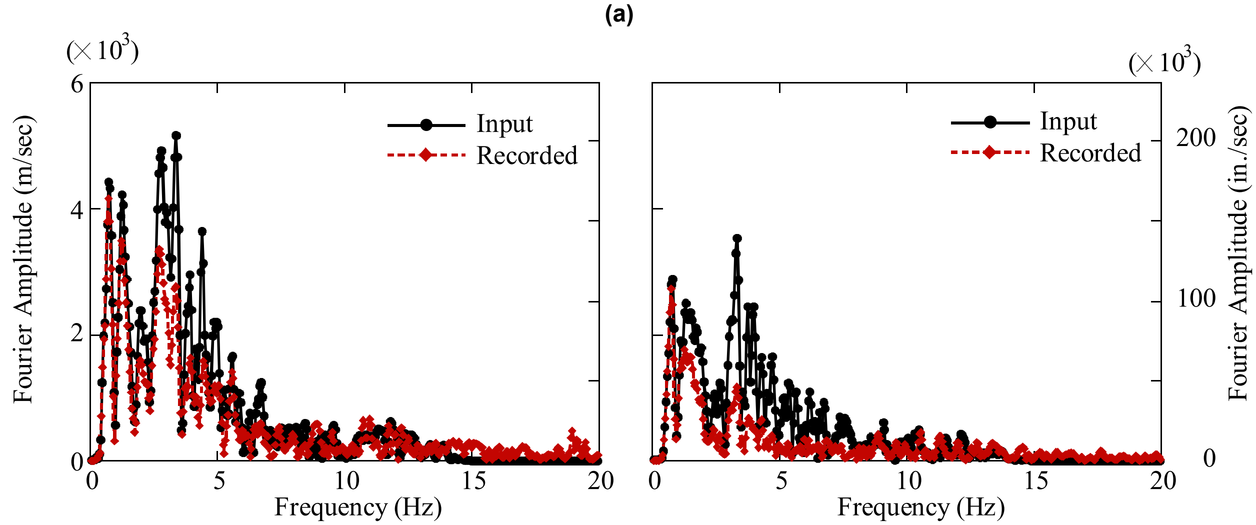

(b)

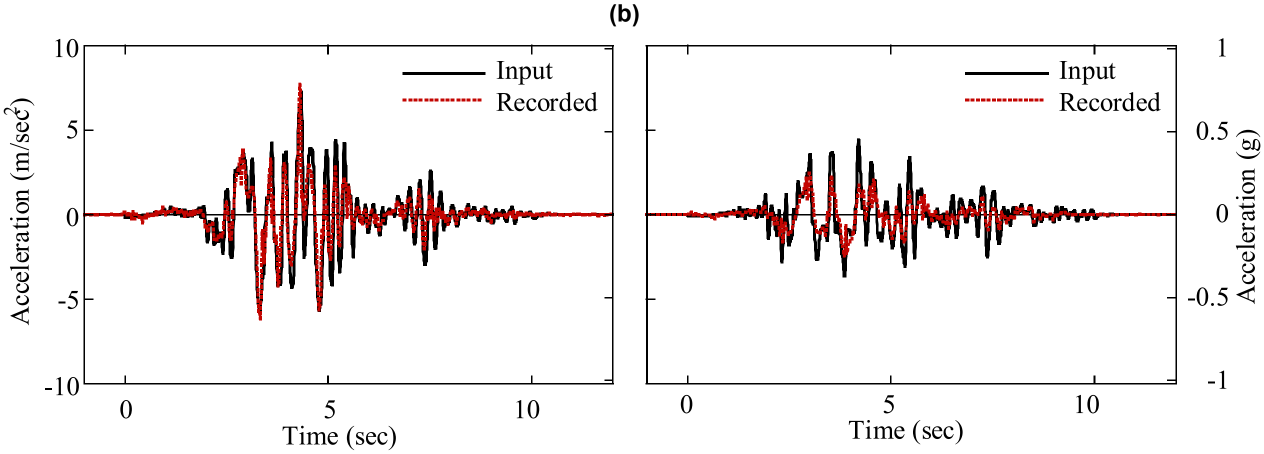

(c)

***X*-direction (NF03)** ***Y*-direction (NF04)**

Figure E.2(d) Fourier spectra and acceleration time histories for the maximum-level test for conventional reinforced concrete column specimen (B-3-23); (a) Fourier spectra for entire range; (b) Fourier spectra under 20 Hz; and (c) acceleration measured at footing.

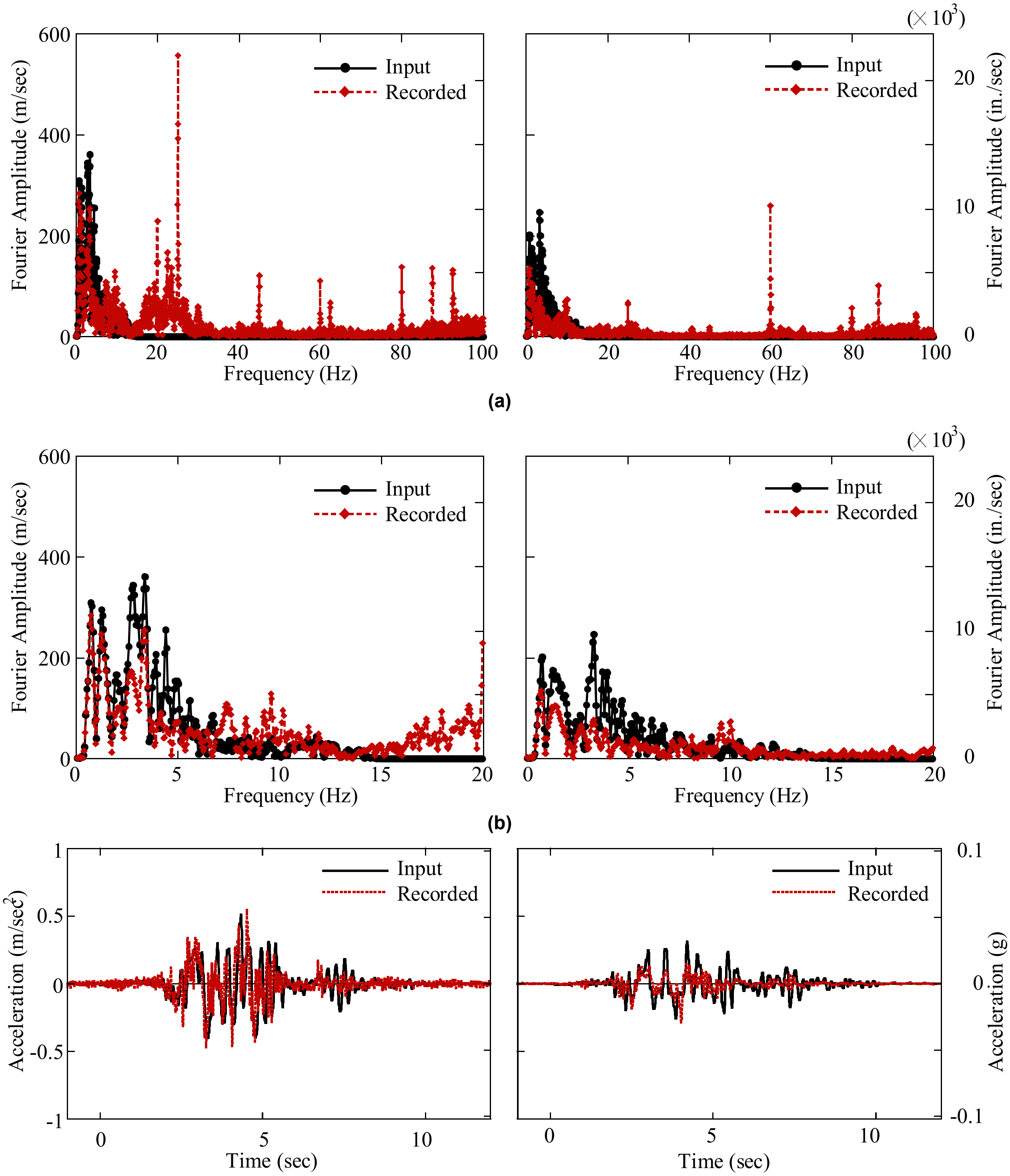

(c)

***X*-direction (NF03)** ***Y*-direction (NF04)**

Figure E.2(e) Fourier spectra and acceleration time histories for the elastic-level test for the prestressed concrete column specimen (C-10); (a) Fourier spectra for entire range; (b) Fourier spectra under 20 Hz; and (c) acceleration measured at footing.

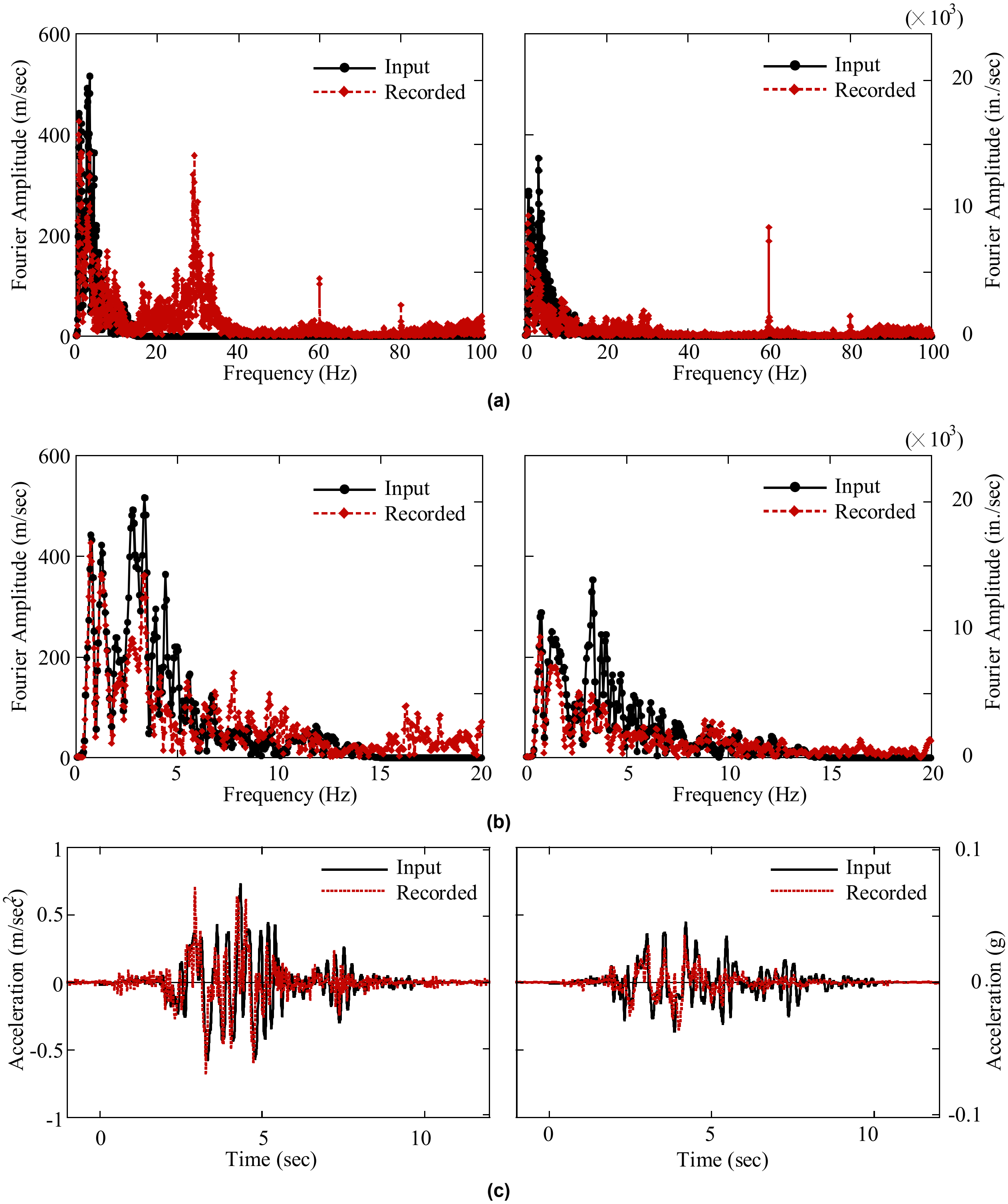

***X*-direction (NF03)** **_Y_-direction (NF04)**

Figure E.2(f) Fourier spectra and acceleration time histories for the yield-level test for the partially prestressed concrete column (C-11); (a) Fourier spectra for entire range; (b) Fourier spectra under 20 Hz; and (c) acceleration measured at footing.

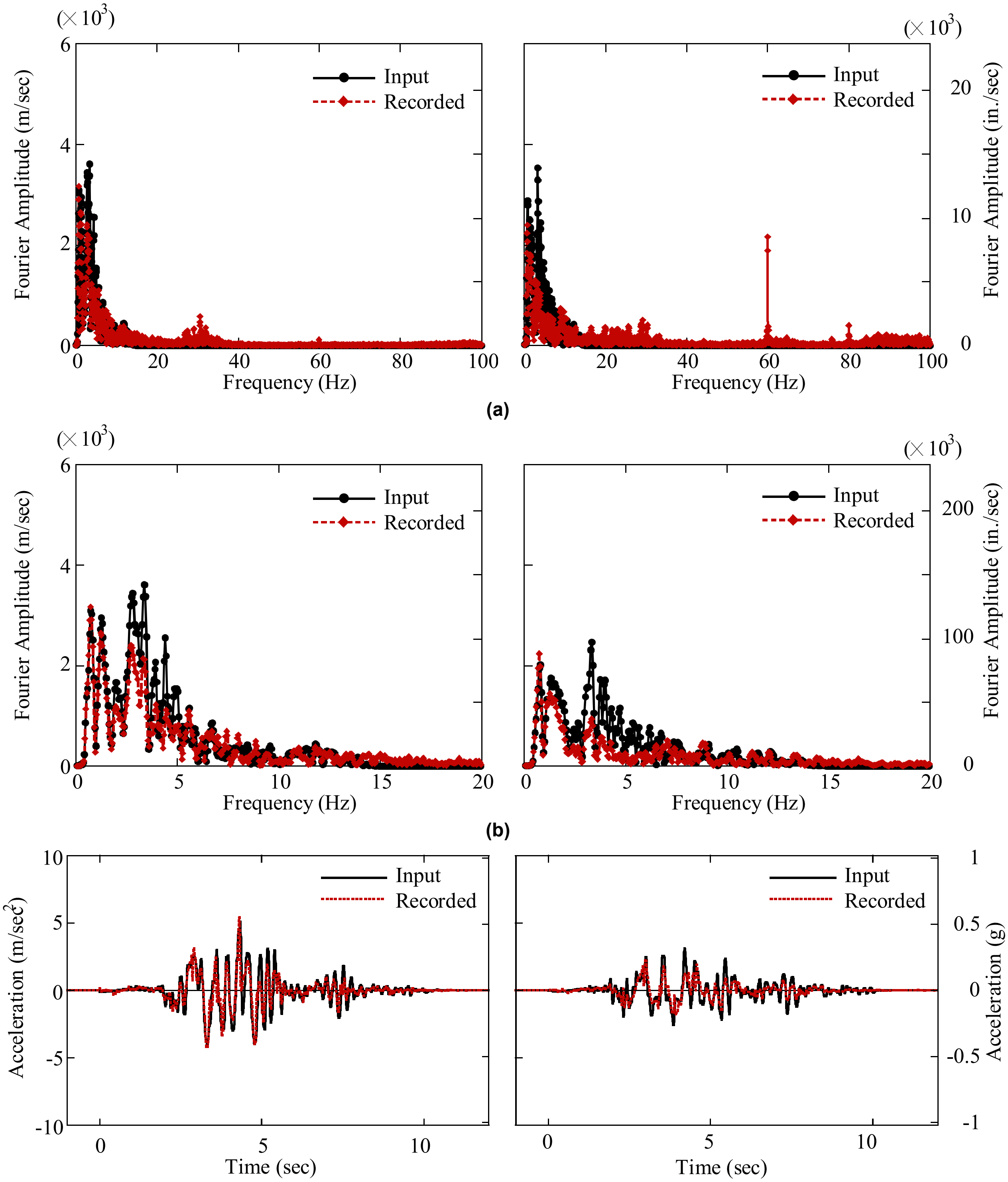

***X*-direction (NF03)** ***Y*-direction (NF04)**

Figure E.2(g) Fourier spectra and acceleration time histories for the design-level test for the partially prestressed concrete column (C-15); (a) Fourier spectra for entire range; (b) Fourier spectra under 20 Hz; and (c) acceleration measured at footing.

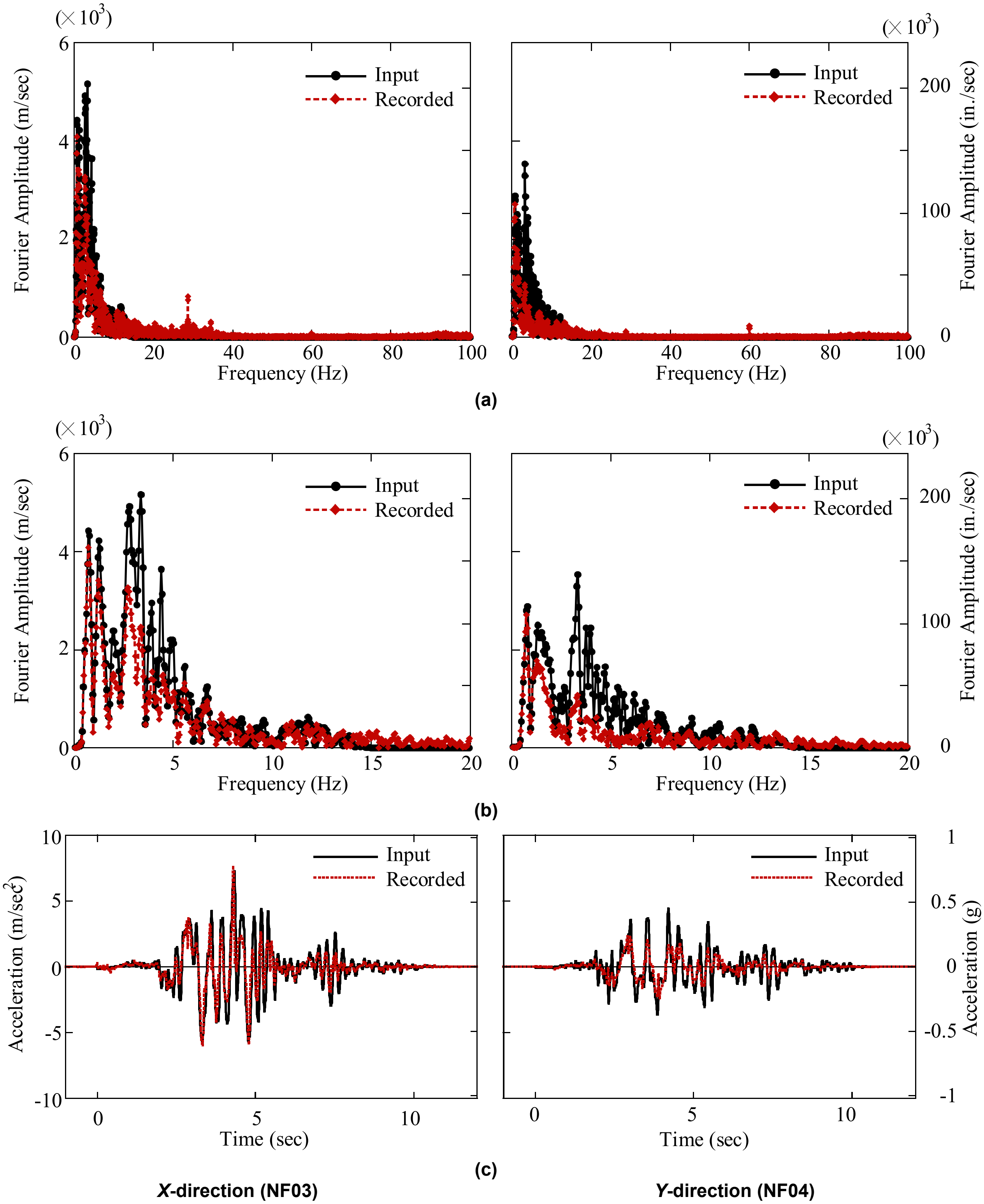

Figure E.2(h) **Fourier spectra and acceleration time histories for the maximum-level level test for the partially prestressed concrete column (C-19); (a) Fourier spectra for entire range; (b) Fourier spectra under 20 Hz; and (c) acceleration measured at footing.**

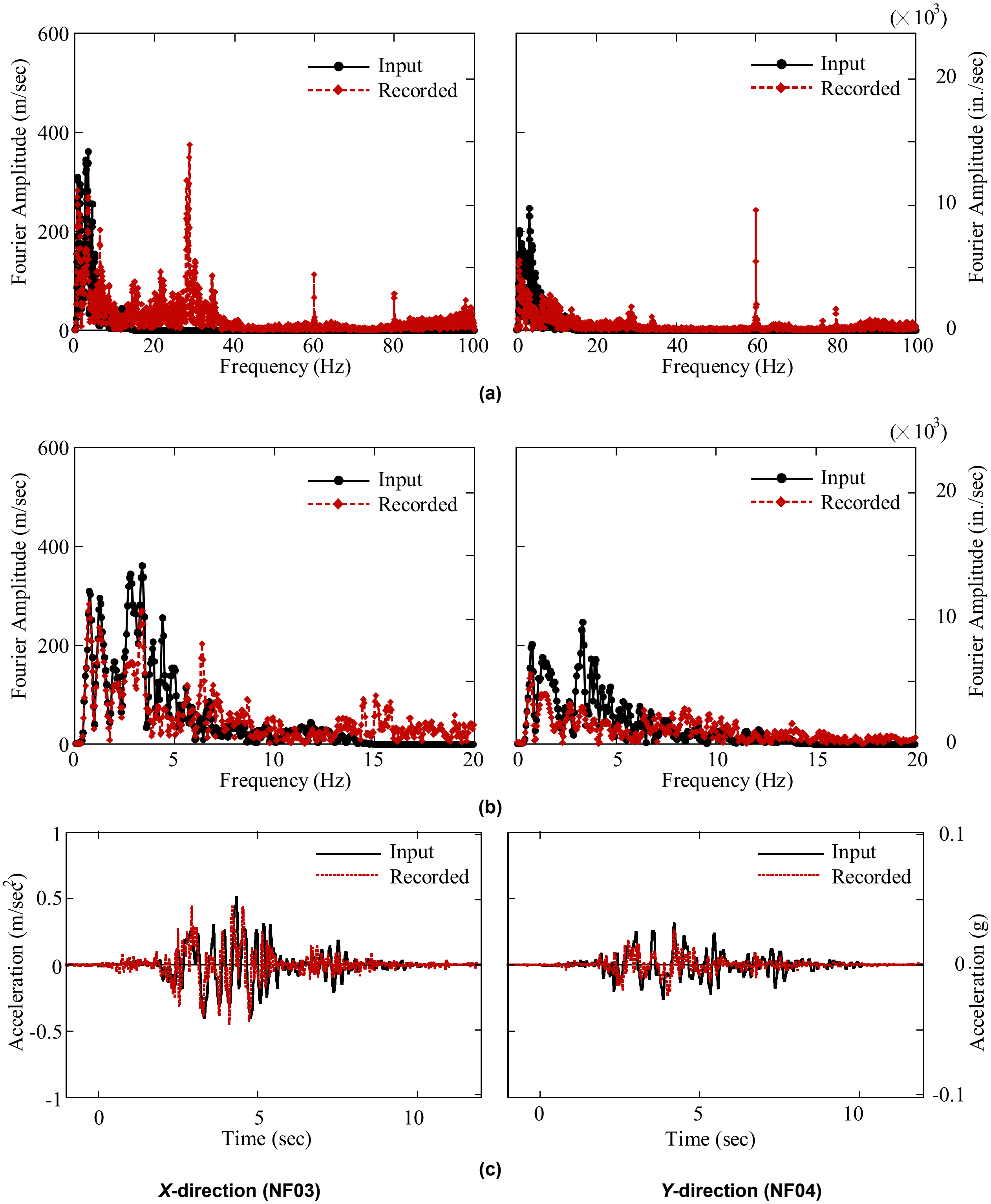

Figure E.2(i) **Second elastic-level test for conventional reinforced concrete specimen (C-23); (a) Fourier spectra for entire range; (b) Fourier spectra under 20 Hz; and (c) acceleration measured at footing.**

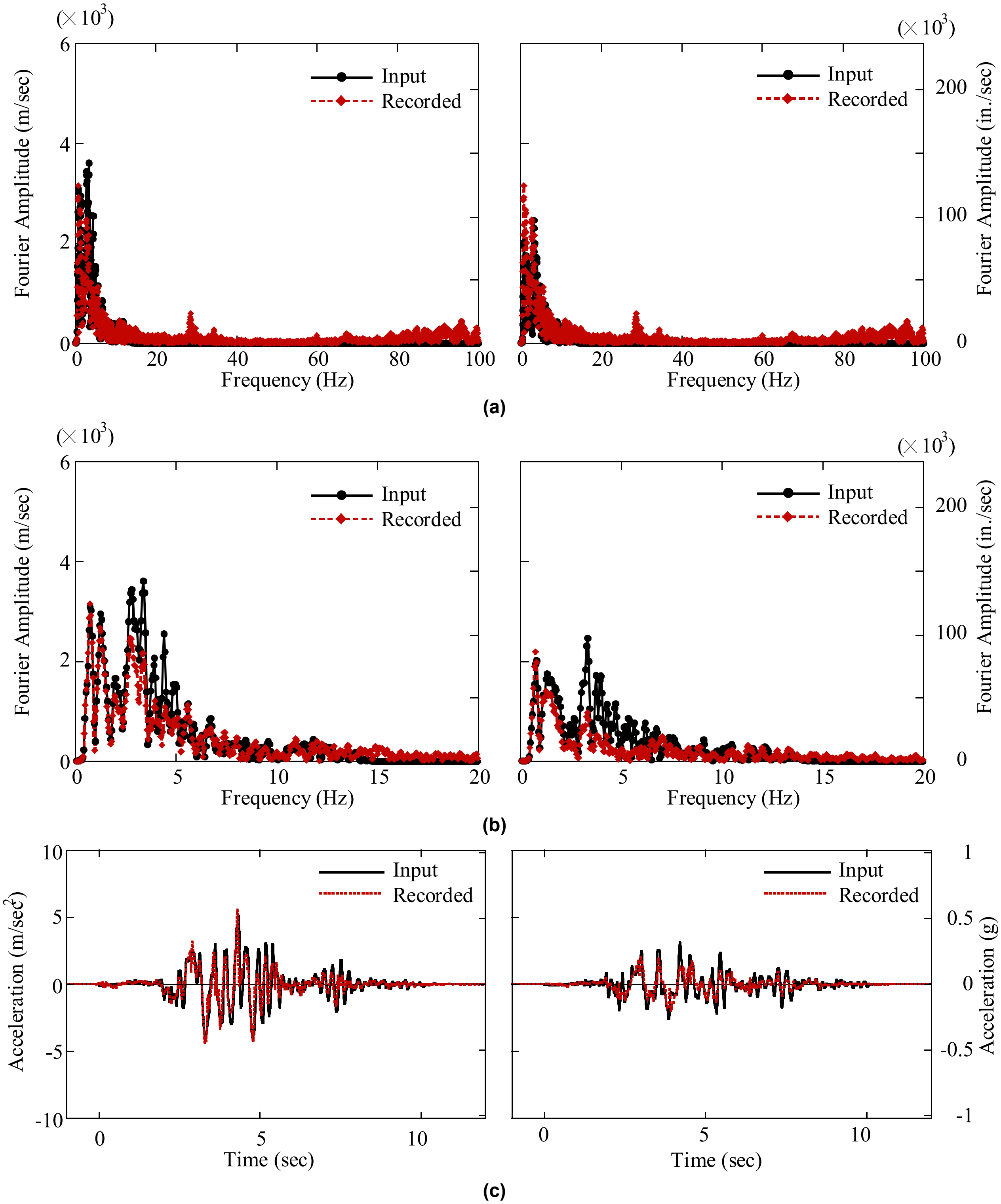

***X*-direction (NF03)** **_Y_-direction (NF04)**

Figure E.2(j) Second design-level test for the conventional reinforced concrete specimen (C-24); (a) Fourier spectra for entire range; (b) Fourier spectra under 20 Hz; and (c) acceleration measured at footing.

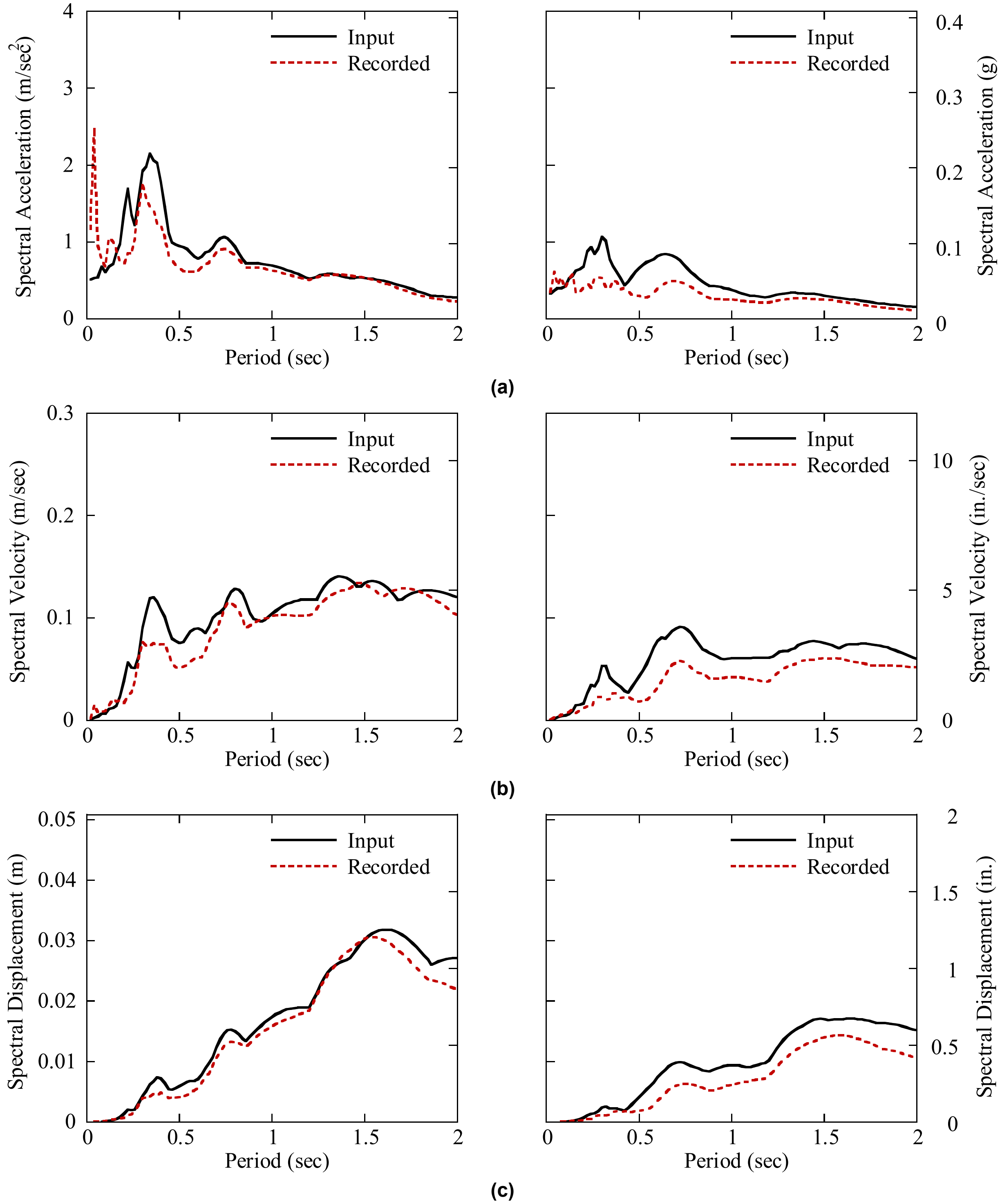

***X*-direction (NF03)** ***Y*-direction (NF04)**

Figure E.3(a) Elastic-level test for the conventional reinforced concrete specimen (B-3-14); (a) acceleration response spectra; (b) velocity response spectra; and (c) displacement response spectra.

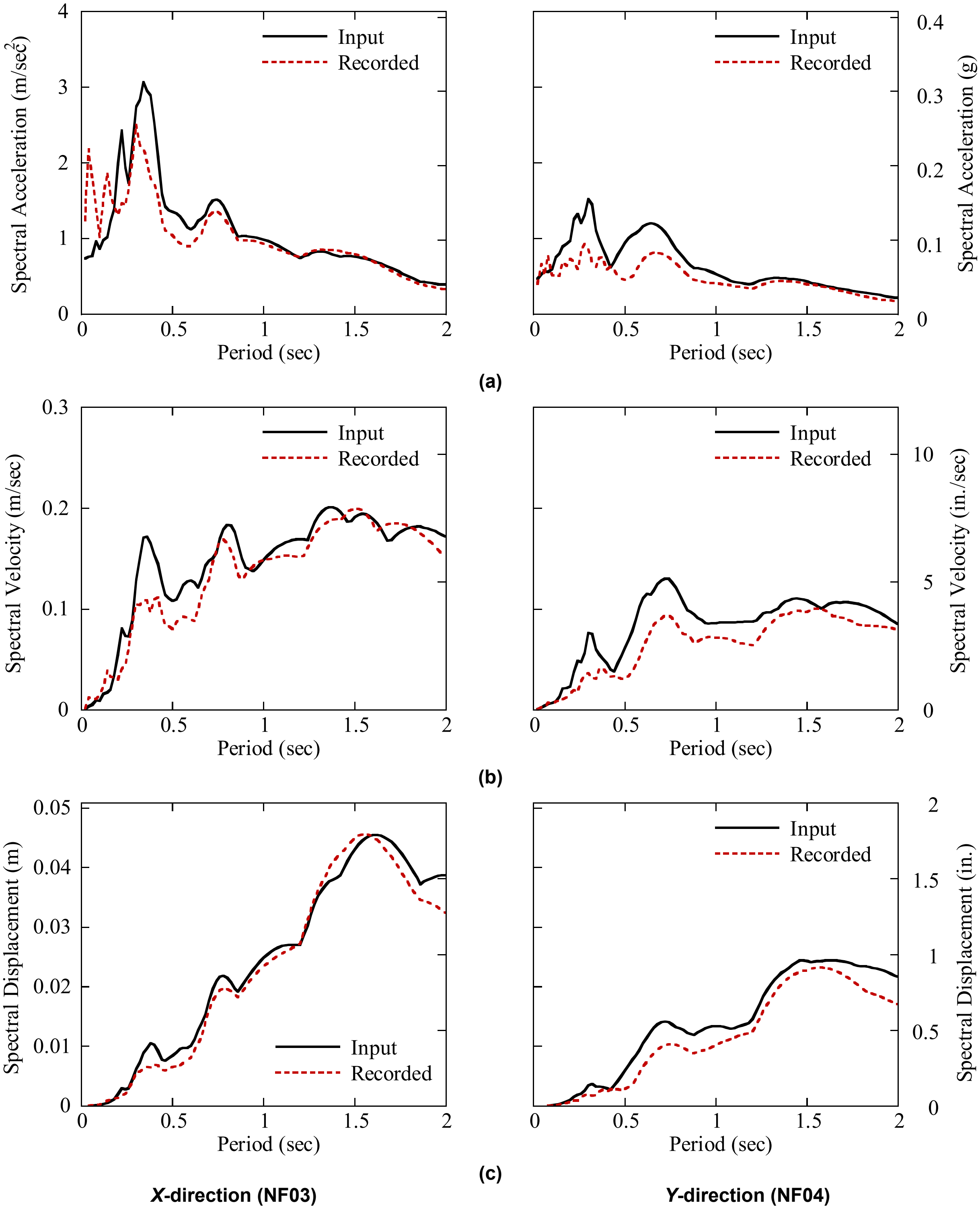

Figure E.3(b) Yield-level test for the conventional reinforced concrete specimen (B-3-15); (a) acceleration response spectra; (b) velocity response spectra; and (c) displacement response spectra.

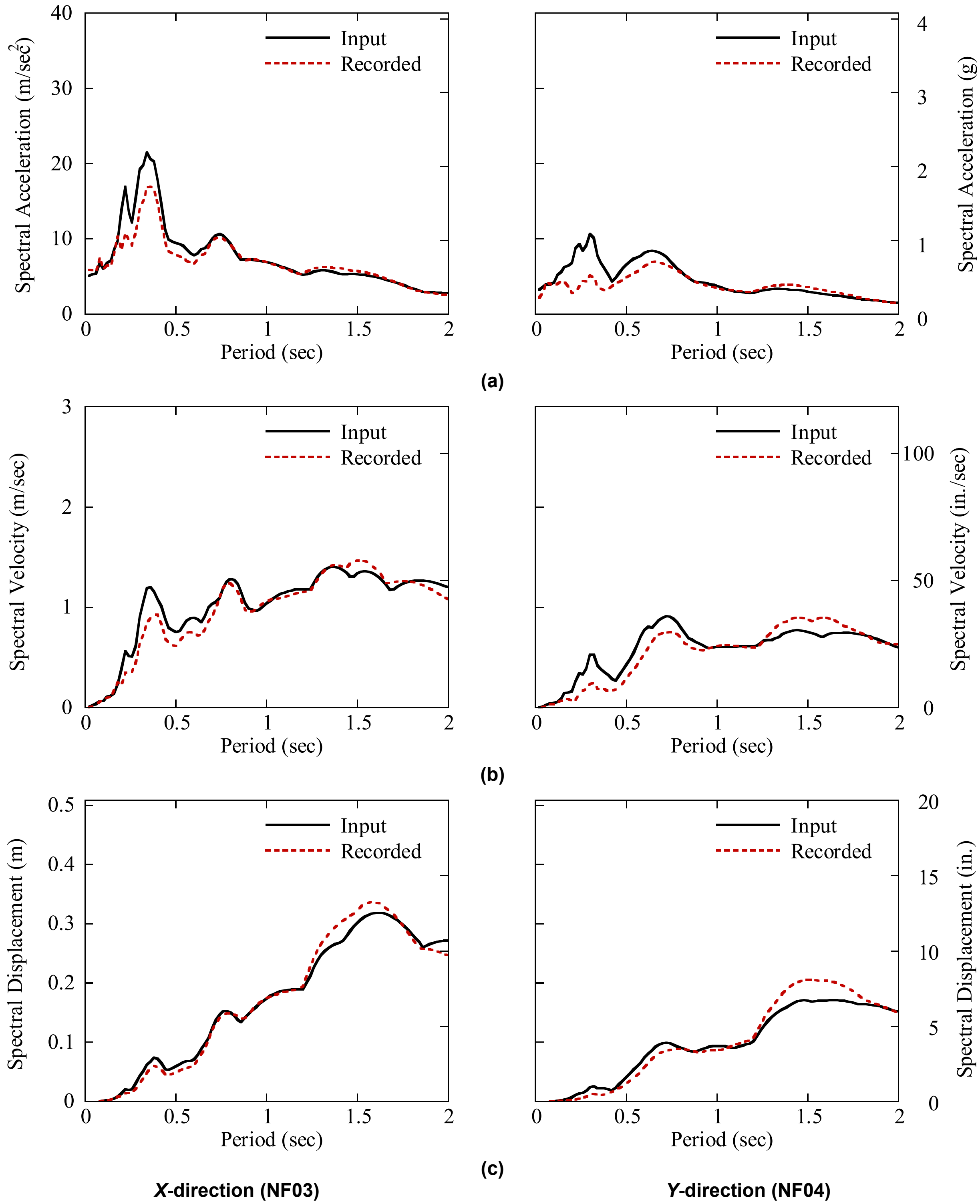

Figure E.3(c) Design-level test for the conventional reinforced concrete specimen (B-3-19); (a) acceleration response spectra; (b) velocity response spectra; and (c) displacement response spectra.

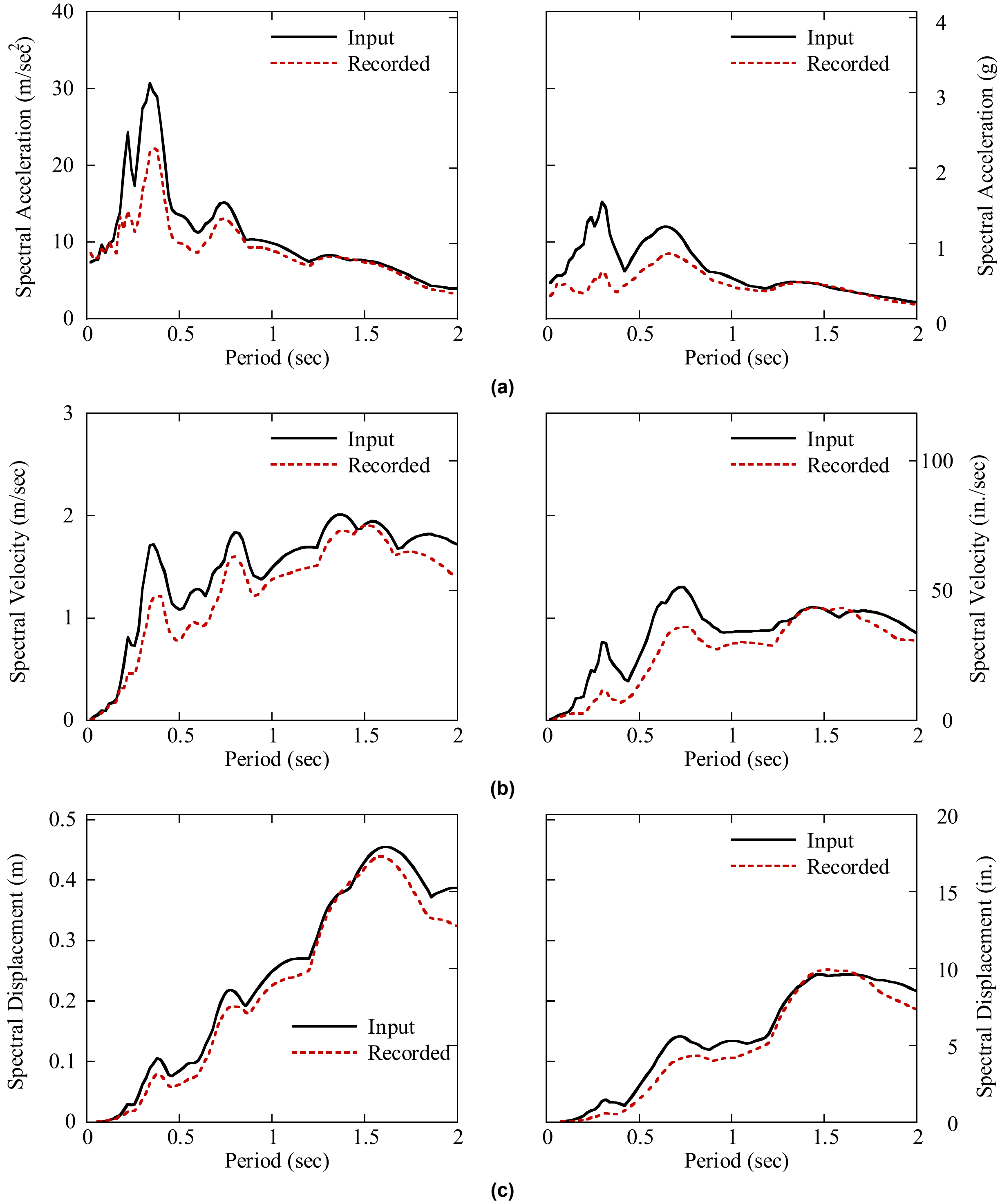

X-direction (NF03) **Y-direction (NF04)**

Figure E.3(d) Maximum-level test for the conventional reinforced concrete specimen (B-3-23); (a) acceleration response spectra; (b) velocity response spectra; and (c) displacement response spectra.

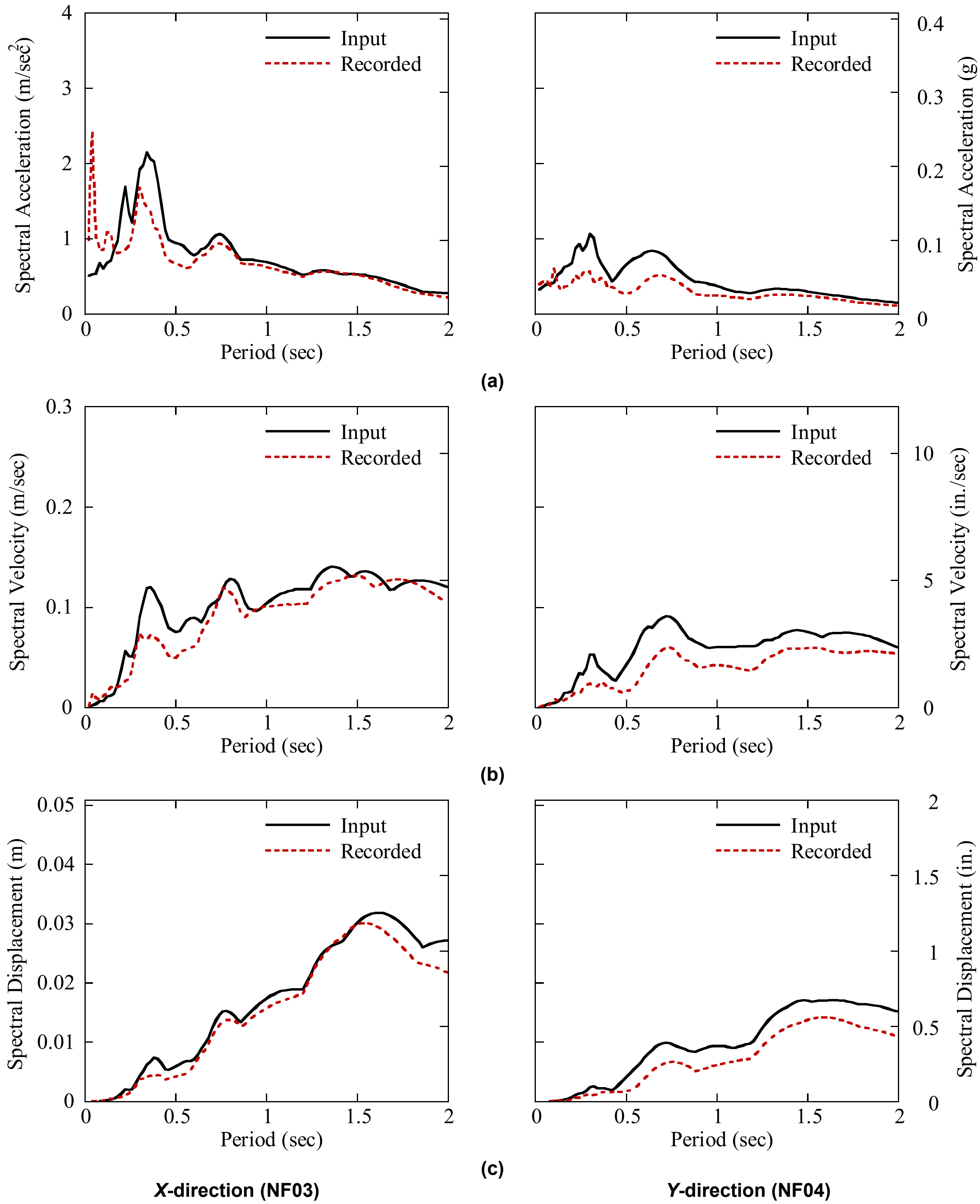

Figure E.3(e) **Elastic-level test for the partially prestressed concrete column specimen (C-10); (a) acceleration response spectra; (b) velocity response spectra; and (c) displacement response spectra.**

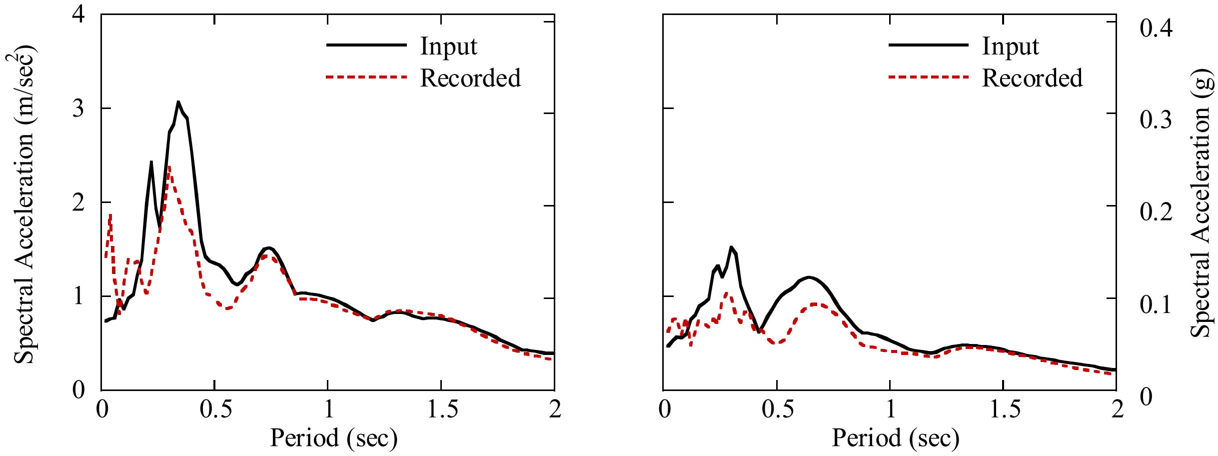

(a)

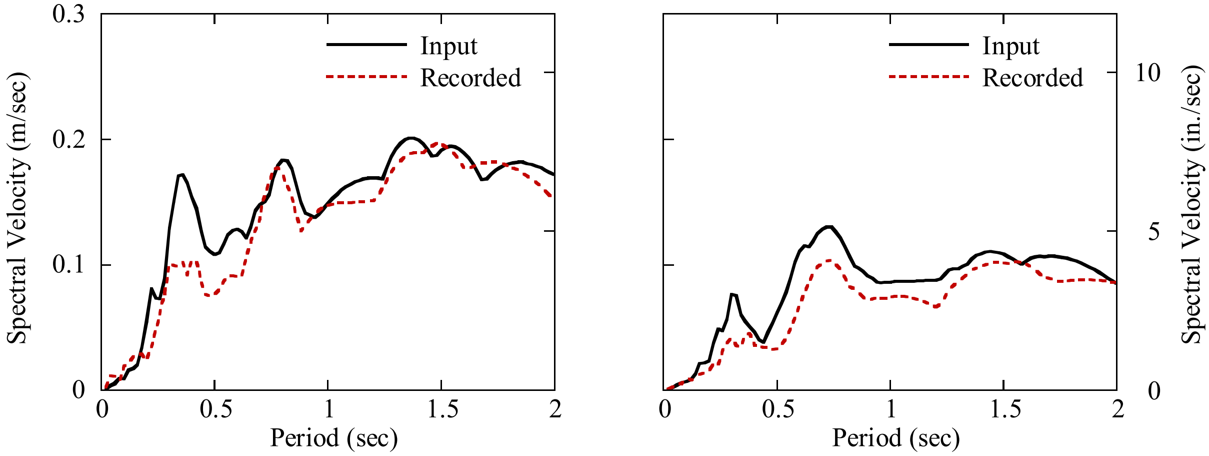

(b)

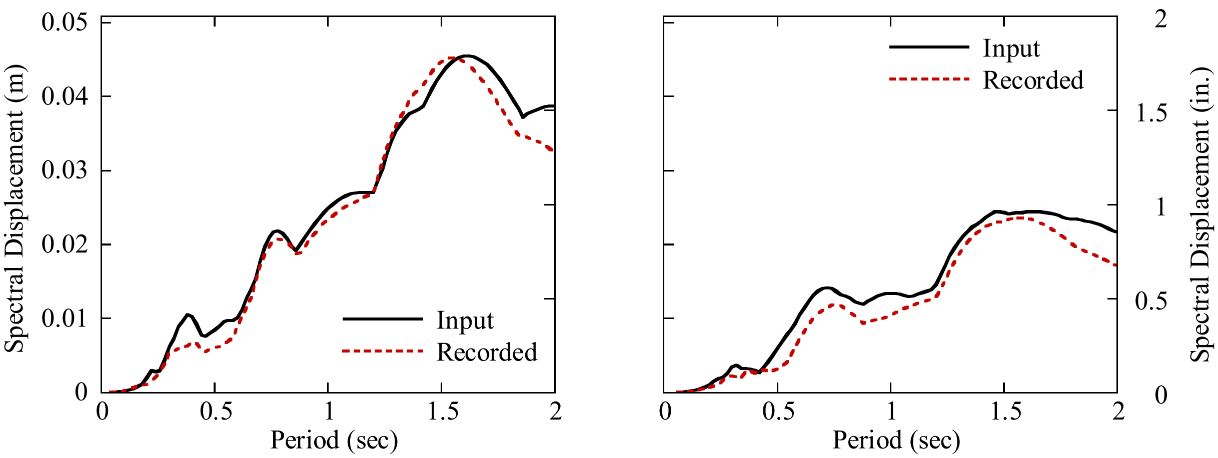

(c)

***X*-direction (NF03)** **Y-direction (NF04)**

Figure E.3(f) Yield-level test for the partially prestressed concrete column specimen (C-11); (a) acceleration response spectra; (b) velocity response spectra; and (c) displacement response spectra.

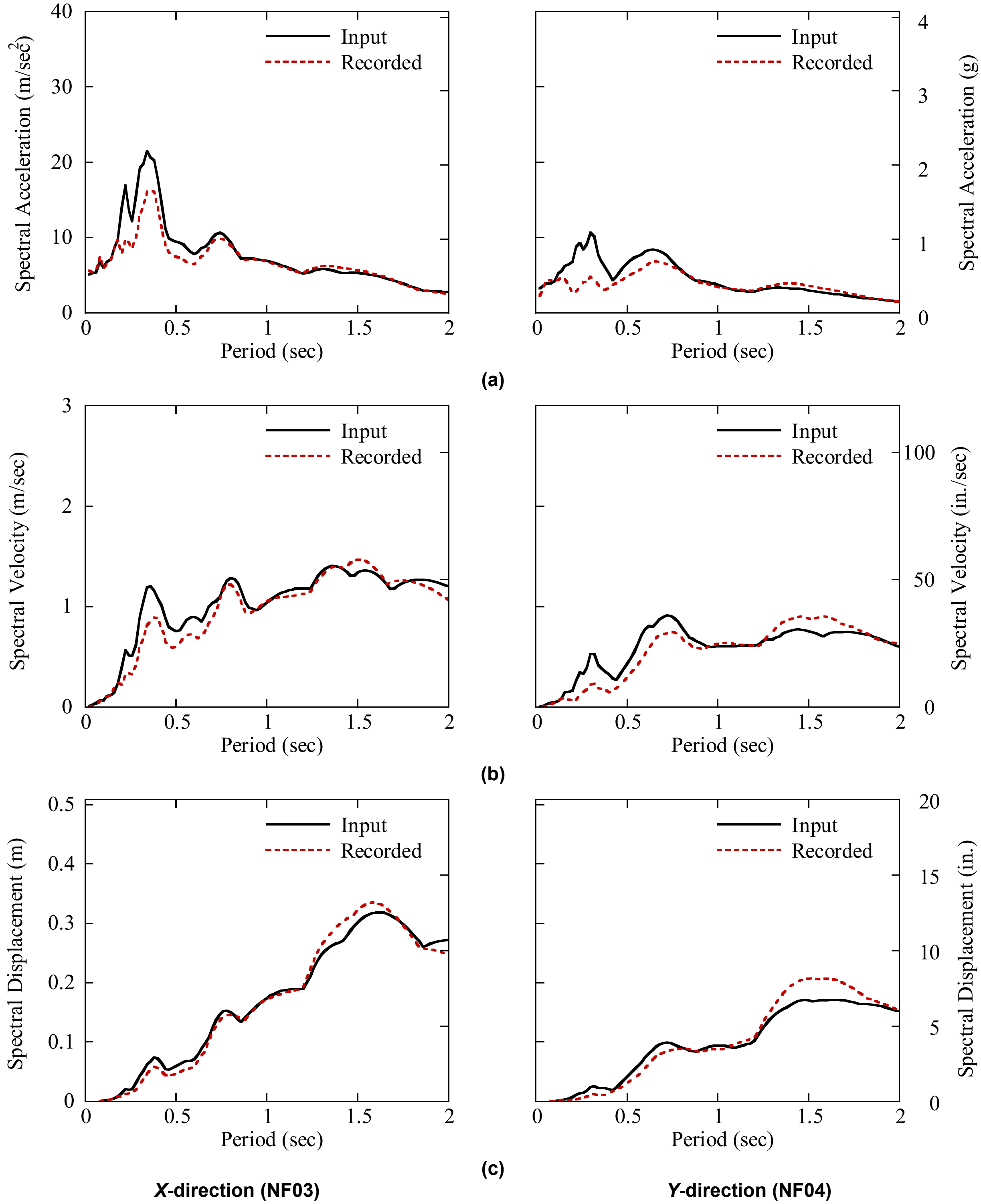

Figure E.3(g) Design-level test for partially prestressed concrete column specimen (C-15); (a) acceleration response spectra; (b) velocity response spectra; and (c) displacement response spectra.

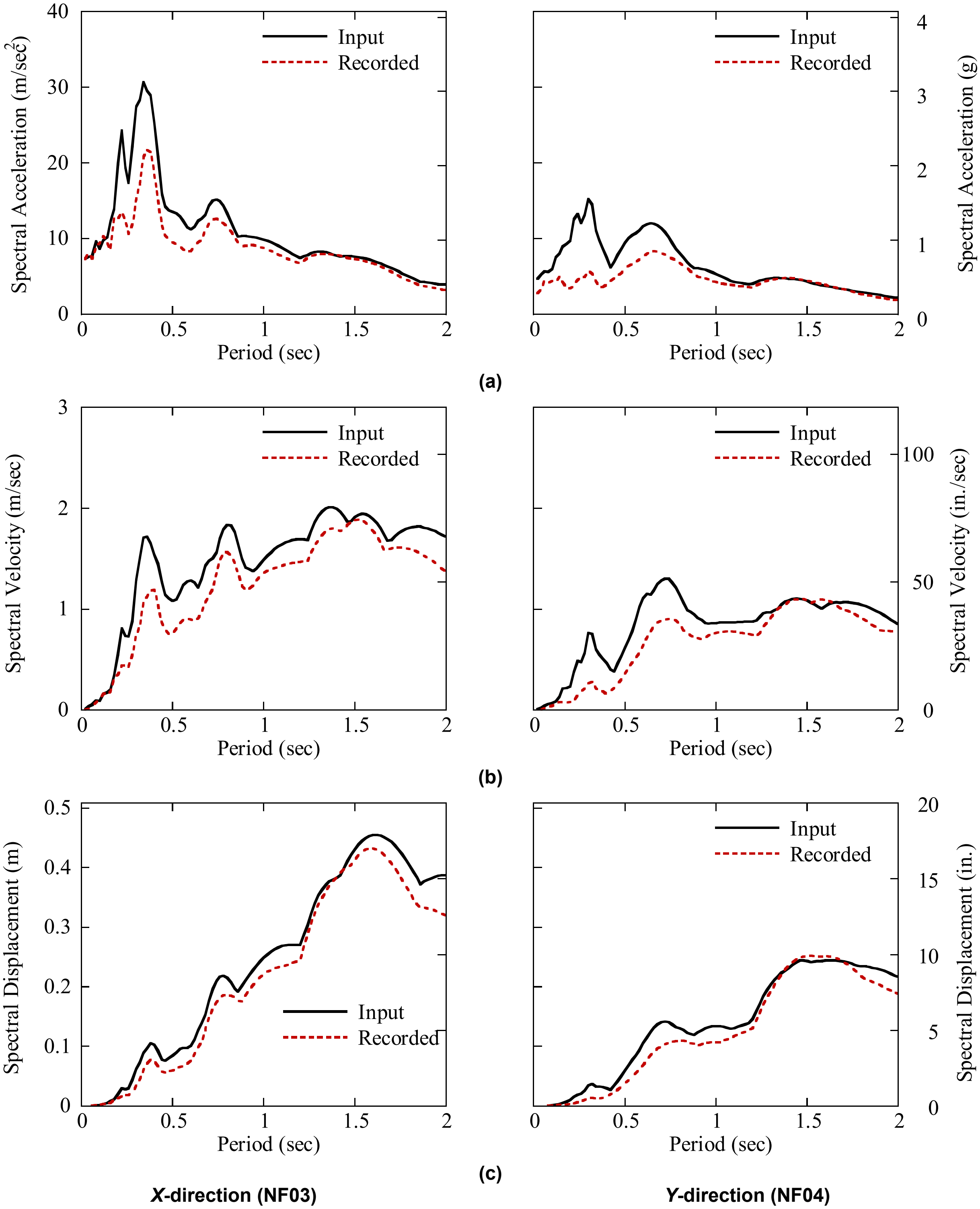

Figure E.3(h) Maximum-level test for partially prestressed concrete column specimen (C-19); (a) acceleration response spectra; (b) velocity response spectra; and (c) displacement response spectra.

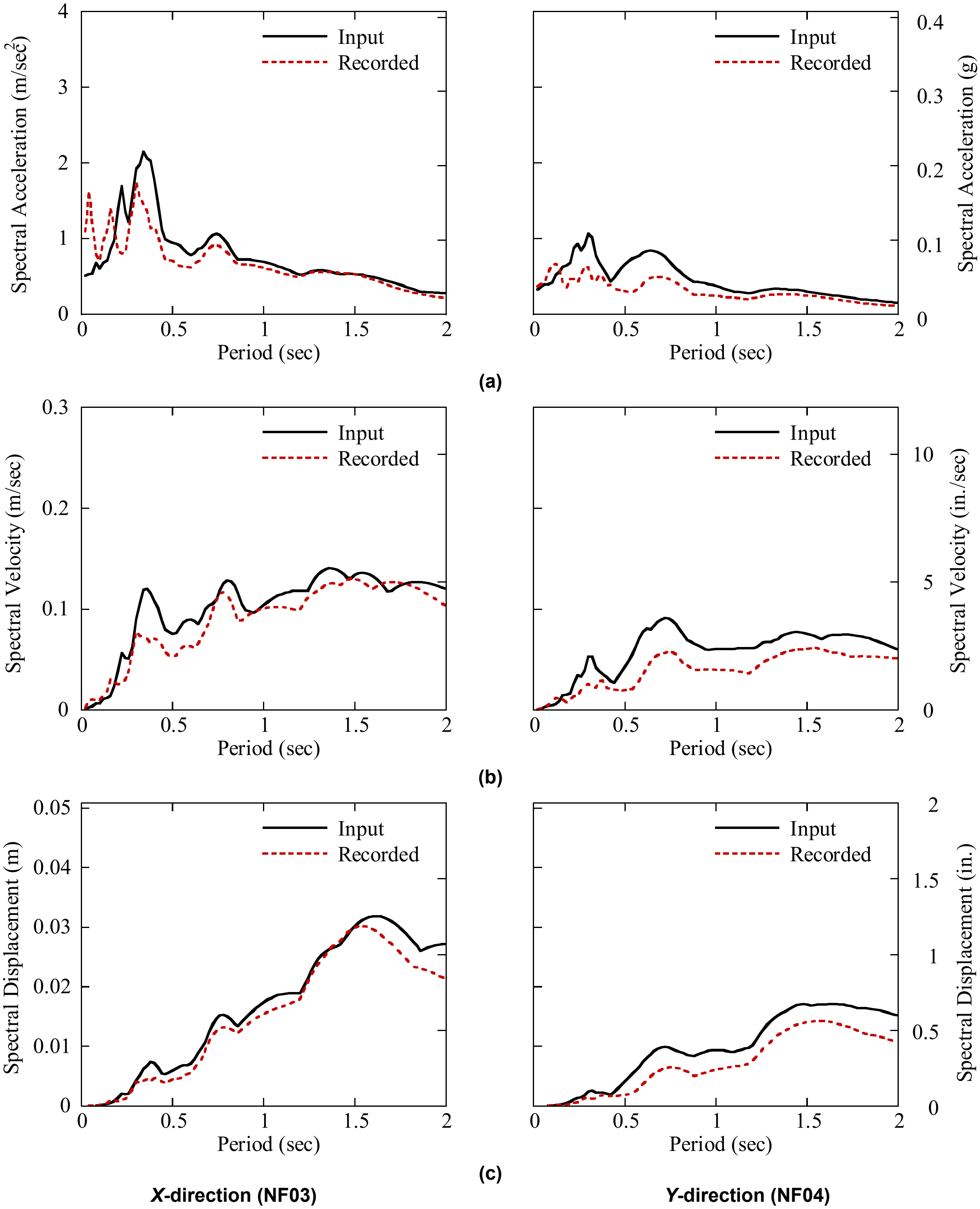

Figure E.3(i) **Second elastic-level test for the conventional reinforced concrete specimen (C-23); (a) acceleration response spectra; (b) velocity response spectra; and (c) displacement response spectra.**

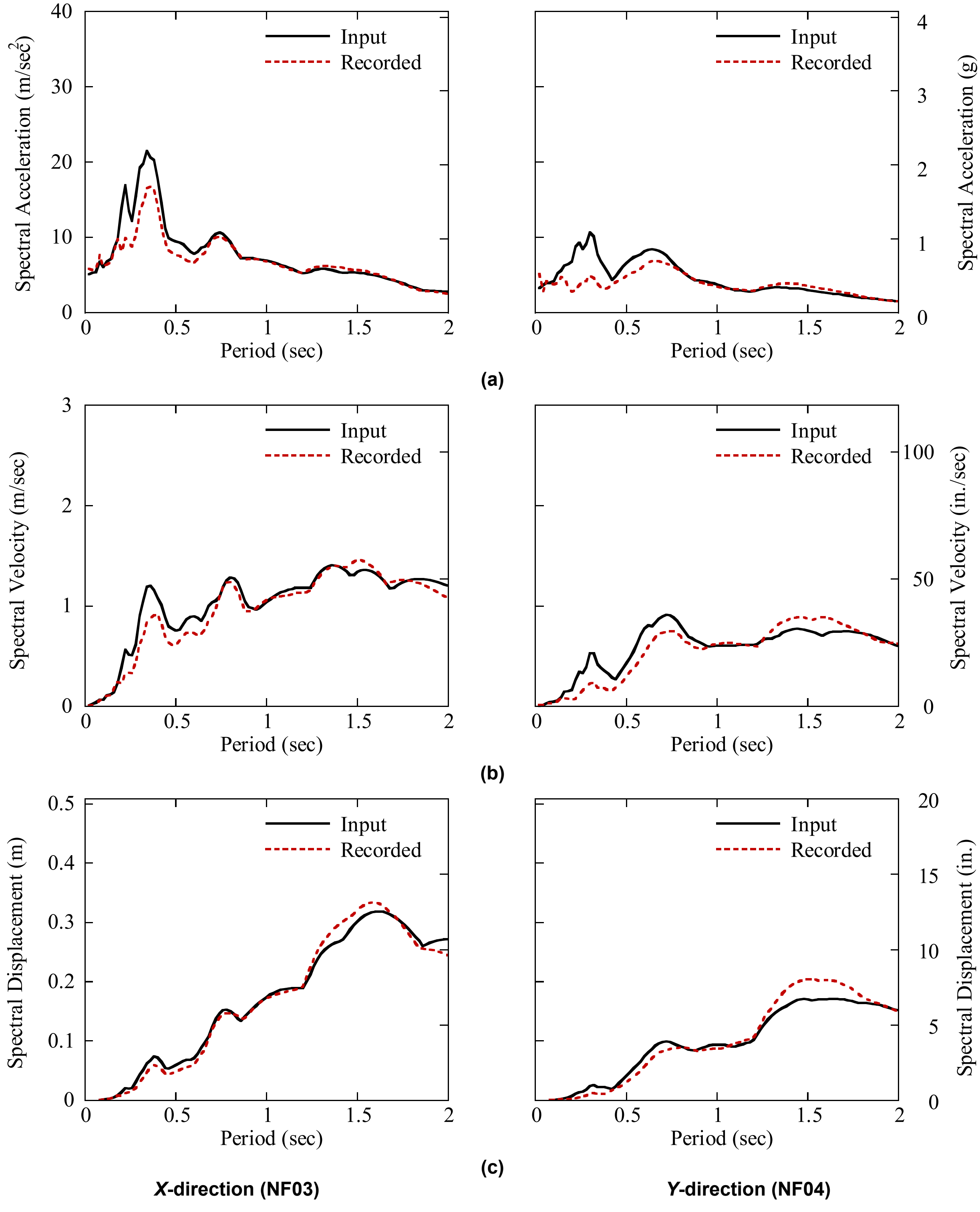

Figure E.3(j) **Second elastic-level test for the conventional reinforced concrete specimen (C-24); (a) acceleration response spectra; (b) velocity response spectra; and (c) displacement response spectra.**

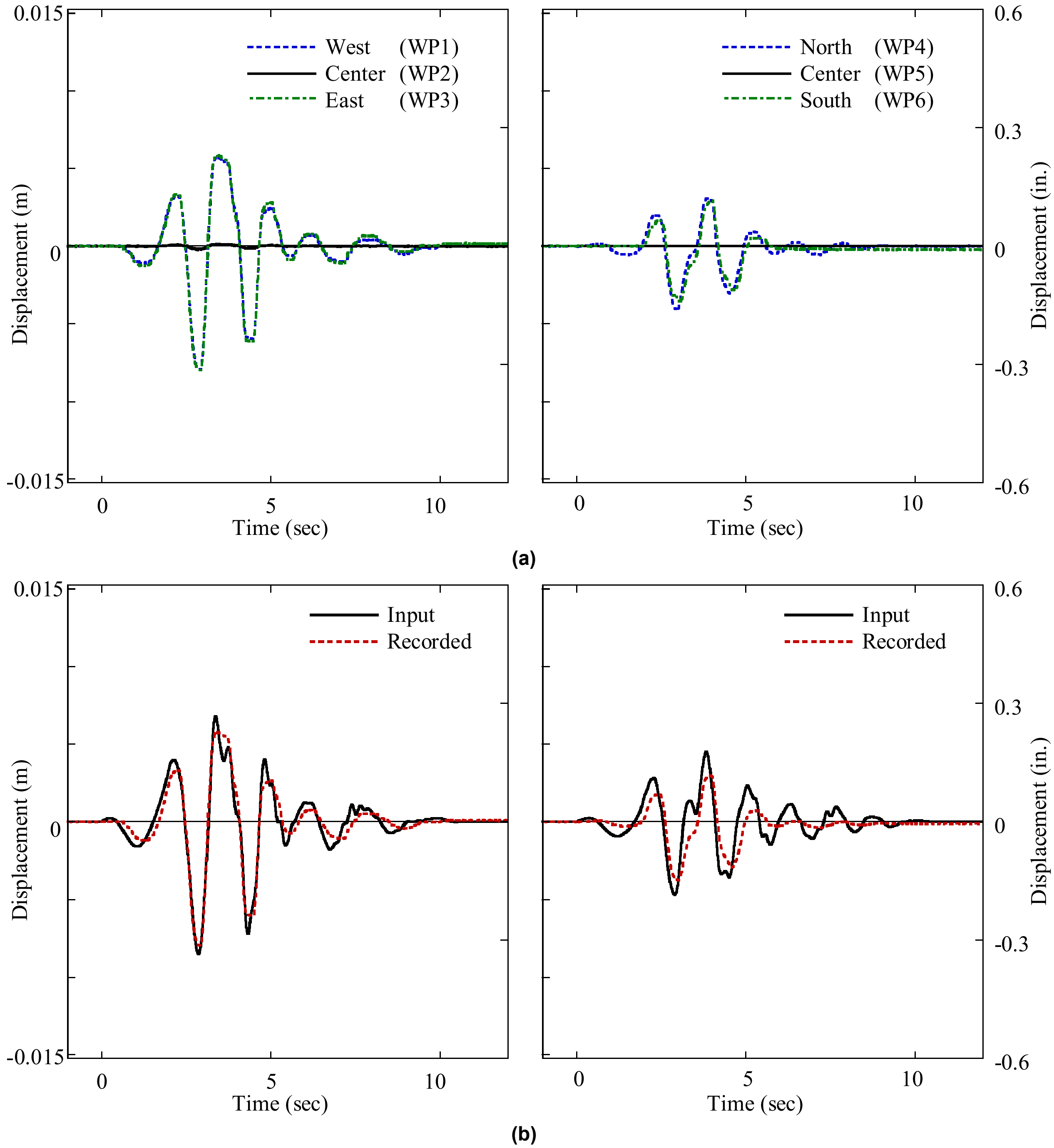

X-direction (NF03) *Y*-direction (NF04)

Figure E.4(a) Elastic-level test for the conventional reinforced concrete specimen (B-3-14); (a) displacements measured at footing; and (b) re-produceability of simulator in terms of displacements.

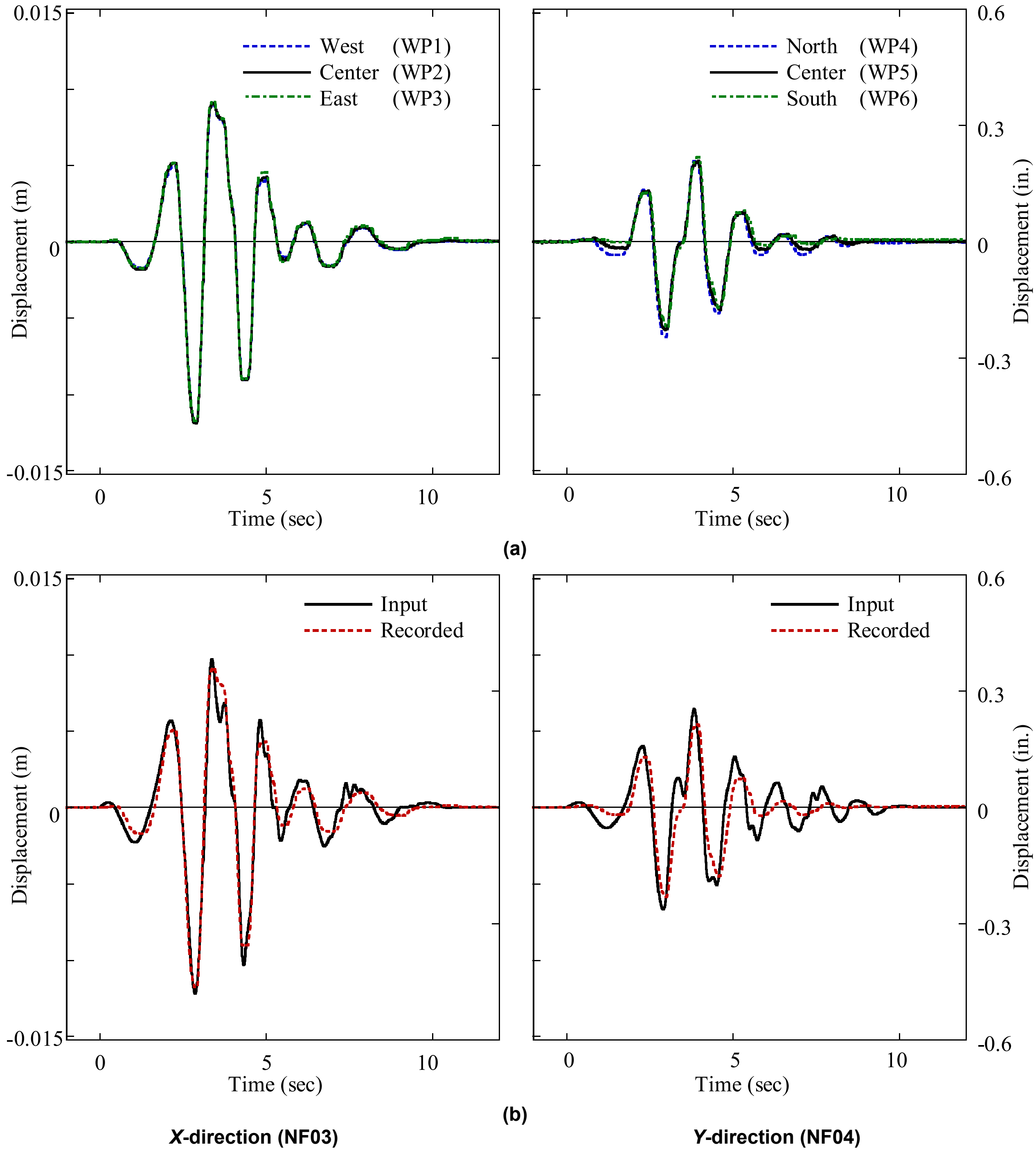

Figure E.4(b) Yield-level test for the conventional reinforced concrete specimen (B-3-15); (a) displacements measured at footing; and (b) re-produceability of simulator in terms of displacements.

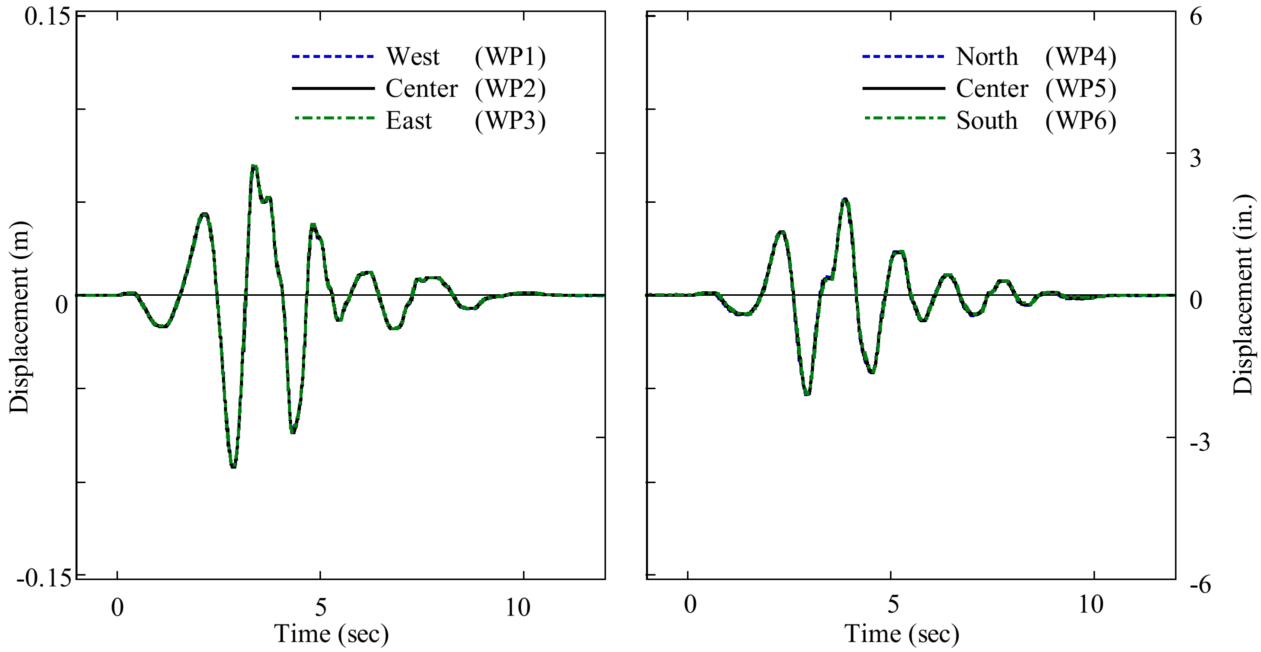

(a)

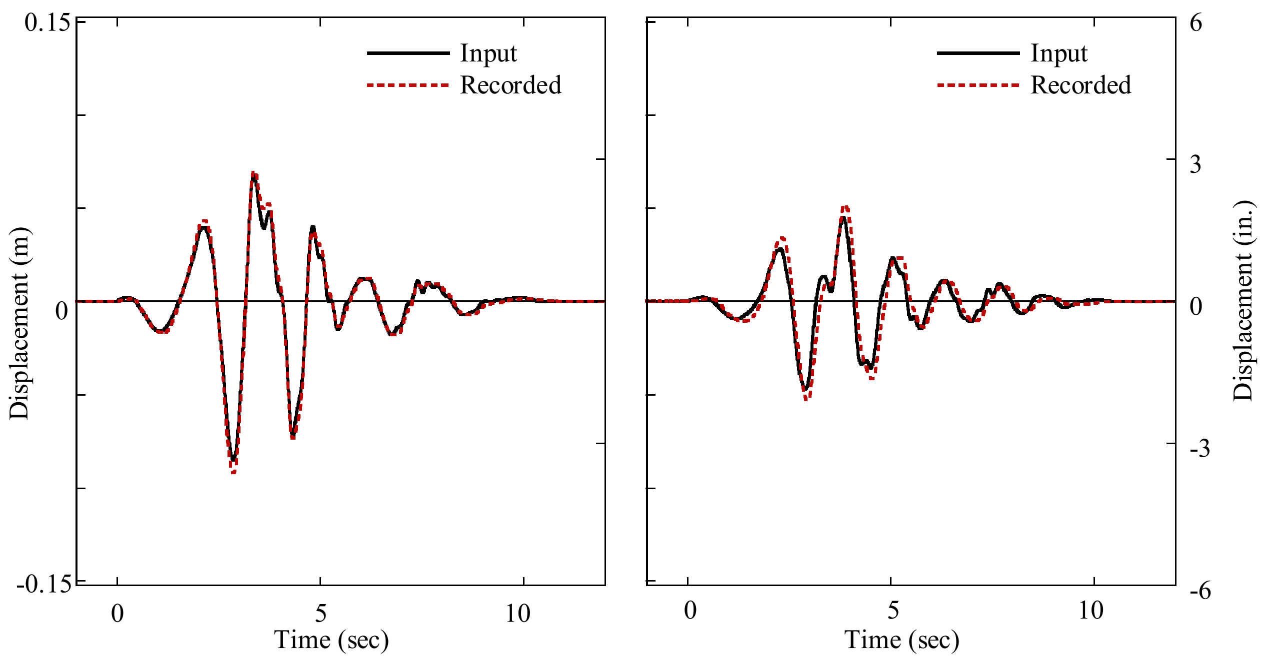

(b)

***X*-direction (NF03)** ***Y*-direction (NF04)**

Figure E.4(c) Design-level test for the conventional reinforced concrete specimen (B-3-19); (a) displacements measured at footing; and (b) re-produceability of simulator in terms of displacements.

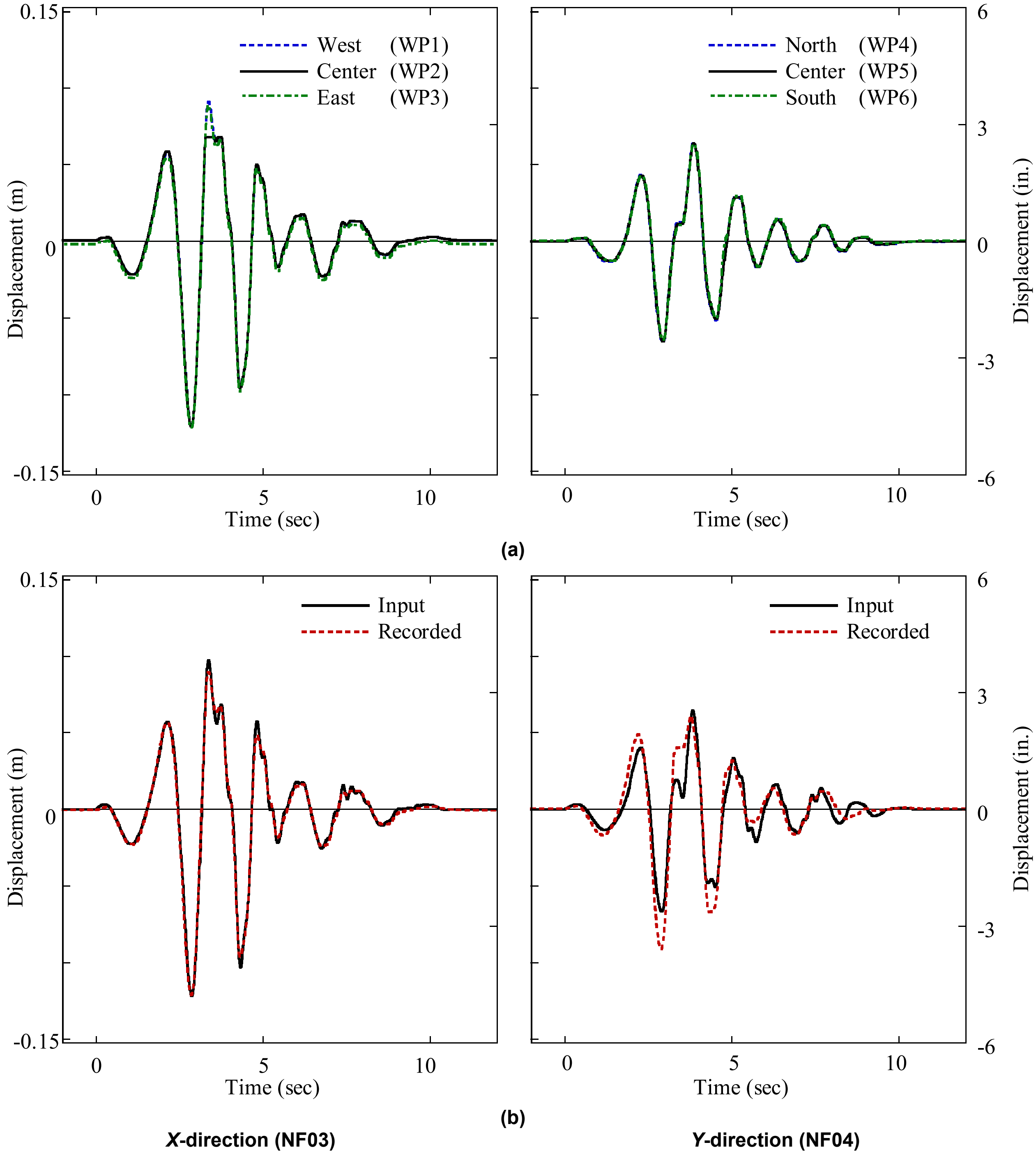

Figure E.4(d) Maximum-level test for the conventional reinforced concrete specimen (B-3-23); (a) displacements measured at footing; and (b) re-produceability of simulator in terms of displacements.

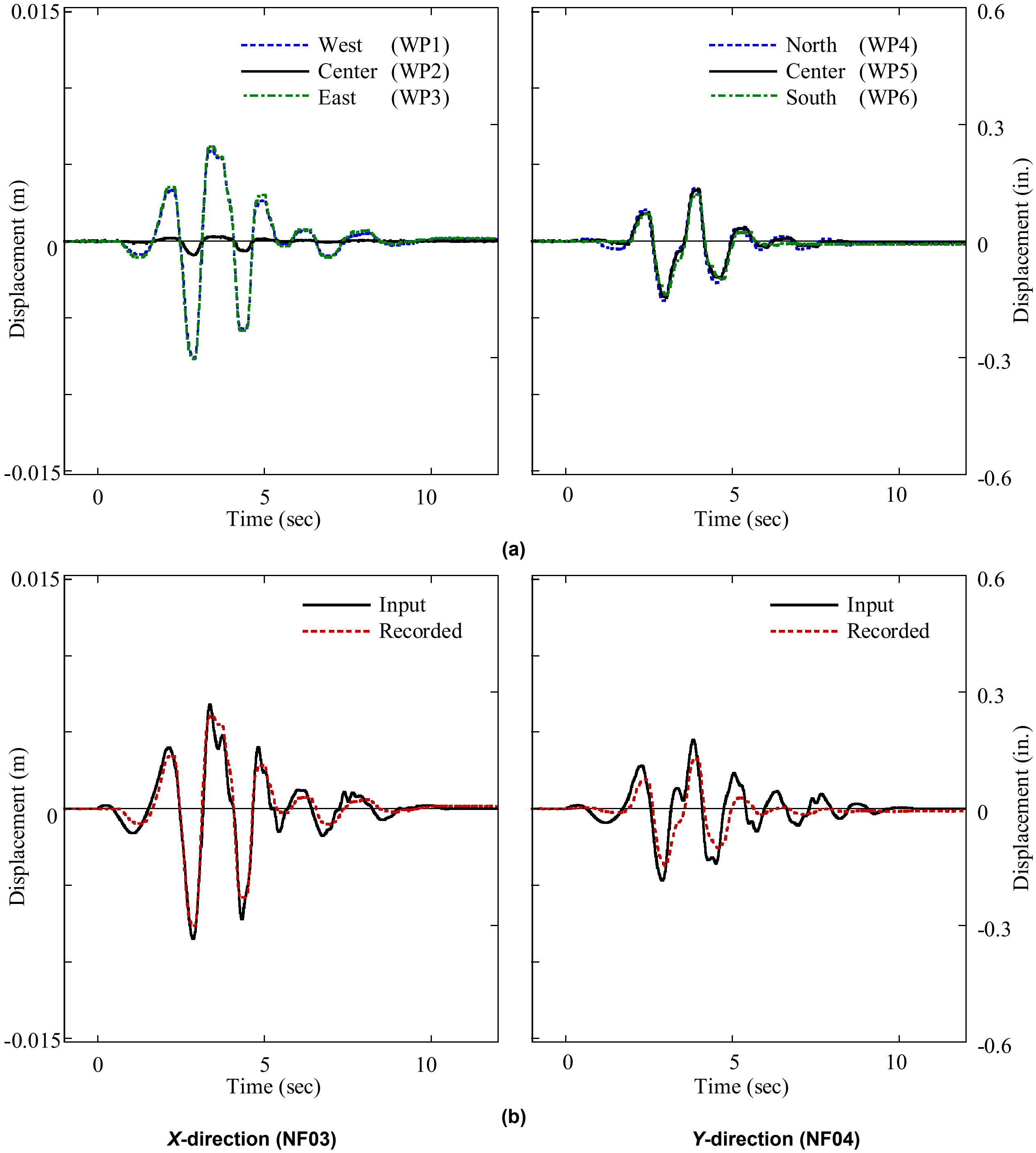

Figure E.4(e) **Elastic-level test for the partially prestressed concrete column specimen (C-10); (a) displacements measured at footing; and (b) re-produceability of simulator in terms of displacements.**

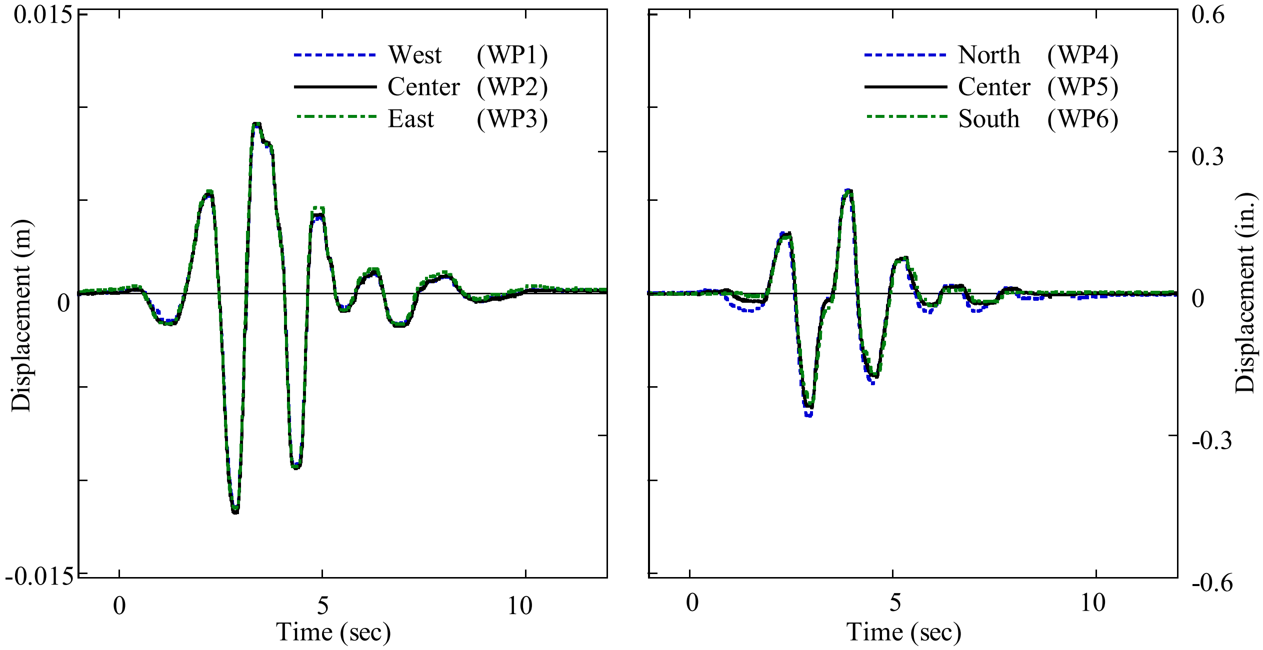

(a)

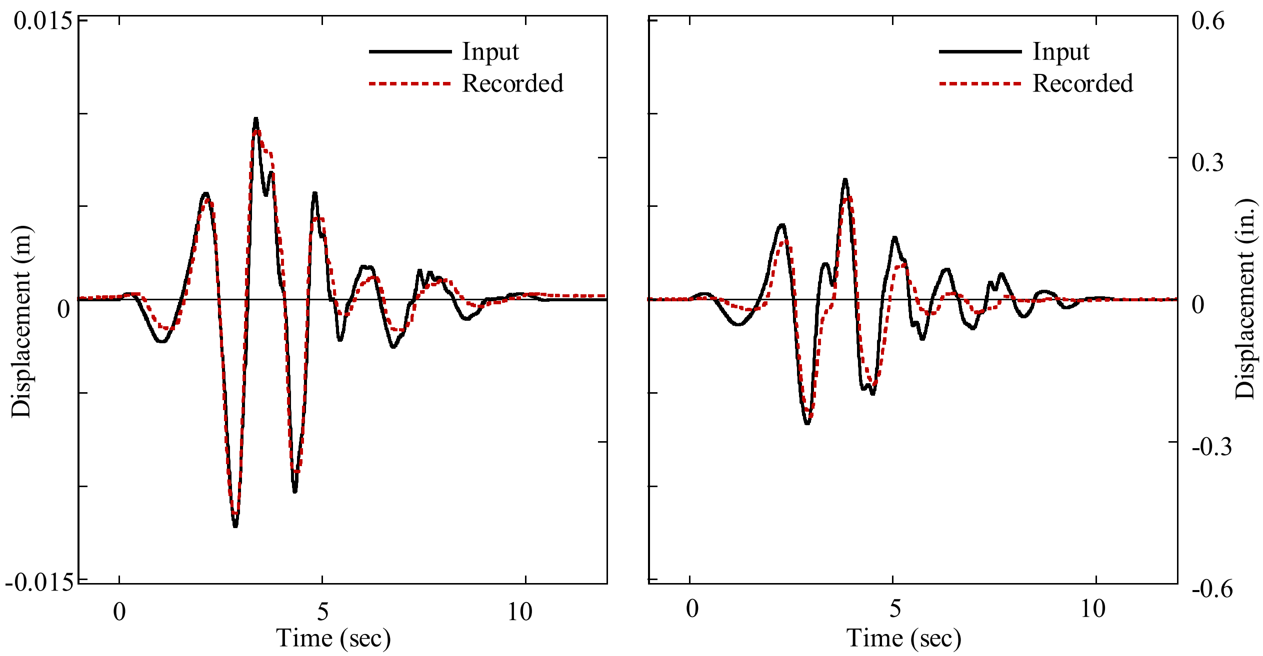

(b)

***X*-direction (NF03)** ***Y*-direction (NF04)**

Figure E.4(f) Design-level test for the partially prestressed concrete column specimen (C-15); (a) displacements measured at footing; and (b) re-produceability of simulator in terms of displacements.

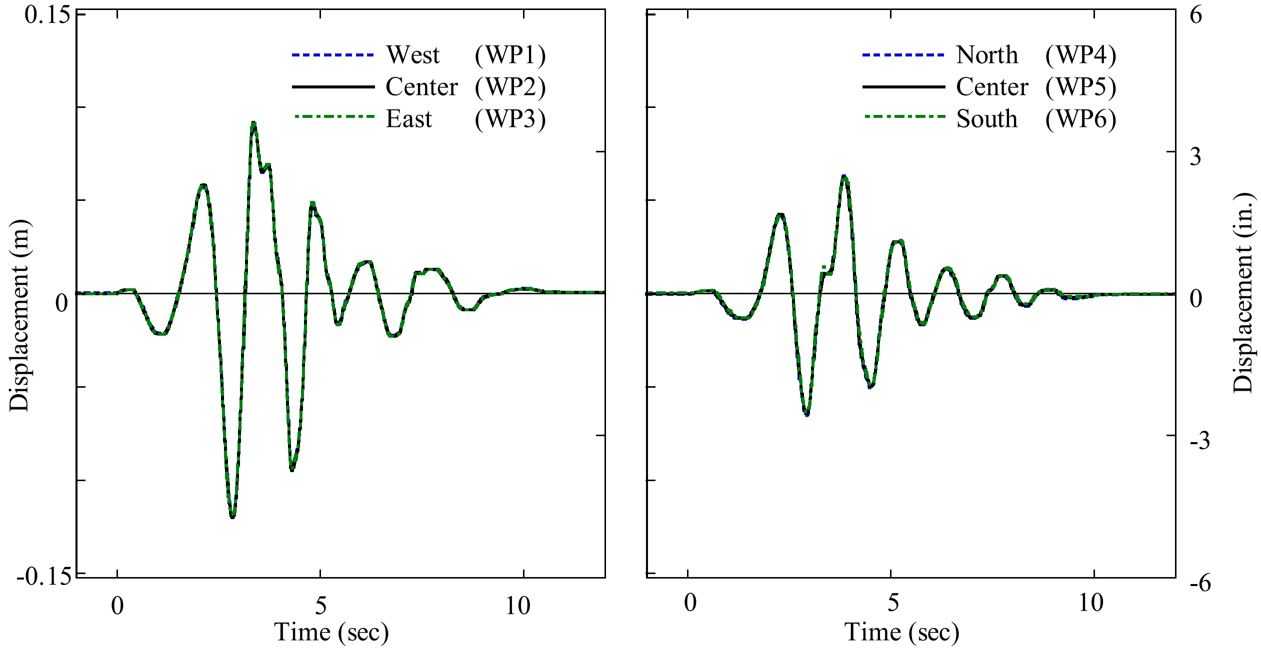

(a)

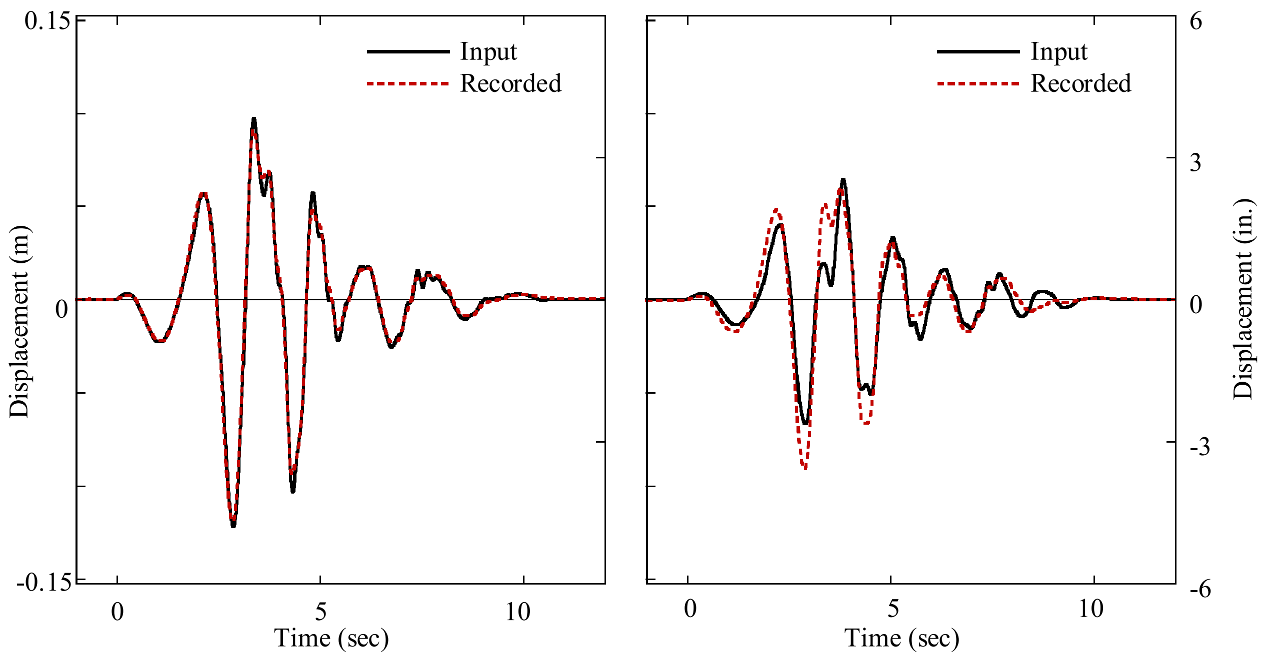

(b)

***X*-direction (NF03)** ***Y*-direction (NF04)**

Figure E.4(g) Maximum-level test for the partially prestressed concrete column specimen (C-19); (a) displacements measured at footing; and (b) reproduceability of simulator in terms of displacements.

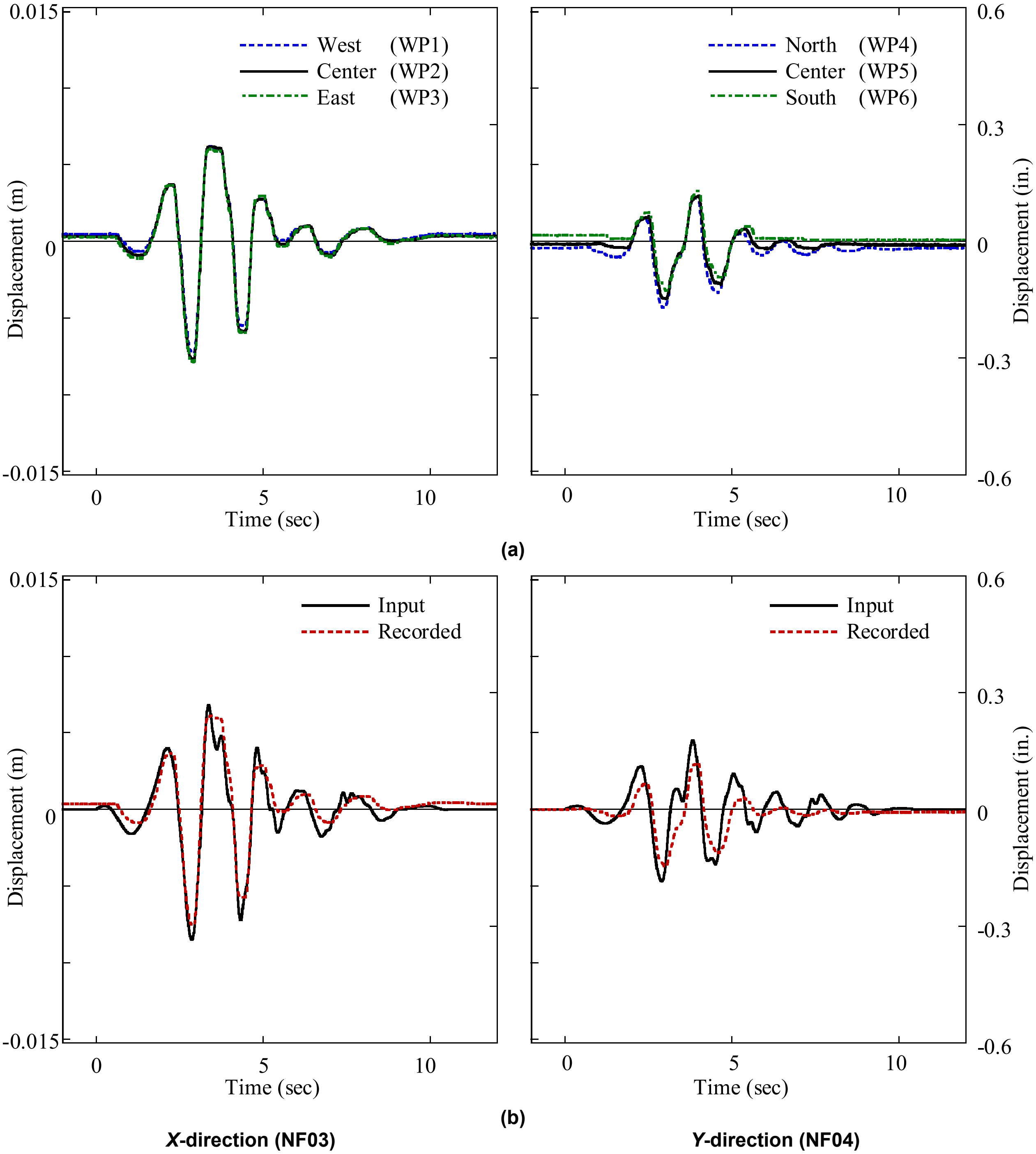

Figure E.4(h) Second elastic-level test for conventional reinforced concrete specimen (C-23); (a) displacements measured at footing; and (b) re-produceability of simulator in terms of displacements.

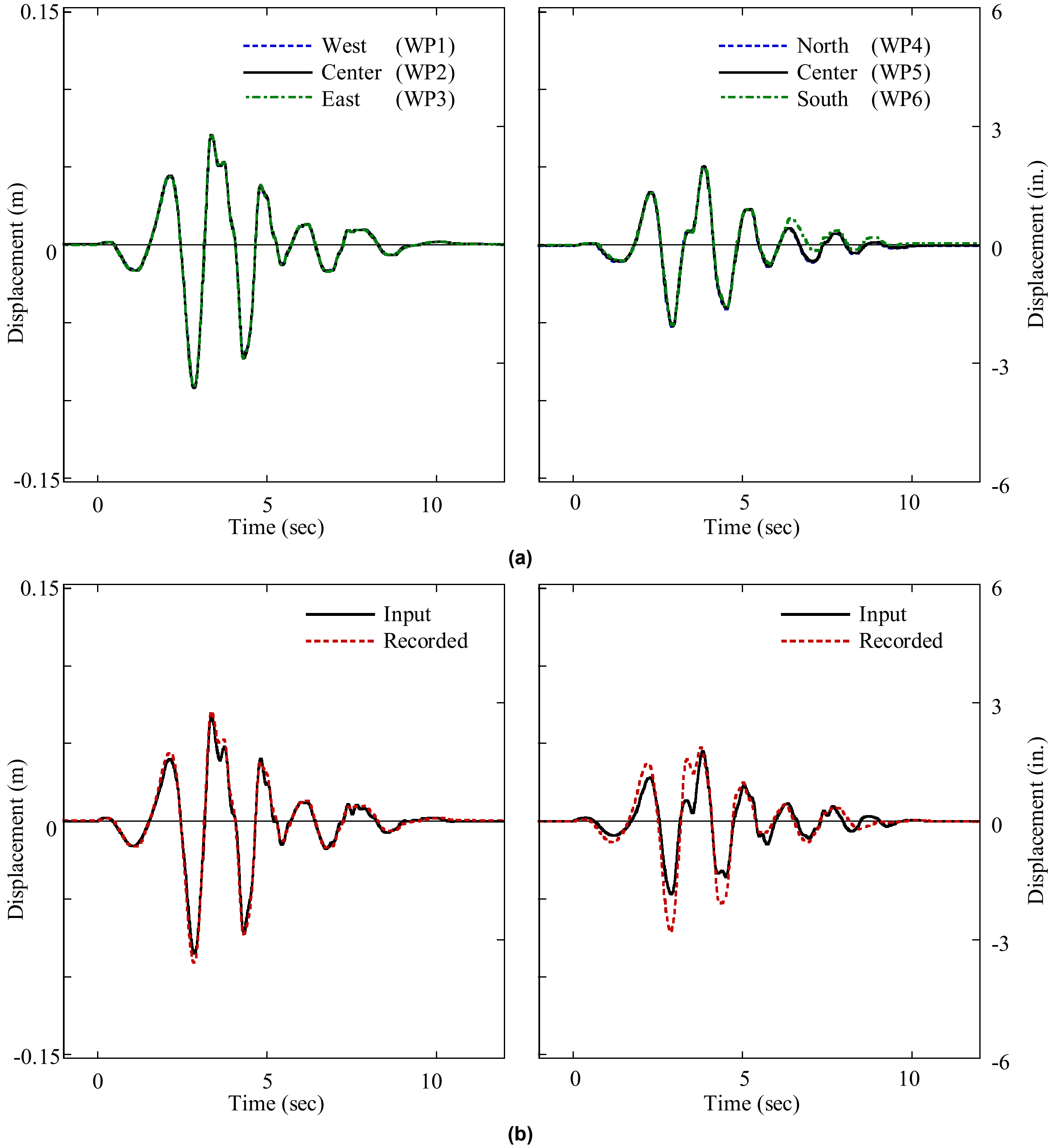

***X*-direction (NF03)** | ***Y*-direction (NF04)**

Figure E.4(i) Second design-level test for conventional reinforced concrete specimen (C-24); (a) displacements measured at footing; and (b) re-produceability of simulator in terms of displacements

PEER REPORTS

PEER reports are available as a free PDF download from http://peer.berkeley.edu/publications/peer_reports_complete.html. Printed hard copies of PEER reports can be ordered directly from our printer by following the instructions at http://peer.berkeley.edu/publications/peer_reports.html. For other related questions about the PEER Report Series, contact the Pacific Earthquake Engineering Research Center, 325 Davis Hall, Mail Code 1792, Berkeley, CA 94720. Tel.: (510) 642-3437; Fax: (510) 642-1655; Email: peer_center@berkeley.edu.

PEER 2005/16 *Seismic Response and Reliability of Electrical Substation Equipment and Systems.* Junho Song, Armen Der Kiureghian, and Jerome L. Sackman. April 2006.

PEER 2005/15 *CPT-Based Probabilistic Assessment of Seismic Soil Liquefaction Initiation.* R. E. S. Moss, R. B. Seed, R. E. Kayen, J. P. Stewart, and A. Der Kiureghian. April 2006.

PEER 2005/14 *Workshop on Modeling of Nonlinear Cyclic Load-Deformation Behavior of Shallow Foundations.* Bruce L. Kutter, Geoffrey Martin, Tara Hutchinson, Chad Harden, Sivapalan Gajan, and Justin Phalen. March 2006.

PEER 2005/13 *Stochastic Characterization and Decision Bases under Time-Dependent Aftershock Risk in Performance-Based Earthquake Engineering*. Gee Liek Yeo and C. Allin Cornell. July 2005.

PEER 2005/12 *PEER Testbed Study on a Laboratory Building: Exercising Seismic Performance Assessment.* Mary C. Comerio, Editor. November 2005.

PEER 2005/11 *Van Nuys Hotel Building Testbed Report: Exercising Seismic Performance Assessment.* Helmut Krawinkler, Editor. October 2005.

PEER 2005/10 *First NEES/E-Defense Workshop on Collapse Simulation of Reinforced Concrete Building Structures.* September 2005.

PEER 2005/09 *Test Applications of Advanced Seismic Assessment Guidelines.* Joe Maffei, Karl Telleen, Danya Mohr, William Holmes, and Yuki Nakayama. August 2006.

PEER 2005/08 *Damage Accumulation in Lightly Confined Reinforced Concrete Bridge Columns.* R. Tyler Ranf, Jared M. Nelson, Zach Price, Marc O. Eberhard, and John F. Stanton. April 2006.

PEER 2005/07 *Experimental and Analytical Studies on the Seismic Response of Freestanding and Anchored Laboratory Equipment.* Dimitrios Konstantinidis and Nicos Makris. January 2005.

PEER 2005/06 *Global Collapse of Frame Structures under Seismic Excitations*. Luis F. Ibarra and Helmut Krawinkler. September 2005.

PEER 2005//05 *Performance Characterization of Bench- and Shelf-Mounted Equipment.* Samit Ray Chaudhuri and Tara C. Hutchinson. May 2006.

PEER 2005/04 *Numerical Modeling of the Nonlinear Cyclic Response of Shallow Foundations.* Chad Harden, Tara Hutchinson, Geoffrey R. Martin, and Bruce L. Kutter. August 2005.

PEER 2005/03 *A Taxonomy of Building Components for Performance-Based Earthquake Engineering.* Keith A. Porter. September 2005.

PEER 2005/02 *Fragility Basis for California Highway Overpass Bridge Seismic Decision Making*. Kevin R. Mackie and Božidar Stojadinović. June 2005.

PEER 2005/01 *Empirical Characterization of Site Conditions on Strong Ground Motion.* Jonathan P. Stewart, Yoojoong Choi, and Robert W. Graves. June 2005.

PEER 2004/09 *Electrical Substation Equipment Interaction: Experimental Rigid Conductor Studies.* Christopher Stearns and André Filiatrault. February 2005.

PEER 2004/08 *Seismic Qualification and Fragility Testing of Line Break 550-kV Disconnect Switches.* Shakhzod M. Takhirov, Gregory L. Fenves, and Eric Fujisaki. January 2005.

PEER 2004/07 *Ground Motions for Earthquake Simulator Qualification of Electrical Substation Equipment.* Shakhzod M. Takhirov, Gregory L. Fenves, Eric Fujisaki, and Don Clyde. January 2005.

PEER 2004/06 *Performance-Based Regulation and Regulatory Regimes.* Peter J. May and Chris Koski. September 2004.

PEER 2004/05 *Performance-Based Seismic Design Concepts and Implementation: Proceedings of an International Workshop.* Peter Fajfar and Helmut Krawinkler, Editors. September 2004.

PEER 2004/04 *Seismic Performance of an Instrumented Tilt-up Wall Building.* James C. Anderson and Vitelmo V. Bertero. July 2004.

PEER 2004/03 *Evaluation and Application of Concrete Tilt-up Assessment Methodologies.* Timothy Graf and James O. Malley. October 2004.

PEER 2004/02 *Analytical Investigations of New Methods for Reducing Residual Displacements of Reinforced Concrete Bridge Columns.* Junichi Sakai and Stephen A. Mahin. August 2004.

PEER 2004/01 *Seismic Performance of Masonry Buildings and Design Implications.* Kerri Anne Taeko Tokoro, James C. Anderson, and Vitelmo V. Bertero. February 2004.

PEER 2003/18 *Performance Models for Flexural Damage in Reinforced Concrete Columns.* Michael Berry and Marc Eberhard. August 2003.

PEER 2003/17 *Predicting Earthquake Damage in Older Reinforced Concrete Beam-Column Joints.* Catherine Pagni and Laura Lowes. October 2004.

PEER 2003/16 *Seismic Demands for Performance-Based Design of Bridges.* Kevin Mackie and Božidar Stojadinović. August 2003.

PEER 2003/15 *Seismic Demands for Nondeteriorating Frame Structures and Their Dependence on Ground Motions.* Ricardo Antonio Medina and Helmut Krawinkler. May 2004.

PEER 2003/14 *Finite Element Reliability and Sensitivity Methods for Performance-Based Earthquake Engineering*. Terje Haukaas and Armen Der Kiureghian. April 2004.

PEER 2003/13 *Effects of Connection Hysteretic Degradation on the Seismic Behavior of Steel Moment-Resisting Frames.* Janise E. Rodgers and Stephen A. Mahin. March 2004.

PEER 2003/12 *Implementation Manual for the Seismic Protection of Laboratory Contents: Format and Case Studies*. William T. Holmes and Mary C. Comerio. October 2003.

PEER 2003/11 *Fifth U.S.-Japan Workshop on Performance-Based Earthquake Engineering Methodology for Reinforced Concrete Building Structures*. February 2004.

PEER 2003/10 *A Beam-Column Joint Model for Simulating the Earthquake Response of Reinforced Concrete Frames.* Laura N. Lowes, Nilanjan Mitra, and Arash Altoontash. February 2004.

PEER 2003/09 *Sequencing Repairs after an Earthquake: An Economic Approach*. Marco Casari and Simon J. Wilkie. April 2004.

PEER 2003/08 *A Technical Framework for Probability-Based Demand and Capacity Factor Design (DCFD) Seismic Formats*. Fatemeh Jalayer and C. Allin Cornell. November 2003.

PEER 2003/07 *Uncertainty Specification and Propagation for Loss Estimation Using FOSM Methods.* Jack W. Baker and C. Allin Cornell. September 2003.

PEER 2003/06 *Performance of Circular Reinforced Concrete Bridge Columns under Bidirectional Earthquake Loading*. Mahmoud M. Hachem, Stephen A. Mahin, and Jack P. Moehle. February 2003.

PEER 2003/05 *Response Assessment for Building-Specific Loss Estimation.* Eduardo Miranda and Shahram Taghavi. September 2003.

PEER 2003/04 *Experimental Assessment of Columns with Short Lap Splices Subjected to Cyclic Loads*. Murat Melek, John W. Wallace, and Joel Conte. April 2003.

PEER 2003/03 *Probabilistic Response Assessment for Building-Specific Loss Estimation*. Eduardo Miranda and Hesameddin Aslani. September 2003.

PEER 2003/02 *Software Framework for Collaborative Development of Nonlinear Dynamic Analysis Program*. Jun Peng and Kincho H. Law. September 2003.

PEER 2003/01 *Shake Table Tests and Analytical Studies on the Gravity Load Collapse of Reinforced Concrete Frames*. Kenneth John Elwood and Jack P. Moehle. November 2003.

PEER 2002/24 *Performance of Beam to Column Bridge Joints Subjected to a Large Velocity Pulse.* Natalie Gibson, André Filiatrault, and Scott A. Ashford. April 2002.

PEER 2002/23 *Effects of Large Velocity Pulses on Reinforced Concrete Bridge Columns.* Greg L. Orozco and Scott A. Ashford. April 2002.

PEER 2002/22 *Characterization of Large Velocity Pulses for Laboratory Testing.* Kenneth E. Cox and Scott A. Ashford. April 2002.

PEER 2002/21 *Fourth U.S.-Japan Workshop on Performance-Based Earthquake Engineering Methodology for Reinforced Concrete Building Structures*. December 2002.

PEER 2002/20 *Barriers to Adoption and Implementation of PBEE Innovations.* Peter J. May. August 2002.

PEER 2002/19 *Economic-Engineered Integrated Models for Earthquakes: Socioeconomic Impacts.* Peter Gordon, James E. Moore II, and Harry W. Richardson. July 2002.

PEER 2002/18 *Assessment of Reinforced Concrete Building Exterior Joints with Substandard Details.* Chris P. Pantelides, Jon Hansen, Justin Nadauld, and Lawrence D. Reaveley. May 2002.

PEER 2002/17 *Structural Characterization and Seismic Response Analysis of a Highway Overcrossing Equipped with Elastomeric Bearings and Fluid Dampers: A Case Study*. Nicos Makris and Jian Zhang. November 2002.

PEER 2002/16 *Estimation of Uncertainty in Geotechnical Properties for Performance-Based Earthquake Engineering*. Allen L. Jones, Steven L. Kramer, and Pedro Arduino. December 2002.

PEER 2002/15 *Seismic Behavior of Bridge Columns Subjected to Various Loading Patterns*. Asadollah Esmaeily-Gh. and Yan Xiao. December 2002.

PEER 2002/14 *Inelastic Seismic Response of Extended Pile Shaft Supported Bridge Structures.* T.C. Hutchinson, R.W. Boulanger, Y.H. Chai, and I.M. Idriss. December 2002.

PEER 2002/13 *Probabilistic Models and Fragility Estimates for Bridge Components and Systems.* Paolo Gardoni, Armen Der Kiureghian, and Khalid M. Mosalam. June 2002.

PEER 2002/12 *Effects of Fault Dip and Slip Rake on Near-Source Ground Motions: Why Chi-Chi Was a Relatively Mild M7.6 Earthquake*. Brad T. Aagaard, John F. Hall, and Thomas H. Heaton. December 2002.

PEER 2002/11 *Analytical and Experimental Study of Fiber-Reinforced Strip Isolators*. James M. Kelly and Shakhzod M. Takhirov. September 2002.

PEER 2002/10 *Centrifuge Modeling of Settlement and Lateral Spreading with Comparisons to Numerical Analyses***.** Sivapalan Gajan and Bruce L. Kutter. January 2003.

PEER 2002/09 *Documentation and Analysis of Field Case Histories of Seismic Compression during the 1994 Northridge, California, Earthquake*. Jonathan P. Stewart, Patrick M. Smith, Daniel H. Whang, and Jonathan D. Bray. October 2002.

PEER 2002/08 *Component Testing, Stability Analysis and Characterization of Buckling-Restrained Unbonded Braces™*. Cameron Black, Nicos Makris, and Ian Aiken. September 2002.

PEER 2002/07 *Seismic Performance of Pile-Wharf Connections.* Charles W. Roeder, Robert Graff, Jennifer Soderstrom, and Jun Han Yoo. December 2001.

PEER 2002/06 *The Use of Benefit-Cost Analysis for Evaluation of Performance-Based Earthquake Engineering Decisions*. Richard O. Zerbe and Anthony Falit-Baiamonte. September 2001.

PEER 2002/05 *Guidelines, Specifications, and Seismic Performance Characterization of Nonstructural Building Components and Equipment*. André Filiatrault, Constantin Christopoulos, and Christopher Stearns. September 2001.

PEER 2002/04 *Consortium of Organizations for Strong-Motion Observation Systems and the Pacific Earthquake Engineering Research Center Lifelines Program: Invited Workshop on Archiving and Web Dissemination of Geotechnical Data, 4–5 October 2001*. September 2002.

PEER 2002/03 *Investigation of Sensitivity of Building Loss Estimates to Major Uncertain Variables for the Van Nuys Testbed*. Keith A. Porter, James L. Beck, and Rustem V. Shaikhutdinov. August 2002.

PEER 2002/02 *The Third U.S.-Japan Workshop on Performance-Based Earthquake Engineering Methodology for Reinforced Concrete Building Structures*. July 2002.

PEER 2002/01 *Nonstructural Loss Estimation: The UC Berkeley Case Study.* Mary C. Comerio and John C. Stallmeyer. December 2001.

PEER 2001/16 *Statistics of SDF-System Estimate of Roof Displacement for Pushover Analysis of Buildings.* Anil K. Chopra, Rakesh K. Goel, and Chatpan Chintanapakdee. December 2001.

PEER 2001/15 *Damage to Bridges during the 2001 Nisqually Earthquake.* R. Tyler Ranf, Marc O. Eberhard, and Michael P. Berry. November 2001.

PEER 2001/14 *Rocking Response of Equipment Anchored to a Base Foundation.* Nicos Makris and Cameron J. Black. September 2001.

PEER 2001/13 *Modeling Soil Liquefaction Hazards for Performance-Based Earthquake Engineering*. Steven L. Kramer and Ahmed-W. Elgamal. February 2001.

PEER 2001/12 *Development of Geotechnical Capabilities in OpenSees*. Boris Jeremić. September 2001.

PEER 2001/11 *Analytical and Experimental Study of Fiber-Reinforced Elastomeric Isolators*. James M. Kelly and Shakhzod M. Takhirov. September 2001.

PEER 2001/10 *Amplification Factors for Spectral Acceleration in Active Regions.* Jonathan P. Stewart, Andrew H. Liu, Yoojoong Choi, and Mehmet B. Baturay. December 2001.

PEER 2001/09 *Ground Motion Evaluation Procedures for Performance-Based Design.* Jonathan P. Stewart, Shyh-Jeng Chiou, Jonathan D. Bray, Robert W. Graves, Paul G. Somerville, and Norman A. Abrahamson. September 2001.

PEER 2001/08 *Experimental and Computational Evaluation of Reinforced Concrete Bridge Beam-Column Connections for Seismic Performance*. Clay J. Naito, Jack P. Moehle, and Khalid M. Mosalam. November 2001.

PEER 2001/07 *The Rocking Spectrum and the Shortcomings of Design Guidelines.* Nicos Makris and Dimitrios Konstantinidis. August 2001.

PEER 2001/06 *Development of an Electrical Substation Equipment Performance Database for Evaluation of Equipment Fragilities*. Thalia Agnanos. April 1999.

PEER 2001/05 *Stiffness Analysis of Fiber-Reinforced Elastomeric Isolators.* Hsiang-Chuan Tsai and James M. Kelly. May 2001.

PEER 2001/04 *Organizational and Societal Considerations for Performance-Based Earthquake Engineering*. Peter J. May. April 2001.

PEER 2001/03 *A Modal Pushover Analysis Procedure to Estimate Seismic Demands for Buildings: Theory and Preliminary Evaluation*. Anil K. Chopra and Rakesh K. Goel. January 2001.

PEER 2001/02 *Seismic Response Analysis of Highway Overcrossings Including Soil-Structure Interaction*. Jian Zhang and Nicos Makris. March 2001.

PEER 2001/01 *Experimental Study of Large Seismic Steel Beam-to-Column Connections.* Egor P. Popov and Shakhzod M. Takhirov. November 2000.

PEER 2000/10 *The Second U.S.-Japan Workshop on Performance-Based Earthquake Engineering Methodology for Reinforced Concrete Building Structures*. March 2000.

PEER 2000/09 *Structural Engineering Reconnaissance of the August 17, 1999 Earthquake: Kocaeli (Izmit), Turkey.* Halil Sezen, Kenneth J. Elwood, Andrew S. Whittaker, Khalid Mosalam, John J. Wallace, and John F. Stanton. December 2000.

PEER 2000/08 *Behavior of Reinforced Concrete Bridge Columns Having Varying Aspect Ratios and Varying Lengths of Confinement*. Anthony J. Calderone, Dawn E. Lehman, and Jack P. Moehle. January 2001.

PEER 2000/07 *Cover-Plate and Flange-Plate Reinforced Steel Moment-Resisting Connections.* Taejin Kim, Andrew S. Whittaker, Amir S. Gilani, Vitelmo V. Bertero, and Shakhzod M. Takhirov. September 2000.

PEER 2000/06 *Seismic Evaluation and Analysis of 230-kV Disconnect Switches.* Amir S. J. Gilani, Andrew S. Whittaker, Gregory L. Fenves, Chun-Hao Chen, Henry Ho, and Eric Fujisaki. July 2000.

PEER 2000/05 *Performance-Based Evaluation of Exterior Reinforced Concrete Building Joints for Seismic Excitation*. Chandra Clyde, Chris P. Pantelides, and Lawrence D. Reaveley. July 2000.

PEER 2000/04 *An Evaluation of Seismic Energy Demand: An Attenuation Approach*. Chung-Che Chou and Chia-Ming Uang. July 1999.

PEER 2000/03 *Framing Earthquake Retrofitting Decisions: The Case of Hillside Homes in Los Angeles.* Detlof von Winterfeldt, Nels Roselund, and Alicia Kitsuse. March 2000.

PEER 2000/02 *U.S.-Japan Workshop on the Effects of Near-Field Earthquake Shaking*. Andrew Whittaker, Editor. July 2000.

PEER 2000/01 *Further Studies on Seismic Interaction in Interconnected Electrical Substation Equipment.* Armen Der Kiureghian, Kee-Jeung Hong, and Jerome L. Sackman. November 1999.

PEER 1999/14 *Seismic Evaluation and Retrofit of 230-kV Porcelain Transformer Bushings*. Amir S. Gilani, Andrew S. Whittaker, Gregory L. Fenves, and Eric Fujisaki. December 1999.

PEER 1999/13 *Building Vulnerability Studies: Modeling and Evaluation of Tilt-up and Steel Reinforced Concrete Buildings*. John W. Wallace, Jonathan P. Stewart, and Andrew S. Whittaker, Editors. December 1999.

PEER 1999/12 *Rehabilitation of Nonductile RC Frame Building Using Encasement Plates and Energy-Dissipating Devices*. Mehrdad Sasani, Vitelmo V. Bertero, James C. Anderson. December 1999.

PEER 1999/11 *Performance Evaluation Database for Concrete Bridge Components and Systems under Simulated Seismic Loads*. Yael D. Hose and Frieder Seible. November 1999.

PEER 1999/10 *U.S.-Japan Workshop on Performance-Based Earthquake Engineering Methodology for Reinforced Concrete Building Structures*. December 1999.

PEER 1999/09 *Performance Improvement of Long Period Building Structures Subjected to Severe Pulse-Type Ground Motions*. James C. Anderson, Vitelmo V. Bertero, and Raul Bertero. October 1999.

PEER 1999/08 *Envelopes for Seismic Response Vectors.* Charles Menun and Armen Der Kiureghian. July 1999.

PEER 1999/07 *Documentation of Strengths and Weaknesses of Current Computer Analysis Methods for Seismic Performance of Reinforced Concrete Members*. William F. Cofer. November 1999.

PEER 1999/06 *Rocking Response and Overturning of Anchored Equipment under Seismic Excitations*. Nicos Makris and Jian Zhang. November 1999.

PEER 1999/05 *Seismic Evaluation of 550 kV Porcelain Transformer Bushings.* Amir S. Gilani, Andrew S. Whittaker, Gregory L. Fenves, and Eric Fujisaki. October 1999.

PEER 1999/04 *Adoption and Enforcement of Earthquake Risk-Reduction Measures.* Peter J. May, Raymond J. Burby, T. Jens Feeley, and Robert Wood. August 1999.

PEER 1999/03 *Task 3 Characterization of Site Response General Site Categories*. Adrian Rodriguez-Marek, Jonathan D. Bray and Norman Abrahamson. February 1999.

PEER 1999/02 *Capacity-Demand-Diagram Methods for Estimating Seismic Deformation of Inelastic Structures: SDF Systems*. Anil K. Chopra and Rakesh Goel. April 1999.

PEER 1999/01 *Interaction in Interconnected Electrical Substation Equipment Subjected to Earthquake Ground Motions*. Armen Der Kiureghian, Jerome L. Sackman, and Kee-Jeung Hong. February 1999.

PEER 1998/08 *Behavior and Failure Analysis of a Multiple-Frame Highway Bridge in the 1994 Northridge Earthquake*. Gregory L. Fenves and Michael Ellery. December 1998.

PEER 1998/07 *Empirical Evaluation of Inertial Soil-Structure Interaction Effects.* Jonathan P. Stewart, Raymond B. Seed, and Gregory L. Fenves. November 1998.

PEER 1998/06 *Effect of Damping Mechanisms on the Response of Seismic Isolated Structures*. Nicos Makris and Shih-Po Chang. November 1998.

PEER 1998/05 *Rocking Response and Overturning of Equipment under Horizontal Pulse-Type Motions*. Nicos Makris and Yiannis Roussos. October 1998.

PEER 1998/04 *Pacific Earthquake Engineering Research Invitational Workshop Proceedings, May 14–15, 1998: Defining the Links between Planning, Policy Analysis, Economics and Earthquake Engineering*. Mary Comerio and Peter Gordon. September 1998.

PEER 1998/03 *Repair/Upgrade Procedures for Welded Beam to Column Connections*. James C. Anderson and Xiaojing Duan. May 1998.

PEER 1998/02 *Seismic Evaluation of 196 kV Porcelain Transformer Bushings.* Amir S. Gilani, Juan W. Chavez, Gregory L. Fenves, and Andrew S. Whittaker. May 1998.

PEER 1998/01 *Seismic Performance of Well-Confined Concrete Bridge Columns.* Dawn E. Lehman and Jack P. Moehle. December 2000.

The Pacific Earthquake Engineering Research Center (PEER) is a multi-institutional research and education center with headquarters at the University of California, Berkeley. Investigators from over 20 universities, several consulting companies, and researchers at various state and federal government agencies contribute to research programs focused on performance-based earthquake engineering.

These research programs aim to identify and reduce the risks from major earthquakes to life safety and to the economy by including research in a wide variety of disciplines including structural and geotechnical engineering, geology/seismology, lifelines, transportation, architecture, economics, risk management, and public policy.

PEER is supported by federal, state, local, and regional agencies, together with industry partners.

PEER Core Institutions:
University of California, Berkeley (Lead Institution)
California Institute of Technology
Oregon State University
Stanford University
University of California, Davis
University of California, Irvine
University of California, Los Angeles
University of California, San Diego
University of Southern California
University of Washington

PEER reports can be ordered at http://peer.berkeley.edu/publications/peer_reports.html or by contacting

Pacific Earthquake Engineering Research Center
University of California, Berkeley
325 Davis Hall, mail code 1792
Berkeley, CA 94720-1792
Tel: 510-642-3437
Fax: 510-642-1655
Email: peer_center@berkeley.edu

ISSN 1547-0587X